UNIVERSITY
of
GLASGOW

Spectral and Spatial Characteristics of Solar Flare Hard X-ray Emission : A Non-uniformly Ionised Thick Target Approach.

by

Guillian K. M^{c}Arthur B.Sc. Hons.

Thesis
submitted to the
University of Glasgow
for the degree of
Ph.D.

Astronomy and Astrophysics Group
Department of Physics and Astronomy,
University of Glasgow,
Glasgow G12 8QQ

April 2000

ProQuest LLC.
789 East Eisenhower Parkway
P.O. Box 1346
Ann Arbor, MI 48106 – 1346

In memory of Michael Mechan

Acknowledgements

Writting this thesis would not have been possible without the friendly support, encouragement and extereme patience of all the past and present inmates of the A & A group. So here I name and shame those offenders who helped and are therefore also a little responsible for the following.

My supervisors Prof. John Brown and Dr. Alec MacKinnon have what seems endless insight, knowledge and ideas on solar physics. I only hope that I've picked up a fraction of their talent for spotting great ideas. As this thesis is so much a continuation of an idea from John's own thesis, I really have to thank you for introducing me to this problem. No! really I must. It's a clear example of if you wait long enough some sucker (Ph.D. student) will come along. I must also thank Prof. Gordon Emslie, who also showed his own tenaciousness, insight and inspiration with this unique non-unique problem. To Dr. Sarah Matthews thanks for putting up with so many inane emails on *YOHKOH* software and to Dr. Andrew Conway thanks for answering the majority of my BUT WHY questions. Far more importantly Andrew, thanks for all your post-party fry ups, which will forever have a place in my arteries, and has at least taught me how to fry an egg properly.

The people who have suffered the most throughout these wilderness years are all those I've shared and office with. I apologise now for the mess of my desk and turning the office into a sanctuary for lost rottweillers. Condolenseces especially must go to Dr. Noelle "Nellie" Daly, who endured three whole years. I firmly believe that it was the need to leave the Rottie sanctuary that encouraged her to finish well on time and not that she's Super-Limerick lass, willing to fight any injustice and wrongdoing from pollution, third world debt to badly designed milk cartoon lids. Thanks have to go to Dr. Keith Macpherson for introducing me to hangovers; to Dr. Andy Woods for keeping your trousers on in the office most of the time; to Suzanne Martland for that sunny smile and for believing me when

I told you tomatoes were alcoholic; to Dr. Aidan Keane for keeping your alterego White Van Man under control; to Paul "Windy" Millar for not drenching me with beer; to Paul Allan for telling me I'm such an idiot but still asking for my IDL advice and finally to Esther Howells for some much needed sanity.

Now in oscar style I also have to thank Eve for her advice and dirty jokes; to Helen for demonstrating the STEPS dances and to Gail for not. To Neal and Hugh thanks for the DIY advice; to Martin for knowing so much pub quiz trivia; to Iain for dancing in Godspell and Chris thanks for being another ginger (but I don't bitch!) To Shashi and Graeme thanks for keeping the system running most of the time and Norman thanks for pointing out that "Landau is a MAN!". To Scott and Victor thanks for finding the police station, British Consulate and every steak house in Boston and Daphne thanks for trying to keep us organised. Lastly in the group I have to thank Dr. Richard Barrett, not only have you encouraged, advised and inputed more to this work than I could of asked for, but you and Ute have helped merryily pass away many night in the pub.

I would like to also thank my friends outside the department, especially Craig, for all their encouragement over the years and my family for feeding and wateing me at regular intervals over the years.

Summary

Hard X-ray emission in flares is a signature of high energy electron populations in the solar plasma. The major role these populations have in many solar flare models means that the spectral, spatial and temporal characteristics of hard X-rays will be associated with many of the diverse plasma processes ocuring during a flare. These include where and how energy release occurs, which mechanism may accelerate the particles, some methods of energy transport through the flare and eventually the radiative and atmospheric response to the distribution of the flare energy budget.

The work of this thesis has been concerned with the effects introducing the non-uniform ionisation profile of the flare atmosphere has on the thick target HXR spectra and consequent interpretation of the spectra. This has involved both the theoretical modelling and observational analysis of X-ray flare emission. The data for this research was primarily obtained from the instruments on board the *YOHKOH* satellite. These instruments include a hard X-ray spectrometer (HXS), a grazing incidence soft X-ray telescope (SXT) and a Fourier-synthesis hard X-ray telescope (HXT). Also available is high resolution hard X-ray spectra taken by the *HIREX* balloon experiment.

Chapter 1 gives an overview of hard X-ray observations from solar flares and describes how these observations are interpreted in the context of the varying hard X-ray production models and the implications therefore on acceleration mechanisms. This chapter also includes a brief descripition of other flare emissions, mechanisms for energy release and how these mechanisms are incorporated into the physical model of flares.

Chapter 2 introduces the formulation used in this analysis for including a non-uniform ionisation profile into the the thick target model of HXR production. Using this formalism, comparisons are made of HXR yields and inferred electron spectra for the fully ionised atmosphere with a more realistic step-function atmosphere. In doing so the differing spectral

characteristics of these models are desrcribed, the ultimate effect on energy and number flux budgets for these differing spectra determined and the resultant non-uniqueness of the HXR bremsstrahlung inversion for a non-uniform atmosphere discussed.

From this point the analysis of HXR spectra moves in two directions. Firstly in Chapter 3 high resolution data from the *HIREX* balloon experiment is inverted using regularisation techniques. In previous analyses of this dataset, which are described in detail during this chapter, the features in the photon spectra and inferred electron spectra were thought to be suggestive of a particular mechanism of acceleration (d.c. field acceleration). In our analysis, we investigate if these features in the inferred electron spectra can instead be reproduced by choosing an appropriate atmospheric struture, and therefore cannot be considered signatures of any particular acceleration mechanism.

In chapter 4 a second approach is taken to utilise HXR spectra as a diagnostic of the flare atmosphere. By assuming that the observed spectral features are caused entirely by the effects on non-uniform ionisation, (i.e. the electron population is featureless, so any break is caused by the propagation effect) and incorporating the response function of the spectrometer we attempt to relate HXR spectra to particular coronal column density.

In chapter 5 this approach is used for HXR spectral observations taken by the hard X-ray spectrometer onboard *YOHKOH*. Based on these spectral observations estimates of the amount of material between the acceleration site and the top of the chromosphere are made. These values can be compared to estimates of the column density for the SXR loops using SXT and also those given by time of flight analysis of the hard X-ray bursts to determine if the estimates are physically realistic.

Finally, in chapter 6, results of the previous chapters are drawn together, providing a summary of the work achieved in this thesis. At the same time improvements to the analysis are discussed as are the possibilites for this analysis with the expected festival of data available soon from HESSI.

Contents

List of Tables

List of Figures

Chapter 1

Solar Flare Hard X-rays: Observations and Theory

"Solar Flares are complex ..."

(Sweet, 1969)

1.1 Introduction

Sweet, (1969) described solar flares as "complex, transient excitations of the solar atmosphere above the magnetically active regions of the surface involving enhanced thermal and radio emission, hard X-rays, cosmic rays and plasma ejection. Their origin is not yet understood after more than a century of study since the first recorded observations." Since then, great progress has be en made in the understanding of flares, through continual advances in both space and ground based instrumentation, with magnetic reconnection now the pillar of solar flare theory

In this chapter, I intend to review the spectral, temporal and spatial observations of flare hard X-rays, to hopefully discuss their main theoretical implications and limitations. A theme to all flare review literature, though, must be an emphasis of the diverse phenomena that solar flares exhibit. Rapid enhancement across the electromagnetic spectrum, lightning acceleration of particles, ejection of plasma configurations and transformation of magnetic field lines are all observed during solar flares. Inevitably, with such diverse features, to interpret observations of hard X-rays other flare related phenomena must be

discussed, though not as comprehensively.

1.2 Flare Structure, Models and Classification Systems

Generally a flare is observed to develop through three main phases as seen in Figure 1.1, overall releasing $10^{28} - 10^{32}$ ergs most of which is radiated in the soft X-ray range.

• Pre-flare Phase : Indicated by a gradual brightening in H_α, soft X-rays and cm radio emission typically lasting $\approx$ few minutes. The pre-flare phase is common but is not observed in all flares.

• Impulsive Phase : Characterised by rapid, intense brightening in H_α and hard X-rays, when the rate of energy release is highest and emission from highest energy particles detected, typically lasting less than 5 minutes.

• Gradual Phase : The flare reaches its largest area and energy output. Most of the energy is radiated in soft X-rays from hot plasma between 1-3$\times 10^7$K. The gradual phase lasts for tens of minutes.

Spatially a flare covers less than 1% of the solar surface and flares are divided into two main categories : large two ribbon flares or small compact flares (Pallavicini et al., 1977). In large two ribbon flares, as seen in Figure 1.2, the foot-point emission forms two bright ribbons in H_α, which are observed to move apart as the flare progresses. As well as emission from the foot-points emission also occurs in an arcade of post flare loops. Small, compact flares occur in small loops lower in the corona.

1.2.1 Classification Systems

The object of classifying flares is to construct some order out of the many varied observables, to eventually gain some insight into the ongoing physical process. Historically this classification has been based on the H_α appearance of the flare.

H_α Significance

H_α flares are ranked by importance on the the area of the H_α brightening. The area, corrected for projection effects, is used because it can be easily measured. The relationship

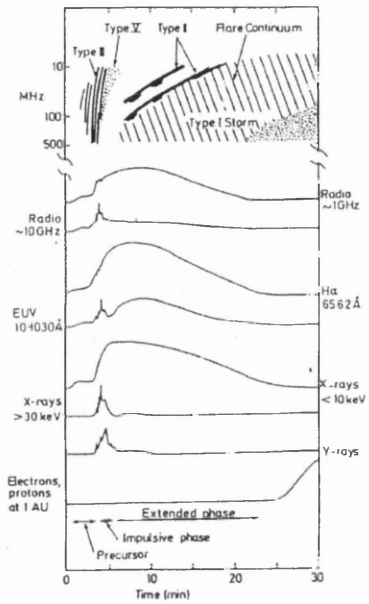

Figure 1.1: The temporal development of varying types of flare emission during the different phases of the flare (from Kane, 1974).

Figure 1.2: The great 'sea horse' flare of Aug. 1972, a typical example of a large two ribbon flare. The image taken in the blue wing of H_α (H_α-0.5 Å) shows the two-ribbon structure late in the event. The ribbons have separated and elongated, the space between them being filled by loop prominences condensing from the corona at the loop tops. The fibril structure also becomes perpendicular to the loops (Zirin and Tanaka, 1973).

between corrected area and H_α class can be seen in Table 1.1 below. In addition the

Corrected Area		Relative Intensity
Square degrees	Millionth of hemisphere	Evaluation
≤2.0	≤200	S (*f,n,b*)
2.1-5.1	200-500	1 (*f,n,b*)
5.2-12.4	500-1200	2 (*f,n,b*)
12.5-24.7	1200-2400	3 (*f,n,b*)
>24.7	>2400	4 (*f,n,b*)

Table 1.1: H_α flare classification scheme, from Zirin, 1988 (p. 347).

intensity of the flare is indicated by the suffix (*f,n,b*) denoting the flare as faint,normal or bright.

Soft X-ray (GOES) Class

As a large fraction of a flare's radiated energy appears in the soft X-ray region , this classification scheme is based on the energy flux detected in the 1-8 Åwaveband as observed by the GOES satellite series. The broad classification uses a letter (B, C, M or X) followed by a number. The letter denotes the order of magnitude of flux detected, (10^{-4}, 10^{-3}, 10^{-2}, 10^{-1} erg $cm^{-2}s^{-1}$ respectively), while the number denotes the flux in these base amounts.

Hard X-ray Type

In hard X-rays flares have been classified into three main classes. Unlike the previous classification schemes, which were based on geometric extent or intensity, this scheme is concerned with the duration and shape of the HXR light curve. (Tanaka, 1987) defines these three classes as :

HXR Type	Basic Description
A *Hot Thermal*	Exhibits a smoothly varying flux vs. time profile, with limited and soft HXR emission. Presumably from compact, low altitude sources with T$\sim 3-4\times10^7$ K corresponding to the energisation of a single loop.
B *Impulsive*	Exhibits 'spiky' flux vs. time profile. Associated with 'spiky' microwave emission and larger loops. The HXR and microwave emission is presumed to come from the loop footpoints or low corona.
C *Gradual-Hard*	Has a long-enduring time profile (> 30 min) with gradual peaks and a hard spectrum. Associated with strong microwave emission high in the corona from very large loops (≥ 50,000 km)

Table 1.2: HXR Classification Types.

1.3 Hard X-ray Production Models

The hard X-ray photon energy spectrum was first gauged from two data points, in the 20-500 keV range, obtained by a balloon-borne experiment, observing the 20th March 1958 event (Peterson and Winckler, 1959). They attributed the observations to bremsstrahlung emission from high energy (0.05-1.0 MeV) electrons stopping in the photosphere. Other possible mechanisms for production of X-rays in this energy range do exist. There is inverse Compton scattering of the ambient thermal photons and also magneto-bremsstrahlung. For the physical parameters of a typical flare, Korchak (1967, 1971) concluded that electron-ion collisional bremsstrahlung was the primary mechanism producing hard X-rays. Emission due to magneto-bremsstrahlung was deemed unlikely, as it would require the electron distribution function to extend into the several MeV range and would then imply high energy loss rates. Inverse Compton scattering, although it could significantly contribute to the hard X-rays, would require an extremely low density. McClements and Brown, 1986 revisited these ideas for the special case of flares exhibiting intense microwave emission and found even then extreme source parameters were needed. Thus all models suggested for the production of flare hard X-rays have invoked populations of electrons (20-500 keV) as an essential ingredient.

1.3.1 Non-thermal Models

Having stated that bremsstrahlung production models require a population of high energy electrons, specific models are classified on the the basis of the distribution function of these populations. Non-thermal models for HXR emission invoke a population of electrons incident on a much colder target, i.e. the high energy electrons form a distinct component to the total particle distribution. In many non-thermal models this electron population take the form a of beam incident on the cold target, where a beam is defined loosely where the distribution function has $< v_{\|} > \gg < v_{\perp} >$ to the given direction of the beam. Other signatures which imply electron beams in the corona include radio burst (Types (III),(II) and(I)) although these beams are moving outwards from the corona while for the production of hard X-rays the beams are often assumed to be moving towards the chromosphere.

Characteristics of the electrons escape timescale (τ_e) from, and energy loss timescale

(τ_d) in, the source define whether a non-thermal model is further classified as a 'thick' or 'thin' target model.

Thin Target Limit :- $\tau_e \ll \tau_d$.

In this case the beam electrons leave the hard X-ray source with no significant change in the energy of the electrons. By describing the electrons energy distribution function as $F(E,r)$ for an extended source, the bremsstrahlung flux for photons of energy ϵ, observed at Earth, is

$$I(\epsilon) = \frac{1}{4\pi R^2} \int_V n_p(r) \int_\epsilon^\infty F(E,r) Q_B(\epsilon, E)\, dE\, dV \quad \text{(photons/cm}^2\text{/s/keV)} \qquad (1.1)$$

where $n_p(r)$ is the background proton density, $Q_B(\epsilon, E)$ the differential bremsstrahlung cross-section and $R = 1AU$. In the thin target case the emission is dependent on the volume integral of ambient proton density. Thus the rate of emission depends on the density, volume and geometry of the source (Lin, 1974). Physical flare scenarios where the thin target interpretation is applicable would include electrons propagating outwards into the corona or electrons confined in a low density (no collisions) magnetic trap. Individual small regions of an imaged source, or where some if not most of the target is obscured by the photospheric limb, can also be treated in the thin target limit.

Thick Target Limit :- $\tau_e \gg \tau_d$.

In this case, the electrons lose all of their energy as they propagate through the source. The energy loss mechanism is predominantly Coulomb collisions on the ambient particles, although non-collisional energy loss mechanisms are also applicable. For Coulomb collisions, the energy loss rate through the source can be expressed as

$$\frac{dE}{dt} = -Q_c(E) n_p v(E) E = -4.9 \times 10^{-9} n_p E^{-1/2} \quad \text{(keV/s)} \qquad (1.2)$$

$Q_c(E)$ being the Coulomb energy loss cross-section. When the instrumental time resolution is much longer than τ_d, thick target HXR emission is independent of the density of the source (Brown, 1971). The photon flux from an initial electron distribution of $F_0(E_0)$ would be

$$I(\epsilon) = \frac{1}{4\pi R^2} \int_{E_0=\epsilon}^\infty F_0(E_0) \int_\epsilon^{E_0} \frac{Q_B(\epsilon, E)\, dE}{E Q_E(E)}\, dE_0 \quad \text{(photons/cm}^2\text{/s/keV)} \qquad (1.3)$$

where $Q_E(E)$ is the total energy loss cross-section.

Trap plus Precipitation Model

Another model, for producing non-thermal hard X-rays is the Trap plus Precipitation model (Brown (1975), Melrose and Brown (1976), Bai and Ramaty (1979)). Here electrons are injected into the corona, and while one section of the population is trapped in the low density corona by magnetic mirroring, the remaining electrons precipitate down to the much denser chromospheric footpoints. Thus for the trapped electrons, bremsstrahlung emission is treated in the thin target limit while for the precipitating electrons emission is treated in the thick target limit. The trap plus precipitation model is a thick target model in the sense that $\tau_e \rightarrow \infty$ for all electrons, but one in which some electrons have lifetimes much longer than the instrumental time resolution.

1.3.2 A Thermal Model

An alternative interpretation of the data was presented by Chubb et al. (1966), that the emission was (free-free) bremsstrahlung from an isothermal plasma, where the isothermal bremsstrahlung spectrum can be written as (Crannell et al., 1978)

$$I(\epsilon) = 1.3 \times 10^{-42}(n^2V)\epsilon^{-1.4}(k_BT)^{-0.1}e^{-\epsilon/k_BT} \quad \text{(photons/cm}^2\text{/s/keV)}. \qquad (1.4)$$

Here the density n, volume V, temperature T and photon energy ϵ are in units cm^{-3}, cm^3, K, keV respectively. This interpretation requires that the temperature of the plasma is in excess of 10^8 K. At such high temperatures the conductive cooling rate would be shorter than the observed burst time. It would also be extremely difficult to confine such a hot plasma because of their long collisional mean free path (Kahler, 1971a,b). These theoretical difficulties of a thermal model have been countered by Brown et al., 1979. As a result of such long mean free paths, the very energetic electrons of the hot source will stream out into the surrounding cooler plasma. The resulting electric field drives return currents unstable to ion-acoustic waves, generating ion-acoustic wave fronts which confine the bulk of the electrons.

1.4 HXR Spectral Characteristics

Through the 60's-70's, with the OGO satellites, the spectral resolution of detectors were enhanced with the use of scintillation detectors. They broadly covered an energy range of

10-200 keV with 8-9 channels. The results of these missions have showed that the hard X-ray emission can in general be described by a power-law having the form

$$I(\epsilon) = a\epsilon^{-\gamma} \qquad (\text{photons/cm}^2\text{/s/keV}), \tag{1.5}$$

with the photon index, γ, varying between 3-8. The range of photon index measurable though is dependent on the detectors spectral resolution, scintillation detectors being unable to observe $\gamma > 8$.

Using the power law description of the HXR spectra, then for the thick and thin model, the parent electron spectra can be similarly parameterised by a power law with a spectral index δ of

$$\delta = \gamma - 1 \qquad \text{Thin Target}$$

$$\delta = \gamma + 1 \qquad \text{Thick Target}$$

and flux constant (number of electrons per second at 1 keV) A of

$$A = 1.05 \times 10^{42} \frac{\gamma - 1}{B\left(\gamma - 1, \frac{1}{2}\right)} . \frac{a}{n_i} \qquad \text{Thin Target}$$

$$A = 3.28 \times 10^{33} \gamma(\gamma - 1) B\left(\gamma - \frac{1}{2}, \frac{3}{2}\right) a \qquad \text{Thick Target}$$

(Hudson et al., 1978), where B denotes the Beta function. The spectral index of the thick target HXR spectrum being two less (harder) than the thin target case for the same electron population of index δ due to the form of $Q_E(E)$ assumed here.

1.4.1 Energy Content of Beam

The parameters characterising the electron distribution are used to estimate the power and and total number of electrons contained in the non-thermal beam, the power being,

$$\mathcal{E} = \int_{E_1}^{\infty} A E_o^{-\delta} E_o dE_o = \frac{A}{\delta - 2} E_1^{2-\delta}, \quad \text{Power (keV/s)}. \tag{1.6}$$

For the thick target model, the total energy in the non-thermal electrons is comparable to the total energy content of the flare i.e. several tenths of the budget. This result is essentially a consequence of the low ratio of energy loss through bremsstrahlung to energy loss through collisions.

Severe ambiguity exist in determining to what energy level the non-thermal population extends down to i.e. E_1. Inference of E_1 from changes in the shape of the spectra at low

energy may be possible, but no positive method of determining E_1 has been available. This results primarily from the relatively low energy resolution of detectors, smearing of the HXR spectra caused by the bremsstrahlung cross-section and most seriously the significant contribution of thermal bremsstrahlung from the flare loop heated by the non-thermal electrons. As a result the choice of low energy cut-off in the non-thermal population is arbitrary, most often estimates of 20-25 keV are taken (Hoyng et al., 1976) although observations of a flare with a power law to 5 keV have been suggested (Kane et al., 1979). This could lead to a severe under estimate of the beam energy, as the steepness of the spectra makes the energy content extremely sensitive to the value of E_1.

As a non-thermal electron population is required to form a significant component of the flare energy budget, it leads to the view that they must be the primary product of the energy release mechanism and that their propagation heats the atmosphere gives rise to the thermal response. While this may provide an effective, rapid mechanism for transporting energy through the flare and simplifies the model for secondary flare phenomena, it places powerful constraints on the efficiency of the acceleration mechanism, with such high power requirements during the impulsive phase. Indeed, Smith, 1980 considered in detail various acceleration mechanisms and found that none of them could produce the required efficiency. As the energy demands of a thick target model are the lowest for all non-thermal models, these severe constraints often lead to the favouring of a thermal interpretation.

1.4.2 Electron Number Flux and Return Currents

The number of electrons in the beam passing a point in 1 second can be estimated in a similar method as the energy content.

$$\mathcal{F} = \int_{E_1}^{\infty} A E_o^{-\delta} dE_o = \frac{A}{\delta - 1} E_1^{1-\delta}, \quad \text{Number Flux (electrons/s).} \tag{1.7}$$

By this method, the total number of electrons in the beam has been estimated to be as high as $\sim 10^{36}$ s^{-1}. This would not only imply a region comparable to the total flare size supplying the electrons but, if they all travel in the same direction, that the motion of this vast number of electrons would invoke a magnetic field $B \sim 10^8$ Gauss around a beam of radius 10^9 cm. This magnetic field is not only unobserved but would have an associated energy of $\sim 10^{42}$ ergs, ten orders of magnitude greater than the total energy of the flare

process and a current in excess of 10^{17} A.

For the currents involved here to propagate then a return current (cf. Section 2.2.4) of background electrons must be generated. Here the much denser background electrons must slowly drift in the opposing direction to the beam such that

$$n_{\rm back} v_D \approx n_{\rm beam} v_{\rm beam},$$

(where v_D is the drift velocity of the ambient plasma, $n_{\rm back}$ the ambient plasma density, $n_{\rm beam}$ is the beam density and $v_{\rm beam}$ the speed associated with the mean energy of the particles in the beam). The drift of background electrons locally neutralise these large beam currents but contains much less energy than the propagating electron beam as long as the beam is dilute i.e. $n_{\rm beam} << n_{\rm back}$.

The return current is maintained by a small electric field and this field also acts on the beam electrons slowing them down. In effect energy is taken from the beam to drive the return current. The return current losses for a stable return current is treated simply as the Ohmic losses of the electron beam against the small electric field and are low in comparison with Coulomb losses. The return current though can become unstable, if the drift velocity exceeds a threshold for generating an plasma wave, such as ion-acoustic, then return current losses and collisional losses can be of similar magnitude.

Thus return currents while neutralising the beam current and providing a mechanism for replenishing the acceleration region of electrons, their existence only worsens the energy demands of the model, increasing the already high efficiency of the acceleration mechanism required.

1.4.3 Spectral Index Evolution

It was recognized that, during an event, the spectral index of the flare evolves. Most often, (Kane and Anderson, 1970, Dennis et al., 1981), the hard X-ray spectrum has a soft-hard-soft pattern, indeed during each flux peak the spectral index is observed to harden on the rise and soften on decay. This evolution pattern is one of the criteria for classifying the flare as an impulsive (type B) flare. Gradually varying hard X-ray bursts (type C flares) exhibit a progressively hardening spectral (soft-hard-harder) evolution over the duration of the peaks (Cliver et al., 1986, Kosugi et al., 1988). The pattern of spectral index evolution then constitutes a constraint on the combined acceleration (heating) and

propagation (cooling) of hard X-ray producing electrons.

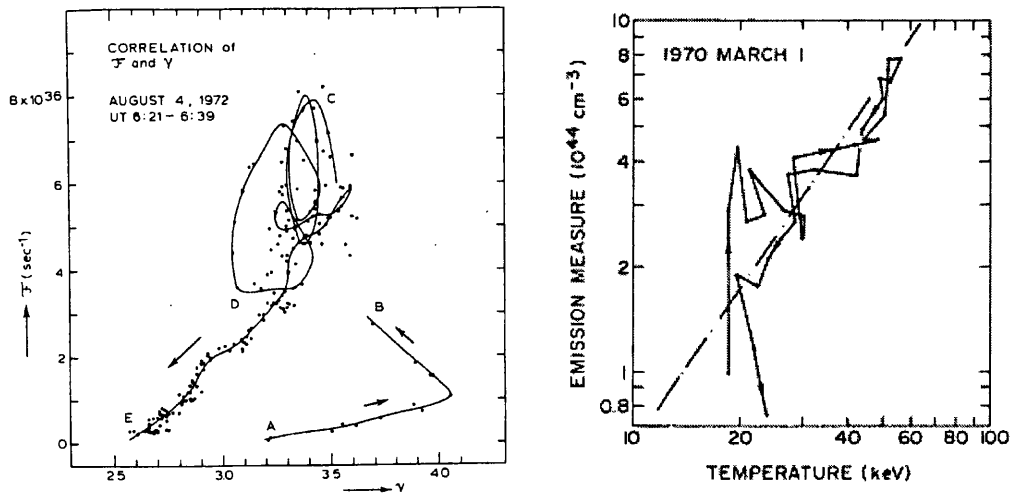

(a) (b)

Figure 1.3: Correlation Diagrams between (a) Flux and Spectral Index measured during the course of an Impulsive Flare, showing the general 'soft-hard soft' pattern. (b) the inferred Emission Measure and Temperature evolution of an impulsive flare, with the dash-dotted line representing the relationship for an adiabatic process with index $\kappa = 5/3$.

For a thermal model (Brown et al., 1979), the predicted evolution of spectral index contradicts those of observations. The spectral evolution, in thermal terms, can be modelled as the temperature and emission measure increasing with rising flux, and decreasing with flux decay Matzler et al. (1978). The plasma though is expected to cool as it expands, i.e. the spectrum softens as the flux increases. Refinements to a thermal model have been suggested, to explain the observed signature of Em and T. These include temporally extending the energy release and invoking adiabatic compression by magnetic field variations (Emslie, 1981a). Alternatively having many small thermal sources with effective lifetimes below the instrumental time resolution (Brown et al., 1980) could reproduce the observed behaviour of EM against T. Specifically as the flaring process began hot sources would be produced at an increasing rate with increasing temperature until burst peak, thereafter at a declining rate and temperature. This situation is closely analogous to the continuous injection thick target model, where as the energy loss time is much less than the instrumental resolution, so the evolution of spectral index is governed only by the modulations of the acceleration process. Events with progressive hardening have been

shown to have relatively strong microwave emission with comparatively low peak frequency (Bai and Dennis, 1985) and also closely associated with high energy interplanetary proton events (Kiplinger, 1995). This indicates progressively hardening events occur at higher altitudes, where the magnetic field strength is weaker, the particle density lower and release of accelerated protons is more favourable. The weaker magnetic field strength is inferred from the lower peak frequency of the gyro-synchrotron emission of field orbiting electrons. In fact, for a typical gradual limb flare the hard X-ray source is located $\approx 5 \times 10^4$ km above the chromosphere, while for an impulsive flare the site is located $\approx 10^4$ km above. This indicates that loop structures in hardening flares have a higher mirror ratio, so more trapped electrons exist and that the spectral hardening could be explained by decay of electrons in the trap (Bai and Dennis, 1985).

1.4.4 Double Power Law

The widespread use of a power law description for HXR spectra does not mean that such a generalisation is the only or most accurate description of the spectra. Neither does it mean that one general characterisation is satisfactory over the whole hard X-ray range. Indeed, in a study of energy spectra from OSO-7 events (Elcan, 1978) it was found that the majority of events were better characterised by a double power law (broken power law) expressed by

$$\begin{aligned} I(\epsilon) &= A_1 \epsilon^{-\alpha}, & \epsilon \leq \epsilon_{br}; \\ &= A_2 \epsilon^{-\beta}, & \epsilon > \epsilon_{br}; \end{aligned} \tag{1.8}$$

$$\text{where } A_2 = A_1 \epsilon_{br}^{\beta-\alpha}. \tag{1.9}$$

This is also the case for of a flare observed with exceptionally high spectral resolution and analysed by Lin and Schwartz (1987).

The break energy ϵ_{br} observed by Lin and Schwartz (1987) was between 40-60 keV, while previously others have estimated the break in the 60-100 keV range (Frost, 1969; Kane and Anderson, 1970; Frost and Dennis, 1971. The 60-100 keV range is consistent with the break energy determined at peak flux from flares observed by the HXRBS onboard SMM, (Dulk et al., 1992, Winglee et al., 1991a,b). Here the break energy at peak flux was $\sim$ 100 keV and the spectrum almost always breaks down i.e. $\beta > \alpha$ by $\sim 1 - 2$ (cf.

Figure 1.4). This study also showed that there is little or no dependence between the spectral slopes, total hard X-ray flux or break energy.

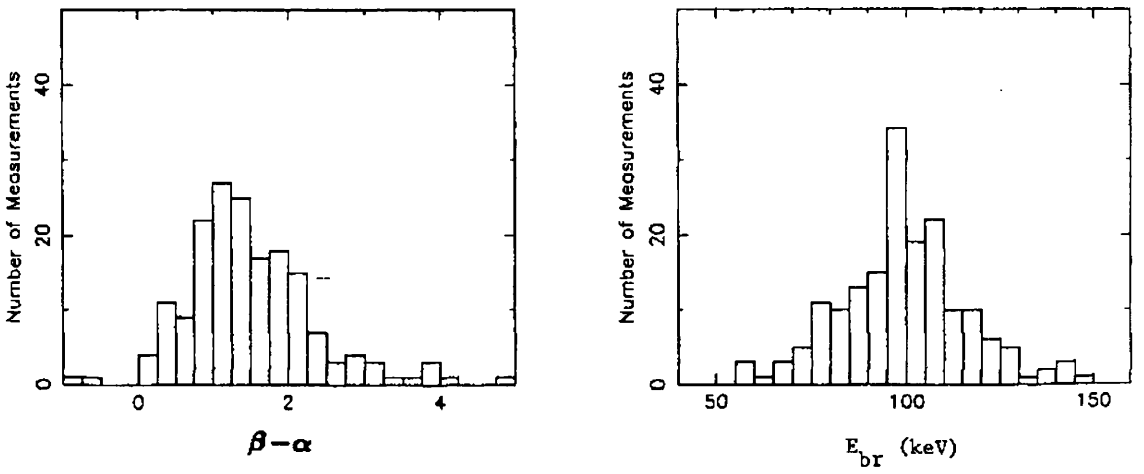

Figure 1.4: Histograms of the difference in spectral index $\beta - \alpha$ and the break energy ϵ_{br} for the 174 bursts during 93 flares observed by the HXRBS onboard SMM. (From Dulk et al., 1992).

The existence of this break in the spectral index is presented by Lin and Schwartz (1987) and Winglee et al. (1991a,b) as evidence of the important role electric fields play in the particle acceleration process. The situation is thought analogous to the d.c. electric fields present in the Earth's auroral zone (Mozer et al., 1980) which accelerate electrons into an energy distribution which peaks at the energy corresponding to the potential drop experienced by the electrons and then decreases more rapidly. If this distribution of electrons was responsible for thick target bremsstrahlung then the spectrum would resemble a broken power law with break energy at the electron energy peak and hence corresponds to the potential drop accelerating the electrons.

1.4.5 Super Hot Component

During the peak of emission of the flare observed by the 1980 balloon and examined by Lin et al. (1981), the spectra exhibited a strong steepening below $\approx$ 40keV. The upturn was thought consistent with thermal bremsstrahlung emission (Emslie et al., 1989) from a 'superhot' component ($\approx 3 \times 10^7$K). In addition soft X-ray diagnostics on Fe_{XXVI} lines (Tanaka, 1987) has indicated the presence of ($T \gtrsim 30$ MK). Nitta and Kentaro (1997)

reported the first direct X-ray imaging of the location of superhot plasma for a solar flare. While the dominant soft X-ray emission is from a small loop structure, superhot temperatures are inferred in a longer loop structure which overlaps with the low-energy hard X-ray sources.

1.4.6 γ-ray Emission and Proton Beams

During a flare γ-ray emission is commonly produced, both as continuum (< 1 MeV) bremsstrahlung emission and nuclear line emission. The continuum, which can be dominant to 10 MeV, for electron dominant flares shows that acceleration of electrons of this energy is required, while the line emission demands the existence of accelerated proton/ion populations. The γ-ray lines are the most direct probe of nuclear processes in flares. From line ratios and line fluences (Ramaty, 1986) details of the nucleonic energy spectrum, including number and energy content of particles can be inferred. In addition chemical composition of the ambient medium and energetic particle can be inferred in particular estimation of the ^{3}He abundances.

Substantial energy can be contained by MeV protons as well and have a significant effect heating the preflare chromosphere (Emslie et al., 1996). Such protons have no associated proton-electron bremsstrahlung, as MeV protons travel much more slowly than deka keV electrons. Observational evidence for these energetic protons involves more indirect diagnostics, such as impact polarisation of chromospheric lines, or the shape of H_α (Henoux et al., 1990) and Ca^{II} line profiles (Henoux et al., 1993). Analysis of the ^{20}Ne gamma-ray line (Share and Murphy, 1995) led to the conclusion that the flux of protons in the $\sim$1MeV range is higher than previously supposed. This suggests that the total energy budget in accelerated protons may in fact rival that in the electrons (Ramaty et al., 1995).

Simnett (1996), proposed that protons are the dominant species responsible for the energy transport during the impulsive phase. He proposed that the bulk of the energy released in the impulsive phase in fact goes into 0.1-1 MeV protons, rather than electron beams, which stream down the field lines producing high temperature plasma at the loop footpoints ($T_e \sim 10^8 - 10^9$) K from which hard X-ray emission is produced. Alternatively (Simnett and Haines, 1991) the hard X-rays may be emitted by electrons which are accelerated in a runaway process caused by the electric field generated as the proton beam with neutralising electrons at the same speed enter the chromosphere where the electrons

and protons experience substantially different drags.

1.5 Spatial Structure of HXR Sources

1.5.1 Multiple Foot-points

In the early observations of *HINOTORI* and SMM, several authors reported a double-source structure in the hard X-ray images from a limited number of flares (Tanaka and Zirin, 1985, Duijveman et al., 1982). The low temporal resolution and energy resolution of these instruments though did not allow the differentiation between non-thermal and thermal model (MacKinnon et al., 1985), or determining if these double source configurations were fundamental in the flaring process or simply chance encounters.

A study using the HXT on *YOHKOH* (Sakao, 1994) confirmed that double source structure of the hard X-rays. The observations suggest that the hard X-ray double sources, seen in the purely non-thermal energy range ($\geq 30rmkeV$), are magnetically conjugate i.e. non-thermal X-rays are emitted from the footpoints of a single flaring magnetic loop. In several flares the double sources correspond to the footpoints of the flaring loops seen in soft X-rays and H_α. Apart from these observed double sources, the rest of the flares show single or multiple source structure. The multiple sources may well be an ensemble of double sources. This is supported by several combined HXT and SXT imaging observations, where the multiple sources correspond to footpoints of individual flaring loops seen in SXT.

The hard X-ray fluxes from the double sources show good simultaneity, consistent with a time lag $\Delta\tau$ of 0.1s within 1σ level. The fact that the double sources emit hard X-ray simultaneously strongly suggests that the hard X-rays are emitted by accelerated electrons which stream down towards the footpoints of a single flaring magnetic loop. The simultaneity constrains how asymmetric the injection site must be. In terms of a thermal model or proton injection model (Simnett and Haines, 1991), the speed of the conduction front or proton population implies that the injection site must be $\sim$ 200 km or $\sim$ 900 km respectively from the apex of the loop to be able to obtain this simultaneity i.e. $<<$ 4% of the loop length.

Sakao (1994) also discovered that the brighter footpoints tend to have a harder spectrum. Also the brighter footpoints are located in weaker longitudinal magnetic field region. This suggests that the brighter footpoint has less magnetic field convergence thus having

more electron precipitation. Therefore we see that the magnetic configuration plays an essential part in determining the structure of the hard X-ray source.

1.5.2 Loop Top Impulsive Source

With HXT, impulsive hard X-ray sources above the soft X-ray flaring loop were discovered in limb flares. The characteristics of the hard X-ray sources above the loop-top are given in Masuda (1993) and Masuda et al. (1995) and summarised below

- In addition to double footpoints sources, a hard X-ray source is located well above ($> 5 \times 10^8$ cm) the corresponding soft X-ray loop.
- The temporal behaviour of this source is almost similar to that of the double footpoint sources within a time resolution of $\sim$ 10 s.
- This source is less intense than the footpoint sources by a factor of $\sim$ 5.
- The source occupies a small portion of the high temperature (>20 MK) region in the temperature map derived from SXT observations (Tsuneta et al., 1997).
- The source is located at slightly higher altitudes at higher X-ray energies.
- The source is compact ($\sim$7000$\times$7000km). During the impulsive phase its position and size does not show significant change.

Several studies have attempted to explain these results (Shibata, 1995; Fletcher,1995 and 1996; Wheatland and Melrose, 1995). Tsuneta et al. (1997) associate a hard X-ray source with the site of the cooling outflow jet lying between the slow shocks of a magnetic reconnection site. The hard X-ray source source is assumed to be thermal with a temperature of 100-150 MK heated by the fast shock emanating from the reconnection site. Alexander and Metcalf (1997) claim that PIXON reconstruction of the 13 January event shows that during the peak a single temperature interpretation is inconsistent with the temperature derived from channel count ratios. They claim that at the peak the source is non-thermal with a low energy cut-off in the spectrum and suggest that trapping in the corona is the only tenable option.

1.6 Hard X-ray Timing Profiles

1.6.1 Rapid Fluctuations

Data obtained from the Hard X-ray Burst Spectrometer (HXRBS) on the Solar Maximum Mission (SMM) has shown spikes of duration ~400 ms superimposed upon the more slowly varying background of hard X-rays (Kiplinger et al., 1983, Kiplinger et al., 1984). The existence of this fine scale structure in the hard X-ray emission has been confirmed by observations made with BATSE on CGRO (Machado et al., 1993). The timescales of these small bursts termed "energy release fragments" (ERFs) therefore constrains the timescale for accelerating the non-thermal electrons to $\sim$ 100 keV.

Employing a nonthermal model Kiplinger et al. (1984) deduced that about 2×10^{34} electrons were accelerated to energies greater than 20 keV in one of these spikes. Thus $\sim 5 \times 10^{34}$ electrons s^{-1} need to be energised above 20 keV over ~400 ms in order to account for an ERF. These ERFs are apparent only in smaller flares, where the number that are firing at any time is sufficiently small for them to be observed separately. In larger events, they presumably blend together to from a smoother hard X-ray emission time profile.

1.6.2 Slowly Varying Structures

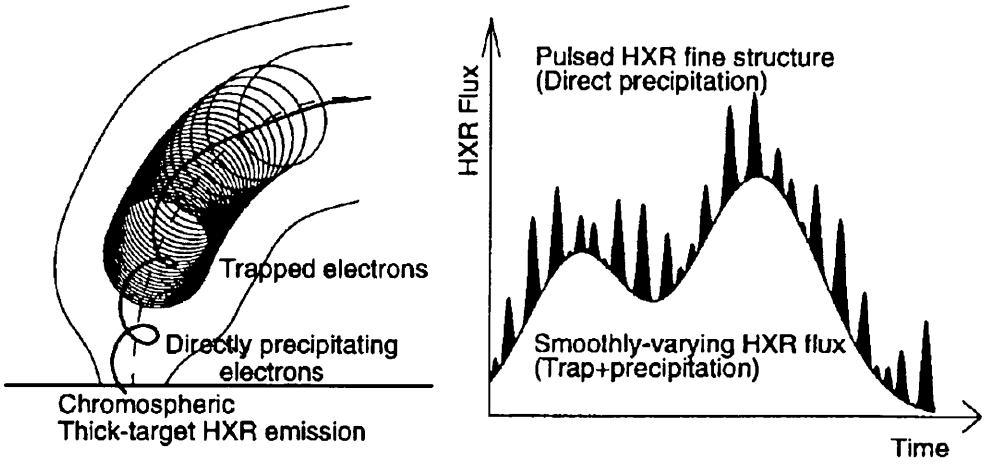

Figure 1.5: Observed HXR time structure : Electrons with small pitch angles precipitate directly and produce rapidly varying HXR pulses, while electrons with large pitch angles become trapped and produce a smoothly-varying HXR flux when they eventually precipitate.

Assuming that fast HXR time structures are attributed to the acceleration or injection function, then it is only the directly precipitating electrons that preserve this temporal pattern in chromospheric HXR emission. Electrons with relatively large pitch angles which have been temporarily trapped in the coronal magnetic bottle lose their memory about the time phase of their injection during their many bounces of their mirror motion in the flare loop. When they eventually precipitate, the HXR time profile is a smeared out slowly varying function of the injection profile. Thus trapping delays are largely manifested in the slowly varying HXR flux.

There are two limits of trapping times : the weak-diffusion limit, which is dominated by collisional deflection times, and the strong-diffusion limit, which occurs on faster time scales due to wave-resonant pitch angle scattering. The precipitation rate ν_p is approximated is follows

$$\begin{aligned} \nu_p &\propto E^{\frac{-3}{2}} \qquad \text{Weak Limit} \\ \nu_p &\propto E^{\frac{1}{2}} \qquad \text{Strong Limit} \end{aligned} \tag{1.10}$$

(Sakao, 1994). Therefore in the weak diffusion limit high energy electrons will be trapped longer resulting in high energy flux delays or hardening of the electron spectra in the trap. Alternatively for the strong diffusion limit, low energy electrons are delayed more, with a softening of the spectra in the trap.

In a systematic study of 44 flares observed by COMPTON and CGRO, the time delays of the smoothly varying HXR flux in the 20-200 keV energy range was consistent with trapping times in terms of collisional deflection (Aschwanden and Benz, 1997). This therefore provides evidence that the electron trapping is in the weak limit and that wave-resonant pitch-angle scattering in the strong-diffusion limit (for electron energy 20-200 keV) is less relevant. The determined trap densities were within $n_e^{\rm trap} \sim 10^{10} - 10^{12}{\rm cm}^{-3}$, consistent with independent density measurements from SXR emission measures.

1.6.3 Time of Flight Differences

A small, but systematic time delay in the sub-second HXR pulses was discovered using the large-area detectors of BATSE by Aschwanden *et* al, 1995a/nociteasch95a. Typically the low energy (25-50 keV) HXR pulses were found to lag high-energy (50-100 keV) pulses by $\sim$ 10-10 ms. The lag of low energy electrons is consistent with the functional dependence

of time delays expected from electron time-of-flight differences. Using suitable conversion factors between electron energy and photon energy (typically 1.5-2.0 for $\gamma = 4 - 6$), then the HXR delays $\tau(\epsilon)$ can be scaled into an electron time-of-flight difference and lead to a determination of the time-of flight distance L (Aschwanden *et al* 1996a, b, c).

These time-of-flight distances L were found to scale with the loop size. For over 43 flares with loop radii varying from $r = 3 \times 10^8 - 2.5 \times 10^9$ cm, a scaling law of $L/r = 1.43 \pm 0.30$ was found, (Aschwanden *et al* 1996c). Therefore this scaling law indicates an acceleration site above the loop-top, consistent with Masuda (1993).

This analysis is limited in that the uncertainties in the time-of-flight results are substantial and that from the sample of flares only 46 out of 103 satisfy the model. Furthermore is is difficult to reconcile these time delay results with the overall photon spectral evolution (namely soft-hard-soft). Time-of-flight differences should result in spectral softening over the duration of the emission but these observations have not been sustained (Newton and Giblin, 2000). There are alternative explanations for the time delays observed by Aschwanden *et al*. Brown et al. (1998a) demonstrate that time and energy-dependent variations in the accelerated spectra can produce apparent time-of-flight differences. Alternatively LaRosa and Shore (1998) allow the spectral evolution to be essentially random, arising from the peculiarities of a spatially fragmented acceleration process which causes the light curve to consist of a superposition of uncoordinated energy release events.

1.7 Polarisation and Directionality

Theoretical simulations of both thick target and thermal emission using bremsstrahlung cross-sections differential in direction and polarisation of the outgoing photon have been carried out (e.g. Brown, 1972; Leach and Petrosian, 1983; Emslie and Brown, 1980). The polarisation of thick target emission is typically expected to be a few tens of percent, dependent on angular distribution of injected electrons and variation of magnetic field strength. Thermal models are expected to have only few percent, due to temperature gradients in the source. Theoretically then, polarisation would be a useful diagnostic in differentiating between thermal and thick target models. No agreement though on the level of polarisation observed has been achieved and meaningful comparison of observation with theory is impossible.

Directivity effects can be investigated either by studying centre-to-limb brightness distributions of flares or to observe the flare from two spacecraft with different viewing angles. At hard X-ray energies, center-to-limb studies are inconclusive (Datlowe et al., 1977), while SMM results at γ-ray energies clearly indicate the preferred emission direction for a downwards beam is downward or at right angles and so only seen on the limb or if the magnetic filed lines are non-vertical. Mutli-spacecraft observations also observed no systematic directionality in the emission (Kane et al., 1988) in the deka keV range, however as directivity increases with energy, variations in spectral index for increasing viewing angles are observed consistent with emission due to a beam of non-thermal electrons (McTiernan et al., 1994).

1.8 Particle Acceleration Mechanisms

A number of mechanisms have been proposed to account for the energetic solar particles. The processes tend to be separated into three main classes : stochastic acceleration by waves, shock acceleration and direct field (d.c.) acceleration. However a successful model must fulfill the following criteria.

• The model must be capable of accelerating electrons and ions to energies in excess of 100 keV and 100 MeV, respectively, in order to account for the hard X-ray and gamma ray line emission. It should also allow for the possibility of energising electrons to about 10 MeV and protons to 1 GeV, in order to account for the ultra relativistic electron bremsstrahlung in electron dominant events and pion radiation.

• The model must be able to accelerate electrons and ions to the lower energies in less than 1 s.

• The model must provide electron and ion distributions that are consistent with (i.e. can be used to successfully fit) high resolution X-ray and nuclear gamma ray line spectra.

• For large flares, the model must produce as many as 10^{37} electrons s^{-1} above 20 keV over a period of 10-100s.

• It should be clear how the local acceleration model can be incorporated into the large scale coronal structure, as observed by *YOHKOH*. The following is a brief description of the main types of acceleration mechanisms applied to solar flares.

1.8.1 Stochastic Acceleration

Stochastic acceleration may be broadly defined as any process in which a particle can either gain or lose energy in a short interval of time, but where the particles systematically gain energy over longer times. The most important example of this is acceleration by waves, most specifically the result of resonant pitch angle scattering from Alfvèn waves with wavelengths of the order of a particle gyro-radius or from interactions with magnetosonic waves whose wavelength is much greater than the particle gyro-radius.

In the context of plasma turbulence, the particles are accelerated by adiabatic collisions with waves of $\lambda >>$ particle gyro-radius as well as a distribution of amplitudes. The energy of the particles will tend towards the mean energy density of the turbulence, and the temperature associated with the hydromagnetic turbulence turns out to be quite large. Thus, on average particles will gain energy in such a process.

For turbulent interactions, then, mirroring by magnetic fluctuations is analogous to elastic scattering, but since the collisions are adiabatic $\frac{p^2_\perp}{B}$ is conserved. This also implies that there is a systematic gain of parallel momentum during the acceleration process. However, the result of this gain is a loss in accelerator efficiency since mirroring does not occur as efficiently as the pitch angle decreases. To offset this problem rapid pitch angle scattering from short wavelength waves of unspecified origin is needed to maintain the isotropy of the particle distribution.

In the context of coronal magnetic reconnection it is thought that the high speed jets commonly formed will produce the long wavelength waves needed through the interaction of a sub-Alfvènic jet with the plasma or shear flow instability.

1.8.2 Shock Acceleration

Shocks have been invoked as highly efficient acceleration mechanisms in space physics. They are usually separated into two types : drift and diffusive. Drift acceleration involves particles moving along the shock front, gaining energy from the shock electric field. Acceleration is fast in solar situations $<<$ 1s but its effectiveness is limited in that once the particle has gained energy, it tends to escape and acceleration takes place only when the direction of propagation of the shock gets to within 1 or 2 degerees of being perpendicular to the magnetic field. Thus while electron drift acceleration can successfully account for a number of observations at the Earth's bow shock, it is far too restrictive to be considered

seriously in flares.

In diffusive shock acceleration, the particles undergo a systematic energy gain by interacting with moving scattering centres, with these scattering centres moving toward each other in the rest frame of the shock. There is first order energy gain with each interaction so the acceleration is much faster. Only fast mode shocks are of interest as the scattering centres do not converge in slow shocks (Isenberg, 1986). Numerical simulations have shown that heated shocked plasma readily leaks into the upstream region and generates low-frequency electromagnetic waves which in turn resonantly scatter the ions. Ions with high energies (100 MeV) can be reached in <1 s (Ellison and Ramaty, 1985) since the turbulence generated by the the particles keeps them from escaping from the shock (Lee, 1982). In addition as the acceleration is prompt ($<< 1s$) diffusive shock must be viewed as a viable process for ion acceleration.

For electrons though, in order to resonate with turbulent Alfvèn. Whistlers have a lower threshold energy but need to be located near the electron cyclotron frequency for this threshold to lie near thermal energies. In the shock itself though there are d.c. electric fields (Goodrich and Scudder, 1984) which could directly produce energetic particles.

A major issue for shocks is the question of formation. Shocks are a common feature of reconnection models, in the Petschek model (Petschek, 1964) shocks are part of the structure of reconnecting fields. Alternatively they can be generated by intense plasma heating associated with magnetic reconnection or super-Alfvènic plasma jets entering into the neighbouring plasma. For fast mode shocks to form through jets, the jet speed must be super-Alfvènic to the total field. In reconnection the jets speed is approximately Alfvenènic with respect to the reconnecting component, a small fraction of the total field, therefore it may not be possible to form a shock this way (Forbes et al., 1989). Forming a fast mode shock through heating may also not be possible as for preflare conditions ($n_e \approx 10^{10}$ cm^{-3} and $B = 300G$) a temperature of at least $5 \times 10^9 K$ is required. This presents particle confinement problems and is inconsistent with all hard X-ray observations.

1.8.3 D.C. Field

Sub-Dreicer Fields

A sub-Dreicer D.C. electric field model of solar flares has been extensively investigated in recent years. (Holman, 1985; Tsuneta, 1985; Moghaddam-Taaheri and Goertz, 1990;

Benka and Holman, 1992, 1994; Holman and Benka, 1992; Dennis et al., 1994; Zarro et al., 1994) providing a mechanism for heating and accelerating particles. The model assumes the presence of one or more discrete current channels and as the corona has a low but non zero resistivity then a macroscopic electric field must be present. The current channels will dissipate energy at a rate of $Q = \mathbf{J}.\mathbf{E}$ erg cm^{-3}s^{-1} and so the plasma the current channels are embedded in will emit thermal X-rays which may extend into the hard X-ray region.

At the same time, electrons over a critical velocity v_c are freely accelerated by the electric field, unhindered as the energy loss through collisions decreases with increasing electron energy. Their final energy will be dependent on the electric field strength and the length of time the electron spends in the field. This critical velocity is given by the relationship

$$v_c = \left(\frac{E_D}{E}\right)^{1/2} v_e \; = \left(\frac{v_e}{v_d}\right)^{1/2} v_e \tag{1.11}$$

where v_d is the drift velocity of the current carrying electrons, v_e the thermal velocity $((kT/m)^{1/2})$ and E_D the Dreicer field. The Dreicer field is defined such that an electron with velocity equal to v_e will be accelerated by the electric field as much as it is decelerated by collisions and is given by

$$E_D = 2.33 \times 10^{-8} n_9 T_7^{-1} (\ln\Lambda/23.2) \text{ statvolts cm}^{-1}.$$

n_9 and T_7 being the plasma density and temperature in units of 10^9 cm^{-3} and 10^7 K respectively. It is these runaway electrons which on entering the denser chromosphere emit thick target HXR from the footpoints or escape to interplanetary space. In the presence of a strong magnetic field, the Joule heated plasma can also emit thermal gyro synchrotron radiation. Nonthermal gyrosynchrotron emission requires runaway electrons moving perpendicular to the field lines, which may occur through scattering or mirroring.

The model therefore will have observational implications for soft X-rays, hard X-rays and microwaves. The relationship between these observations i.e. the relative importance of thermal or non-thermal emission will depend on the ratio of Joule heating rate to runaway electron production rate $\dot{N}$. Holman (1985) and Holman et al. (1989) showed that this ratio is given by

$$\frac{Q}{\dot{N}} = 3.92 \times 10^9 T_7 \left(\frac{E_D}{E}\right)^{-19/8} \exp\left[\left(\frac{2E_D}{E}\right)^{1/2} + \frac{E_D}{4E} + C\right], \tag{1.12}$$

C being a relativistic factor negligible if v_c is small compared to the speed of light. For sub-Dreicer fields ($E << E_D$), Joule heating will dominate since there are few electrons with velocity above v_c. Therefore thermal soft X-ray would dominate relative to non-thermal high energy HXRs. By increasing E/E_D, acceleration and HXR emission will begin to dominate.

Therefore in a typical flare, initially with a low ratio of E/E_D, most of the energy released will go into Joule heating in the loop, thus producing soft X-ray emission while the currents in and conduction to the low corona and chromosphere will produce chromospheric evaporation, i.e. typical preflare observations. If E/E_D increases either due to E increasing or E_D decreasing with decreasing temperature then significant runaway and HXR production will result. As the relation between heating and acceleration depends strongly on E/E_D then the change between significant runaway acceleration and dominant thermal could be very rapid, explaining the subsecond to second time scale observed in the impulsive phase. With a significant population of runaway electrons, chromospheric evaporation would increase. As such the Dreicer field will increase, due to the increased density in the corona, decreasing the amount of HXR emission while the soft X-ray emission would continue, as Joule heating continues as long as the electric field remains.

The D.C. model also makes predications about the spatial distribution of HXRs. If the current channels are aligned with the closed magnetic field structures in the corona, the Joule heating will result in an extended coronal source at low energy with a soft spectrum. The runaway electrons will result in one or more compact non-thermal source located at the footpoints of the loop, extending to higher energy than the coronal source with a harder spectrum. As Benka and Holman (1994) found that the spikes in the time profile of HXR bursts was consistent will simple runaway accelerated thick target emission, then the footpoint emission during a spike is expected to increase while the coronal source remains constant.

Numerous flare observations are consistent with the predictions of this model; HXR emission form footpoints, thermal sources in corona which on the disk envelopes the HXR footpoint, increased shear in magnetic field consistent with stronger currents correlated to increased coronal heating, higher temperature at loop tops possibly requiring direct heating. Therefore it is clear the the D.C. field model has great potential in providing

a physical context to flare observations linking together thermal and non-thermal observations. However the question unanswered is which of these predictions could also be satisfied by injection of any non-thermal population independent of acceleration mechanism.

Super-Dreicer Field

Solar flare models which employ super-Dreicer fields have also been proposed e.g. Litvinenko (1996), Martens (1988). The geometry of Litvenenko's model is that of a large reconnecting current sheet above a bipolar magnetic loop or arcade. The sheet has height and length $\approx 10^9$ cm and width of a few hundred meters and contains an electric field along the length of the sheet whose strength is ≈ 10 V cm^{-1}. The potential drop along the length of the sheet is ≈ 10 GeV, but this will not be realised as a finite magnetic field component normal to the electric field causes the particles to move slightly in the transverse direction and hence causes them to escape from the sheet over distances of the order 10^4 cm. Litvenenko's model can yield electron energies and fluxes consistent with the magnitude of hard X-ray observation but the nature of the predicted electron spectra has yet to be investigated. Replenishment of the current sheet can be accomplished by either bulk plasma reconnection inflows or flows upward from the chromosphere. The later flows can be co-spatial with the downward moving electrons, since there is no electric field in the region of space.

Chapter 2

Thick Target Spectra from Non-uniformly Ionised Plasma

"Making a mountain out of... a small step-function"

2.1 Introduction

The spectral characteristics of thick target bremsstrahlung spectra are intrinsically linked not just to the parent electron spectra, but also to the bremsstrahlung cross-section used (Brown and Emslie, 1988), by bremsstrahlung directivity effects (e.g. Brown, 1972) and the electron rate of energy loss in the target (MacKinnon and Brown, 1989). The inferred flux of energetic electrons accelerated during the solar flare, of fundamental importance as a signature of the acceleration process and energy transport mechanism, will be seriously affected by the choice of bremsstrahlung cross-section or model of energy loss used.

Brown's (1971) analysis considered only Coulomb collisional energy losses in an ionised plasma but led to the electron spectra being recognised as the second derivative of the photon spectra, to be inferred from solving the integral equation. It is clear however that other energy losses, such as return current dissipation and wave generation will exist in the source. The generalisation of the thick target inversion with non-collisional energy losses (Brown and MacKinnon, 1985) can be loosely regarded as perturbations to Brown (1971). Such perturbations can change the structure of the inversion dramatically leading to ill-posedness of the inversion.

The reduction of collisional energy losses as electrons move into a weakly ionised plasma affects the relation between the HXR bremsstrahlung spectrum and the electron injection spectrum (Brown, 1973a). The consequences of the non-uniform ionisation effect on HXR spectra and the corresponding inverse problem are addressed here. In this chapter a general form for thick target emission for a general form of ionisation structure is formulated. The inversion properties for a special case of ionisation structure, a step-function, will be studied, the results of which can also be found in Brown et al. (1998b).

2.2 Energy Losses of Electron Beam

2.2.1 Coulomb Collisions

Coulomb collisions are assumed to dominate the evolution of the electron beam. As the electrons move along the magnetic field lines, they interact with ambient particles and undergo Coulomb collisions through which they lose energy and have their trajectories modified. For a pure Coulomb potential, interactions are by their nature long range, therefore the analysis of multi-electron interactions is complicated as the test electron is influenced more by its interactions with the large number of distant particles than those with the few nearby field particles. The presence of a test electron, though, perturbs the distribution of ambient particles in such a way that particles at greater than the Debye length are screened from the test electron. Thus only interactions within the Debye sphere need be considered. In the corona the number of such interactions is of the order 10^9.

The consequences of these collisions are best expressed in the rate of energy loss and rate of change of pitch angle cosine $\mu = \cos(\theta)$, θ being the angle between the incident particle direction and the electron velocity. The expected values for an electron interacting with a fully ionised target are

$$\left\langle \frac{dE}{dt} \right\rangle = \frac{-2\pi e^4 n v \Lambda}{E} \quad \text{and} \quad \left\langle \frac{\mathrm{d}\mu}{\mathrm{dt}} \right\rangle = \frac{-2\pi \mathrm{e}^4 \mathrm{n} \mathrm{v} \Lambda \mu}{\mathrm{E}^2} \tag{2.1}$$

Λ the Coulomb logarithm corresponding to the log of maximum value of impact parameter (distance of closest approach for an undeflected particle) i.e. the screening distance. In a thermal plasma this would be taken as the Debye length but as a cold target approximation is more appropriate for a suprathermal beam the mean free path η (Landau and Lifshitz, 1960), or in a high magnetic field, the Larmor radius r_L (Sweet, 1959) is used. The

occurrence of the quantity in log means the result is not sensitive to the value chosen, an order of magnitude change on the log term only results in a 10 percent change in the value of Λ. Thus for the solar corona, typical values of Λ are between 20-25.The detailed method of determining these collision co-efficients, including those for proton bombardment and for a neutral target can be found in Emslie (1978) and Leach (1984).

The mean scattering treatment of electron collisional evolution is constructed from Equation 2.1 and neglects all spread in electron direction. Re-arranging these in terms of E and μ an analytic solution is possible (Brown, 1972) to determine where, on average the electrons will be, in terms of column density N, and what their average pitch angle will be once they have been degraded to energy E. If the injection energy and pitch angle are E_o and μ_o then for non to mildly relativistic electrons

$$\frac{E}{E_o} = \frac{\mu}{\mu_o} = \left(1 - \frac{N}{\frac{2}{3}\mu_o N_s}\right)^{1/3} \tag{2.2}$$

where

$$N_s(E_o) = \frac{E_o^2}{4\pi e^4 \Lambda} \approx 10^{17} \mu_o \left[E_o(\mathrm{keV})\right]^2, \quad \mathrm{cm}^{-2} \tag{2.3}$$

N_s being the column density along the electrons path that is required to reduce its energy to zero (in reality the electron will thermalise before this).

For most modelling purposes the analytic mean particle treatment is very effective, however for understanding aspects of spatial structure, directivity and polarisation of emitted hard X-rays the pitch angle distribution and spatial spreading of electrons is required. For this to be determined the Fokker-Planck equation, taken to order Λ, is solved i.e. for non-relativistic electrons in a cold hydrogen plasma the evolution of the velocity distribution is described by

$$\frac{\partial f}{\partial t} + \mu v \frac{\partial f}{\partial z} - C \frac{\partial}{\partial v}\left(\frac{f}{v^2}\right) - \frac{c}{v^3}\frac{\partial}{\partial \mu}\left((1-\mu)\frac{\partial f}{\partial \mu}\right) = 0 \tag{2.4}$$

The important feature of this treatment beyond mean scattering is embodied in the $\frac{\partial}{\partial \mu}$ term; being second order rather than first-order this represents the spread of electrons in pitch angle. Analytic solutions have been found for special cases but in general Monte Carlo or other numerical methods (Bai, 1982; Hamilton et al., 1990; MacKinnon and Craig, 1991) are employed, such as in modelling stereoscopic observations of flares including treatments of directivity (McTiernan and Petrosian (1990b)). Fletcher (1995, 1996) modelled the "above the loop top" HXR sources and height distribution of HXR sources

in this way and found that electrons injected with large pitch angles would remain long enough in the corona, without magnetic trapping or density enhancements, to explain the above loop-top source, a property which is not revealed by considering mean particle properties alone (Conway et al., 1998).

2.2.2 Converging Magnetic Field

The magnetic field along the length of the flaring loop is not uniform. The strength in the chromosphere is much greater than that in the corona. An inevitable consequence of this field convergence between the coronal and chromospheric parts of the loop is the formation of a magnetic bottle and partial trapping of beam electrons.

As the electrons move through the varying magnetic field their pitch angles are changed by the Lorentz force. However this process has *adiabatic invariants* - constants of motion. If the helical path of the electron has a pitch angle of θ with respect to the magnetic field direction z then the magnetic moments $p_\perp^2/B$ is an adiabatic invariant implying

$$\frac{1-\mu^2}{B} = \frac{1-\mu_o^2}{B_o}$$

where $\mu = \cos\theta$ and the subscript $_o$ refers to an arbitrary reference point. Electrons injected where $B = B_o$, with pitch angle cosine μ_o, will have converted all their momentum into transverse momentum when $\mu = 0$ i.e. where

$$B = \frac{B_o}{1-\mu_o^2}$$

This point is the mirror point for particles with initial $\mu = \mu_o$ from which they cannot pass into the region of greater magnetic field strength.

For a given ratio of coronal B_{cor} and chromospheric B_{chrom} magnetic field strengths, then if

$$\mu_{\rm inj} \leq \left(\frac{B_{cor}}{B_{chrom}}\right)^{\frac{1}{2}} \quad \text{the electron is trapped in the corona,}$$

or if

$$\mu_{\rm inj} > \left(\frac{B_{cor}}{B_{chrom}}\right)^{\frac{1}{2}} \quad \text{the electron enters the chromosphere.}$$

Electrons which precipitate into the chromosphere are considered to be in the 'loss-cone'; however scattering can enable electrons to enter or leave the 'loss-cone'. For Coulomb scattering the higher energy electrons will therefore be trapped on average longer than the low energy electrons assuming the distribution of injection pitch angles is independent of

energy. As such the time delays (cf. Section 1.6.2) or spectral evolution (Section 1.4.3) can be interpreted as due to particle trapping. The time trapped depends on whether the scattering is weak or strong (this depends on the density and scattering mechanism in the target) and the spatial dependence of field convergence, which if not abrupt, requires a full Fokker-Planck scattering treatment as the loss-cone analysis is inadequate (Fletcher, 1997).

2.2.3 Plasma Instabilities

For a large electron beam, as it passes through the plasma, the total (beam + plasma) electron number distribution in velocity space may have a 'bump', region of positive gradient, at high energy (cf. Figure 2.1). Such distributions may stimulate the growth of

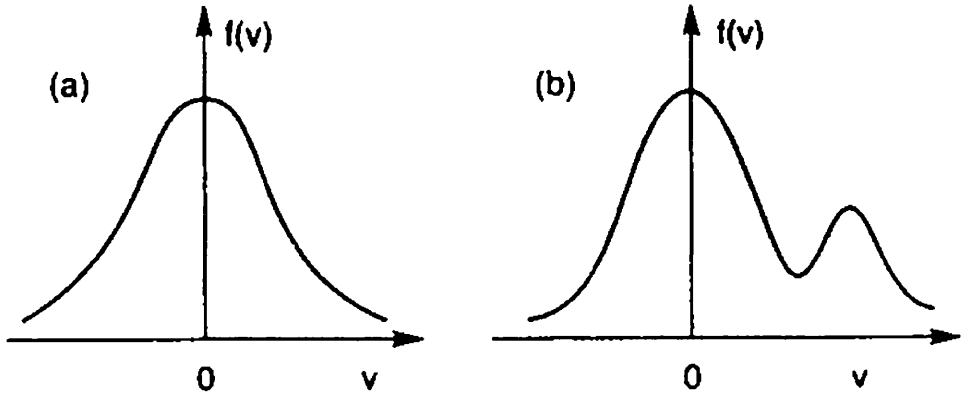

Figure 2.1: Examples of (a) Maxwellian one dimensional velocity distribution of background plasma and (b) Maxwellian distribution with beam of suprathermal particles included forming 'bump'.

Langmuir turbulence and plasma waves and redistribute the beam energy. This requires that the beam density be sufficiently high and that the 'bump' in the velocity distribution be sufficiently steep and separated from the main body of the distribution. Even for an initially stable beam, Emslie and Smith (1984) suggested that Coulomb collisions may cause the beam to become unstable. Passage through a region of decreasing temperature may also produce this effect.

Estimates of the level of wave generation and turbulence is reached and the effect this would have on the electron beam and resultant hard X-ray emission vary. For a quasilinear formalism McClements (1987), assuming strong beaming, found the resulting

X-ray emission is not greatly affected, contrary to Hoyng et al. (1979) (isotropic). If the Langmuir turbulence becomes extremely strong (i.e. solitons and cavitations) the turbulence may stabilise the beam. The soliton formation will inhibit further wave growth (Rowland and Vlahos, 1985). It is estimated then that the beam will lose only $10^{-3} - 10^{-4}$ of its energy to wave generation i.e. the target would be considered collision-dominated as the Langmuir waves are collisionally damped. However if the electron beams occur on short timescales the energy losses may be more substantial.

2.2.4 Return Currents

As discussed in Section 1.4.2, the number flux of beam electrons inferred from the intensity and spectral index of HXR emission, carries a current I well above the Alfvén-Lawson Current Propagation Limit (Alfvén, 1939; Lawson, 1957). In order for the vast number of beam electrons to propagate through the flare atmosphere a return current of ambient electrons must arise to locally neutralise the beam current. Beam energy losses in generating such a return current will be invoked. These losses can be significant compared to Coulomb losses, and for certain flare parameters dominate over Coulomb energy losses.

Alfvén-Lawson Current Propagation Limit

Considering the beam as a cylinder of radius r_o, carrying a current I, then the self-magnetic field at r_o is

$$B_o = \frac{\mu_o I}{2\pi r_o} \qquad \text{(S.I. units)}. \tag{2.5}$$

For a beam of uniform current density, the field inside the beam is $\propto r$ and outside $\propto 1/r$. The radius of curvature of the electrons around the self-magnetic field is

$$R = \frac{\gamma m_e v}{eB}, \tag{2.6}$$

where m_e is the mass of the electron, e the electron charge, v the speed and γ the Lorentz factor. As illustrated in Figure 2.2, if $R > r_o$ then the beam can propagate downwards, while for $R \sim r_o$ the electrons have figure of eight types orbits. For $R < r_o$ the electrons experience a net motion backwards i.e. the orbit in the self-magnetic field prevents the electrons propagating in the direction of the beam. Thus the relation of $R < r_o$ implies a maximum current that can flow, and this current is independent of r_o. The Alfvén-Lawson limit on the current is then

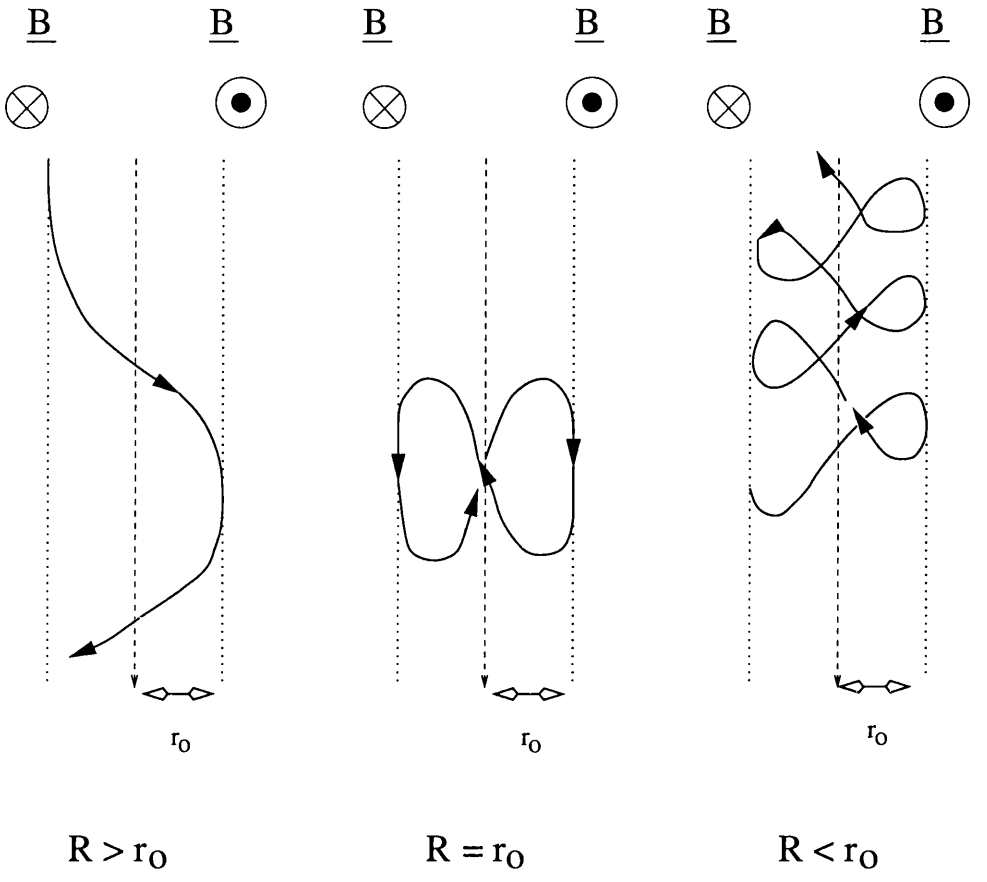

Figure 2.2: Propagational directions of beam electrons in a current below (a), at (b) and above (c) the Alfvén-Lawson limit.

$$I_A = \frac{2\pi m_e \gamma v}{e\mu_o} = 1.7 \times 10^4 \beta\gamma \qquad \text{A.} \tag{2.7}$$

For a beam of $\geq$ 20keV electrons then the limiting current is $\sim 10^3$A, some 10^{14} orders of magnitude less then the current associated with the 10^{36} electronss^{-1}.

Currents in excess of the Alfvén-Lawson limit can only flow under one of two conditions. One, if an ambient magnetic field exists whose strengths exceeds that of the self-magnetic field, then the particle orbits would be governed more by the ambient field than the self-magnetic field. Alternatively, if the ambient medium is much denser than the beam, the background particles set up a return current such that the local current density is small and the self-magnetic field of this neutralised current is insignificant. As the observed magnetic field of an active region $B \sim 0.15T$, I is still restricted to $\leq 10^{12}$ A. Thus for the currents involved in a non-thermal model to propagate return currents must exist co-spatially with them.

Generation of Return Currents

The charge displacement caused by the beam will result in the creation of an electric field, which causes the plasma electrons to redistribute in such a way as to neutralise local charge build up in the plasma. Because this electric field is caused by charge effects, it is commonly referred to as an electrostatic field. If the current in the plasma varies in magnitude, immediately an inductive electric field will also be created in such a way as to prevent magnetic field variations on a timescale shorter than the magnetic diffusion time. Both the electrostatic and the inductive electric field will effectively result in an electron plasma current which is in the opposite direction to the beam current.

The relative importance of electrostatic (Brown and Bingham, 1984) and inductive (Spicer and Sudan, 1984) effects in generating and maintaining the return current has been somewhat controversial. van den Oord (1990) showed that this question is irrelevant for the full electrodynamic treatment. Electrostatic effects permit the plasma to redistribute the excess charge imposed by the beam and the inductive effects prevent the magnetic field from changing on a timescale less than the diffusion time. To explore how a return current is set up in detail requires a model for the acceleration of the electrons and their escape from the acceleration region. Also, with a current neutralisation of one part in $\sim 10^{14}$ in all places at all times, the way in which the return current is driven needs to be considered on both the scale of the beam itself and the scale of the smallest current to be neutralised. One model by Winglee et al (1988a,b) found that the direct and return currents are not co-spatial on a microscopic scale. The implications of this for the overall generation of the return current are however unclear (van den Oord, 1994).

Return Current Energy Losses

As the return current is maintained against dissipation by the electric field, this field also slows the beam electrons. In effect, energy is taken from the beam to drive the current. While the drift velocity v_D of the ambient plasma,

$$v_D = \frac{n_b v_b}{n_p},$$

(where n_b is the beam density, n_p the ambient plasma density and v_b the speed associated with the mean energy of the particles in the beam) is less than the threshold for a current-driven instability then the resistivity η of the plasma can be assumed to be classical, given

by Spitzer (1962) as

$$\eta = \frac{m_e \nu(v)}{n_e e^2} \qquad \nu = \frac{4\pi n_e e^4 \log \Lambda}{m_e^2 (k_B T_e)^{3/2}}.$$

Assuming classical resistivity and a mean particle treatment for collisions, Brown and Melrose (1977) and Emslie (1980) found that with increasing electron flux the return current losses became more significant until for large electron flux ($F_{20keV} > 10^{19}$electrons cm^{-2} s^{-1}), the X-ray intensity $I(\epsilon)$ is *independent* of the electron flux. For beams at the upper flux limit, i.e. a marginally stable beam, the ratio of return current energy losses to Coulomb energy losses (dependent on the density and electron to ion temperature ratio θ of the background plasma) would be significant for the low $\theta \approx 1$ of the pre-flare atmosphere and the low density of a coronal injection site (Emslie, 1981b). However for expected values of θ during an impulsive flare the return current loss will be small in comparison to Coulomb losses. HXR spectra with return current effects have not only been modelled to be softer than for Coulomb only losses (Emslie, 1980) but for beam evolution models with collision, return current and converging magnetic fields, (Zharkova and Syniavskii, 1997), a dip in the HXR spectra is predicted.

If the beam flux is large and the ambient density of electrons small, the return current drift velocity may exceed the threshold for the growth of various plasma waves. The turbulent plasma waves scatter the drifting electrons causing enhanced momentum and energy loss which leads to the onset of anomalous resistivity. In some cases the resistivity is enhanced up to a factor 10^5 (Papadopoulos, 1977). As current instabilities arise on timescales shorter than the magnetic diffusion time, any total current changes are required to be slow by Amperés law, so the induced electric field must increase by this factor. Hence a sudden increase in resistivity leads to greatly enhanced localised heating (Cromwell et al., 1988), a possible mechanism to produce an increased thermal component in hard X-ray (Holman, 1985) or white-light emission from the deep chromosphere (Matthews et al., 1998).

2.2.5 Treatment of Beam Energy Losses

The following analysis considers only the effect of Coulomb energy losses on the evolution of the beam and hard X-ray spectral signature, omitting energy loss processes such as radiation and beam-beam interactions which have a small effect upon the beam. Also

omitted are the extremely non-linear processes such as reverse currents and plasma turbulence scattering effects and the pitch angle scattering directivity effects. Neglecting these processes is justified for dilute beams, as our main aim is to compare the hard X-ray spectra for uniform and non-uniformly ionised targets.

2.3 Thick Target Approach for Non-uniformly Ionised Plasma

The general formulation of thick target bremsstrahlung spectra from a non-uniformly ionised source is derived following Brown (1972, 1973a). For an electron, of initial energy E_o, the total yield of photons of energy ϵ during the electron's lifetime from the short-range interactions experienced with background particles can be expressed by

$$\nu(\epsilon, E_0) = \int nvQ_B(\epsilon, E)dt = \int_{\epsilon}^{E_0} \frac{nvQ_B(\epsilon, E)dE}{\left|\frac{dE}{dt}\right|} dE_o. \tag{2.8}$$

where $Q_B(\epsilon, E)$ is the bremsstrahlung cross section, n the background density cm^{-3} and $v(t)$ the velocity of the electron as it propagates through the atmosphere. It should be noted that we can change variable from time to electron energy, E, along the path since the electrons lifetime in the source is assumed to be much shorter than the time resolution of observations. Therefore for a distribution of injected electrons $F_o(E_o)$ (electrons s^{-1} keV^{-1}) the bremsstrahlung photon emission $J(\epsilon)$ (photons s^{-1} keV^{-1}) is

$$J(\epsilon) = \int_{\epsilon}^{\infty} F_o(E_o) \int_{\epsilon}^{E_0} \frac{nvQ_B(\epsilon, E)dE}{\left|\frac{dE}{dt}\right|}. \tag{2.9}$$

2.3.1 Energy Loss Rates

Considering the energy loss as purely collisional and neglecting pitch-angle scattering,

$$\left|\frac{dE}{dt}\right| = nvQ_{\text{Coul}} \tag{2.10}$$

The Coulomb cross-sections for ionised (Spitzer, 1962) and neutral media (Mott and Massey, 1965), differ due to the electrostatic screening of the bound electron.

$$(Q_{\text{Coul}})_{\text{ionised}} = \frac{-2\pi e^4 \Lambda_{ee}}{E} \qquad (Q_{\text{Coul}})_{\text{neutral}} = \frac{-2\pi e^4 \Lambda_{eH}}{E}$$

Generalising for any ionisation fraction x , and defining

$$\Lambda = \Lambda_{ee} - \Lambda_{eH} \qquad \text{and} \qquad \lambda = \frac{\Lambda_{eH}}{\Lambda},$$

then the energy loss rate is expressed as

$$\left(\frac{dE}{dt}\right) = \frac{-2\pi e^4 \Lambda n v}{E}\left(\lambda + x(E, E_0)\right)$$

For the solar atmosphere, assuming a pure hydrogen composition, then $\Lambda \approx 17.0$, while $\lambda \approx 0.55$ (Brown, (1973a)) i.e. the energy loss rate in a neutral medium is $(1.0 + 1.0/\lambda) \approx 2.818$ times less than an ionised medium.

2.3.2 Effective Collisional Column Density

The total (free and bound) target electron column density $N(\mathrm{cm}^{-2})$ from the injection site is a central parameter in describing the electron energy loss. Given a profile of ionisation fraction through the atmosphere, $x(N)$, then the rate of change of electron energy with column density N is simply (Emslie, 1978)

$$\frac{dE}{dN} = -\frac{2\pi e^4 \Lambda}{E}\left[\lambda + x(N)\right] \tag{2.11}$$

such that

$$E^2(N) = E_o^2 - 2K\int_0^N (\lambda + x(N'))dN', \tag{2.12}$$

with $K = 2\pi e^4 \Lambda$. Clearly as the energy loss is dependent on $x(N)$ it would be more convenient to replace the depth measure N by an 'effective' collisional column density. A depth measure for which the energy loss rate is constant. This can be achieved by defining

$$M(N) = \int_0^N \left[\lambda + x\left(N'\right)\right] dN' \tag{2.13}$$

$$M = \frac{E_0^2 - E^2}{2K}.$$

The 'effective' column density $M(\ \mathrm{cm}^{-2})$ therefore is not just a measure of how much material the beam has encountered, but a weighted measure of how effective this material is at stopping the beam.

2.3.3 Integral Equation for a Non-Uniformly Ionised Plasma

Since $M(N)$ is monotonic, it is always possible to rewrite any model atmosphere $x(N)$ as $x\left(M = \frac{E_o^2 - E^2}{2K}\right)$. Hence the generalised equation for thick target bremsstrahlung emission from a non-uniformly ionised source is expressed as

$$J(\epsilon) = \frac{Q_o}{K\epsilon}\int_{\epsilon}^{\infty} F_o(E_o)\int_{\epsilon}^{E_o}\frac{q(\epsilon,E)\,dE\,dE_o}{\lambda + x\left(\frac{E_o^2-E^2}{2K}\right)} \tag{2.14}$$

In this analysis Kramer's cross-section ($q(\epsilon,E) = 1$) is an adequate approximation for the bremsstrahlung cross-section to allow the relative effects of $x(M)$ on the relationship between $F_o(E_o)$ and $J(\epsilon)$ to be determined. There is no significant change in the bremsstrahlung cross-section as the electrons enter the chromosphere and interact with neutral hydrogen. As a result of being short-range interactions with hydrogen nucleus there is effectively no screening by the bound electron (Kock and Motz, 1959). Continuing the method of Brown (1971), the integral equation between $F_o(E_o)$ and $J(\epsilon)$ is derived by reversing the order of integration in Equation 2.14 and differentiating with respect to ϵ. This yields

$$\int_{\epsilon}^{\infty} F_o(E_o)k(E_o^2-\epsilon^2)dE_o = -H'(\epsilon) = -\frac{K}{Q_o}\frac{d}{d\epsilon}(\epsilon J) = L(\epsilon), \tag{2.15}$$

where

$$k(E_o^2-\epsilon^2) = \frac{1}{\lambda + x\left(\frac{(E_o^2-\epsilon^2)}{2K}\right)} \tag{2.16}$$

This is an integral equation for $F_o(E_o)$ to be solved for given data $H(\epsilon)$ and for the kernel function k defined by $x(M)$ in a model target atmosphere. Due to the dependence of k on E_o^2 and ϵ^2 it is more convenient to transform Equation 2.15 to energy squared dependence. Defining

$$\xi = \frac{\epsilon^2}{E_1^2}\ , \qquad \eta = \frac{E_o^2}{E_1^2} \tag{2.17}$$

$$\text{such that} \qquad f(\eta)d\eta = \frac{F_o(E_o)}{F_o(E_1)}\ , \qquad g(\xi) = \frac{L(\epsilon)}{L(E_1)}$$

$$\text{and} \qquad k(E_o^2-\epsilon^2) = k(\eta-\xi),$$

then Equation 2.15 becomes

$$g(\xi) = \int_{\xi}^{\infty} f(\eta)k(\eta-\xi)d\eta, \tag{2.18}$$

a general convolution with kern^{-1}

$$g(\xi) = \int_{\xi}^{\infty} f(\eta)k(\eta-\xi)d\eta,$$
$$k(\eta-\xi) = 0 \qquad \text{for} \quad \xi > \eta.$$

As such it can in principle be solved for a variety of standard methods, (cf. Craig and Brown (1986)), for any kernel function k specified by $x(M)$.

2.4 Functional Equation of Step Function Ionisation

The ionisation of the solar atmosphere falls sharply with N across the transition region. This steep decline can be approximated to a step-function whose simplified form allows further analytic investigation into the solutions to Equation 2.18. We first justify this approximation in terms of what is known observationally about the atmospheric structure of a flare loop.

2.4.1 Ionisation Profile of Flaring Atmosphere

Determining the variation of ionisation fraction x with column density N could be obtained self-consistently using beam dynamics to determine the energy deposition with depth, balancing the energy losses due to radiation, conduction, and mass motion in order to determine $n(N)$, $T(N)$, and so, via ionisation balance, $x(N)$ (Brown, 1973b). With a host of secondary heating processes, the difficulty of dealing with optically thick radiative transport and time-dependent ionisation balance, this approach is difficult and unreliable.

Instead, use could be made of semi-empirical models of atmospheric parameters derived from flare observations over a wide spectral range. Briefly, a semi-empirical model is one in which a temperature structure is calculated, to yield the best possible fit to the strength and shape of a number of important spectral lines. The equations of hydrostatic equilibrium, of statistical balance and non-LTE radiative transfer are then solved self-consistently over the emitting region to yield density distributions of protons, electrons and atomic particles in various levels of excitation This involves the calculation of ionisation levels, absorption and emission co-efficients and radiative fluxes etc. throughout the atmosphere ensuring that all global and local constraints are satisfied. Examples of such semi-empirical models can be found for flare atmospheres in Machado et al. (1980) and Machado and Linsky (1975). These semi-empirical models are limited in that they have been developed from only a few separate flare events and therefore may not represent the majority of flares.

The ionisation for such a semi-empirical model is shown in Figure 2.3a for the F1 flare

atmosphere described in Machado et al. (1980). For this model atmosphere the HXR flux spectrum was derived for an electron power-law flux $\delta = 5$ as was the HXR spectrum assuming a step-function atmosphere with the same electron spectra. The ratio of these two HXR fluxes is plotted in Figure 2.3b for steps occurring in N at $1.65, 1.85, 1.90 \times 10^{20}\text{cm}^{-2}$ clearly showing that the differences in HXR spectra are negligible, i.e. the HXR emission from the transition region is insignificant.

2.4.2 Deriving Functional Equation

For a simple step-function approximation to the ionisation structure of a flare loop,

$$x = 1 \quad \text{for} \quad N \leq N_1 \qquad x = 0 \quad \text{for} \quad N > N_1$$

or

$$x = 1 \quad \text{for} \quad M \leq M_1 \qquad x = 0 \quad \text{for} \quad M > M_1 = (\lambda + 1)N_1$$

where N_1 is the column density between the acceleration site and the transition region, then the kernel of integral Equation 2.15 is simply

$$k(E_o^2 - \epsilon^2) = \begin{cases} \frac{1}{(\lambda+1)} & M \leq M_1 \\ \\ \frac{1}{\lambda} & M > M_1. \end{cases} \tag{2.19}$$

Transforming this kernel into η space by choosing the characteristic energy $E_1 = (2KM_1)^{1/2}$, such that $\eta = 1$ equates to an electron having just enough energy to reach the transition region, then

$$k(\eta - \xi) = \begin{cases} \frac{1}{(\lambda+1)} & \eta \leq \xi + 1 \\ \\ \frac{1}{\lambda} & \eta > \xi + 1. \end{cases} \tag{2.20}$$

Thus Equation 2.18 with a step-function $x(N)$ can be rewritten as

$$\frac{1}{(\lambda+1)} \int_{\xi}^{\xi+1} f(\eta) d\eta + \frac{1}{\lambda} \int_{\xi+1}^{\infty} f(\eta) d\eta = g(\xi) \tag{2.21}$$

which, on differentiation with respect to ξ, reduces to the non-integral form

$$f(\eta) + \nu f(\eta + 1) = -(\lambda + 1) g'(\eta). \tag{2.22}$$

Here $\mu = \frac{\lambda}{\lambda+1}$. Just as a step-function atmosphere is a special case of Equation 2.18, so is the uniformly ionised atmosphere, (Brown, 1971), k for this case being constant at

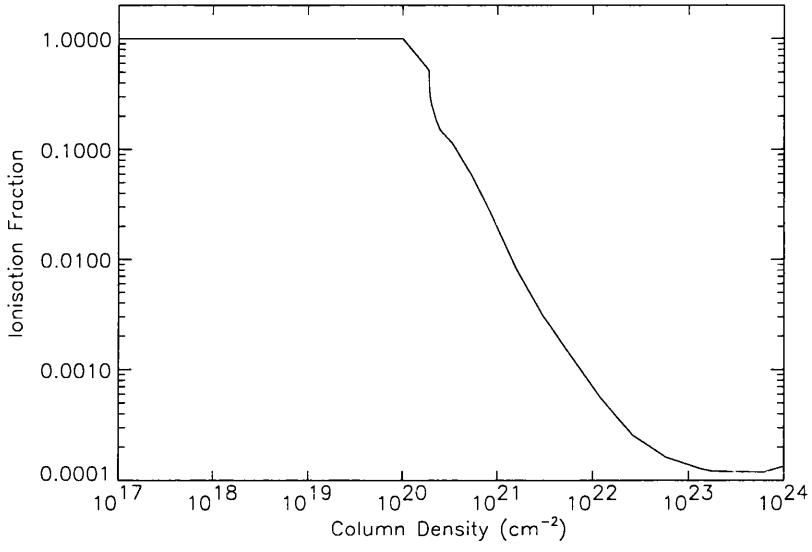

(a)

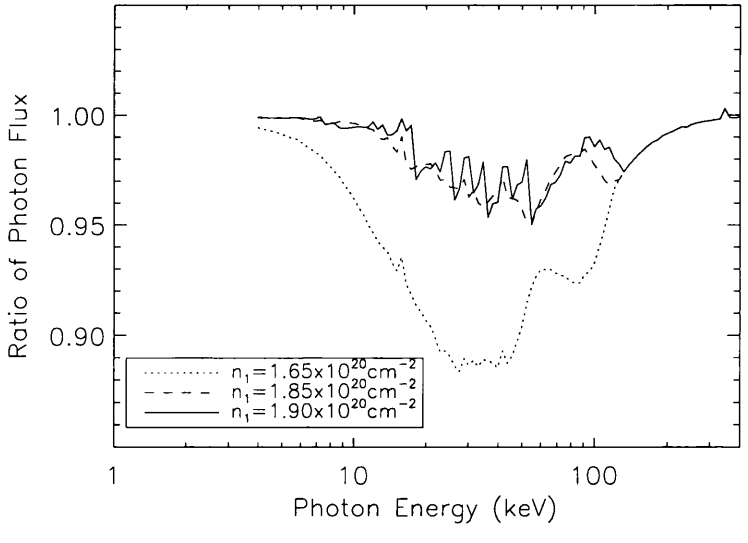

(b)

Figure 2.3: (a) Variation of ionisation fraction with column density for the semi-empirical flare model F1 from Machado *et al*, (1980). (b) Ratio of photon flux derived for a non-uniformly ionised thick target with ionisation profile given by F1 flare of from Machado *et al*, (1980) compared to step-function ionisation profiles with N_1 at$1.65, 1.85, 1.90 \times 10^{20}\mathrm{cm}^{-2}$.

$\frac{1}{\lambda+1}$ for all $\eta > \xi$. As such we can express the relationship between bremsstrahlung spectra $g(\xi)$ and electron spectra $f^*(\eta)$ for a totally ionised atmosphere in a similar manner to Equations 2.21, 2.22. i.e.

$$g(\xi) = \frac{1}{\lambda+1}\int_{\xi}^{\infty} f^*(\eta)d\eta, \qquad \text{or} \qquad -(\lambda+1)g'(\eta) = f^*(\eta).$$

Thus if a photon spectrum $g(\xi)$ was observed, the inferred electron spectrum $f^*(\eta)$ assuming a uniformly ionised target, is related to electron spectrum $f(\eta)$, inferred from an atmosphere with a realistic step-function ionisation profile, by

$$f(\eta) + \nu f(\eta+1) = f^*(\eta), \tag{2.23}$$

a functional equation (Kuczma, 1968) dependent only on η. In terms of the original variables $F_o(E_o)$ and $F_c^*(E_o)$ the relationship between the two electron distribution functions is

$$F_o^*(E_o) = F_o(E_o) + \frac{\nu F_o\left((E_o^2+E_1^2)^{\frac{1}{2}}\right)}{(E_o^2+E_1^2)^{\frac{1}{2}}}. \tag{2.24}$$

2.5 Comparing $F_o(E_o)$ to $F_o^*(E_o)$

For any electron distribution $f(\eta)$ in a non-uniformly ionised (step-function) target, the equivalent distribution $f^*(\eta)$ can be inferred from Equation 2.23. Thus differences in electron distribution, energy and electron number fluxes, inferred from a photon spectrum assuming a uniform or step-function ionisation profile for the flare atmosphere can be investigated.

2.5.1 Mono-energetic Beam

By considering the case of a mono-energetic beam incident on a thick target from Equation 2.23, the concept that the inferred $f^*(\eta)$ must include a secondary component at energy $\eta - 1$,$(E_o^2 - E_1^2/E_1^2)$, can be clearly shown. Describing $f(\eta)$ as

$$f(\eta) = \delta(\eta - \eta_s),$$

with δ the delta function then Equation 2.23 implies

$$f^*(\eta) = \delta(\eta - \eta_s) + \nu\delta(\eta - (\eta_s - 1)).$$

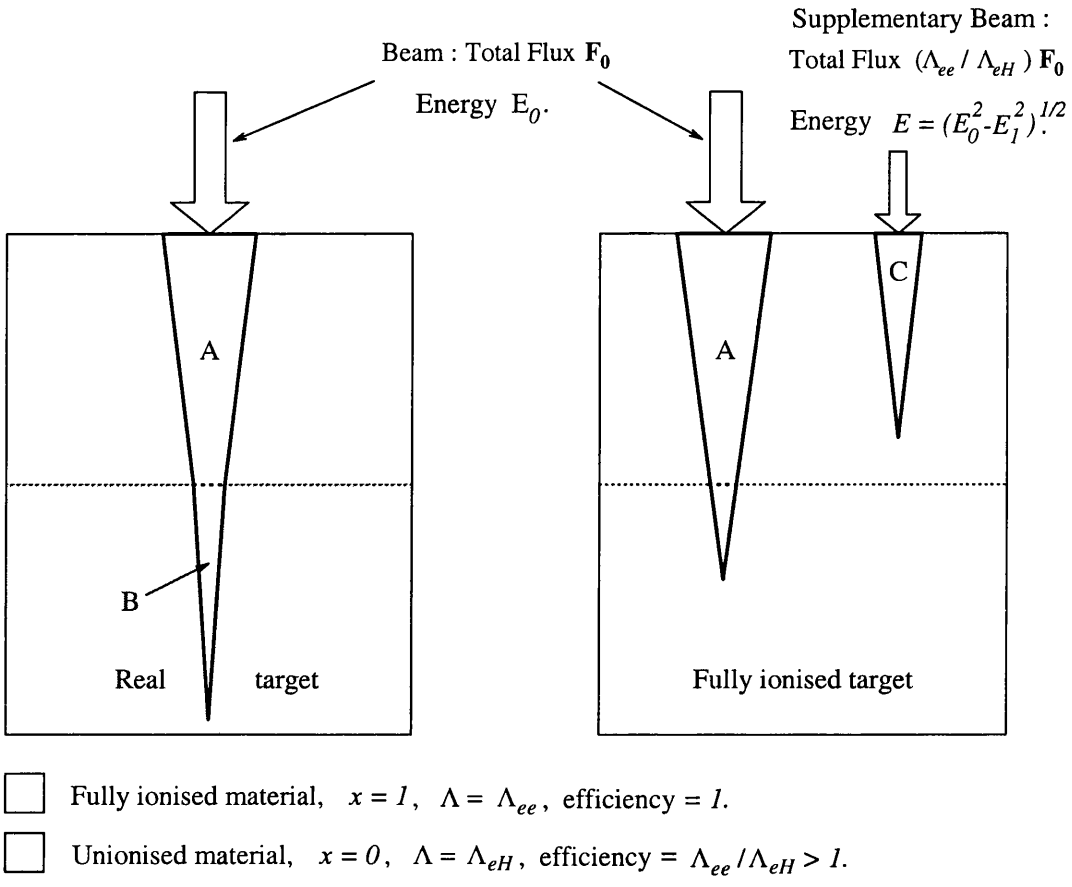

Figure 2.4: Injection of an electron beam of total flux $\mathbf{F_0}$ and energy E_o into a target with step function ionisation (left panel) produces bremsstrahlung in the upper ionised target with 'efficiency' 1 then enters the lower target as a beam of flux $\mathbf{F_0}$ at energy $(E_o^2 - E_1^2)^{1/2}$, where it produces bremsstrahlung with efficiency $\Lambda_{ee}/\Lambda_{eH}$. Injection of the same initial beam alone into an ionised target (right panel) produces less bremsstrahlung by an amount equal to that from a beam of energy $(E_o^2 - E_1^2)^{1/2}$ and flux $(\Lambda_{ee}/\Lambda_{eH} - 1)\mathbf{F_0}$. To match the bremsstrahlung from the left panel, therefore, an ionised target requires the injection of a supplementary beam with these parameters.

In the case of $\eta_s \leq 1$, then no electron would pass through the step in ionisation hence $f* \equiv f$. Where $\eta_s > 1$ then for a step-function atmosphere, as the electrons enter the chromosphere, ($x \approx 0$), the energy of the beam will be $\eta - 1$ (see Figure 2.4). As the Coulomb energy losses are reduced by the lower effective Coulomb logarithm of the neutral atmosphere, production of photons of energy $< \eta - 1$ is enhanced by a factor ≈ 2.818 i.e. $(\Lambda_{ee}/\Lambda_{eH})$. Thus, for a fully ionised target to reproduce the photon spectrum, an additional flux of electrons must be injected with the primary mono-energetic beam. This secondary beam must have energy $(\eta - 1)$ and a flux of $1.818 = \nu$ times the flux of the primary beam. Figure 2.5, shows the result for $\eta_s = 3$.

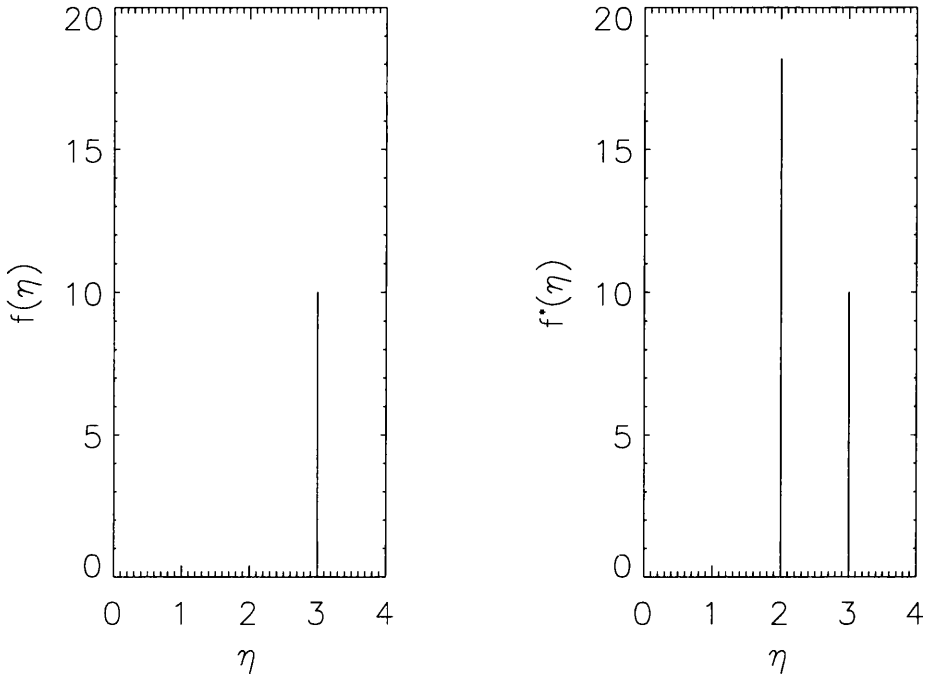

Figure 2.5: Injection Spectrum F^* required for an ionised target to yield the same photon spectrum as a mono-energetic beam (δ-function) f injected into a step-function ionised target.

Although in a non-uniform model, enhanced photon production occurs in the chromosphere, photon production from a uniformly ionised thick target is independent of where the beam is injected in the atmosphere. Thus the secondary beam need not be injected at chromospheric depths, but can be injected along with the primary beam at the coronal injection site. This simple explanation for a mono-energetic beam has made no reference to the form of bremsstrahlung cross-section $q(\epsilon, E)$ used. Therefore the general results of this analysis, i.e. the requirement of an additional electron flux component at energy equivalent to $\eta - 1$ should be independent of bremsstrahlung cross-section used.

2.5.2 Power Law Injection

Hard X-ray spectral observations suggest that the electron population can be approximated by an electron distribution decreasing with energy in a power-law. For a single power-law form $f(\eta) = \eta$ at all η, then the corresponding $f^*(\eta)$ is the sum of a power law

and shifted power law :

$$f^*(\eta) = \eta^{-\alpha} + \nu(\eta + 1)^{-\alpha}$$

Here the spectral index α in η space corresponds to the usual flux spectral index δ in E_o space by

$$\alpha = \frac{\delta + 1}{2}$$

The comparison of $f(\eta)$ and $f^*(\eta)$ for $\alpha = 3$ ($\delta = 5$) is shown in Figure 2.6. The difference

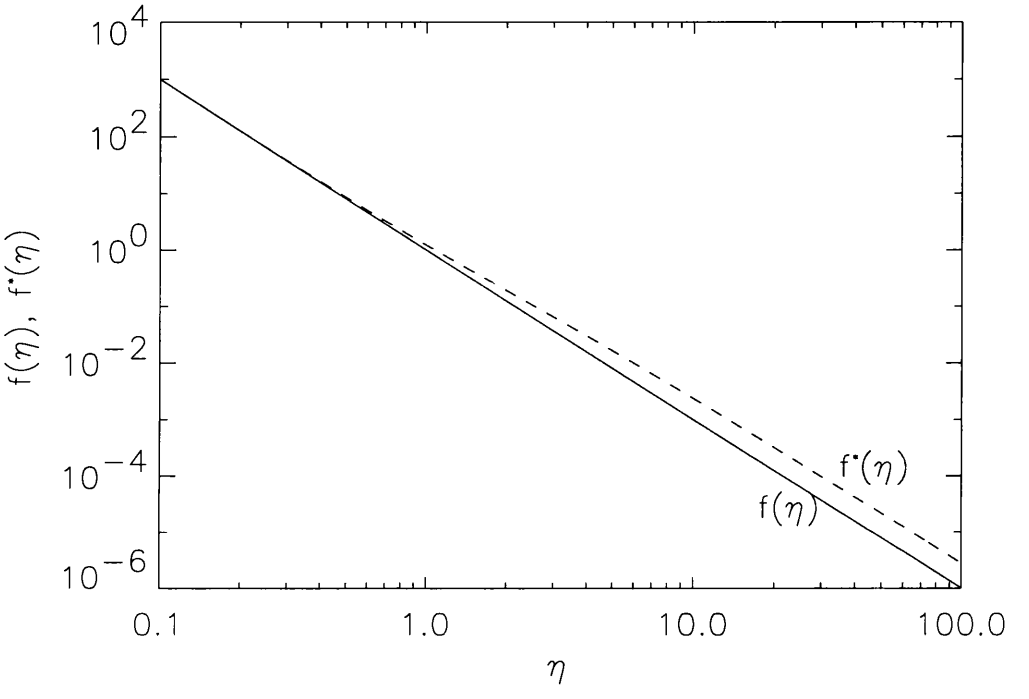

Figure 2.6: Injection Spectrum f^* required for an ionised target to yield the same photon spectrum as a pure power-law spectrum f injected into a step-function ionised target.

is most significant at high η, where it reaches the maximum possible of $\nu + 1 \approx 2.8181$.

At low η ($\eta < 1$) $f(\eta)$ and $f^*(\eta)$ are approximately equal. This is due to the steep decline of the electron population with energy in the power law. For $\eta < 1$ the number of electrons at η compared to $\eta+1$ is significantly greater by up to a few orders of magnitude. Thus even though ν is greater than 1, the total number of electrons in $f^*(\eta)$ at low η is dominated by the primary component i.e $f(\eta) \approx f^*(\eta)$. At high η, the power law flux of $f(\eta)$ is such that $f(\eta) \approx f(\eta + 1)$. Hence the total $f^*(\eta) \approx (\nu + 1)f(\eta)$.

Physically, as a result of the steep power law, the majority of low energy photons ($\epsilon << E_1$) are emitted by interactions of electrons with low initial energy E_o. As these electrons are stopped in the corona, then the ionised model is a good approximation. For high energy photons ($\epsilon >> E_1$), the majority are produced by electrons which reach the chromosphere and hence the electron flux assuming an ionised atmosphere will be a factor of 2.818 larger than required. If we compared instead $f(\eta)$ with the flux inferred from a totally unionised atmosphere $f^{\diamond}(\eta)$, then we would find at high η, $f(\eta) \approx f^{\diamond}(\eta)$, while at low η, $f^{\diamond}(\eta)$ would be a factor of 2.818 to low.

2.5.3 Spectral Cut-Offs

By far the most striking differences between $f(\eta)$ and $f^*(\eta)$ occur for electron distributions with sharp features e.g. mono-energetic beam rather than for smooth ones like unbroken power laws. For example if $f(\eta)$ is a top-hat function, non-zero over the range $\eta_1 < \eta < \eta_2$ then by Equation 2.23, $f^*(\eta)$ is non-zero over the ranges $\eta_1 < \eta < \eta_2$ and $\eta_1 - 1 < \eta < \eta_2 - 1$ which overlap if $\eta_1 < \eta_2 - 1$. This is shown in Figures 2.7 a, b for $f(\eta) = 1$ in $1 < \eta < 1.5$, and in $1 < \eta < 3$ respectively. The case of a power law with low energy cut-off at $\eta = \eta_1$ is also shown in Figures 2.8 a, b for power-law index $\alpha = 3$ and $\eta_1 = 0.5,\ 1.5$.

The spectral characteristics of $f(\eta)$ and $f^*(\eta)$ have very significant differences. For the flat top-hat function not only could $f^*(\eta)$ be interpreted as having two separate components but when the width of the top-hat function is greater than 1, the electron distribution $f^*(\eta)$ could be inferred as peaking around the center of the top-hat width (clearly not flat). Also in reproducing the photon spectrum produced by $f(\eta)$, in a fully ionised atmosphere $f^*(\eta)$ often requires electrons in low energy ranges where $f(\eta) = 0$.

2.5.4 Shape Preserving Spectra

Clearly for the previous examples of $f(\eta)$, the required $f(\eta)^*$ have different spectral characteristics. This is not always the case. For $f(\eta)$ and $f^*(\eta)$ to have the same shape then we need $f(\eta + 1) = af(\eta)$, where a is a constant. The simplest example of $f(\eta)$ which meets this criterion is

$$f(\eta) = e^{\beta\eta}, \quad \text{thus} \quad f(\eta + 1) = e^{\beta}e^{\beta\eta} \quad \text{i.e.} \quad a = e^{\beta}.$$

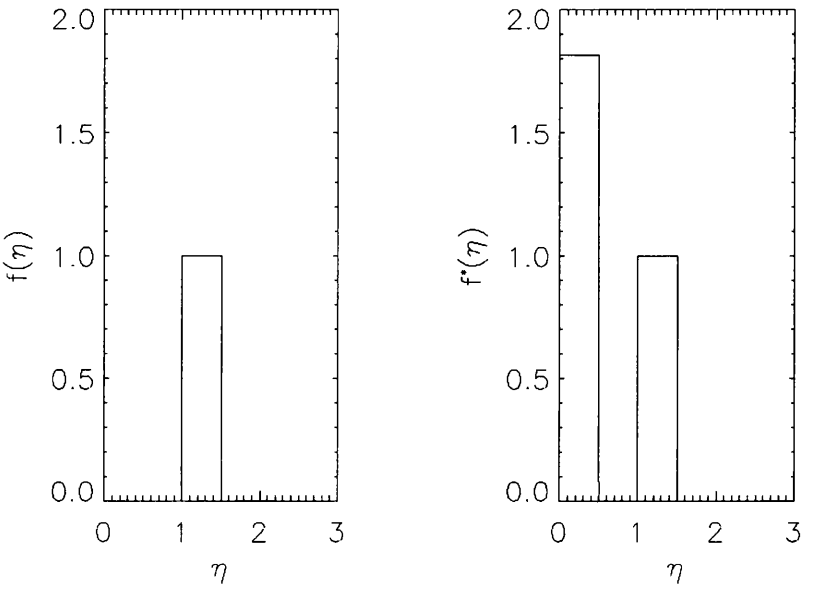

(a)

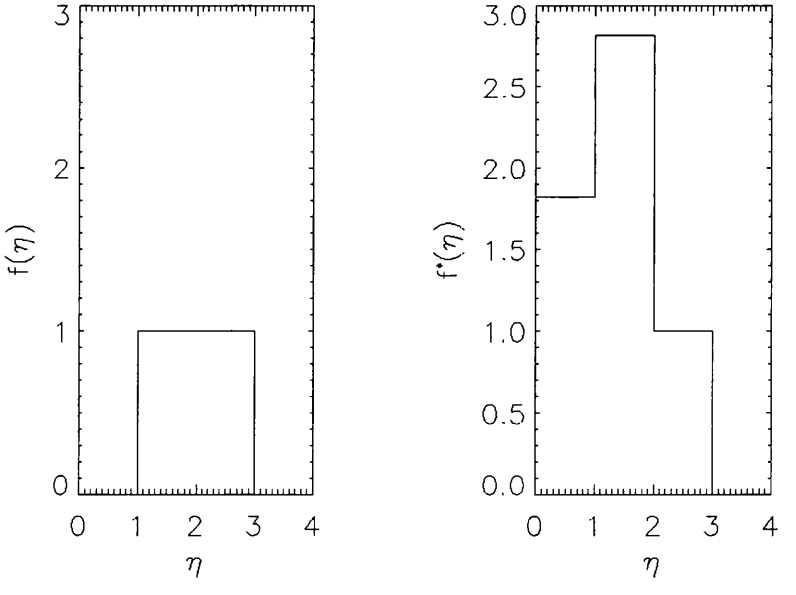

(b)

Figure 2.7: Injection Spectrum f^* required for an ionised target to yield the same photon spectrum as a 'top-hat' spectrum f injected into a step-function ionised target, for two different 'top-hat' locations. (a) For $f(\eta) = 1$ in $1 < \eta < 1.5$. (b) For $f(\eta) = 1$ in $1 < \eta < 3$.

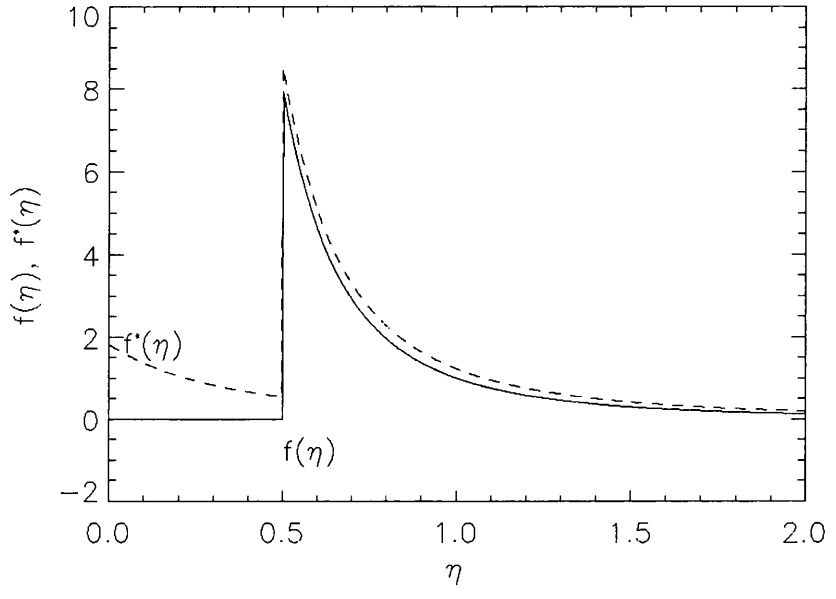

(a)

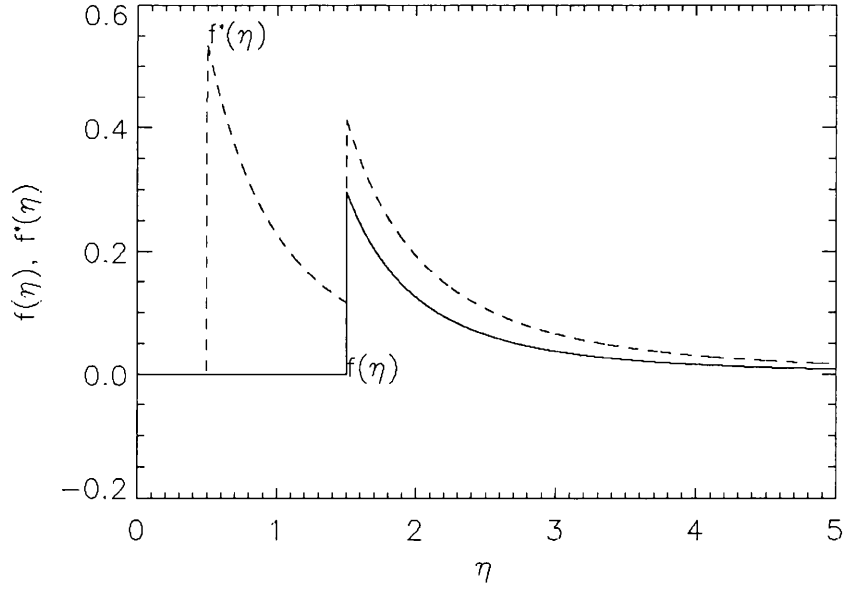

(b)

Figure 2.8: Injection Spectrum f^* required for an ionised target to yield the same photon spectrum as a power-law spectrum f with low cut-off injected into a step-function ionised target, for two different cut-off values. (a) $\alpha = 3$, $\eta_1 = 0.5$, (b) $\alpha = 3$, $\eta_1 = 1.5$.

Therefore for exponential spectra (exponential in η, not E_o), $f(\eta)$ and $f^*(\eta)$ have identical spectral behaviour, differing only in amplitude. This is true whether $\beta = 0$ (completely flat spectrum) or $\beta < 0$. For $\beta > 0$, if the spectrum is to be physical, there must be an upper cut-off in which case the translational invariance of functional operation 2.23 breaks down. In the case of complex β in general the shape is preserved with a phase shift as well as an amplitude change i.e. if

$$f(\eta) = A + Be^{(C+i\omega)\eta}$$

where A has been added to ensure $f(\eta) > 0$, then $f^*(\eta)$ has the form as in Figure 2.9

$$f^*(\eta) = a_1 + a_2 f(\eta)$$

as shown in Figure 2.9. This form is still shape preserving but no longer simply scalar.

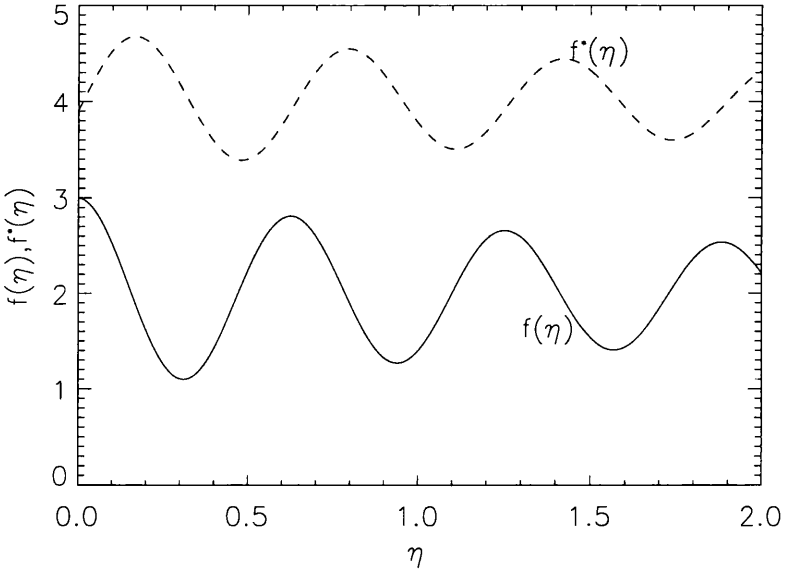

Figure 2.9: Injection Spectrum f^* required for an ionised target to yield the same photon spectrum as an exponential/harmonic spectrum $f(\eta) = A + Be^{(C=i\omega)\eta}$ injected into a step-function-ionised target. Here $A = 2$, $B = 1$, $C = 1/3$ and $\omega = 10$.

In general then, from the analysis of Equation 2.23 we see that assuming the form of $f(\eta)$ in order to yield the same photon spectrum for a fully ionised target it is necessary to enhance the number of electrons $f^*(\eta)$ everywhere compared to the electron injection spectrum $f(\eta)$ which is injected into a step-function ionised target. This includes electron ranges where no electrons are required in $f(\eta)$. The inference of these electrons, by

inversion of a bremsstrahlung spectrum wrongly assuming a fully ionised target model, will result in incorrect spectral shapes. Thus any conclusion concerning the acceleration mechanism based on these spectral shapes cannot be trusted (cf. Chapter 3). Also these additions to the spectra can significantly affect the inferred total electron beam power of the flares, particularly if the inferred spectrum is extrapolated, using the wrong spectral shape, outside the range in which it is directly inferred from HXR data, as is often done (Brown, 1971).

2.6 Inversion of Functional Equation

In determining the electron spectrum from HXR spectral observations, the photon spectrum we observe $J(\epsilon)$, in an ideal world with no data noise, discretisation or truncation, by differentiating twice leads directly to the electron spectrum $F_o^*(E_o)$ required for a fully ionised target i.e.

$$F_o^*(E_o) = \frac{(\lambda+1)K}{Q_o}\left[\frac{d^2}{d\epsilon^2}(\epsilon J)\right]_{\epsilon=E_o}. \tag{2.25}$$

Thus in the terms of Equation 2.23, the problem is not to derive $f^*(\eta)$ for a given $f(\eta)$ but rather the converse which turns out to be a nontrivial task. The solution and determination of the conditions for such solutions to be unique is non-trivial for this type of functional equation. Here the main facets for such criteria most relevant to Equation 2.23 are explored.

2.6.1 Mono-energetic Beam

Consider the photon spectrum which corresponds to that from a mono-energetic beam in a fully ionised target, i.e. $f^*(\eta) = \delta(\eta - \eta_s)$ where $\eta_s = m + \Delta m$, m is an integer and $0 \leq \Delta m < 1$. For f to be physical, i.e positive, then it is required that

$$f(\eta) = 0 \text{ for } \eta > \eta_s \quad \text{and hence} \quad f(\eta_s) = f^*(\eta_s).$$

Thus from Equation 2.23, for $\eta \leq \eta_s$

$$f(\eta) = \sum_{i=0}^{m}(-\nu)^i \delta(\eta - \eta_s - i), \tag{2.26}$$

illustrated in Figure 2.10 for $\eta_s = 4.5$. Here each 'primary' contribution to $f^*(\eta)$ from the δ-function at $\eta = \eta_s - 1$ in $f(\eta)$ cancels the 'secondary' contribution to $f^*(\eta)$ from the

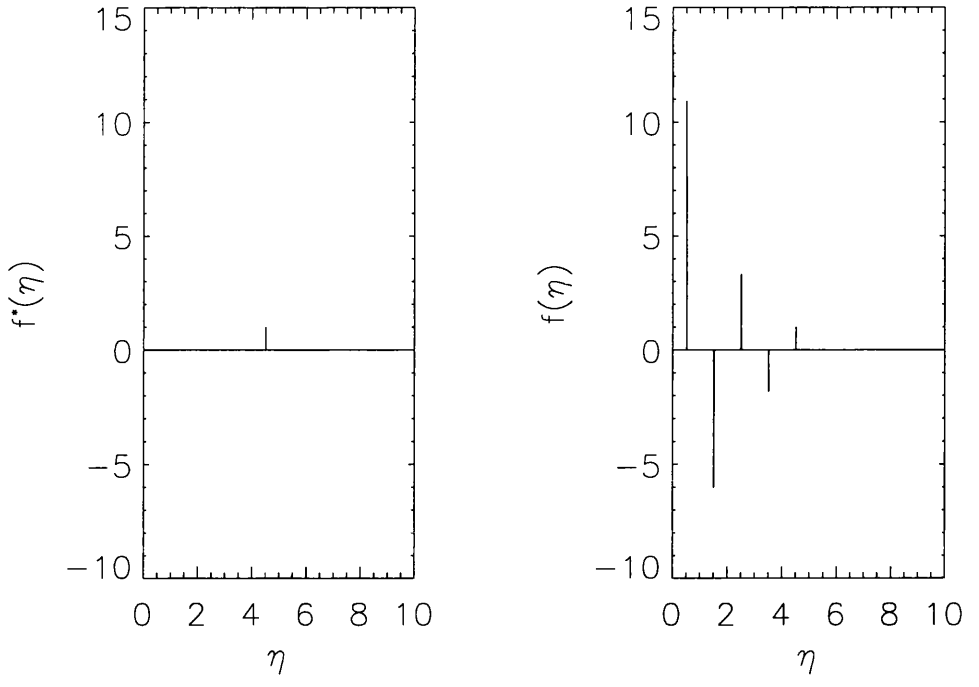

Figure 2.10: Injection spectrum f required for a step-function-ionised target to yield the same photon spectrum as a single spike (delta function) spectrum f^* injected into an ionised target.

δ-function at $\eta = \eta_s$. The δ-function at $\eta_s = 0.5$ has no 'secondary' component (since all the electrons have stopped in the ionised corona), therefore no additional 'primary' components are required and the series of δ-functions in $f(\eta)$ is finite. Thus, unless $\eta_s < 1$, the solution for $f(\eta)$ for a δ-function $f^*(\eta)$ is a geometric series of δ-functions with increasing amplitudes and alternating signs, which is completely unphysical.

The amplitude of the δ-functions is increasing with decreasing η since $\nu > 1$. If $\nu < 1$ (e.g. if the ionisation level in the chromosphere were $x > 0.225$) then the δ-functions would decrease with decreasing η. If $\nu < 0$, corresponding to the injection of electrons in the chromosphere moving into the corona, then $f(\eta)$ would be a series of non-alternating δ-functions. Due to the decreased efficiency in the second part of the target in that case there are insufficient photons produced from below energy $\eta - 1$. Therefore an additional beam must be injected, but if it too enters the corona, again the bremsstrahlung production at energy $\eta - 2$ will be depleted. Therefore additional components will be required until the last component stops entirely in the chromosphere.

2.6.2 Non-uniqueness of Unconstrained Mathematical Solution

Without imposing any physical requirements on the nature of the electron distributions, it can be shown that the solution of Equation 2.23 for $f(\eta)$ can never be unique for any $f^*(\eta)$. To any solution $f(\eta)$ of Equation 2.23, then it is possible to add a solution f_o of the homogeneous form of Equation 2.23 given by

$$f_o(\eta + 1) = -\lambda f_o(\eta) \tag{2.27}$$

The above is not an equation for f_o but only a recursion relation expressing $f_o(\eta + 1)$ in terms of $f_o(\eta)$. f_o can have any functional form whatsoever. So defining $f_o(\eta) = \phi(\eta)$ in the interval $0 < \eta \leq 1$ then in interval $(\eta + j, \eta + j + 1]$ it is

$$f_o(\eta_o + j) = (-\lambda)^j \phi(\eta_o). \tag{2.28}$$

This can be written as $f_o(\eta) = (-\lambda)^j \phi(\eta_o)$ where j is the largest integer strictly less than η ($j < \eta$) and η_o is defined by $\eta = j + \eta_o$, so that $0 < \eta_o \leq 1$. This notation will be used frequently in what follows. Such functions f_o belong to the null space of the operator defining functional Equation (2.23) i.e. they contribute nothing to the data $f^*(\eta)$. Addition of any arbitrary combination of them cannot be excluded without use of prior assumptions on $f(\eta)$, such as those based on physical acceptability. That is, if some function $f_1(\eta)$ satisfies Equation (2.23) then so does $f_1(\eta) + (-\lambda)^j \phi(\eta_o)$ (again with $\eta = \eta_o + j$) for any function $\phi(\eta_o(\eta))$ whatsoever defined on $(0, 1]$. *So, without physical constraints there exist an infinity of solutions to the thick target bremsstrahlung inversion problem for a step-function ionised target.*

2.6.3 Independence of Non-Uniqueness from $q(\epsilon, E)$

It can be shown that the existence of functions f_o which are the solutions to the homogeneous form of the thick target problem and therefore contribute nothing to the eventual photon spectrum is independent of the exact form of bremsstrahlung cross-section $q(\epsilon, E)$ chosen. Considering Equation 2.14 i.e.

$$J(\epsilon) \propto \int_{E_o=\epsilon}^{\infty} F_o(E_o) \int_{\epsilon}^{E_o} \frac{q(\epsilon, E)\, dE\, dE_o}{\lambda + x(M(E_o, E))} \tag{2.29}$$

By reversing the order of integration then $J(\epsilon)$ can be expressed as being

$$\propto \int_{\epsilon}^{\infty} q(\epsilon, E) \int_{E}^{\infty} \frac{F_o(E_o)\, dE_o\, dE}{\lambda + x(E_o, E)}$$

When a step-function ionisation profile in substituted, this becomes

$$J(\epsilon) \propto \frac{1}{\lambda+1}\int_{\epsilon}^{\infty} q(\epsilon,E)\int_{E}^{\sqrt{E^2+E_1^2}} F_o(E_o)\,dE_o\,dE$$
$$+\frac{1}{\lambda}\int_{\epsilon}^{\infty} q(\epsilon,E)\int_{\sqrt{E^2+E_1^2}}^{\infty} F_o(E_o)\,dE_o\,dE$$

Defining $\mathcal{F}(E) = \int_E^\infty F_o(E_o)\,dE_o$ then

$$J(\epsilon) = \frac{1}{\lambda+1}\int_{\epsilon}^{\infty} q(\epsilon,E)\,\mathcal{F}(E)\,dE + \frac{1}{\lambda(\lambda+1)}\int_{\epsilon}^{\infty} q(\epsilon,E)\,\mathcal{F}\left((E^2+E_1^2)^{1/2}\right)\,dE$$

which on differentiating with respect to ϵ becomes

$$J'(\epsilon) = \frac{1}{\lambda+1}\int_{\epsilon}^{\infty} q'(\epsilon,E)\,\mathcal{F}(E)\;\,dE + \frac{1}{\lambda(\lambda+1)}\int_{\epsilon}^{\infty} q'(\epsilon,E)\,\mathcal{F}\left((E^2+E_1^2)^{1/2}\right)\,dE$$

provided the cross-section $q(\epsilon,E)$=0 for $E = \epsilon$. Similarly for a fully ionised source we could express $J'(\epsilon)$ as

$$J'(\epsilon) = \frac{1}{\lambda+1}\int_{\epsilon}^{\infty} q'(\epsilon,E)\,\mathcal{F}^*(E)\,dE$$

Hence the relationship between $F_o(E_o)$ and $F_o^*(E_o)$ is governed by

$$\int_{\epsilon}^{\infty} q'(\epsilon,E)\,\mathcal{F}(E)\;\,dE + \nu\int_{\epsilon}^{\infty} q'(\epsilon,E)\,\mathcal{F}\left((E^2+E_1^2)^{1/2}\right)\,dE = \int_{\epsilon}^{\infty} q'(\epsilon,E)\,\mathcal{F}^*(E)\,dE \tag{2.30}$$

which has null space solutions if

$$\mathcal{F}(E) = -\nu\mathcal{F}\left(\sqrt{(E^2+E_1^2)}\right).$$

Hence any non-unique electron spectra inferred from a step-function-ionisation atmosphere is not a consequence of assuming a simple form for the bremsstrahlung cross-section.

2.6.4 Physically Acceptable Non-Unique Solutions

Physical constraints on the form of $f(\eta)$ can be imposed. It may therefore be thought that these constraints restrict the addition of homogeneous solutions such that only one physically acceptable $f(\eta)$ can be inferred. The most liberal restrictions on $f(\eta)$ are that $f(\eta) \geq 0$ and that $f(\eta)$ is bounded. Similarly the total electron beam flux and power should also be finite. This requires that $f(\eta) \to 0$ as $\eta \to \infty$ faster than $\eta^{-3/2}$ and that $f(\eta) \to \infty$ as $\eta \to 0$ slower than η^{-1}. Demanding that the inferred $f(\eta)$ be continuous is too restrictive. There is no physical reason why the accelerated electrons

would be continuous and any discontinuity could well be a useful signature for a particular acceleration mechanism. By using the above constraint, beginning initially with $f(\eta) > 0$, it can be shown that physically acceptable non-unique solutions can still be inferred.

If a solution of Equation 2.23 exists and is

$$f(\eta) = \phi(\eta) \quad \text{in some interval} \quad \eta_1 < \eta \leq \eta_1 + 1,$$

which is chosen without loss of generality to be $0 < \eta \leq 1$, then the solution over the whole range can be obtained recursively. From Equation 2.23

$$f(\eta) = \lambda[f^*(\eta - 1) - f(\eta - 1)]$$

then for $1 < \eta \leq 2$ and defining $\eta = \eta_o + j$ where j integer and $0 < \eta_o < 1$ we obtain

$$f(\eta_o + 1) = \lambda[f^*(\eta_o) - \phi(\eta_o)]$$

Subsequently for $2 < \eta \leq 3$

$$\begin{aligned} f(\eta_o + 2) &= \lambda[f^*(\eta_o + 1) - f(\eta_o + 1)] \\ &= \lambda[f^*(\eta_o + 1) - \lambda[f^*(\eta_o) - \phi(\eta_o)] \\ &= \lambda f^*(\eta_o + 1) - \lambda^2 f^*(\eta_o) + \lambda^2 \phi(\eta_o) \end{aligned}$$

By recursive use of this argument we finally obtain an expression for $f(\eta)$ i.e.

$$f(\eta_o + j) = (-\lambda)^j \left[\phi(\eta_o) - \sum_{i=0}^{j-1} (-\nu)^i f^*(\eta_o + i) \right]. \tag{2.31}$$

To ensure $f(\eta) \geq 0$ for all j and all $0 < \eta_o \leq 1$ Equation 2.31 requires

$$\sum_{i=0}^{2k-1} (-\nu)^i f^*(\eta_o + i) \leq \phi(\eta_o) \leq \sum_{i=0}^{2k} (-\nu)^i f^*(\eta_o + i) \tag{2.32}$$

for all $k \geq 0$ and all $0 < \eta_o \leq 1$, where k has been introduced to distinguish between even $j = 2k$ and odd $j = 2k + 1$ to deal with the opposite signs of the inequality for even and odd j. It follows that $\phi(\eta_o)$ is unique if the sums in Equation 2.32 converge absolutely, i.e. if

$$S(\eta_o) = \sum_{i=0}^{\infty} \left| (-\nu)^i f^*(\eta_o + i) \right| = \sum_{i=0}^{\infty} \nu^i f^*(\eta_o + i) \tag{2.33}$$

converges.

If $|\nu| < 1$ the series converges. $|\nu| < 1$ corresponds to the case where the ratio of efficiencies in the two targets are in the range $0 < \Lambda_1/\Lambda_2 < 2$. From a fully ionised first target the ionisation factor of the second target must be greater than 0.225 for convergence. For the present case of $\nu > 1$ the convergence condition for a unique solution is more restrictive. It requires that as $i \to \infty$

$$\text{as } i \to \infty, \qquad \nu^i f^*(\eta_o + i) = e^{i \log(\nu)} f^*(\eta_o + i) \to 0 \text{ faster than } i^{-1},$$

for which a sufficient condition is $f^*(\eta_o + i) \sim e^{-ai}$ with $a > \log \nu$.

This situation can be understood in terms of null functions as follows. The homogeneous solutions, Equation (2.28), behave as $f_o(\eta_o + j) = (-\lambda)^j \phi(\eta_o)$. Since $\nu = 1/\lambda > 1$ these decline like $e^{-j \log \nu}$ at large η but alternate in sign. If a solution $f(\eta)$ of (2.23) declines faster than this, then addition of any null function solutions $\phi(\eta_o)$ in $0 < \eta_o \leq 1$ would result in unphysical negative values of $f(\eta)$ at large η. Consequently the physical condition $f \geq 0$ demands that no non-uniqueness be introduced by addition of null function solutions.

Such exponential decline of $f^*(\eta)$ is not guaranteed by the physical requirement of finite beam flux or power and is not satisfied by power-law $f^*(\eta)$ extending to infinite energies. It follows that the solution of (2.23), with step-function representation of the real solar ionisation structure, for $f(\eta)$ is not unique unless $f^*(\eta)$ and hence the associated photon spectrum has sufficiently rapid exponential decline at high energy.

Laplace and Fourier Transform Solutions

A solution of Equation 2.23 can be found by applying a Laplace transform to it. Defining $F(s)$ by

$$f(\eta) = \int_0^\infty F(s) e^{-s\eta} ds = \mathcal{L}\left[F(s); \eta\right]$$

so that $F(s)$ is the inverse Laplace transform of $f(\eta)$, and similarly define $F^*(s)$ in terms of $f^*(\eta)$. It then follows that

$$f(\eta + 1) = \mathcal{L}\left[e^{-s} F(s); \eta\right]$$

so on taking the inverse Laplace transform of (2.23) we obtain

$$F(s) + \nu e^{-s} F(s) = F^*(s) \tag{2.34}$$

and hence the solution

$$f(\eta) = \mathcal{L}\left[\frac{F^*(s)}{1+\nu e^{-s}};\eta\right] = \int_0^\infty \frac{\mathcal{L}^{-1}[f^*(\eta);s]}{1+\nu e^{-s}} e^{-s\eta} ds.$$

This form enables computation of $f(\eta)$ in cases where $\mathcal{L}^{-1}[f^*(\eta);s]$ exists and hence consideration of existence and physical acceptability for different $f^*(\eta)$. Note that for the null solution (Eq 2.28), $\mathcal{L}^{-1}$ does not exist, because of the discontinuities in $f(\eta)$. This may be formally proved by noting that the null solution $f^*(\eta) = 0$ requires $F^*(s) = 0$ and hence, equation (2.34) (since $1 + \nu e^{-s} > 0$ for all s) that $F(s) = 0$. Hence the only null solution with an inverse Laplace transform is the trivial case $f(\eta) = 0$. In a similar fashion explicit inversion formulae for Equation 2.23 can be obtained by Fourier transforming i.e.

$$f(\eta) = \mathcal{F}^{-1}\left\{\frac{\tilde{f}^*(\omega)}{1+\lambda e^{i\omega}};\eta\right\},$$

For a pure power-law $f^*(\eta)=\eta^{-\alpha}$,

$$F^*(s) = \frac{s^{\alpha-1}}{\Gamma(\alpha)}$$

and so

$$f(\eta) = \frac{1}{\Gamma(\alpha)} \int_0^\infty \frac{s^{(\alpha-1)} e^{-s\eta}}{1+\nu e^{-s}} ds. \tag{2.35}$$

(This Laplace Transform solution to the inverse problem for a power-law $f^*(\eta)$ is precisely the integral definition of the special function '$\Phi(\eta,\alpha,s)$' in Gradshtein and Rhyzik (Section 9.55 Equation 9.556), who give the equation $f(x) + \nu f(x+1) = f^*(x)$ as one of the properties of this function, which appears to be related to the Riemann Zeta function).

Thus $f(\eta)$ is the spectrum required to be injected into a step-function-ionised target to produce a pure power-law photon spectrum. It is clearly ≥ 0 and has the same properties as $f^*(\eta)$, in that $f \to 0$ as $\eta \to \infty$ and $f \to \infty$ as $\eta \to 0$. Its form is given in Figure 2.11 for $\alpha = 3$ which shows, as expected that $f(\eta)$ is suppressed relative to f^* at high η by a factor of up to $\lambda + 1$ because of the reduced collisional energy losses there.

Also shown in Figure 2.12 is $f(\eta)$ for a displaced power-law $f^* = (\eta + \eta_o)^{-\alpha}$, which is more physically realistic since $f^*(0)$ is finite. For $f(\eta) = (\eta + \eta_o)^{-\alpha}$ then

$$F^*(s) = \frac{e^{\eta_o s} s^{\alpha-1}}{\Gamma(\alpha)}$$

and hence

$$f(\eta) = \frac{1}{\Gamma(\alpha)} \int_0^\infty \frac{s^{(\alpha-1)} e^{-s(\eta+\eta_o)}}{1+\nu e^{-s}} ds.$$

This solution is also non-negative everywhere and remains finite as $\eta \to 0$.

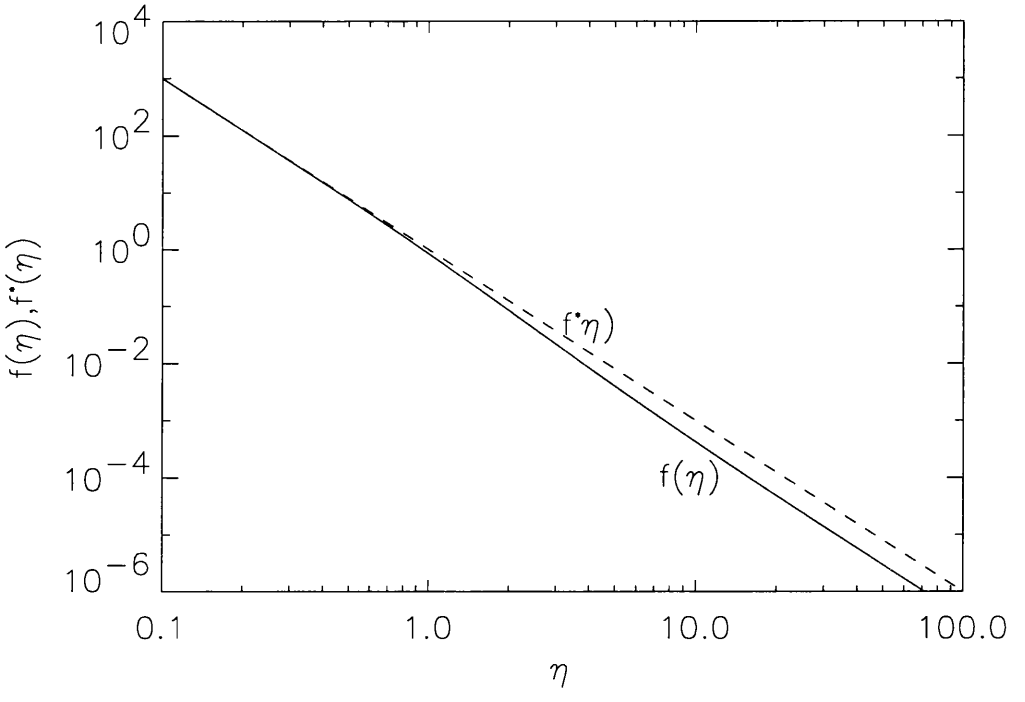

Figure 2.11: Injection spectrum f required for a step-function-ionised target to yield the same photon spectrum as a pure power-law spectrum f^* injected into an ionised target.

Examples of Physically Acceptable Non-Unique Solutions

To give a particular example of non-uniqueness of a physically acceptable solutions consider the 'data' spectrum

$$f^*(\eta) = \eta^{-\beta} + \nu(\eta + 1)^{-\beta}$$

for which, by design, $f_1(\eta) = \eta^{-\beta}$ is a physically acceptable solution of Equation (2.23). To this a homogeneous null-function solution of type (2.28) can be added. By adopting for simplicity a constant ϕ,

$$f_o(\eta) = f_o(j + \eta_o) = (-\lambda)^j A, \text{ for } j < \eta \leq j + 1$$

(i.e. $\phi(\eta_0) = A$ in $0 < \eta_o \leq 1$) where A is a constant. Thus the sum, f_2, of $f(\eta) = \eta^{-\beta}$ and $f_o(\eta)$,

$$f_2(\eta) = (j + \eta_o)^{-\beta} + (-\lambda)^j A,$$

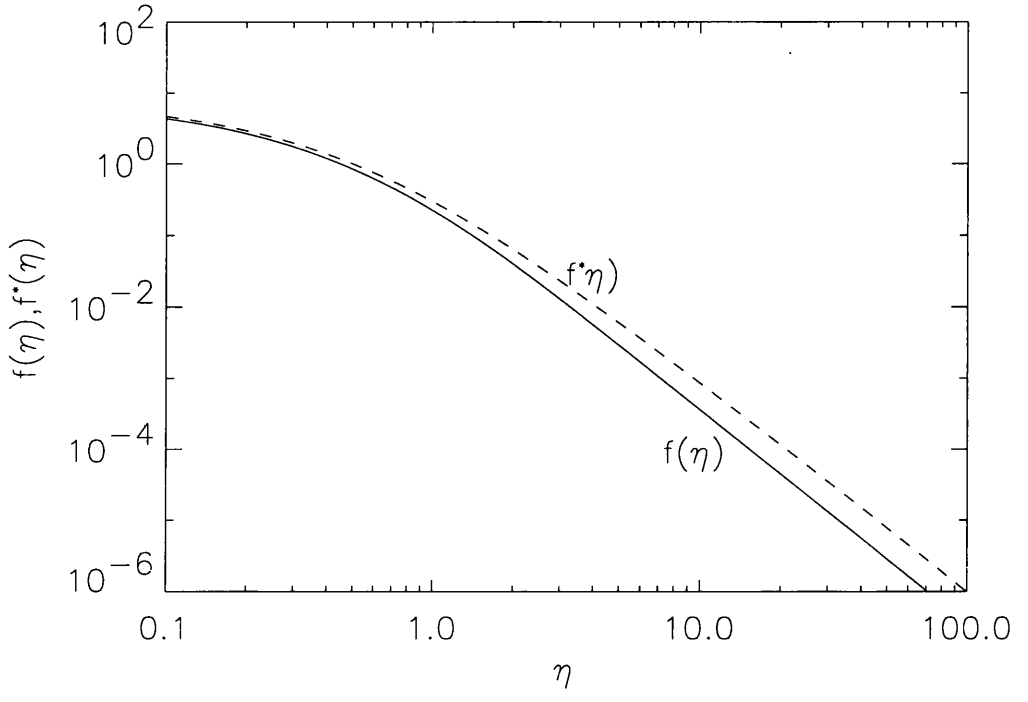

Figure 2.12: Injection spectrum f required for a step-function-ionised target to yield the same photon spectrum as a displaced power-law spectrum f^* injected into an ionised target.

is also a solution of (2.23). This will be physically acceptable provided A is small enough to ensure that $(j+\eta_o)^{-\beta} \geq A\lambda^j$. Now

$$(j+\eta_o)^{-\beta} - A\lambda^j \geq (j+1)^{-\beta} - A\lambda^j$$

so a sufficient condition to guarantee $f_2 \geq 0$ is

$$A \leq \nu^j (j+1)^{-\beta} \tag{2.36}$$

for all j. Setting to 0 the derivative with respect to j of the right side of (2.36) yields the maximum permissible value

$$A_{max} = \frac{1}{\nu}\left[\frac{e\log\nu}{\beta}\right]^{\beta}$$

such that

$$f_2(\eta) = (j+\eta_o)^{-\beta} + A_{max}(-\lambda)^j \geq 0$$

for all $\eta \geq 0$. In Figure (2.13a) we show one of the infinity of such solutions with $A < A_{max}$ is shown together with f_1. *Any* such spectrum f_2 yields precisely the same photon spectrum from a step-function-ionised target.

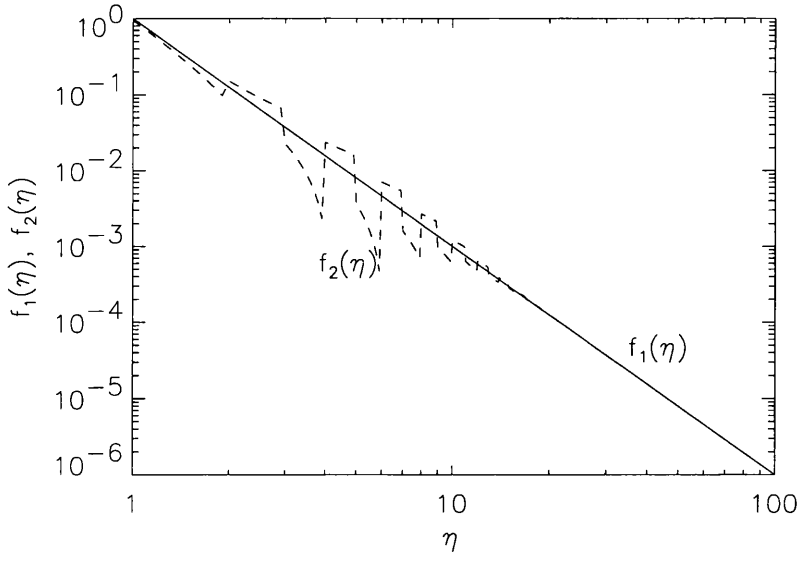

(a)

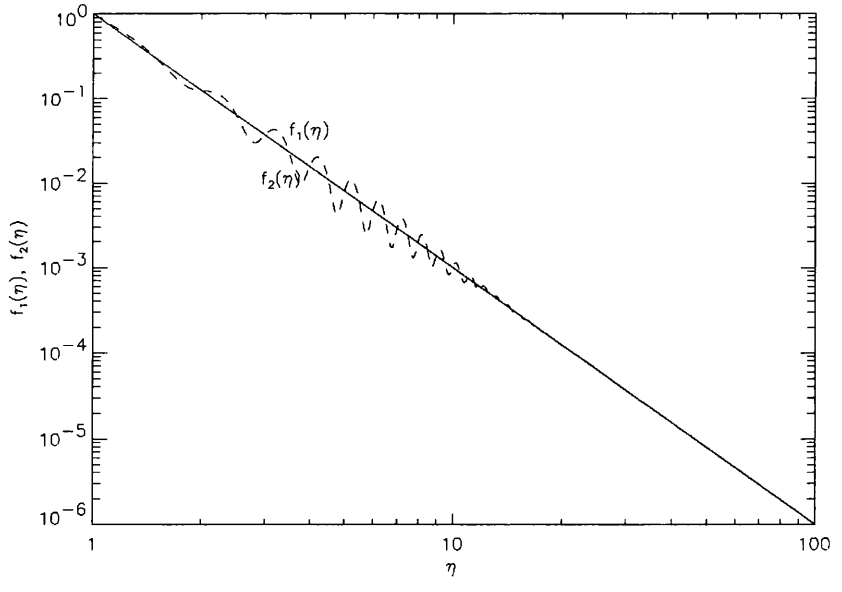

(b)

Figure 2.13: (a) Two injection spectra $f_1(\eta)$ (power-law spectrum) and $f_2(\eta)$ (power-law plus homogeneous solution with $\phi = constant$) which produce precisely the same bremsstrahlung photon spectra in a step-function-ionised target. (b) Two injection spectra $f_1(\eta)$ (power-law spectrum) and $f_2(\eta)$ (power-law plus homogeneous solution with $\phi = sin(\eta)$) which produce precisely the same bremsstrahlung photon spectra in a step-function-ionised target.

The example in Figure (2.13a) is for a null function which has infinitely many discontinuities at intervals $\Delta\eta = 1$ because $\phi(\eta_0)$=constant. There is however a subset of the null function f_0 space which is continuous. For continuity Equation (2.28) requires that $f_0 \rightarrow 0$ at all points where it changes sign. It also requires that f_0 decrease by a factor ν over all intervals $\Delta\eta = 1$. These conditions are satisfied by the form

$$f_0(\eta) = A_k \nu^{-\eta} \sin[(2k+1)\eta + \eta_k]$$

where k is any integer ≥ 0, and A_k, η_k are arbitrary phase and amplitude, or more generally by

$$f_0(\eta) = \sum_0^\infty A_k \nu^{-\eta} \sin[(2k+1)\eta + \eta_k]$$

In Figure (2.13b) an example of this is shown where the null function with the lowest frequency component ($k = 0$) only and with $A_k < A_{max}$ have been added to the smoothed power law solution. η_k has been chosen so that the sum is non-negative everywhere. This shows that the non-uniqueness occurs through the action of the kernel on the bremsstrahlung spectrum to filter out completely all damped harmonic components in the electron spectrum $f(\eta)$ with 'frequencies' which are odd multiples of that associated with the transition zone depth energy E_1.

2.6.5 Recursion Relation Solutions-Spectral Cut-Offs

A photon spectrum with a high energy cut-off is a stringent example of spectra which has sufficiently rapid decline at high energy to ensure uniqueness. If $f^*(\eta) = 0$ for $\eta > \eta_1$ from Equation 2.23 then

$$f(\eta) = 0 \qquad \text{for} \quad \eta \geq \eta_1$$

Therefore in the interval

$$\begin{aligned} \eta_1 - 1 \geq \eta > \eta_1 \quad & \text{then} \quad f(\eta) = f^*(\eta) \\ \text{i.e. if} \quad \eta = \eta_1 - 1 + \Delta\eta \quad & \text{where } 0 \leq \Delta\eta < 1 \\ \text{then} \quad f(\eta_1 - 1 + \Delta\eta) = \quad & f^*(\eta_1 - 1 + \Delta\eta) \end{aligned}$$

By repeating this step in the interval $\eta_1 - 2 \geq \eta > \eta_1 - 1$ then

$$f(\eta_1 - 2 + \Delta\eta) \quad = f^*(\eta_1 - 2 + \Delta\eta) - \nu f(\eta_1 - 1 + \Delta\eta)$$

$$= f^*(\eta_1 - 2 + \Delta\eta) - \nu f^*(\eta_1 - 1 + \Delta\eta).$$

and for $\eta_1 - 3 \geq \eta > \eta_1 - 2$

$$\begin{aligned} f(\eta_1 - 3 + \Delta\eta) &= f^*(\eta_1 - 3 + \Delta\eta) - \nu f(\eta_1 - 2 + \Delta\eta) \\ &= f^*(\eta_1 - 3 + \Delta\eta) - \nu f^*(\eta_1 - 2 + \Delta\eta) + \nu^2 f^*(\eta_1 - 1 + \Delta\eta). \end{aligned}$$

Thus a unique recursive solution starting from the high energy cut-off can be constructed to give $f(\eta)$ for all η below η_1 i.e.

$$f(\eta_1 - j + \Delta\eta) = \sum_{i=1}^{j} (-\nu)^{j-i} f^*(\eta_1 - i + \Delta\eta).$$

$f(\eta)$ for all $\eta > \eta_1$ must be 0.

If $f^*(\eta) = 0$ for $\eta < \eta_1$, i.e. a low energy cut-off, then by 2.23

$$f(\eta) + \nu f(\eta + 1) = 0 \quad \text{in} \quad 0 < \eta < \eta_1$$

which in order for f to be ≥ 0 requires that

$$f(\eta) = 0, \quad \text{in} \quad 0 < \eta < \eta_1 \quad \text{and in} \quad 1 < \eta < \eta_1 + 1$$

For $\eta_1 < 1$ this implies that $f(\eta)$ has, like $f^*(\eta)$, a cut-off below η_1, but has, in addition, a gap, i.e. $f = 0$ in the range $1 < \eta < \eta_1 + 1$. For $\eta_1 > 1$, the two ranges overlap and $f(\eta)$ has a low energy cut-off at $\eta = \eta_1 + 1$ (a cut-off in $F_o(E_o)$ at $E_o = E_c = (E_c^{*2} + E_1^{*2})^{1/2}$ where E_c^* is the cut-off energy in F_o^* corresponding to η_1.) This argument can then be applied to successive intervals of η to yield a recursive solution for $f(\eta)$. Considering again the case $\eta_1 > 1$ by (2.23), since $f(\eta) = 0$, for $\eta < \eta_1 + 1$,

$$\lambda[f^*(\eta) - f(\eta)] = \lambda f^*(\eta), \text{where } \eta_1 < \eta < \eta_1 + 1$$

which defines $f(\eta)$ in $\eta_1 + 1 < \eta < \eta_1 + 2$. Repeating this processes yields

$$f(\eta + j) = -\sum_{i=0}^{j-1} (-\lambda)^{j-i} f^*(\eta + i)$$

This solution for $f(\eta)$ is unique as, $f^*(\eta)$ being zero over at least an interval of one in η, the only physically acceptable $f(\eta)$ for this region is $f(\eta) = 0$; this excludes the possibility of adding any homogeneous solutions.

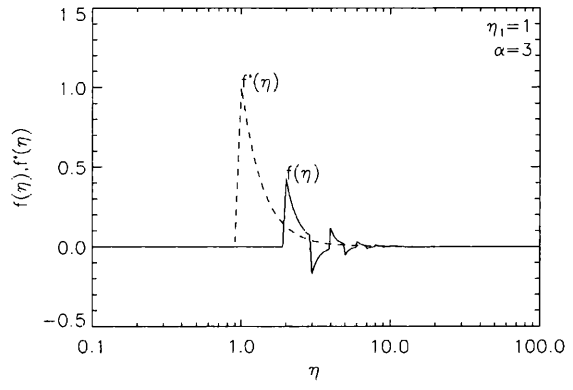

(a)

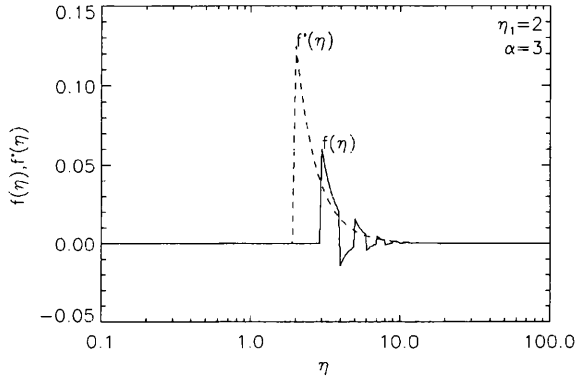

(b)

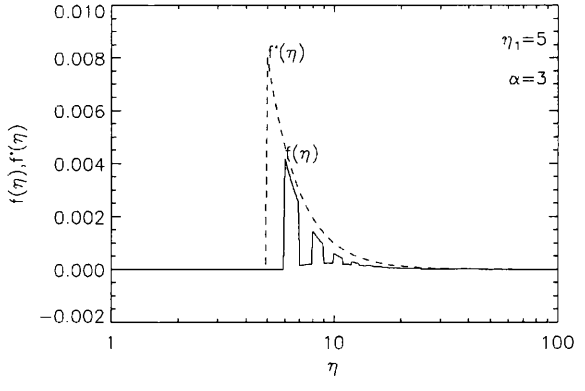

(c)

Figure 2.14: Injection spectrum f required for a step-function-ionised target to yield the same photon spectrum with low cut-off f^* injected into an ionised target. The cut-off in f^* occur at η_1=1,2,5 while the spectral index of the power-law in η space = 3.

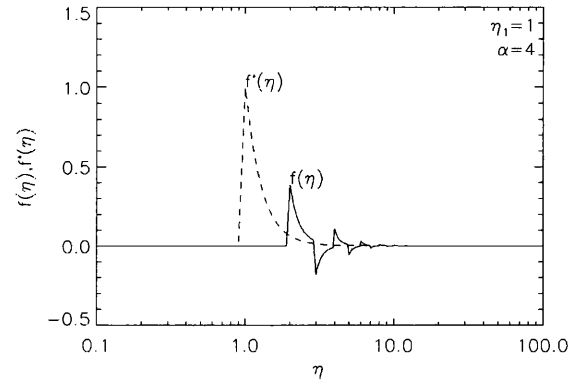

(a)

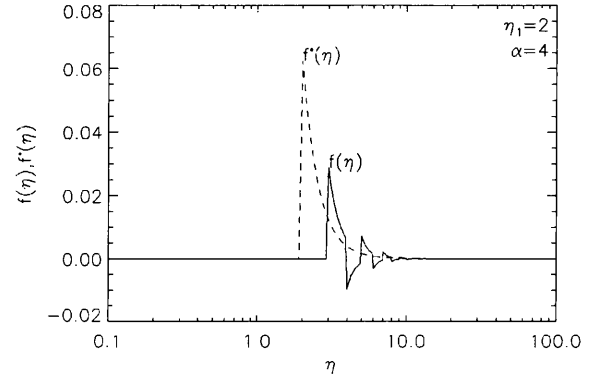

(b)

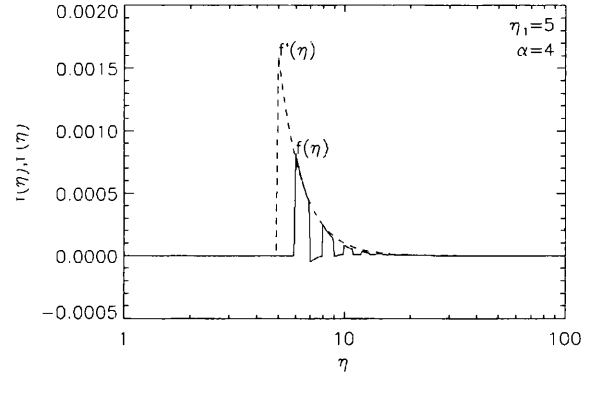

(c)

Figure 2.15: Injection spectrum f required for a step-function-ionised target to yield the same photon spectrum with low cut-off f^* injected into an ionised target. The cut-off in f^* occur at η_1=1,2,5 while the spectral index of the power-law in η space = 4.

Figures 2.14 (a)-(c) show $f(\eta)$ for low energy cut-off power-laws in $f^*(\eta)$ with $\alpha = 3$ and cut-offs at $\eta_1 = 1, 2, 5$ respectively. Similarly in Figures 2.15(a)-(c) $f(\eta)$ is shown for $f^*(\eta)$ with $\alpha = 4$ and same η_1 values. It is clear that physically acceptable solutions for f (≥ 0) exist only for sufficiently large η_1, the actual value depending on α. In addition it is noted that, even when $f \geq 0$ the solution is oscillatory and highly structured (with infinitely many discontinuities) at $\eta = 1$ spacings. This would imply the acceleration mechanism properties are linked to the column density between injection site and transition region which is physically not sensible. This means that many photon spectra produced by reasonable $f^*(\eta)$ in a fully ionised target cannot be produced by a 'physically plausible' $f(\eta)$ in a plasma with an ionisation structure like the solar atmosphere.

2.7 Constraints on Beam Electron and Energy Fluxes

Also important are the total beam injection rate and power. It has already been noted that inference of the wrong shape for the electron injection spectrum, by use of incorrect target ionisation structure, can lead to miss-diagnosis of the acceleration process and incorrect inference (usually exaggeration) of the total beam flux and power by extrapolation of an incorrect spectral shape. If complete information is available over the whole spectral range then the total electron fluxes and energy are constrained. An obvious upper limit on any non-negative solution of (2.23) is $f(\eta) \leq f^*(\eta)$ - i.e. no acceptable solutions for $f(\eta)$ can exceed the fully ionised solution f^* anywhere. Integration of Equation (2.22) yields the total electron number required in the two models (target configurations) needed to give the same photon spectrum. The total (scaled) electron fluxes f_{tot} are given by $\int_0^\infty f d\eta$ (and similarly for f^*_{tot}), so by integrating Equation 2.23

$$f_{tot} = \frac{\lambda}{\lambda+1} f^*_{tot} + \frac{1}{\lambda+1} \int_0^1 f(\eta) d\eta \geq \frac{\lambda}{\lambda+1} f^*_{tot}. \tag{2.37}$$

Therefore in terms of electron numbers (directly inferred, rather than extrapolated), the step-function-ionised target can never require fewer electrons than the fraction $\lambda/(\lambda+1)$ of the number required for a fully ionised target. If f has a lower cut-off at $\eta \geq 1$ the electron number reduction factor is always precisely $\lambda/(\lambda+1)$ (since the integral term in (2.37) is zero) regardless of the shape of f above the cut-off.

The total (scaled) electron energy fluxes (powers) P are given by $\int_0^\infty f\eta^{1/2} d\eta$, (and

similarly for P^* in terms of f^*), so by (2.23)

$$P = P^* - \frac{1}{\lambda}\int_1^\infty f(\eta)(\eta - 1)^{1/2} d\eta \tag{2.38}$$

If f is non zero only in $\eta \leq 1$ then of course $P = P^*$ since all the bremsstrahlung is produced in the ionised region of the target. If f is concentrated at η close to, but partially above, $\eta = 1$ then P approaches the value P^* . If f is concentrated at $\eta \gg 1$ then the integral term in (2.38) approaches P/λ and so $P \to P^*\lambda/(\lambda + 1)$. These values of P/P^* represent the extremes of the possible range which are the same as those for f_{tot}/f^*_{tot}.

2.8 Conclusions

This analysis of thick target bremsstrahlung from a non-uniformly ionised target has extended the work of Brown, (1973a), by dealing with the inverse problem and showing that the inferred form of the electron injection spectrum depends crucially on the form of the ionisation structure of the target. By simply approximating the solar ionisation profile by a step-function it has been shown that physically acceptable solutions for the case with this ionisation structure may not exist or may be non-unique (even though unique acceptable solutions exist for the fully ionised case), unless the electron spectrum in the fully ionised case has a low energy cut-off or a rapid decline at high energies. Even in the case of smooth electron spectra, the shape differs significantly between the two, especially for energies just above the electron energy required to reach the transition zone, because of the reduction in collisional losses there. For injection spectra containing sharp features, the two target models can give very different answers, even when these are unique.

Solutions for an ionised target, typically used for data analysis, will contain spurious additional electrons. Thus particular caution has to be exercised for results where secondary components appear to be present in results obtained using ionised target formulae, such as the thick target analysis by Johns and Lin (1992) of data with a 'superhot' component (Lin and Schwartz, 1987) subtracted. Also when the spectral range of the non-thermal bremsstrahlung data covered is incomplete, due to instrument bandwidth or overlap of a 'superhot' component at low energies, these erroneous inferences at low energies are likely to lead to exaggerated estimates of total electron flux by extrapolation of the incorrect spectrum.

Another important feature is that almost all of these results have been discussed in terms of $\eta = (E_o/E_1)^2$ rather than of energy E_o itself, E_1 being taken as known. In practice E_1 will not be well known, depending on the column depth of the transition zone. However, if we have independent estimates of or bounds on $F_o(E_o)$, accurate measurements of the HXR spectrum may enable us to estimate E_1 and hence the depth of the transition zone and potentially how it evolves with time through chromospheric evaporation. Even just the requirement that the inversion should yield $F_o(E_o) \geq 0$ may suffice to constrain E_1 on which we have shown the form of solution to depend.

It is important to realise that the non-uniqueness involved is far more than just the inability to resolve small scale features that is commonly encountered in inverse problems in astrophysics (and elsewhere) cf. Chapter 3. It is frequently the case with continuous inverse problems such as image reconstruction that discrete sampling (not to mention data errors) renders the small-scale features in the image unrecoverable - in other words there is a lack of resolution. In practice, the use of regularisation (cf. Craig and Brown, 1986) permits extraction of information about larger-scale features that *is* contained in the data.

In the problem described here, although HXR spectra are not fully resolved, the non-uniqueness of the solution is a much more fundamental limitation. There can exist many distinct exact solutions to the inverse problem (Equation (2.23)) (for a given data spectrum $f^*(\eta)$) that differ by much more than just small-scale features. For example, two exact solutions such as in Figure 2.13, differing by a null function obviously do not differ only by short-wavelength variations. The null function will contain some periodic variation of period $\Delta\eta = 1$ on top of the $\nu^{-\eta}$ trend, corresponding to variations in the electron spectrum over an energy range equal to $\Delta E \sim E_1 \sim 30$keV which is certainly not a small-scale variation in the solution. Furthermore, although the periodic variation may appear implausible, they fit the data and there is nothing about them that in especially marks them out as pathological or non-physical, that would permit one particular solution to be singled out as being physically more reasonable.

A natural question to ask is whether the non-uniqueness established here is an artifact of our approximation of the transition zone as a discontinuity in $x(M)$, i.e in $k(\zeta)$, where $\zeta = (\eta - \xi)$ as before (Equation (2.19)). A more realistic form would be to take $k(\zeta)$ as a linear ramp up from $k = 1/(\lambda + 1)$ at $\zeta = 1$ to $k = 1/\lambda$ at $\zeta = 1 + \Delta$ where Δ is a finite transition zone thickness. It is straightforward to show that Equation (2.23) is then

replaced by

$$f(\eta) + \nu f(\eta+1) + \left[\nu \int_{\eta+1}^{\eta+1+\Delta} \frac{f(\eta')d\eta'}{\Delta} - f(\eta+1)\right] = f^*(\eta) \tag{2.39}$$

The 'correction' to Equation (2.39) in the [...] term of this equation amounts to the contribution to $f^*(\eta)$ of the bremsstrahlung emission in the transition zone, which will be very small unless $f(\eta')$ is nearly singular at $\eta+1$ (i.e is a delta function or is concentrated in a range of $\eta \leq \Delta$ around $\eta+1$) as the transition region is very thin. Therefore it is thought that a smoother ionisation profile will have little effect on the above conclusion. Even if mathematically the solution for $f(\eta)$ were formally unique, as a thin transition region always gives insignificant emission then with real discretised noisy data, the high frequency components of the electron spectra will be unrecoverable.

Chapter 3

Numerical Inversion of High Resolution HXR Spectra from Non-uniformly Ionised Targets

"A hen is an egg's way of making another egg."

Samuel Butler

3.1 Introduction

Hard X-ray observations have shown that acceleration of 10^2 keV electrons is common place during the impulsive phase of solar flares. The energy distribution of these electrons and ultimately the hard X-ray spectral shape, can provide an indication as to the type of electron acceleration process at work in the flare. In particular spectral 'knees' (broken power law) observed in many hard X-ray spectra between 50-100 keV are sometimes considered signatures of D.C. field acceleration. The electron spectra inferred for a thick target model for high resolution hard X-ray observed by HIREX on June 27 1980 has been interpreted as consisting of two components, a slowly varying powerlaw extending downward to 20 keV and an impulsive spike component peaking at $\approx$ 50 keV (Lin and Johns, 1993). This too has been interpreted as strongly indicating a D.C. field acceleration mechanism.

In the previous chapter it was shown that, for a thick target, as the electron beam

enters the chromosphere the rapid change in ionisation level reduces the energy loss from Coulomb collisions and therefore produces hard X-rays more efficiently. The overall effect is that while the hard X-rays at low energy are unaffected the high energy range can be up to 3 times greater than expected (Brown, 1973a). Thus, even for a perfectly smooth power-law electron injection spectrum, the photon spectrum would be characterised by a downward broken power-law. The electron spectra inferred upon wrongly assuming a fully ionised atmosphere would have to be supplemented by a secondary component above the break energy i.e. this component is qualitatively similar to that interpreted in the 27th June 1980 flare.

Therefore in the following chapter the electron spectrum is inferred from the high resolution HIREX data assuming an ionisation jump in the atmosphere at various depths in the hope of determining if the electron spectral features inferred by Johns and Lin, 1992 are real or artifacts of a uniformly ionised model being assumed.

3.2 HIREX Observations of the 27 June 1980 Flare

The HIREX instrument was a balloon-borne array of germanium HXR detectors flown from Palestine, Texas on the 27th of June 1980. Observations of the Sun and Crab Nebula were taken between 1520 UT and 2130 UT. This period included detailed observations of an intense solar flare hard X-ray burst beginning at $\sim 1614:40$. The associated H_α flare began at 1615 UT and peaked at 1617 UT. It was located at S25 W67 in active region 2522 and had an importance of SB. An M6 soft X-ray burst was observed by the GOES 2 spacecraft as well as intense microwave emission (325 sfu at 2800 MHz). The flare was also accompanied by strong type III-V bursts, type II and IV emission and energetic (>10 MeV) protons in interplanetary space (Bai et al., 1983).

3.2.1 Experimental Details

The instrument consisted of two coaligned hard X-ray detector systems : an array of four planar germanium detectors, each 4 cm diameter by 1.3 cm thick, cooled by liquid nitrogen to obtain ≤ 1 keV FWHM energy resolution and a $300cm^2$ NaI/CsI phoswich scintillator for high sensitivity and time resolution. The cryostat housing the germanium detector array is surrounded by a ~ 2" thick CsI anticoincidence well. Graded Z passive

collimators provided a $2.8° \times 5.6°$ field of view. Each Ge detector output goes to a pulsed FET feedback preamplifier, dual fast (400 ns) and slow ($\sim 10\mu s$) shaping amplifier and then a 4096 ADC covering the interval $\sim 11 - 580$ keV (with seven bins per keV). The fast amplifier provides coincidence and pileup rejection, so that rates up to $\sim 20,000$ counts s^{-1} could be detected without any spectral distortion.

Based on information from background lines in the germanium detectors, gain variations throughout the flight were found to be negligible. With all four germanium detector outputs summed together over the flight, the energy resolution is ≤ 1 keV, by far the best ever achieved in observing the 15-200 keV range.

3.2.2 Deconvolution of the Photon Spectra

NaI or CsI scintillation detectors have broad and complicated response functions due to the broad energy resolution of the detectors, the presence of escape peaks in the middle of the energy range and the effects of Compton collisions followed by escape of the scattered photon from the detectors for high energy photons. The complex response function precludes direct inference of the flare photon spectrum from the count rates detected. A spectral shape must first be assumed, the count rate spectrum calculated for that model and compared to the observed. This procedure would lead to artifacts in the spectrum dependent on the assumed trial function (Fenimore et al., 1982).

For the germanium spectrometer the response function is essentially a δ-function over the energy range 13-200 keV. There are no escape peaks above 10 keV and Compton collisions can be detected as the escaping photon triggers the anticoincidence shield, so such events can be rejected. As the field of view is small than any misleading count from Compton scattering in the Earth's atmosphere will be negligible. Therefore the relationship between count rate C_i and flux spectrum $\Phi(\epsilon)$ is

$$C_i = \int_{\epsilon_i}^{\epsilon_{i+1}} d\epsilon_3 \int_0^\infty g(\epsilon_2, \epsilon_3) d\epsilon_2 \int_0^\infty Ar(\epsilon_2, \epsilon_1) f(\epsilon_1) t(\epsilon_1) \Phi(\epsilon_1) d\epsilon_1 \tag{3.1}$$

where $\Phi(\epsilon_1)$ is the source flux at the top of the atmosphere (photons cm^{-2} s^{-1} keV^{-1}), $t(\epsilon_1)$ is the probability of transmission through the atmosphere and the overlying materials, $f(\epsilon_1)$ is the collimator transmission, $r(\epsilon_1, \epsilon_2)$ is the probability of an energy loss ϵ_2 for an incident photon ϵ_1, A is the detector area and $g(\epsilon_2, \epsilon_3)$ the pulse height shape for an energy loss ϵ_2.

The observed counting rates C_i are essentially unbroadened by the convolution with $g(\epsilon_2, \epsilon_3)$ because the FWHM of 1 keV is much less than the scale of the variations of the incident flux. Thus the response effectively simplifies to

$$C_i = \Delta\epsilon A r_1 f t \Phi|_{\epsilon_i}, \tag{3.2}$$

or

$$\Phi_i = \frac{C_i}{\Delta\epsilon A f r_1 t}, \tag{3.3}$$

above 30 keV. Here $\Delta\epsilon = \epsilon_{i+1} - \epsilon_i$ and r_1 is the photopeak efficiency, where both r_1 and t are evaluated at $\sim \epsilon_1$.

Below 30 keV fluorescent X-ray escape and photon stopping at detector surface can become significant ($\geq 1\%$). The important fluorescent X-rays for germanium are at 9.87 and 10.98 keV. Therefore below 30 keV

$$C_i = \Delta\epsilon A f (r_1 t \Phi|_{\epsilon_i} + r_1 t \Phi P_{9.87}|_{\epsilon_i+9.87} + r_1 t \Phi P_{10.98}|_{\epsilon_i+10.98}) \tag{3.4}$$

where $P_{9.87}$ is the probability of the escape of a 9.87 keV photon at $\epsilon_i + 9.87$ keV and similarly for $P_{10.98}$. The photon flux Φ below 30 keV is then obtained by starting at $\epsilon_i = 30$ keV and recursively solving

$$\Phi_i = \frac{C_i - \Delta\epsilon A f (r_1 t \Phi P_{9.87})|_{\epsilon_i+9.87} - \Delta\epsilon A f (r_1 t \Phi P_{10.98})|_{\epsilon_i+10.98}}{\Delta\epsilon A f r_1|_{\epsilon_i}}. \tag{3.5}$$

3.3 Evidence of D.C. Field Acceleration

The spectral characteristics of the photon spectra for the 27 June 1980 flare have been interpreted as suggestive of signatures of D.C. field acceleration, and this has been extensively discussed in Lin et al. (1981), Lin and Schwartz (1987) and Benka and Holman (1994). The main features examined in these analyses are the characterisation of the hard X-ray spectra as a power law with a downward break at high energy, and steep upturn discovered at low energy interpreted by them as a 'superhot' component. In addition the inferrment of two electron populations from thick target inversion of this photon spectra has also been interpreted by Lin and Johns (1993) as suggestive of D.C. field acceleration.

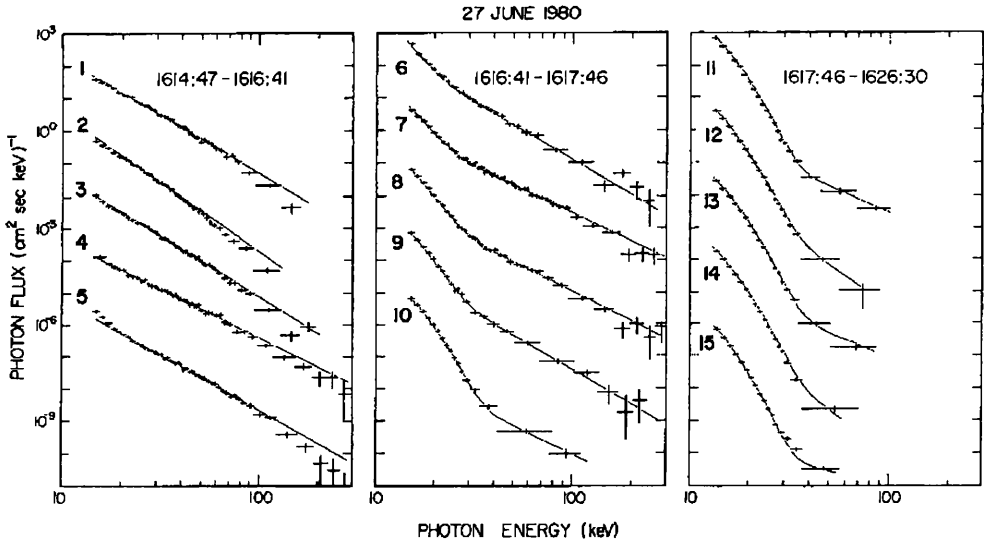

Figure 3.1: Energy Spectra from the germanium array of the 27 June event. The vertical scale applies to the uppermost spectrum, with each succeeding spectrum offset downward by two orders of magnitude. (Lin *et al*, 1981).

3.3.1 Superhot Component

Beginning near the peak of the event at $\sim$ 1616 UT, a steep component is observed at low energies ($<$ 30 keV). The spectral index of this component reached $\gamma = 11$ (a spectral index to large to be observable with scintillation detectors). After $\sim$ 1617 UT when the flux at high energy rapidly drops, the low energy spectra have a curved exponential like shape (cf. Figure 3.1). By fitting the X-ray spectrum with a combination of the expected bremsstrahlung from a Maxwellian distribution at low energy and a power law at high energy, Lin et al. (1981) showed that the low energy upturn in the spectra is consistent with that of an isothermal electron distribution. The evolution of the temperature and emission measure, after this component becomes dominant at low energy, has a temperature peaking at $\sim$ 1617 : 15 UT with 34.2 $\times 10^6$ K, and the emission measure peaking at $\sim$ 1618 UT with 2.9 $\times$ 10^{48}cm^{-3}.

In comparison, the emission measure and temperature inferred for the soft X-ray producing thermal flare (1-8 Å) from GOES had a maximum of $\sim 2 \times 10^7$ K and $\sim \times 10^{49}$cm^{-3} and would produce negligible hard X-ray (>13keV) emission compared to that observed. The energy content of the flare plasma though is much greater than that of the 'superhot' component. Since the flare plasma is expected to consist of a continuous distribution of

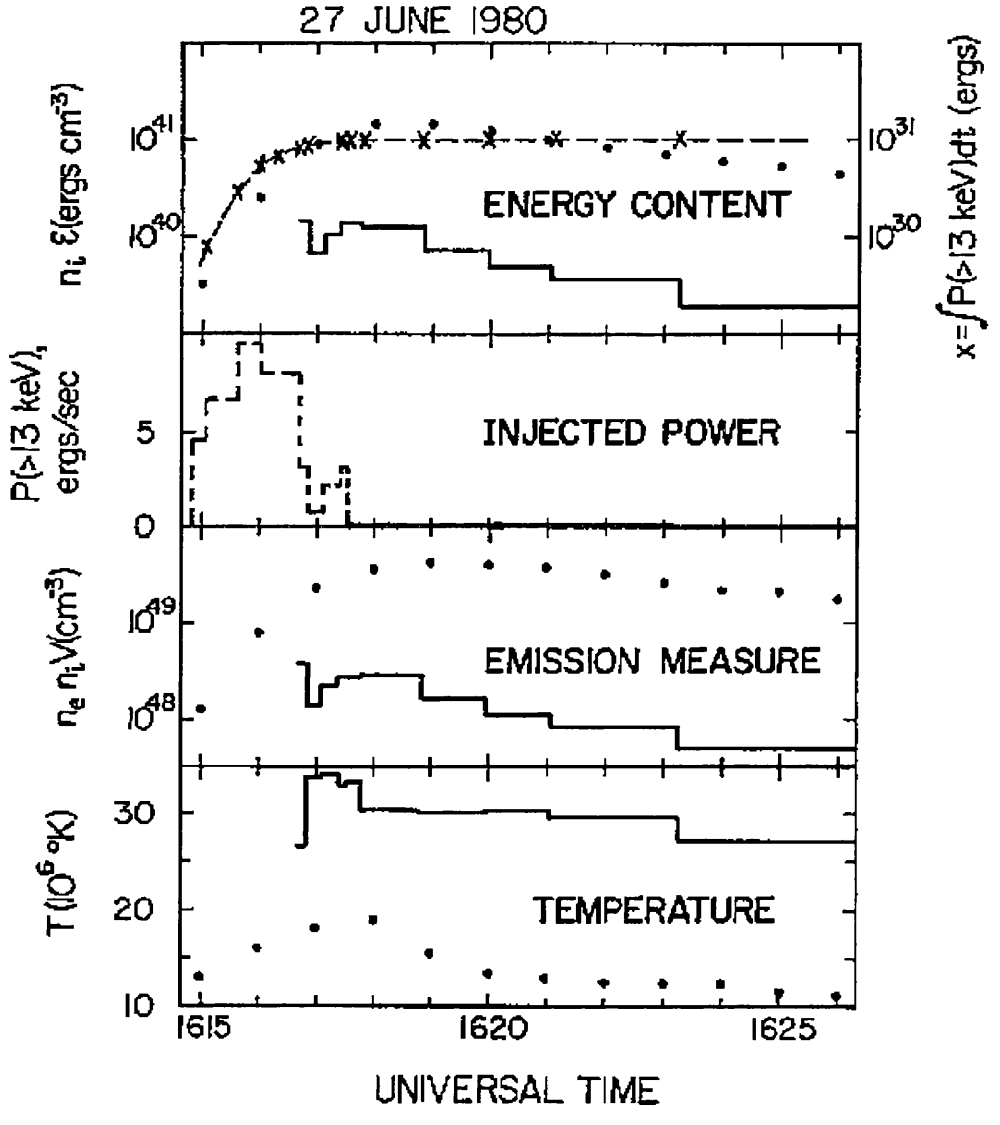

Figure 3.2: The evolution in time of the parameters of the 'superhot' component (solid lines) and the flare plasma (dots). The energy input rate and and cumulative total energy from an electron beam inferred from the power-law component are also shown (dashed and x's respectively), from (Lin *et al*, 1981).

emission measures with temperatures (Moore, 1980), then the 'superhot' component may well be the highest temperature portion of this distribution. Or it may be that the thermal contribution in fact extends to even higher energies (Piana et al., 1995). The time profile of the temperature and emission measure of the 'superhot' component however is independent of the slow smooth profile of the thermal plasma (Figure 3.2) although the evolution of the 'superhot' component before the peak in the hard X-ray spectra is uncertain.

3.3.2 Double Power-law

Excluding the low energy range when an upturn is present, the behaviour of the HXR spectra for this flare was shown to be best characterised by a downward breaking double power law (Lin and Schwartz, 1987). The spectra were divided into two categories, interspike minima and spike maxima. For the interspike minima the characteristic γ_1 below the break point was found to be $\sim$ 3.5 with the spectral index above the break point, which was not as well defined, $\sim 4.5 - 5$. The break point during these minima increased slowly over the event from $\sim$ 25 keV to $\sim$ 100 keV. The sharpest increase in the break energy occurring at $\sim$ 1616 : 00 UT, approximately the same time that the significant upturn at low energy also occurs. For the spectra obtained during the spike maxima, the spectral indices were flatter, $\gamma_1 \leq 3$, below the break point while the break point for spike maxima were always found to be between $\sim$ 30 keV and $\sim$ 65 keV (cf. Figure 3.3). The interpretation of this data was therefore that it suggested two separate components; a slowly varying (timescale $\sim$10 seconds) with low energy spectral index γ_1 of $\sim$ 3.5 and a rapidly varying spike component with a much harder spectrum at low energy.

3.3.3 Thick Target Electron Spectra

Lin and Johns (1993) determined the parent X-ray producing electron spectra assuming that collisions were the dominant loss mechanism and the atmosphere was taken to be fully ionised i.e. the thick target electron distribution for a uniformly ionised target. Using the numerical inversion technique described in Johns and Lin, 1992, the instantaneous X-ray producing population of electrons,

$$N(E,t) = \frac{dF}{dE}\frac{V}{v}$$

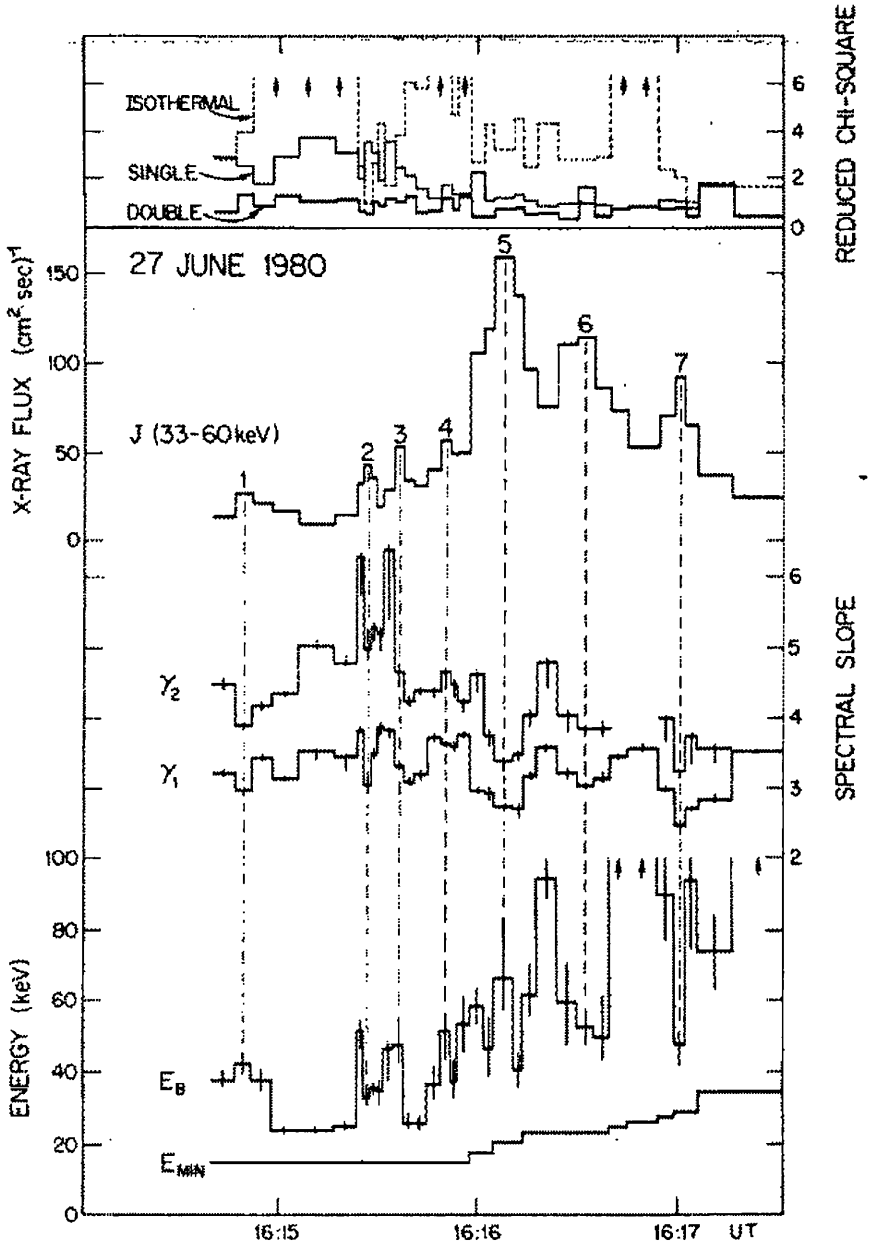

Figure 3.3: Parameters for the double power-law fits to the hard X-ray spectra for short accumulation times to show the temporal variations through the burst. Panel shows J(33-60 keV), the 33-60 keV flux with seven major spikes number; the γ_2 and γ_1 the power-law spectral indices; the energy of the break E_{br} and the E_{min}, the minimum of the energy range used in the fit, from (Lin and Schwartz, 1987).

is inferred by inversion of the instantaneous X-ray emission of an optically thin source (cf. Brown, 1971, Brown and Emslie, 1988) which is expressed by

$$\frac{dJ(\epsilon,t)}{d\epsilon} = \frac{nV}{4\pi R^2}\int^{\infty} \epsilon \frac{dF(E,t)}{dE}\frac{d\sigma(\epsilon,E)}{d\epsilon} d\,E \tag{3.6}$$

where R is the distance to the source; V the volume of the source; n the average number density of hydrogen; dF/de, the differential electron flux at energy E and time, t, in the source; ϵ the photon energy; $d\sigma/d\epsilon$, the differential bremsstrahlung production cross-section. Once the X-ray producing electron population $N(E,t)$ is obtained, it was related to the accelerated electron spectrum $F_o(E,t)$ in units of total number of electrons $\mathrm{keV}^{-1}\mathrm{s}^{-1}$ by the continuity equation i.e.

$$\frac{dN(E,t)}{dt} = F_o(E,t) - \frac{N(E,t)}{\tau_e(e)} - \frac{d}{dE}\left[N(E,t)\frac{dE}{dt}\right] \tag{3.7}$$

where $N(E,t)/\tau_e(E)$ refers to the electron escape from the X-ray emitting region and the last term refers to the energy loss processes. For energy loss due to collisions

$$\frac{dE}{dt} = -4.9 \times 10^{-9} n E^{-1/2} \mathrm{keV\ s^{-1}}.$$

Then neglecting any energy escape term (equivalent to assuming a density $\geq 10^{11}$ cm^{-3}), the thick target electron injection spectrum was reconstructed by Lin and Johns (1993) from hard X-ray spectra at 5 second intervals over broad energy bins. The broad energy bins for both the hard X-ray spectra and the inferred electron spectra were required to provide statistically significant hard X-ray spectra and improve the conditioning (Thompson et al., 1992) of the inversion as no regularisation was applied cf. Section 3.4.1.

Figure 3.4 shows the results of the Lin and Johns (1993) analysis. The two lowest energy channels showed no evidence of impulsive spikes with the slow rise after $\sim$ 130 s interpreted as due to the "superhot" component (Lin et al. (1981)). At higher electron energies, for the main spike at $\sim$ 75 s the electron flux increased by a factor of $\sim$ 4 at 130-252 keV, $\sim$ 6 at 78-130 keV and $<$ 2 at 44-78 and 33-44 keV indicating to Lin and Johns the spike appeared to be dominated by high energy electrons. Besides the spikes, a slowly varying underlying level of electron acceleration was interpreted as present in all channels from $\leq$ 35 s to $\sim$ 150 s, with the low energy power law index, $\gamma \approx 3.5$. Therefore the temporal and spectral characteristics of the inferred accelerated electrons were interpreted by Lin and Johns as two distinct non-thermal components :

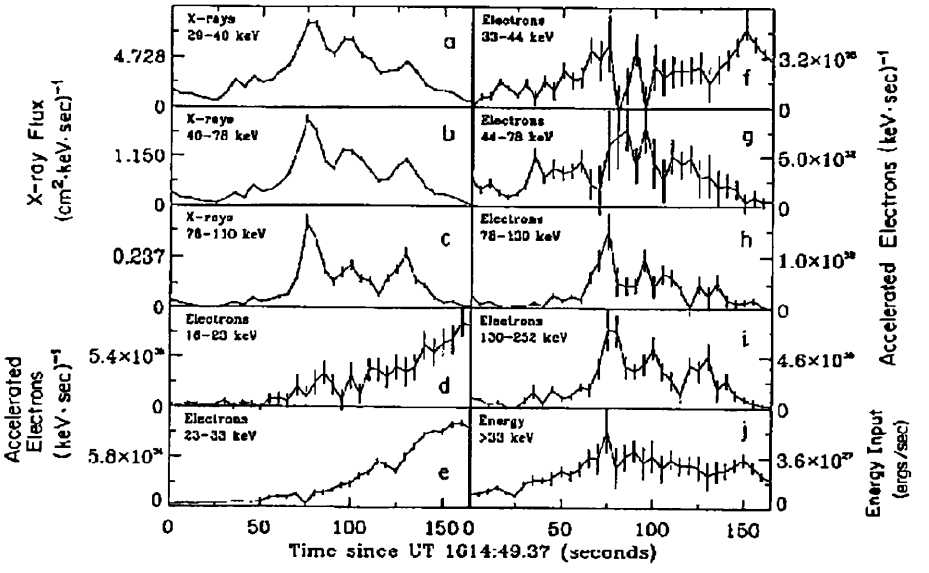

Figure 3.4: Panels (a-c) show three energy channels of the X-ray flux as a function of time for the 27 june 1980 flare. Panels (d-l) show the temporal variations of the accelerated electrons in six energy channels (assuming an ionised ambient atmosphere). Panel j plots the rate of energy release in >> 33 keV electrons (from Lin and Johns, 1993)

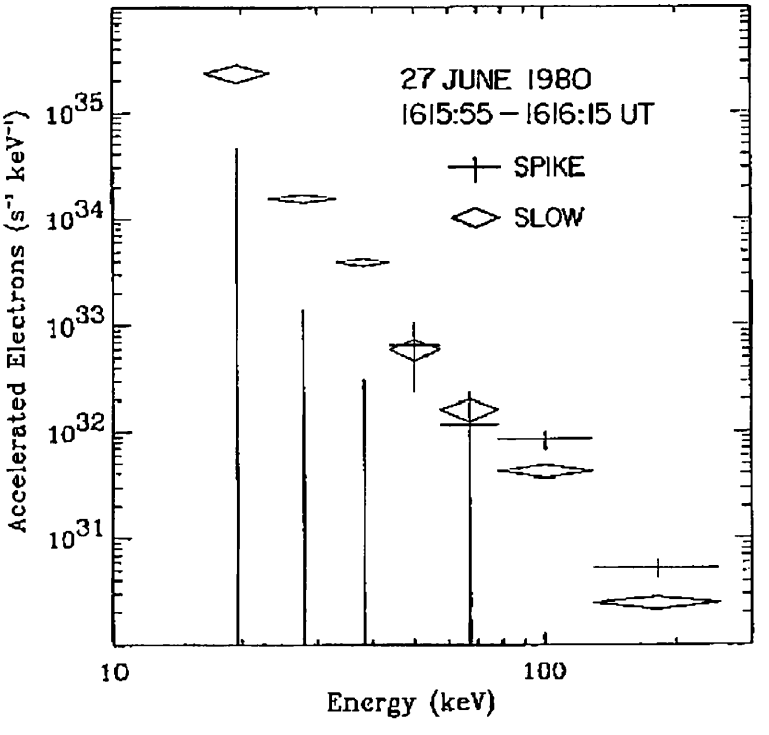

Figure 3.5: The spectra of accelerated electrons in the spike (crosses) and slowly varying components (diamonds) during the main spike between 65 and 85 seconds (see Figure 3.4) (from Lin and Johns, 1993).

slowly varying and spike. When the slowly varying component is removed from the total accelerated electron population, the resulting spectrum of the spike component was found to peak at $\sim$ 50 keV with a cutoff below $\sim$ 40 keV as shown in Figure 3.5.

3.3.4 Why Are These Observations Evidence of D.C. Field Acceleration

With the discovery of the superhot component in the hard X-ray burst, it is difficult to justify interpreting the high energy electrons solely in terms of heating or acceleration. A D.C. field model, such as that proposed by Benka and Holman (1992), is one of several possible mechanisms which could provide simultaneous acceleration and heating. The presence of coronal currents provides for acceleration, through runaway, and heating the ambient plasma by Joule dissipation. Thus simultaneous contributions of both non-thermal and thermal bremsstrahlung in the HXR spectra is expected.

The thermal emission for a D.C. model reflects the temperature of the current sheet, which is presumably the highest temperature plasma in the flare i.e. the superhot component. The superhot component is only expected to become detectable when enough of the plasma surrounding the current sheet has been heated i.e. when its emission measure is large enough.

Runaway processes occur when the systematic acceleration overcome the retardation effects of collisions. For an electric field E greater than the Dreicer field E_D, (cf. Chapter 1), the bulk of the plasma will experience runaway. However if $E < E_D$ then at energies below a critical energy will not be freely accelerated and serve mainly to heat collisionally. Thus the critical energy serves as a low-energy cut-off to the non-thermal electron population. If the interpretation of a gradual and spike component in the inferred electron spectra of Lin and Johns (1993) is taken then such a non-thermal population with low-energy cut-off is observed i.e. the spike component. This peak in the electron spectra being responsible for the break in the HXR spectra. The HXR spectra of June 27th has also been modelled with a sub-Dreicer field model (Benka and Holman, 1994). They found that the HXR emission is consistent with such a model having total potential drop of $\sim$100 keV, electron flux above $\sim$ 35 keV of $\sim 10^{34}$ electrons s^{-1}. The temperature and emission measure of the current sheets were $\sim 3 \times 10^7 - 1.1^8$ K and $\sim 10^{46} - 5 \times 10^{48}$ cm^{-3}. These flux values are in agreement with those of Lin and Johns.

3.4 Inversion of HXR spectra for a Non-uniformly Ionised Thick Target

In the following section, we formulate an effective approach to numerically invert HXR spectra for a thick target atmosphere which also includes a non-uniform ionisation profile. This approach is then applied to the HXR spectra of June 27th 1980 and comparison with the previously estimated thick target electron spectra of Lin and Johns (1993) of this event made.

3.4.1 Inverse Problems

An inverse problem is essentially one in which a desired parameter has to be derived from data by inversion of some smoothing operator, such as an integral. Such problems occur widely in astrophysics, a natural consequence of being primarily limited to remote observations of the electromagnetic spectrum, rather than as density and temperature, which are of primary interest in determining the processes understudy. In many cases the convolution between observed quantity and desired quantity leads to difficulties in solving inverse problems i.e. leading to non-uniqueness and instability of solution. In considering any inverse problems the ill-posedness and poor conditioning of the problem must be addressed.

Ill-Posedness

In modelling any set of observables there can be many source functions which map closely enough to the observed data to be considered a suitable fit within observational errors. Indeed it is possible for differing source functions to map to the same observables i.e. the recovered solutions are non-unique (Chapter 2). This behaviour depends critically on the integral operator (kernel) of the problem. Considering a general integral equation

$$g(y) = \int_0^\infty f(x)k(x,y)dx, \tag{3.8}$$

then the cause of non-uniqueness in the solution is that functions in the kernel's null-space are being linearly superimposed onto the actual solution. The null functions satisfy

$$\int_0^\infty k(x,y)f_o(x)dx = 0$$

and from the linearity of the integral

$$\int_0^\infty k(x,y)(f(x)+f_o(x))dx = g(y)+0 = g(y).$$

These null space functions can take any physical form that satisfies the above condition and can be arbitrarily added to the reconstructed source function without affecting the data but can severely affect the physical nature and implications of the inferred source function.

Poor Conditioning

The properties of the kernel function also determine the amount by which errors in the observed data becomes amplified in the recovered solution. When the problem is discretises to a matrix equation,

$$K\mathbf{f} = \mathbf{g} \tag{3.9}$$

a poorly conditioned kernel i.e a relatively 'flat' matrix, has a strong linear dependence in its rows and, in the worst case scenario, its determinant will tend to 0 as the number of rows increases. Hence K will be singular and no formal solution to the inversion exists. In many physical applications the matrix is very nearly singular and the inverse problem is considered to be poorly conditioned and as such imparts highly oscillatory structure on the solution originating from small data perturbations.

The condition number of the kernel is the quantitive description of how poorly conditioned the problem is. Defined by $C_K = \frac{\sigma_{max}}{\sigma_{min}}$, the ratio of maximum and minimum singular values of K, if $\frac{1}{C_K}$ is of the order of the data noise then the matrix is very poorly conditioned. Random errors on the data are not alone in causing serious numerical instability to the recovered solution. So to do truncation, discretisation errors and any inherent associated error measure of the kernel.

Regularisation

In principle for matrix equations, such as Equation 3.9, the maximum likelihood or least squares solution can be determined. For m recovered data points and n observed data points then the least-squares solution is determined by solving

$$\min_{\hat{f}} \sum_{i=1}^{n} \left(\frac{g_i - \sum_{j=1}^{m} H_{ij}\hat{f}_j}{\sigma_i} \right)^2$$

where $\hat{\mathbf{f}}$ is the estimate of solution $\mathbf{f}$ and σ_i is the variance of the error on the i th observation.

The estimated solution can be highly unstable and unphysical due to ill-posedness our poor conditioning. Solutions can be identified as unphysical if they display behaviour known not to be present in the source function, such as being highly oscillatory or negative. By regularising, this *a priori* information is incorporated into the solution to ensure that the estimated solution exists and is smooth or positive. This means we solve for instead for

$$\min_{\hat{f}} \sum_{i=1}^{n} \left(\frac{g_i - \sum_{j=1}^{m} H_{ij} \hat{f}_j}{\sigma_i} \right)^2 + \lambda \Phi(\hat{f}). \tag{3.10}$$

$\Phi(\hat{f})$ is the smoothing function constraining $\hat{f}$ and λ is the smoothing parameter determining how severely this constraint is upheld (Craig and Brown, 1986). The smoothing function applied will ultimately depend on the physical nature of the problem. Commonly applied smoothing functions include first and second order quadratic regularisation, which minimise the first and second derivative of the solution respectively, and maximum entropy.

The smoothing parameter λ controls the trade off between stabilising the solution and biasing the solution. If λ is too small, the estimated source function will be unstable and noisy. Too large a smoothing parameter and the solution will be stable but bear little relation to the original source function having smoothed out many of its features. A variety of objective data based methods for optimally choosing the smoothing parameter exists. The particular method used will again depend on the physical nature of the inversion.

3.4.2 Formulation of Discrete Matrix Equation

The bremsstrahlung emission for a thick target atmosphere with non-uniform ionisation profile was shown in 2.14 to be

$$I(\epsilon) = \frac{Q_o}{K\epsilon} \int_{\epsilon}^{\infty} F_o(E_o) \int_{\epsilon}^{E_o} \frac{q(\epsilon, E)\, dE\, dE_o}{\lambda + x\left(\frac{E_o^2 - E^2}{2K}\right)}$$

By defining

$$k(\epsilon, E_o) = \int_{\epsilon}^{E_o} \frac{q(\epsilon, E)\, dE}{\lambda + x(E, E_o)}, \tag{3.11}$$

then the photon number spectrum at a distance R from the source can then be written simply as the integral equation

$$J(\epsilon) = \frac{Q_o}{4\pi R^2 K\epsilon} \int_{\epsilon}^{\infty} F_o(E_o) k(\epsilon, E_o)\, dE_o. \tag{3.12}$$

In the case of real data it is impossible to recover a continuous function $F_o(E_o)$ i.e. Equation 3.12 must be replaced by a discretised version. This can be accomplished in a variety of ways. In our analysis the method of product integration (Baker, 1977) is used i.e.

$$J(\epsilon) = \frac{Q_o}{4\pi R^2 K\epsilon} \sum_{j=1}^{m} \int_{E_o\,j}^{E_o\,j+1} F_o(E_o) k(\epsilon, E_o)\, dE_o \tag{3.13}$$

where m is the number of data points observed, $E_{o\,1}$ is set equal to to the lowest photon energy observed and $E_{o\,m+1} = \infty$.

As the HXR photon spectrum always decline steeply for increasing photon energy the inferred electron spectrum is also expected to vary over several orders of magnitude. Craig and Brown (1986), Thompson (1990) note that for such source functions, smoothing towards a flat function with a quadratic smoothing function is prone to producing solutions which are over smoothed in one region but still 'noisy' and unacceptable in another. Thompson (1990) proposed a 'data adaptive' approach where the source function is smoothed to a power law instead. We follow this approach, choosing $F(E_o) = E_o^{-\beta}$ and defining

$$F_{\diamond(E_o)} = \frac{F_o(E_o)}{F(E_o)}.$$

We can then write

$$\int_{E_o\,j}^{E_o\,j+1} F_o(E_o) k(\epsilon, E_o)\, dE_o = \int_{E_o\,j}^{E_o\,j+1} F_\diamond(E_o) F(E_o) k(\epsilon, E_o)\, dE_o \tag{3.14}$$

$$= f_j(\epsilon) \int_{E_o\,j}^{E_o\,j+1} F(E_o) k(\epsilon, E_o)\, dE_o.$$

where f_j is the weighted mean of $F_\diamond$ $(F_o(E_o)/E_o^{-\beta})$ over the interval $(E_{o\,j}, E_{o\,j+1})$, and is assumed to be approximately constant over this interval.

The equation above then reduces to the matrix equation

$$\mathbf{J} = H\,\mathbf{f} \tag{3.15}$$

where $\mathbf{J} = \{J(\epsilon_i)\}$ for $i = 1, n$, $\mathbf{f} = \{f_j\}$ and the matrix H has the elements

$$H_{ij} = \frac{Q_o}{4\pi R^2 K\epsilon} \int_{E_o\,j}^{E_o\,j+1} E_o^{-\beta} k(\epsilon, E_o) dE_o \tag{3.16}$$

i.e.

$$H_{ij} = \frac{Q_o}{4\pi R^2 K\epsilon} \int_{E_o\,j}^{E_o\,j+1} E_o^{-\beta} \int_{\epsilon}^{E_o} \frac{q(\epsilon, E)\, dE}{\lambda + x(E, E_o)} dE_o,$$

and where $E_{o\,1} = \epsilon_1$ and $E_{o\,m+1} = \infty$. As the solution is smoothed toward a power-law instead of a flat function with $\beta \geq 0$, the integral for the matrix H does not diverge and so does not need to be truncated at high energy.

3.4.3 Smoothing Function and Parameter Determining

In this analysis, the second order quadratic smoothing function has been chosen i.e. we solve for

$$\min_{\hat{f}} \sum_{i=1}^{n} \left(\frac{J_i - \sum_{j=1}^{m} H_{ij}\hat{f}_j}{\sigma_i} \right)^2 + \lambda\Phi(\hat{f}), \tag{3.17}$$

with given by

$$\Phi(\hat{f}) = \sum_{j=1}^{m-2} \left(\hat{f}_i - 2\hat{f}_{i+1} + \hat{f}_{i+2} \right)^2.$$

The constraint imposed by second order quadratic smoothing corresponds to ensuring the curvature of $\hat{f}$ is small, but no positivity constraint has been explicitally enforced on the recovered source function.The estimation of the smoothing parameter λ can be approached in numerous ways. For this work, the primary method for choosing the smoothing parameter in the inversion is the method of Generalised Cross Validation (Golub et al., 1979). This method automatically chooses the smoothing parameter λ by minimising

$$\frac{(\mathbf{J} - H(H^T H + \lambda C)^{-1} H^T \mathbf{J})^2}{(\mathrm{trace}(I_m - H(H^T H + \lambda C)^{-1} H^T))^2}. \tag{3.18}$$

where I_m is the identity matrix and C is the Hessian matrix of the smoothing function. This criterion does not require an estimate of the observed error and will in fact give an estimate of the data noise from

$$\hat{\sigma}^2 = \frac{(\mathbf{J} - H(H^T H + \lambda C)^{-1} H^T \mathbf{J})^2}{(\mathrm{trace}(I_m - H(H^T H + \lambda C)^{-1} H^T))}. \tag{3.19}$$

General Cross Validation selection of the smoothing parameter produces an 'optimal' choice in that the total mean squared error of the prediction is often minimised. For small data sets though the solution can be undersmoothed, leading to unacceptably oscillatory solutions.

3.4.4 Estimating the Error on the Recovered Electron Spectra

To determine an estimate of the error on the recovered solution $\hat{f}$ the method described in Thompson et al., 1992 was followed i.e. using Bayes theorem

$$\Pr(\hat{f}|J) = \frac{\Pr(J|\hat{f})\Pr(\hat{f})}{\Pr(J)}$$

where

$$\Pr(J|\hat{f}) = \exp\left(-\sum_{i=1}^{n}\left(\frac{J_i - \sum_{j=1}^{m} H_{ij}\hat{f}_j}{\sigma_i}\right)^2\right)$$

is the likelihood function for $\hat{f}$, and

$$\Pr(\hat{f}) = \exp\left(-\lambda \sum_{j=1}^{m-2}(\hat{f}_i - 2\hat{f}_{i+1} + \hat{f}_{i+1})^2\right)$$

is the prior probability function for f. As Pr(J) is a constant then $\Pr(\hat{f}|J)$ is a multivariate normal distribution the maximum of which corresponds to the regularised estimate of the source function $\hat{f}$. The covariance matrix of this is

$$\Sigma = \left(H_1^T H_1 - \lambda C\right)^{-1}$$

where H_1 is the matrix with elements H_{ij}/σ_i. The standard deviation of $\hat{f}_i$ is then taken to be the diagonal elements of the covariance matrix

$$\delta\hat{f}_i = \sqrt{\Sigma_{ii}}$$

3.5 Electron Spectra of 27th June 1980 inferred for a Non-uniformly Ionised Thick Target

The photon spectra for the 27th of June between 1614:47 and 1617:31 is binned into 9 time intervals. These time intervals are shown, with the time profile of the flare during that interval, in Figure 3.6. The data is also binned into 37 logarithmically spaced energy intervals. This is the same binning of the *HIREX* data previously used when inverting for the instantaneous electron spectra (Thompson et al., 1992) and temperature structure (Piana et al., 1995). The spectral shapes during these 9 intervals are shown in Figures 3.7, 3.10, 3.13, 3.16, 3.19, 3.22, 3.25, 3.28, 3.31 with the parameters commonly used to describe these spectra given in Tables 3.1, 3.2, 3.3, 3.4, 3.5, 3.6, 3.7, 3.8, 3.9. The slight upturn at

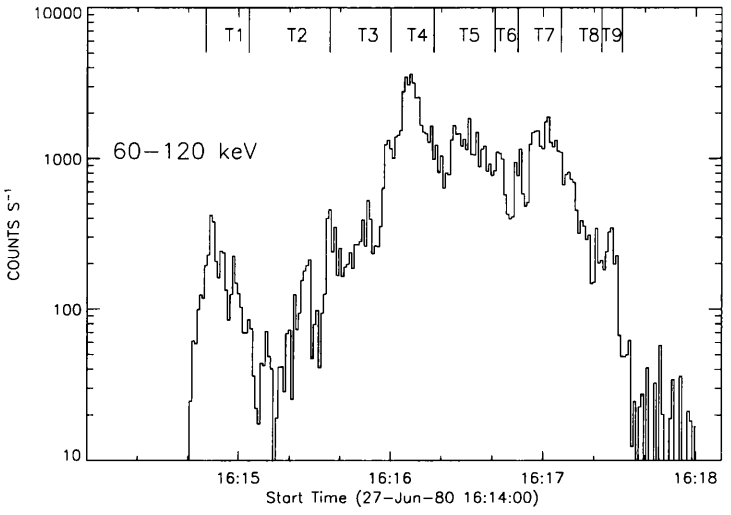

Figure 3.6: Time evolution of the HXR counts detected during the impulsive phase of the 27th June 1980 flare in the binned into 1s time intervals and energy range 60-120 keV. Indicated along the top are the 9 time intervals over which the electron spectra is reconstructed.

low energy (superhot component) is first observed in interval 4, but becomes significant by interval 5, when the spectra changes from break down to break up. The temperature associated with the spectra before this changeover is similar to the peak in the temperature structure derived by Piana et al., 1995.

For a non-uniform atmosphere the ionisation profile was taken to be step-function and the bremsstrahlung cross-section taken to be Kramer's, although evaluation of the matrix kernel does not require these assumptions. The electron spectra were then inverted, at 37 energy points logarithmically spaced, for each time interval over a range of E_1 values including those for an ionised and unionised atmosphere. Apart for the ionised atmosphere this range in E_1 values covered 0-100 keV.

If the superhot component is of thermal origin then inverting the HXR spectra for the thick target electron injection including this component will result in a unrealistic injection spectra. In deriving the instantaneous electron spectra from the hard X-rays no differentiation between thermal or non-thermal sources is made. Only in associating the instantaneous electron spectra to the possible injection spectra is an assumption on whether the emission was thermal or non-thermal is required. However the superhot component has not been conclusively shown to be of thermal origin. Hamilton and Petrosian (1992) dispute the thermal nature of the low energy component. They stated that for a

stochastic acceleration model, the gradual steepening observed by Lin *et al* (1981) could be due to a systematic increase in the density of the plasma (due to evaporation) and the increasing importance of collisions instead of the appearance of a superhot component. Indeed Benka and Holman (1994) discuss conditions for their D.C. model where the plasma heated to superhot temperatures in the current sheet will produce thick target emission. Therefore no superhot component is removed from the spectra before it is inverted for the thick target electron spectra.

The choice of β, the index of the power law by which the recovered solution has been scale, is based on the spectral fit parameters. In intervals 1-4, either β was set to $1+\gamma_2$, the upper spectral index of the power law fit or $1+\gamma$, the spectral index of the power law fit. No appreciable difference was found in the final estimated electron flux given either choice of β. In intervals 5-9, though these values for β often lead to a highly oscillatory solution and negative solution. In these cases increasing β provided realistic estimates of f. However in these cases the smoothing parameter was $\sim 1-2$ orders of magnitude greater than for the other time intervals. Again above these critical values of β, for differing β, no significant differences between estimated accelerated spectra was found.

The resulting estimates of the reconstructed scaled flux and accelerated electron spectra are shown in the following pages. Overplotted on the graphs of estimated accelerated electron spectra are the estimates derived by Lin and Johns for an equivalent time. It is clearly seen that in the majority of time intervals, the estimates of Lin's spectra hereafter LJ_s and our ionised spectra are inconsistent. Specifically, apart for time intervals 2 and 9, in the energy range 40-90 keV the LJ_s spectra are much greater than our estimates. One possible reason for this discrepancy is the different bremsstrahlung cross-section used. The LJ_S spectra were inferred using the Bethe-Heitler cross-section with Elwert factor below 100 keV. It would be expected though that any significant difference between inverted electron spectra using Kramers cross-section rather than Bethe-Heitler's would occur at lower energy, where in fact the spectra are consistent. Above 100 keV Johns and Lin apply an alternative cross-section, valid to 2000 keV is used (Johns and Lin, 1992). This cross-section would have to be less efficient than Kramer's to account for the discrepancy.

Irrespective of the cause of this inconsistency, any comparison between the LJ_s spectra and our own inversion will be meaningless. We cannot then investigate the possible

interpretation that the spike component in the LJ_s spectra is an artifact caused by inversion with a wrongly assumed transition region depth. However by comparing variations in the estimated electron spectra for various E_1 depths with the regularised ionised and unionised atmosphere solutions, we can see that for many non-uniform atmospheres, the recovered solution is much smoother than for the uniform atmosphere. As in Figure 3.8, the recovered solution for the $E_1 = 20.0$ keV atmosphere is almost flat. The corresponding acceleration spectra exhibits featureless power law. The depth of the atmosphere which gives the smoothest reconstructed scaled spectra, f, changes over the duration of the flare. In Figures 3.20 and 3.21 this smoothest spectra corresponds to $E_1 \sim$ 60keV. Thus we have at least shown that possible featureless power law estimates of the the accelerated electron spectra for this event exist. Finally over the last 3 time intervals considered, (T7, T8 and T9,) no smooth estimated spectra are inferred. All of the reconstructed spectra, for all E_1 values, appear to have an upwards break at $\sim$ 40 keV.

Finally for many of the inversions, at high energy, $>$ 150 keV, the estimated spectra quickly tends to zero as in Figure 3.14. In those cases it is thought that the photon data in this range is unreliable and overwhelmed by noise. To overcome this problem we must either rebin the data to improve the signal to noise at high energy, restrict the inversion over a smaller energy range. However this behaviour indicates more that a positivity constraint on the smoothing function, such as maximum entropy, is required for the inversions.

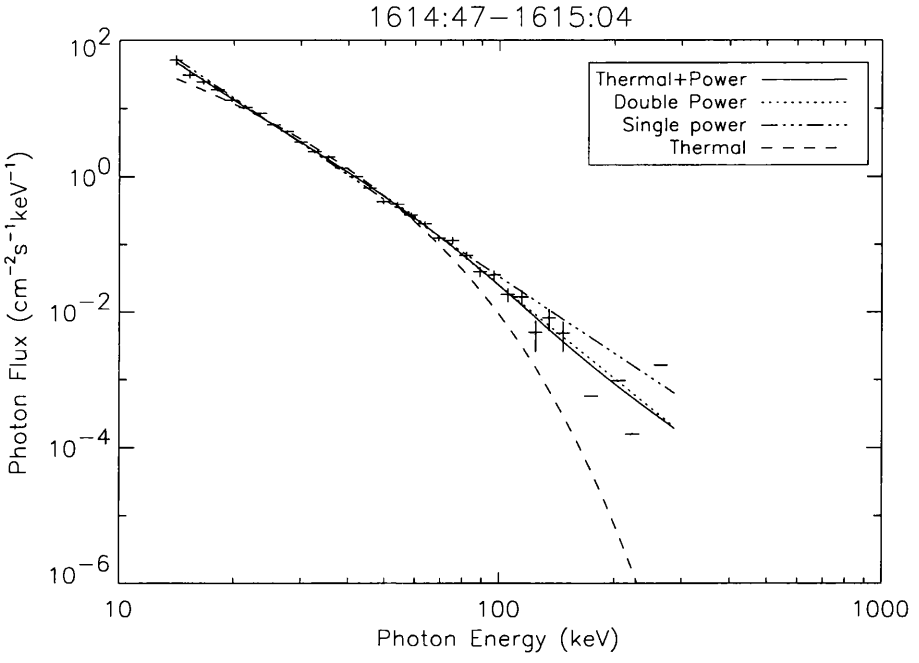

Figure 3.7: Spectral Shape of the photon spectra during the interval 1614:47-1615:04 UT. **Interval 1.**

Fit	A_1	A_2	A_3	A_4	χ^2
Thermal	2.47 e 45 ±8.10 e 43	1.89 e 8 ±3.04 e 6			5.85
Power Law	1.13 e 6 ±13.1	3.77 ±3.37 e -6			4.25
Double Power Law	6.05 e 5 ±0.0023	3.57 ±1.13 e -9	3.46 e 7 ±0.436	4.57 ±1.13 e -9	1.89
Thermal + Power Law	6.13 e 44 ±2.18 e 40	2.56 e 8 ±5.83 e 6	1.79 e 6 ±8.63 e4	4.06 ±0.0155	1.64

Table 3.1: Best fit parameters for thermal, power law, double power law and thermal + power law fits to the photon spectra logarithmically binned into 37 data points over the time interval 1614:47-1615:04 UT. **Interval 1.**

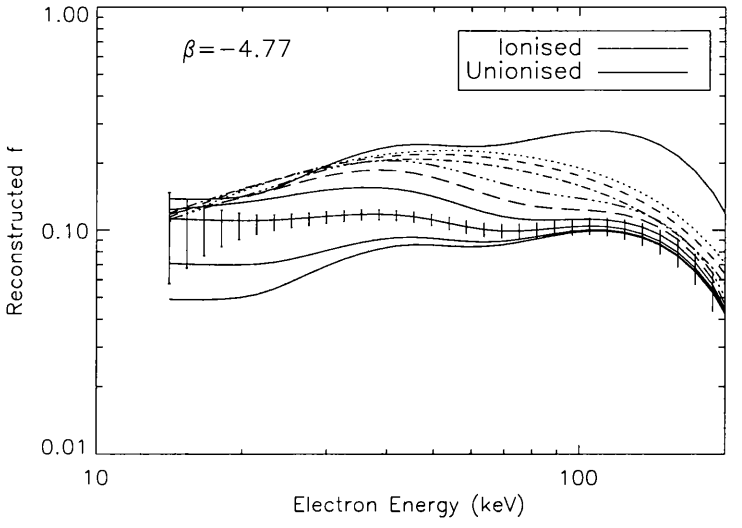

Figure 3.8: Shape of the reconstructed scaled electron spectra f for various transition region column densities over the time interval 1614:47-1615:04 UT. The scaling factor $E^{-\beta}$ for this series of inversion has $\beta = 4.77$. Each line indicates the inversion result for differing E_1 values, the top solid line indicates the electron spectra for an ionised atmosphere. The bottom line indicating showing the spectra for an $E_1 = 0$ unionised atmosphere. The intervening spectra are for E_1 at interval of 10keV. The $E_1 = 20keV$ spectra also shows the typical estimated error values. **Interval 1**.

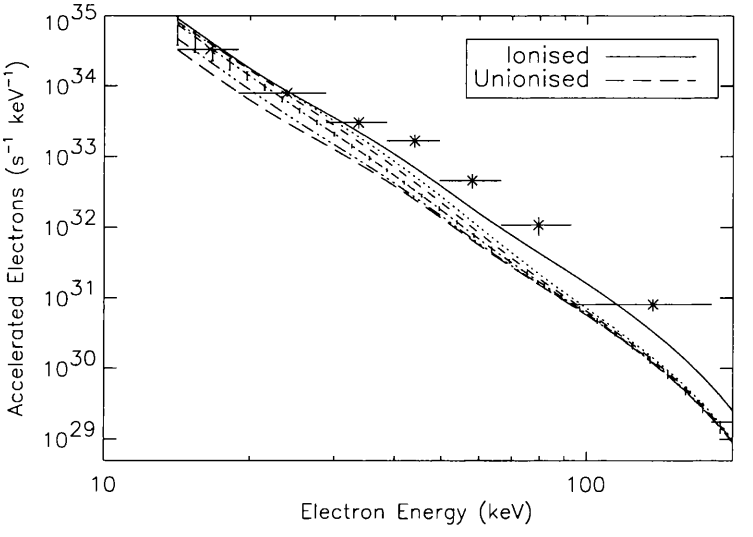

Figure 3.9: Estimated spectra of accelerated electron population for time interval 1614:47-1615:04 UT. Ionised and unionised atmosphere estimates are indicated by full and dashed lines respectively. Spectra between these two are for E_1 values of 10, 20, 30, and 40 keV. Again typical error values indicated on the $E_1 = 20keV$ spectra. The * indicates the estimates for a similar time interval of Lin et al, 1993. **Interval 1**.

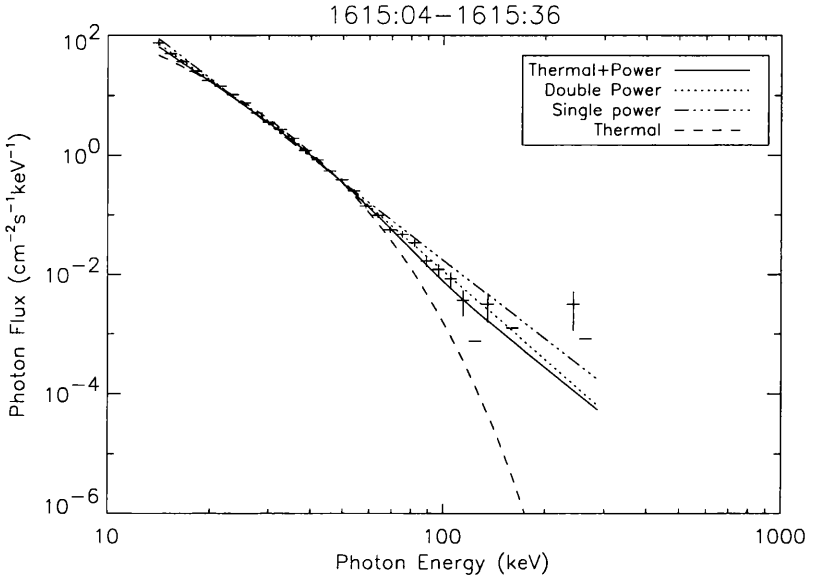

Figure 3.10: Spectral Shape of the photon spectra during the interval 1615:04-1615:36 UT. **Interval 2.**

Fit	A_1	A_2	A_3	A_4	χ^2
Thermal	5.99 e 45 ±1.55 e 44	1.32 e 8 ±1.314 e 6			7.05
Power Law	8.97 e 6 ±5.67 e 5	4.36 ±0.0190			10.3
Double Power Law	2.29 e 6 ±1.88 e 4	3.92 ±0.0026	7.90 e 7 ±9.20 e 5	4.92 ±0.0026	2.69
Thermal + Power Law	2.46 e 45 ±4.05 e 40	1.44 e 8 ±2.65 e 6	6.60 e 6 ±8.75 e5	4.51 ±0.0396	4.02

Table 3.2: Best fit parameters for thermal, power law, double power law and thermal + power law fits to the photon spectra logarithmically binned into 37 data points over the time interval 1615:05-1615:36 UT. **Interval 2.**

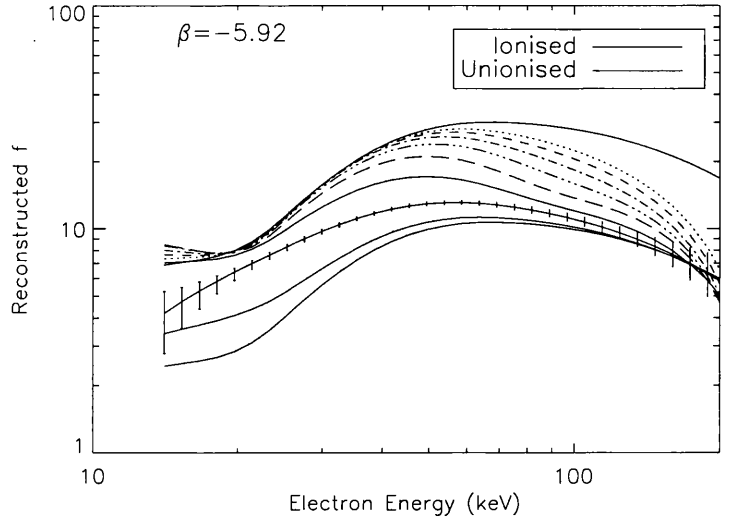

Figure 3.11: Shape of the reconstructed scaled electron spectra f for various transition region column densities over the time interval 1615:05-1615:36 UT. The scaling factor $E^{-\beta}$ for this series of inversion has $\beta = 4.77$. Each line indicates the inversion result for differing E_1 values, the top solid line indicates the electron spectra for an ionised atmosphere. The bottom line indicating showing the spectra for an $E_1 = 0$ unionised atmosphere. The intervening spectra are for E_1 at interval of 10keV. The $E_1 = 20keV$ spectra also shows the typical estimated error values. **Interval 2.**

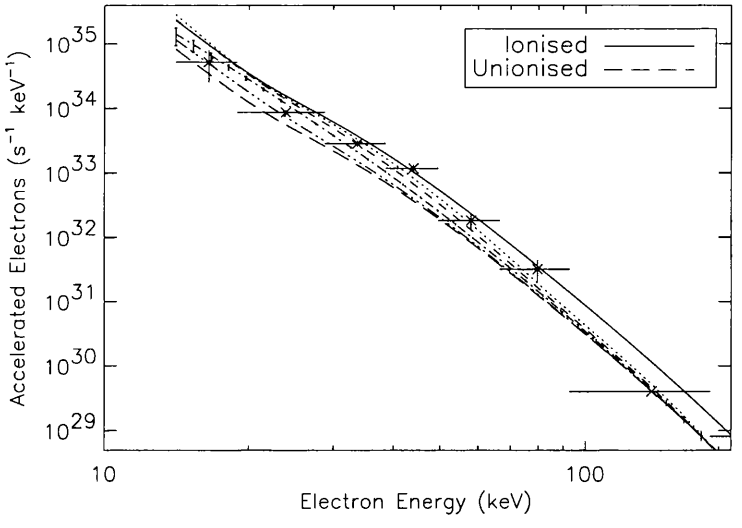

Figure 3.12: Estimated spectra of accelerated electron population for time interval 1615:05-1615:36 UT. Ionised and unionised atmosphere estimates are indicated by full and dashed lines respectively. Spectra between these two are for E_1 values of 10, 20, 30, and 40 keV. Again typical error values indicated on the $E_1 = 20keV$ spectra. The * indicates the estimates for a similar time interval of Lin et al, 1993. **Interval 2.**

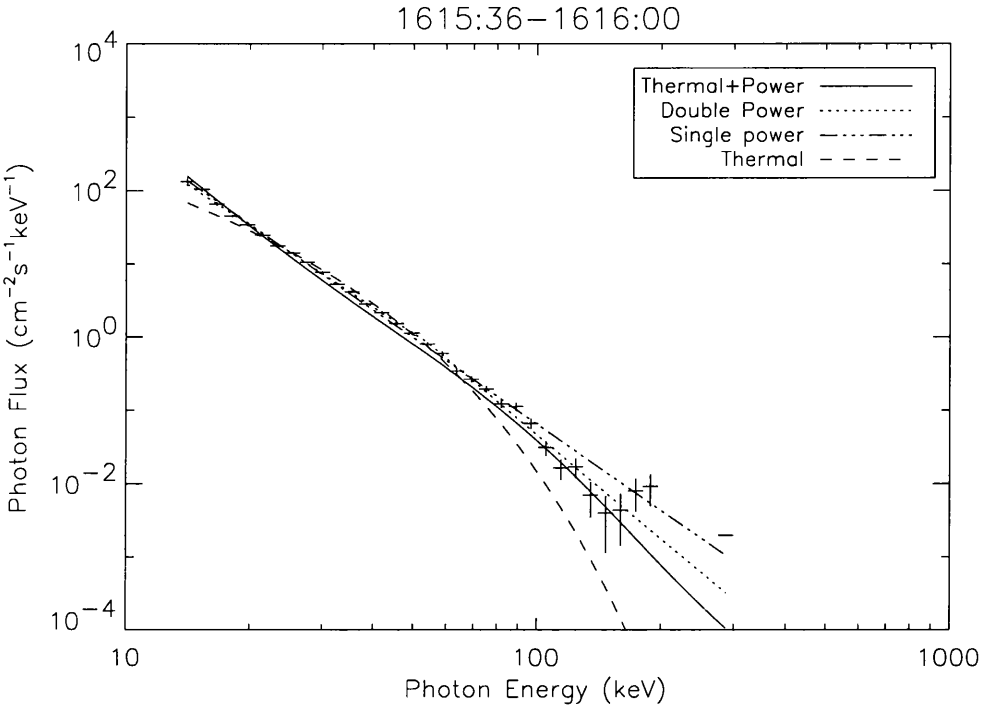

Figure 3.13: Spectral Shape of the photon spectra during the interval 1615:36-1616:00 UT. **Interval 3.**

Fit	A_1	A_2	A_3	A_4	χ^2
Thermal	6.67 e 45 ±1.92 e 44	1.74 e 8 ±2.32 e 6			129
Power Law	5.87 e 7 ±3.40 e 6	4.75 ±0.0190			177
Double Power Law	2.63 e 6 ±1.88 e 4	3.77 ±0.0026	9.27 e 7 ±9.20 e 5	4.77 ±0.0026	170
Thermal + Power Law	2.46 e 45 ±4.05 e 40	1.44 e 8 ±2.65 e 6	6.60 e 6 ±8.75 e5	4.51 ±0.0396	4.02

Table 3.3: Best fit parameters for thermal, power law, double power law and thermal + power law fits to the photon spectra logarithmically binned into 37 data points over the time interval 1615:36-1616:00 UT. **Interval 3.**

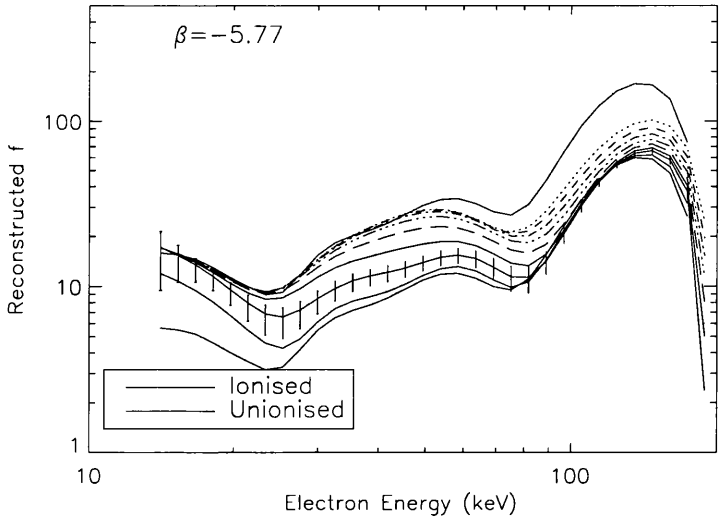

Figure 3.14: Shape of the reconstructed scaled electron spectra f for various transition region column densities over the time interval 1615:36-1616:00 UT. The scaling factor $E^{-\beta}$ for this series of inversion has $\beta = 4.77$. Each line indicates the inversion result for differing E_1 values, the top solid line indicates the electron spectra for an ionised atmosphere. The bottom line indicating showing the spectra for an $E_1 = 0$ unionised atmosphere. The intervening spectra are for E_1 at interval of 10keV. The $E_1 = 20keV$ spectra also shows the typical estimated error values. **Interval 3.**

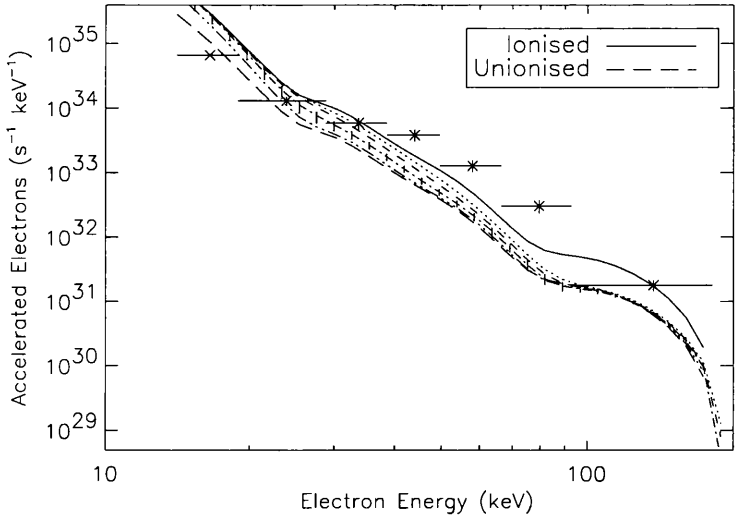

Figure 3.15: Estimated spectra of accelerated electron population for time interval 1615:36-1616:00 UT. Ionised and unionised atmosphere estimates are indicated by full and dashed lines respectively. Spectra between these two are for E_1 values of 10, 20, 30, and 40 keV. Again typical error values indicated on the $E_1 = 20keV$ spectra. The * indicates the estimates for a similar time interval of Lin et al, 1993. **Interval 3.**

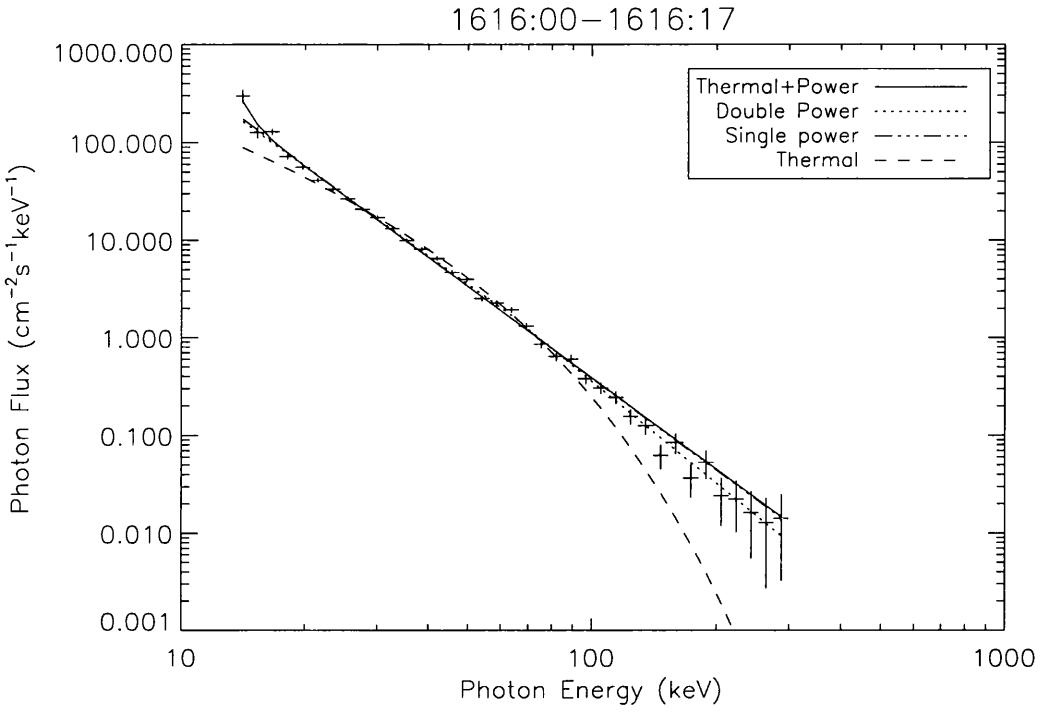

Figure 3.16: Spectral Shape of the photon spectra during the interval 1616:00-1616:17 UT. **Interval 4.**

Fit	A_1	A_2	A_3	A_4	χ^2
Thermal	6.01 e 45 ±1.69 e 44	3.17 e 8 ±6.06 e 6			7.00
Power Law	6.66 e 5 ±5.41 e 4	3.12 ±0.0227			2.40
Double Power Law	4.93 e 5 ±1.89 e 3	3.03 ±0.00112	92.86 e 6 ±2.74 e 4	3.45 ±0.00112	1.57
Thermal + Power Law	1.23 e 45 ±2.20 e 40	4.35 e 8 ±1.92 e 7	8.06 e 5 ±3.35 e 4	3.27 ±0.0125	1.50

Table 3.4: Best fit parameters for thermal, power law, double power law and thermal + power law fits to the photon spectra logarithmically binned into 37 data points over the time interval 1616:00-1616:17 UT. **Interval 4.**

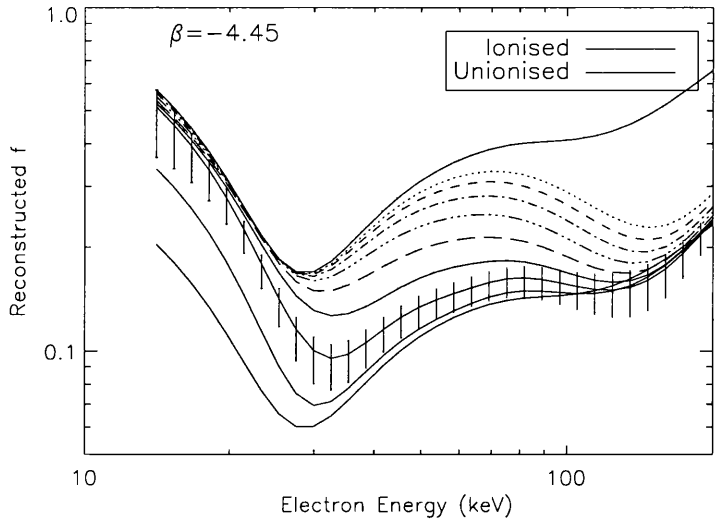

Figure 3.17: Shape of the reconstructed scaled electron spectra f for various transition region column densities over the time interval 1616:00-1616:17 UT. The scaling factor $E^{-\beta}$ for this series of inversion has $\beta = 4.77$. Each line indicates the inversion result for differing E_1 values, the top solid line indicates the electron spectra for an ionised atmosphere. The bottom line indicating showing the spectra for an $E_1 = 0$ unionised atmosphere. The intervening spectra are for E_1 at interval of 10keV. The $E_1 = 20keV$ spectra also shows the typical estimated error values. **Interval 4.**

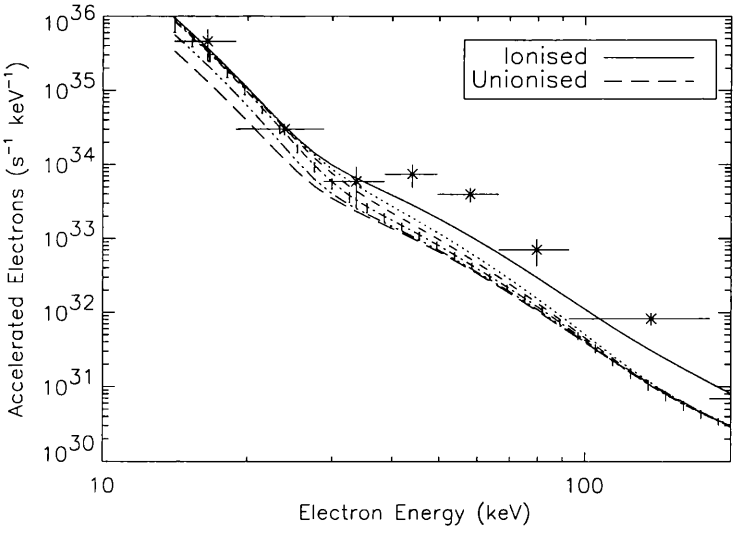

Figure 3.18: Estimated spectra of accelerated electron population for time interval 1616:00-1616:17 UT. Ionised and unionised atmosphere estimates are indicated by full and dashed lines respectively. Spectra between these two are for E_1 values of 10, 20, 30, and 40 keV. Again typical error values indicated on the $E_1 = 20keV$ spectra. The * indicates the estimates for a similar time interval of Lin et al, 1993. **Interval 4.**

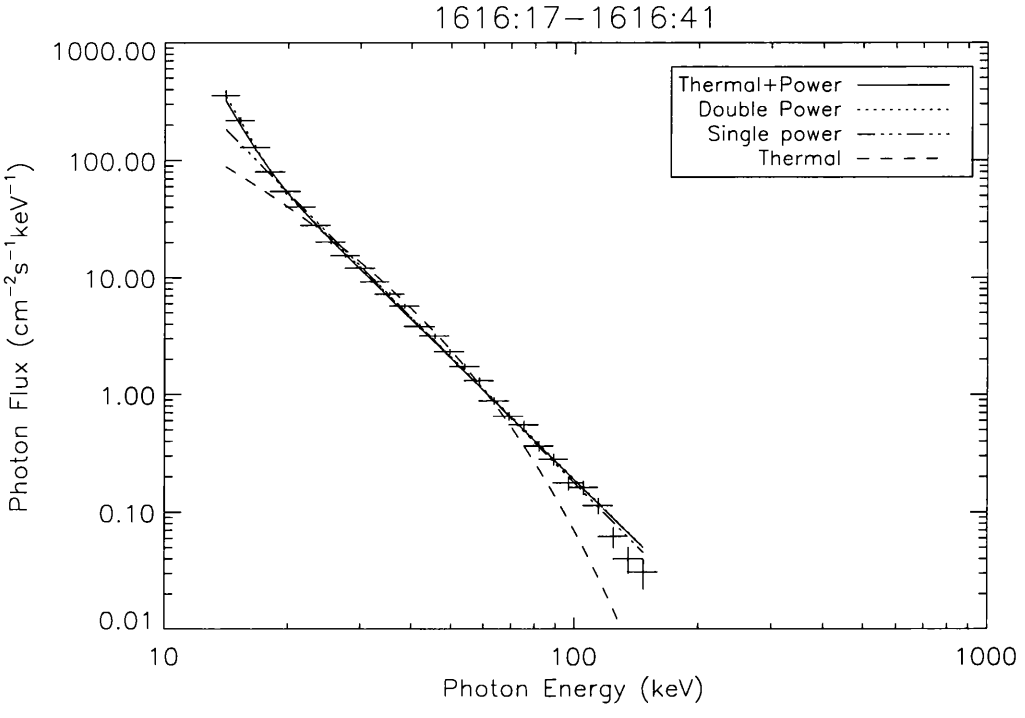

Figure 3.19: Spectral Shape of the photon spectra during the interval 1616:17-1616:41 UT. **Interval 5.**

Fit	A_1	A_2	A_3	A_4	χ^2
Thermal	7.10 e 45 ±1.69 e 44	2.26 e 8 ±6.06 e 6			21.37
Power Law	2.16 e 6 ±1.65 e 5	3.54 ±0.0227			4.45
Double Power Law	2.13 e 0 ±5.08 e 8	5.91 ±0.0864	91.55 e 6 ±1.67 e 4	3.45 ±0.0864	1.80
Thermal + Power Law	6.91 e 48 ±2.20 e 40	2.26 e 7 ±4.25 e 5	1.40 e 6 ±1.15 e 5	3.44 ±0.0187	2.18

Table 3.5: Best fit parameters for thermal, power law, double power law and thermal + power law fits to the photon spectra logarithmically binned into 37 data points over the time interval 1616:17-1616:41 UT. **Interval 5.**

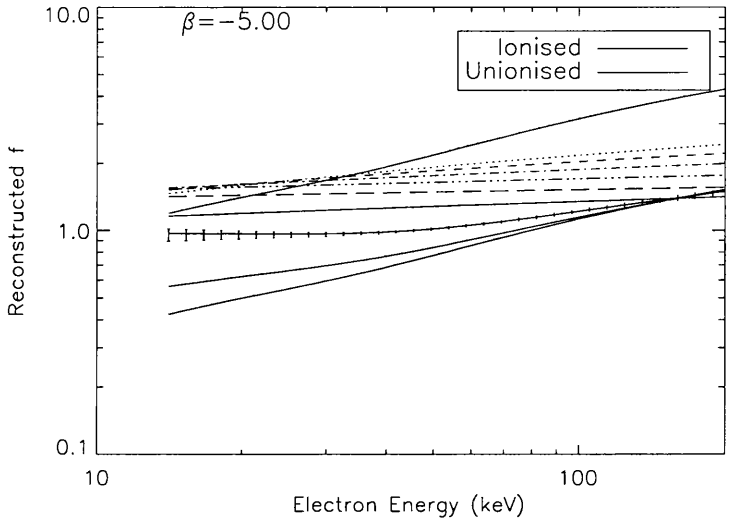

Figure 3.20: Shape of the reconstructed scaled electron spectra f for various transition region column densities over the time interval 1616:17-1616:41 UT. The scaling factor $E^{-\beta}$ for this series of inversion has $\beta = 4.77$. Each line indicates the inversion result for differing E_1 values, the top solid line indicates the electron spectra for an ionised atmosphere. The bottom line indicating showing the spectra for an $E_1 = 0$ unionised atmosphere. The intervening spectra are for E_1 at interval of 10keV. The $E_1 = 20keV$ spectra also shows the typical estimated error values. **Interval 5.**

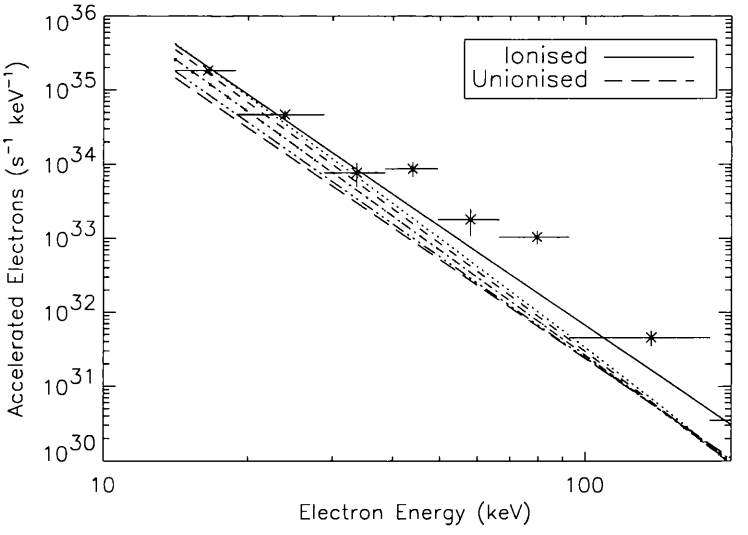

Figure 3.21: Estimated spectra of accelerated electron population for time interval 1616:17-1616:41 UT. Ionised and unionised atmosphere estimates are indicated by full and dashed lines respectively. Spectra between these two are for E_1 values of 10, 20, 30, and 40 keV. Again typical error values indicated on the $E_1 = 20keV$ spectra. The * indicates the estimates for a similar time interval of Lin et al, 1993. **Interval 5.**

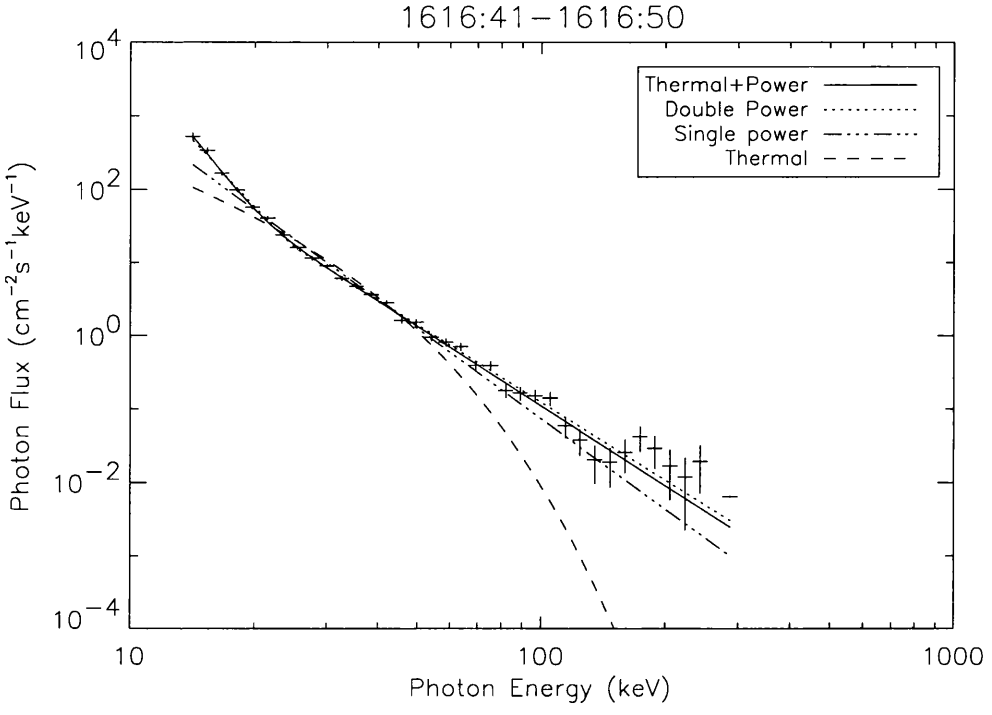

Figure 3.22: Spectral Shape of the photon spectra during the interval 1616:41-1616:50 UT. **Interval 6.**

Fit	A_1	A_2	A_3	A_4	χ^2
Thermal	1.19 e 46 ±7.05 e 44	1.50 e 8 ±3.78 e 6			16.3
Power Law	1.06 e 7 ±1.64 e 6	4.08 ±0.0464			5.89
Double Power Law	3.25 e 9 ±8.07	5.96 ±8.40 e -10	1.31 e 6 ±0.00287	3.51 ±8.40 e -10	1.38
Thermal + Power Law	6.91 e 48 ±2.25 e 41	2.59 e 7 ±1.28 e 6	1.74 e 6 ±5.41 e 5	3.60 ±0.0561	1.17

Table 3.6: Best fit parameters for thermal, power law, double power law and thermal + power law fits to the photon spectra logarithmically binned into 37 data points over the time interval 1616:41-1616:50 UT. **Interval 6.**

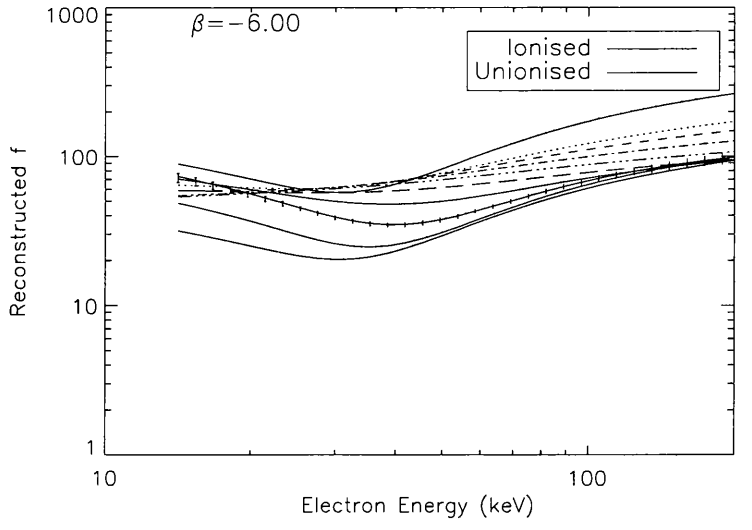

Figure 3.23: Shape of the reconstructed scaled electron spectra f for various transition region column densities over the time interval 1616:41-1616:50 UT. The scaling factor $E^{-\beta}$ for this series of inversion has $\beta = 4.77$. Each line indicates the inversion result for differing E_1 values, the top solid line indicates the electron spectra for an ionised atmosphere. The bottom line indicating showing the spectra for an $E_1 = 0$ unionised atmosphere. The intervening spectra are for E_1 at interval of 10keV. The $E_1 = 20keV$ spectra also shows the typical estimated error values. **Interval 6.**

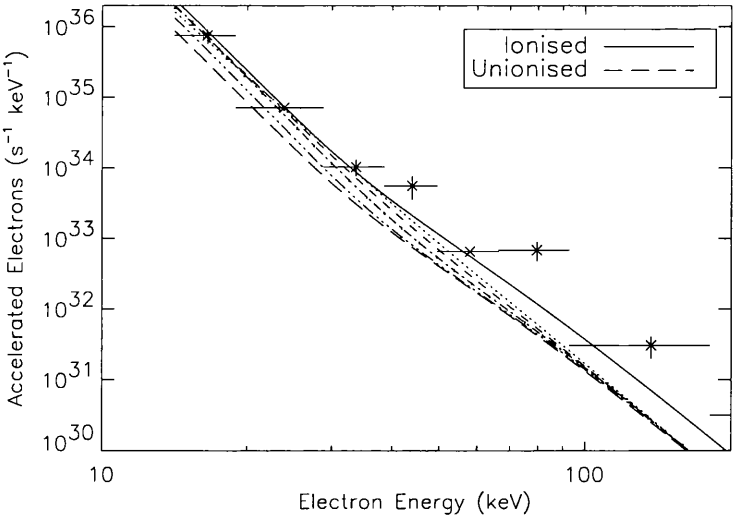

Figure 3.24: Estimated spectra of accelerated electron population for time interval 1616:41-1616:50 UT. Ionised and unionised atmosphere estimates are indicated by full and dashed lines respectively. Spectra between these two are for E_1 values of 10, 20, 30, and 40 keV. Again typical error values indicated on the $E_1 = 20keV$ spectra. The * indicates the estimates for a similar time interval of Lin et al, 1993. **Interval 6.**

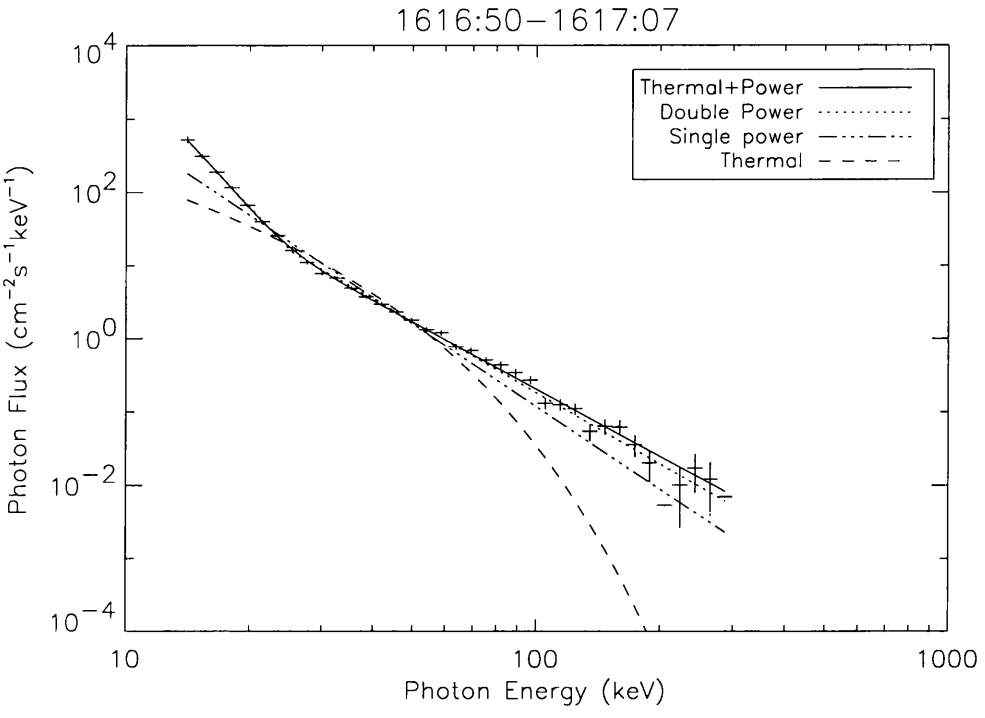

Figure 3.25: Spectral Shape of the photon spectra during the interval 1616:50-1617:07 UT. **Interval 7.**

Fit	A_1	A_2	A_3	A_4	χ^2
Thermal	6.90 e 45 ±3.00 e 44	2.00 e 8 ±4.47 e 6			37.5
Power Law	3.61 e 6 ±4.04 e 5	3.74 ±0.0325			16.8
Double Power Law	3.77 e 9 ±1.126 e 9	5.98 ±0.153	5.08 e 5 ±8.32 e 3	3.22 ±0.153	1.30
Thermal + Power Law	1.93 e 48 ±2.32 e 40	3.32 e 7 ±2.43 e 5	2.42 e 7 ±9.55 e 3	3.04 ±0.0102	1.12

Table 3.7: Best fit parameters for thermal, power law, double power law and thermal + power law fits to the photon spectra logarithmically binned into 37 data points over the time interval 1616:50-1617:07 UT. **Interval 7.**

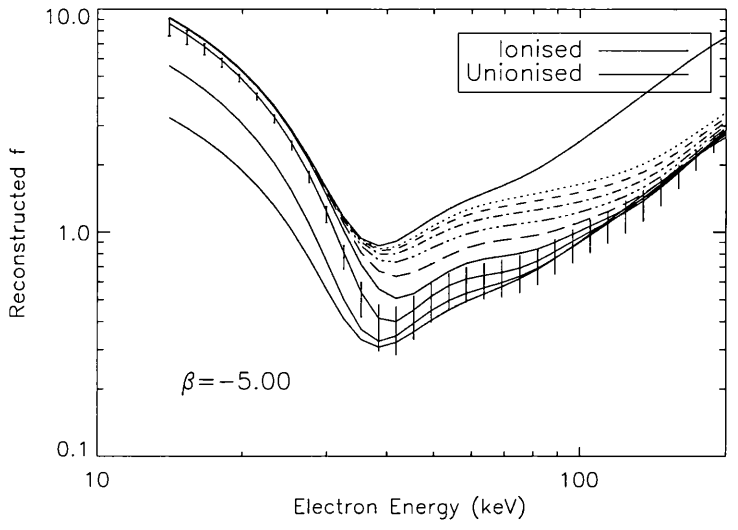

Figure 3.26: Shape of the reconstructed scaled electron spectra f for various transition region column densities over the time interval 1616:50-1617:07 UT. The scaling factor $E^{-\beta}$ for this series of inversion has $\beta = 4.77$. Each line indicates the inversion result for differing E_1 values, the top solid line indicates the electron spectra for an ionised atmosphere. The bottom line indicating showing the spectra for an $E_1 = 0$ unionised atmosphere. The intervening spectra are for E_1 at interval of 10keV. The $E_1 = 20keV$ spectra also shows the typical estimated error values. **Interval 7.**

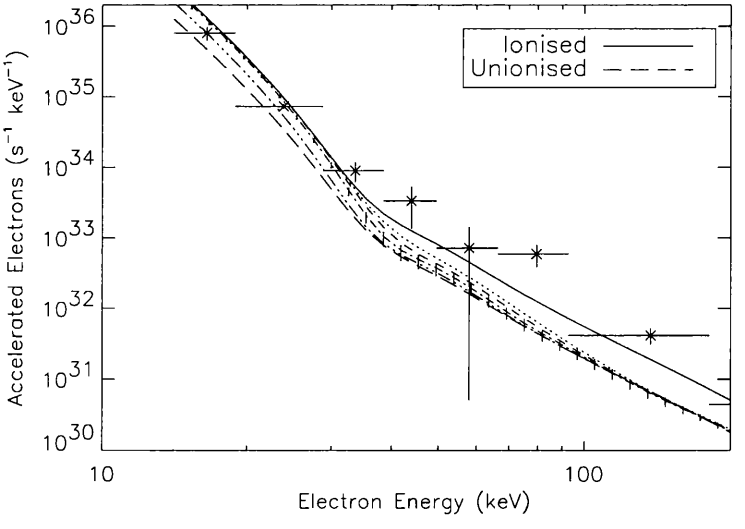

Figure 3.27: Estimated spectra of accelerated electron population for time interval 1616:50-1617:07 UT. Ionised and unionised atmosphere estimates are indicated by full and dashed lines respectively. Spectra between these two are for E_1 values of 10, 20, 30, and 40 keV. Again typical error values indicated on the $E_1 = 20keV$ spectra. The * indicates the estimates for a similar time interval of Lin et al, 1993. **Interval 7.**

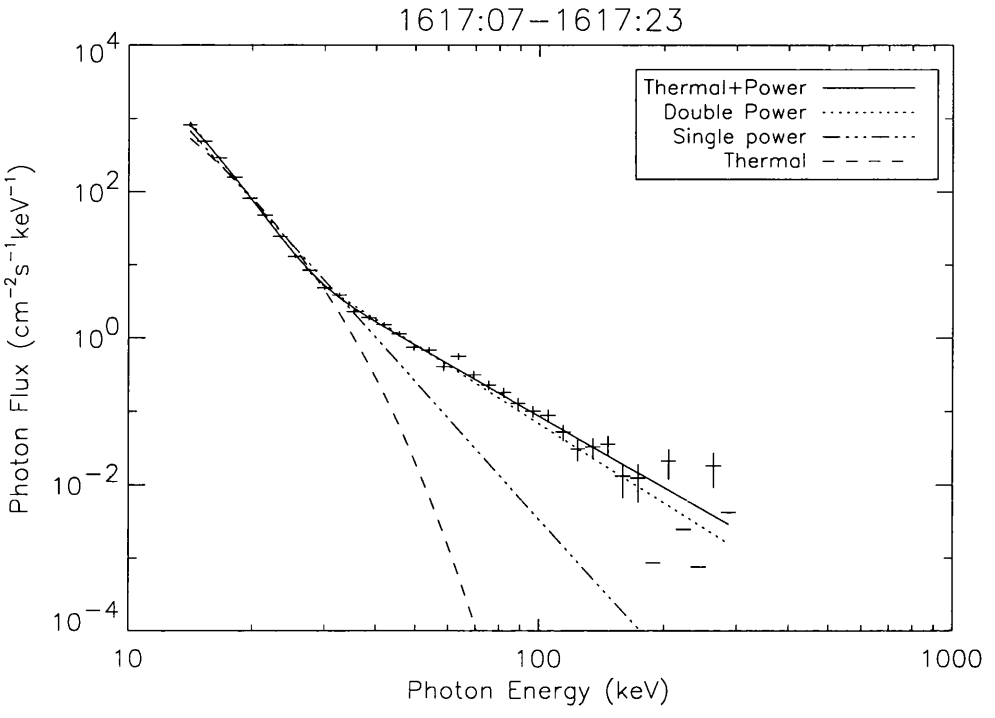

Figure 3.28: Spectral Shape of the photon spectra during the interval 1617:07-1617:23 UT. **Interval 8.**

Fit	A_1	A_2	A_3	A_4	χ^2
Thermal	4.89 e 47 ±3.61 e 46	4.95 e 7 ±6.84 e 5			35.9
Power Law	9.62 e 9 ±1.37 e 9	6.23 ±0.0458			21.0
Double Power Law	1.12 e 11 ±4.06 e 9	7.05 ±0.0123	9.48 e 5 ±2.18 e 4	3.57 ±0.0123	2.01
Thermal + Power Law	3.21e 48 ±7.45 e 39	3.36 e 7 ±7.44 e 4	2.29 e 5 ±4.33 e 3	3.21 ±0.00501	1.50

Table 3.8: Best fit parameters for thermal, power law, double power law and thermal + power law fits to the photon spectra logarithmically binned into 37 data points over the time interval 1617:07-1617:23 UT. **Interval 8.**

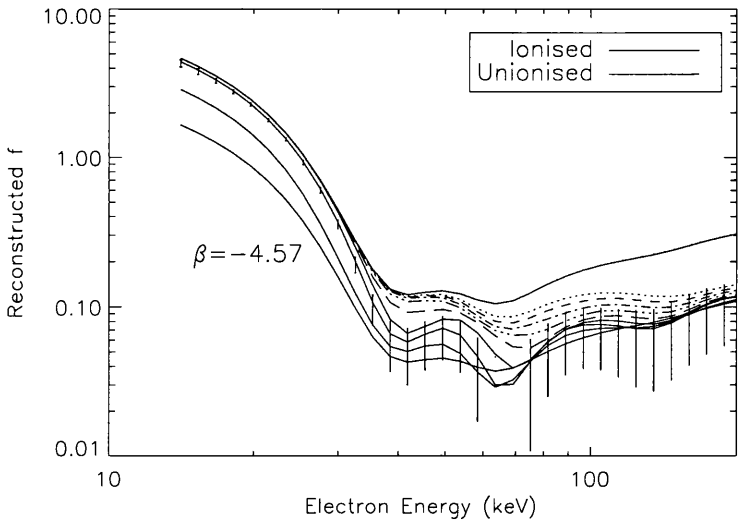

Figure 3.29: Shape of the reconstructed scaled electron spectra f for various transition region column densities over the time interval 1617:07-1617:23 UT. The scaling factor $E^{-\beta}$ for this series of inversion has $\beta = 4.77$. Each line indicates the inversion result for differing E_1 values, the top solid line indicates the electron spectra for an ionised atmosphere. The bottom line indicating showing the spectra for an $E_1 = 0$ unionised atmosphere. The intervening spectra are for E_1 at interval of 10keV. The $E_1 = 20keV$ spectra also shows the typical estimated error values. **Interval 8.**

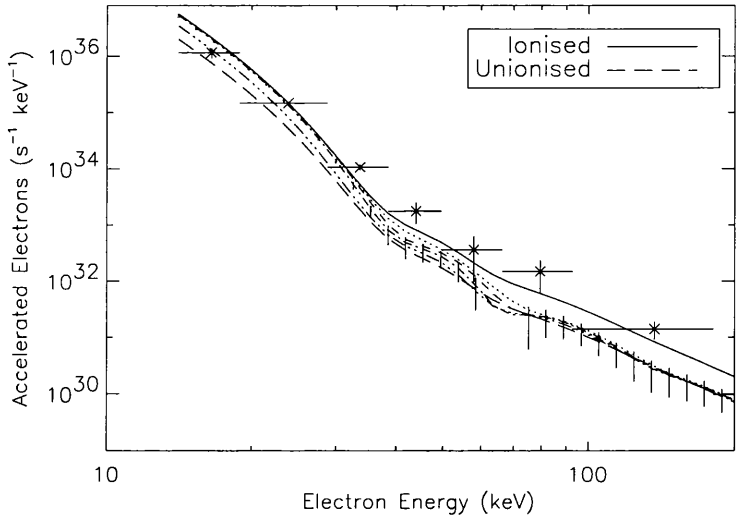

Figure 3.30: Estimated spectra of accelerated electron population for time interval 1614:47-1615:04 UT. Ionised and unionised atmosphere estimates are indicated by full and dashed lines respectively. Spectra between these two are for E_1 values of 10, 20, 30, and 40 keV. Again typical error values indicated on the $E_1 = 20keV$ spectra. The * indicates the estimates for a similar time interval of Lin et al, 1993. **Interval 8.**

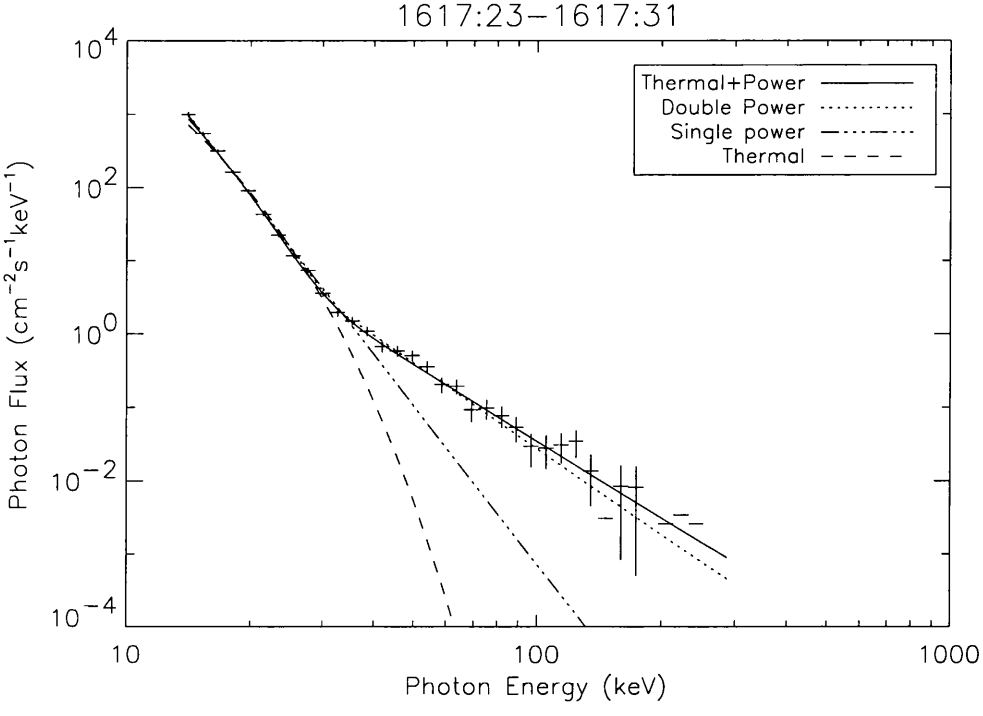

Figure 3.31: Spectral Shape of the photon spectra during the interval 1617:23-1617:31 UT. **Interval 9.**

Fit	A_1	A_2	A_3	A_4	χ^2
Thermal	1.21 e 48 ±1.17 e 47	4.16 e 7 ±7.04 e 5			10.9
Power Law	1.79 e 11 ±3.62 e 10	7.20 ±0.0666			5.61
Double Power Law	2.85 e 11 ±4.61 e 9	7.36 ±0.00540	1.60 e 6 ±5.64 e 4	3.88 ±0.00540	0.731
Thermal + Power Law	3.21 e 48 ±3.04 e 40	3.41 e 7 ±2.42 e 5	2.99 e 5 ±3.23 e 4	3.047 ±0.0282	0.711

Table 3.9: Best fit parameters for thermal, power law, double power law and thermal + power law fits to the photon spectra logarithmically binned into 37 data points over the time interval 1617:23-1617:31 UT. **Interval 9.**

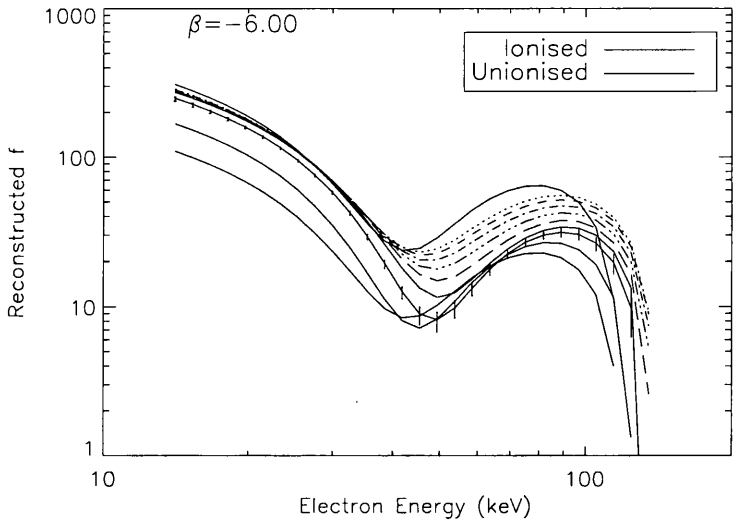

Figure 3.32: Shape of the reconstructed scaled electron spectra f for various transition region column densities over the time interval 1617:23-1617:31 UT. The scaling factor $E^{-\beta}$ for this series of inversion has $\beta = 4.77$. Each line indicates the inversion result for differing E_1 values, the top solid line indicates the electron spectra for an ionised atmosphere. The bottom line indicating showing the spectra for an $E_1 = 0$ unionised atmosphere. The intervening spectra are for E_1 at interval of 10keV. The $E_1 = 20keV$ spectra also shows the typical estimated error values. **Interval 9**.

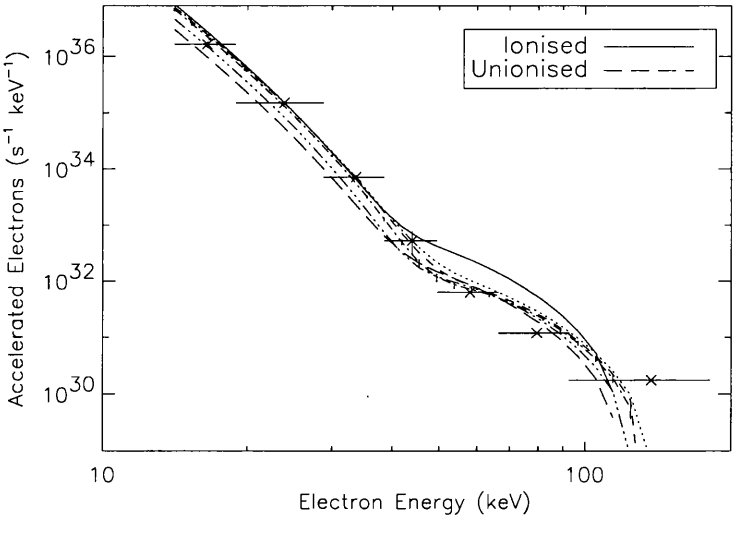

Figure 3.33: Estimated spectra of accelerated electron population for time interval 1617:23-1617:31 UT. Ionised and unionised atmosphere estimates are indicated by full and dashed lines respectively. Spectra between these two are for E_1 values of 10, 20, 30, and 40 keV. Again typical error values indicated on the $E_1 = 20keV$ spectra. The * indicates the estimates for a similar time interval of Lin et al, 1993. **Interval 9**.

Chapter 4

Estimating Coronal Column Density from Hard X-Rays

"It's not size that matters, it's Column Density."

Anonymous

4.1 Introduction

One of the most important parameters influencing the spatial, temporal and spectral characteristics of non-thermal hard X-ray emission is the column density,N, of the coronal plasma. At a critical column density of 10^{20} cm^{-2} the characteristics of emission show marked changes. The larger the coronal column density the brighter the coronal part of the loop. The analysis of non-thermal HXR emission from flares does not, by itself, allow for the direct determination of the column density or electron density, n_e ,in the flaring loop. Estimates can only be derived by modelling the HXR emission process to correctly reproduce the flux, height and time variations observed.

In Chapter 2, we showed that the non-uniform ionisation profile of a flaring atmosphere has a significant effect on the thick target HXR spectrum. At low photon energy, the spectrum is approximately that from an ionised atmosphere, while at high photon energy the spectrum approaches that from an unionised atmosphere. The energy where the spectrum diverges from these approximations is dependent on the coronal column density

of the corona.

In this chapter, we consider the possibility that it is the effect of a non-uniform ionisation profile which is primarily responsible for the observed break in the general power law description of hard X-ray spectra. Thus by determining the break points in HXR spectra we can estimate the coronal column density and its evolution during the flare.

4.2 Column Density Estimates of the Flaring Corona

Soft X-ray Loop

Estimates of the coronal electron density from the soft X-ray flare loop ranges over three orders of magnitude. The lower estimates, inferred mainly during the decay phase of the flare, are of the order $\sim 1 \times 10^9$ cm^{-3} (Pallavicini et al., 1977; Krall et al., 1980). These low values are only slightly higher than the estimates of 'quiet Sun' coronal density e.g $n_e \sim 10^8$ cm^{-3} (Brown and McClymont, 1975). The higher estimates obtained can be in excess of 1×10^{13} cm^{-3}, mostly measured at the time of peak emission for the soft X-ray flare (Feldman et al., 1994; Phillips et al., 1996). Although the density of the flare loop evolves during the course of the flare, even during the decay phase these high coronal density limits of Feldman et al. (1994) and Phillips et al. (1996) are in excess of 1×10^{12} cm^{-3}.

Density Diagnostics Techniques

Filter Ratio (Emission Measure) Method

A great deal of knowledge of the physical conditions of soft X-ray flares is derived from images taken through broad-band filters, such as those of SXT. The emission over such bands encompasses a complex mixture of line and continuum emission and are modelled for coronal abundance values (Mewe et al., 1985; 1986). The ratio of energy fluxes, for a homogeneous isothermal source, in two different filters $R_{12}(T_e)$, is a function only of the plasma temperature T_e. Once the temperature is determined, the value of emission measure, $n_e^2 V$, can be obtained from the absolute flux through one filter. By determining the emission measure of the coronal plasma, when combined with a volume estimate from the image, an indirect density estimate can be provided.

As solar plasmas show wide variations in temperature, the reliability of this method

in the presence of line of sight temperature gradients has been addressed. Underwood and McKenzie (1977) stated that these "effective emission measures" could not be related to the physical state of the plasma. Gerassimenko and Nolte (1978), on the other hand, contended that the technique was physically valid provided appropriate filters were chosen. The physical interpretation of these measurements is therefore still open to some debate.

Line Ratio (Spectroscopic) Method

The intensity ratio of two optically thin lines, which arise from the same ion and have almost the same initial state excitation energies is nearly independent of temperature. If one of these lines is connected to a metastable level, then the line ratio will be extremely sensitive to the electron density and offers a direct means of finding n_e. There are though only a few X-ray lines which produce significant emission at the high temperatures of the soft X-ray loop and in general these lines are only density sensitive for $n_e \geq 10^{12}$ cm^{-3} (Phillips, 1991). The advantage of the line ratio technique is that the filling factor is not required, indeed from emission measure values the emitting volume can be inferred.

Examples of the commonly used line ratios and their respective density estimates are given below.

Line Ratio	**Temperature**	**Density Estimate**	
O VII	2×10^6 K	$1-2\times10^{12}$ cm^{-3}	(McKenzie et al., 1980)
Ne IX	4×10^6 K	$1-2\times10^{12}$ cm^{-3}	(Bhatia et al., 1989)
MgXI	6×10^6 K	5×10^{12} cm^{-3}	(Linford and Wolfson, 1988)
FeXXI, FeXXII	1×10^7 K	1×10^{13} cm^{-3}	(Phillips et al., 1996)

While many of these lines are sensitive only at temperatures well below the maximum (20 MK) of those detected from the soft X-ray loop, they all show similarly high densities. Peaking shortly after the soft X-ray emission peak, the densities then decrease by an order of magnitude during the decay phase. The very small volumes of the emitting region also inferred using this method ($10^{23}-10^{24}$ cm^3), not only indicate extremely small filling factors ($\leq 1\%$), but that the loop must have a complex structure of small dense kernels or filaments.

With loop length estimates in the region of $\sim 10^9$ cm then the column density estimates for the soft X-ray loop range from as low as $10^{18}-10^{22}$ cm^{-2}. The high limit being if the electron beam passed along a high density (10^{13}) filament.

Hard X-ray Modelling

Estimates of the coronal density from hard X-ray observations is mainly based on modelling electron trapping time measurements cf. Chapter 1. Aschwanden and Benz (1997) determined trap densities assuming a weak-diffusion limit and collisional deflection being dominant for flares with *COMPTON* and *BATSE*. The typical values found were $\sim 10^{11}$ cm^{-3} and compared well with the *YOHKOH* SXT estimates. The size of the HXR loops can be determined either by direct imaging or by determining the electron time of flight distances (Aschwanden et al., 1996c). Typical values of these time -of-flight distances are larger than the loop lengths i.e.$\sim 3 \times 10^9$ cm. Thus from these observations coronal column density from hard X-rays is estimated to be $10^{19} - 10^{21}$cm^{-2}.

4.3 Identifying the Relationship Between E_{br} and E_1

For both the soft X-ray and hard X-ray column density estimates, the increased efficiency of the chromosphere would produce features easily detectable within the energy range of most HXR spectrometers. As an example Figure 4.1 illustrates the typical behaviour of the hard X-ray spectra for conservative estimates of E_1 and δ. If the energy range of the spectrometer only covered (50-200) keV, the spectral 'knee' at $\sim$ 80 keV, could well be interpreted as a double power law with the break downwards. In the range 5-50 keV, the spectral 'elbow' at $\sim$ 10 keV would be seen as a double power law with break upwards. As the column density (E_1) increases the whole spectra will shift towards higher energies, and so will the positions of these spectral 'knees' and 'elbows'. In this section we attempt to derive the relationship between the position of these spectral breaks E_{br} and E_1 in order to estimate typical coronal column densities given the general double power law description of HXR spectra discussed in Chapter 1.

4.3.1 Spectral Fitting of Double Power law

Thick target hard X-ray spectra were generated, assuming a power law injection spectra ($AE_0^{-\delta}$) and a non-uniformly ionised atmosphere (step-function at E_1), for a number of models over the parameter space of δ and E_1. The range of electron spectral index (δ) chosen to be examined was between 4.0 and 9.0, i.e. would result in photon spectra with typical observed spectral index values (γ) of $\approx 3.0 - 8.0$. The range of E_1 values (the

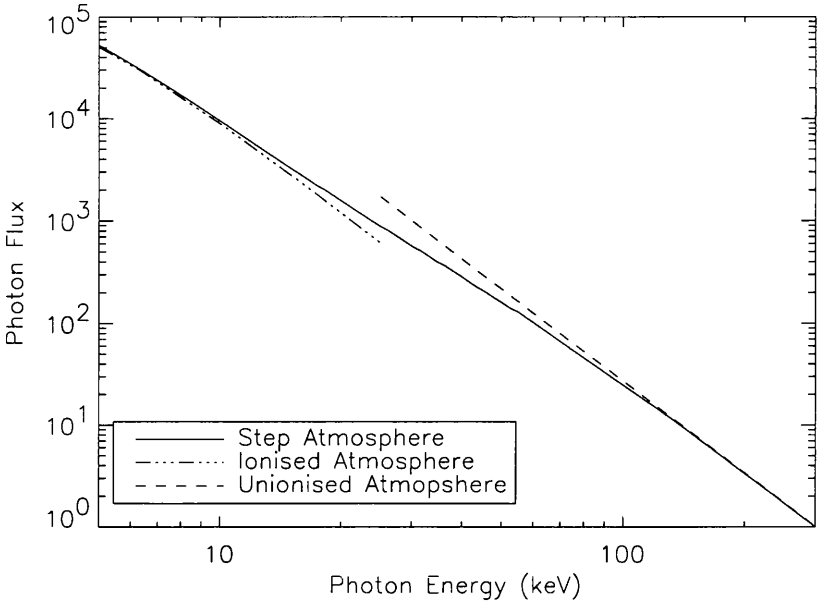

Figure 4.1: Typical hard X-ray spectra for non-uniform, ionised and un-ionised atmospheres. E_1 at $\sim 2.0 \times 10^{20}\text{cm}^{-2}$, δ =5.0.

injected energy of an electron which stops at the transition region) was chosen to range from 5 to 150 keV. As the coronal column density N_1 is simply related to E_1 by

$$N_1 = 1.48 \times 10^{17} E_1^2 \quad (\text{keV})$$

then the coronal column density modelled varied over a range $\approx$ 3.0×10^{18} $- 3.0 \times 10^{21}$ cm^{-2}.

To these spectra, a double power-law was then fitted in order to define primarily the relationship between E_1 and E_{br}. The relationship between the physical parameters (A, δ and E_1) of the model and those of the best fit double power law (a, γ_1, γ_2 and E_{br}) are dependent on the energy range and resolution of the detector. Spectrometers with a relatively low minimum energy ($\sim$ 15 keV) may be able to detect at low energy the part of the spectra approximate to that of an ionised atmosphere, i.e. before the initial break up. This break up may be undetectable for a spectrometer with a higher minimum energy ($\sim$ 30 keV). The fitted break point E_{br} would therefore be observed at higher photon energies. Indeed for the same hard X-ray spectrum, the observed spectra may be defined by one spectrometer as break up while a differing spectrometer determines the spectra to be breakdown. Similarly at higher energy the ability to detect the photon energy

range where the spectra is asymptotic to that of an unionised atmosphere is critical in determining the position of a breakdown E_{br}. This ability depends not only on the upper limit of the spectrometer's energy range but also the size and spectral index of the flare, area of detector and integration time of observation. That to what photon energy range are the count rates statistically significant.

In this analysis then, the energy range and response characteristics of the hard X-ray spectrometer (HXS) on *YOHKOH* was used. The generated HXR spectra were first folded through the response matrix of HXS, before double power laws were fitted to the resultant count rates with added random errors. The spectral fitting routine followed the procedures of the *YOHKOH* analysis software (Morrison, 1994), i.e. was based on the Levenberg-Marquardt Method (Press et al., 1995) (cf. Chapter 5).

As we are only attempting to model the position of the spectral break, any results should be independent of the absolute scale, A, of the electron spectra. However, for a constant value of A, as the spectral index of the electrons (δ) increases the upper photon energy value of statistically significant count rate channels will decrease. Therefore for these models, as δ increases, the value of A also increases so that the number of count rate channels used to fit the double power-law is held constant.

4.3.2 Results

For each generated HXR spectra produced with an electron spectral index of δ and atmosphere depth of E_1, the observed double power law break energy E_{br} and spectral indices γ_1, γ_2 were produced. The surface profiles of how E_{br} varies with δ and E_1 is shown in Figure 4.2. It clearly shows, by the well defined jump in observed E_{br}, that for high coronal column density values, the photon spectra is best fitted by a break up double power law. For lower coronal column densities the spectra is better described by a break down double power law with the break at relatively higher photon energies than the break up cases. We can see in detail this relationship in Figures 4.2-4.7. Observed upwards break points between 50-100 keV are derived when the coronal column density has a stopping energy between 50-150 keV. Over the range of δ the relationship appears linear, differing by a constant term and also the minimum column density at which the spectra appears break up. The great variation in this change over point, (at $\sim$ 50 and 130 keV for δ=9 and 4 respectively), is a consequence of hard electron spectra $\delta \sim 4$ being less dominated

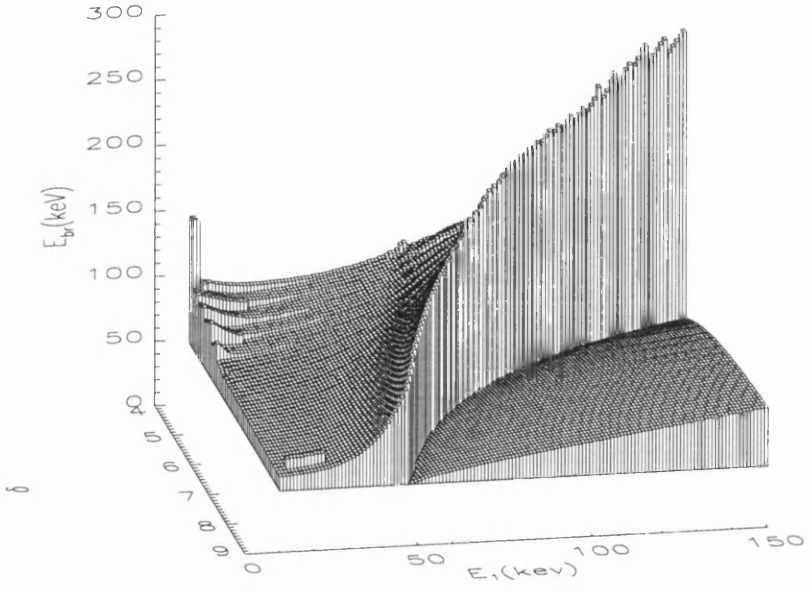

(a)

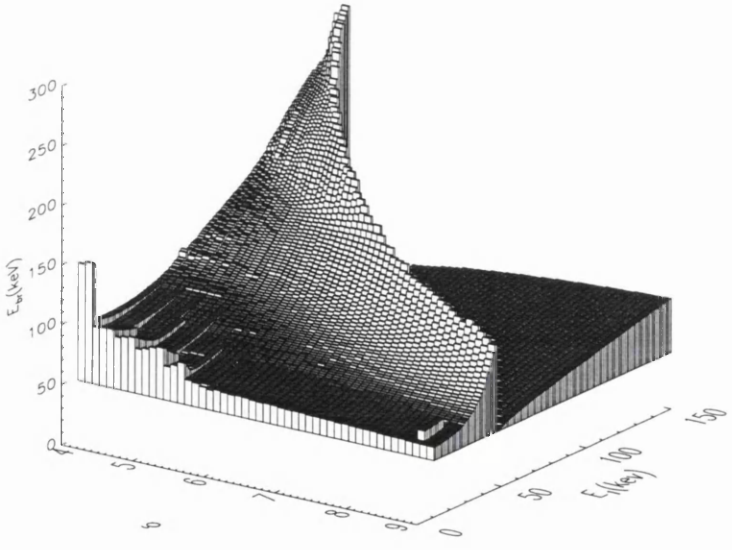

(b)

Figure 4.2: Surface profiles of the modelled observed photon break point with varying ionisation column densities and electron injection spectral indices. Modelled assuming the *YOHKOH* HXS response function for energy range 20-657 keV, using channels 1-30.

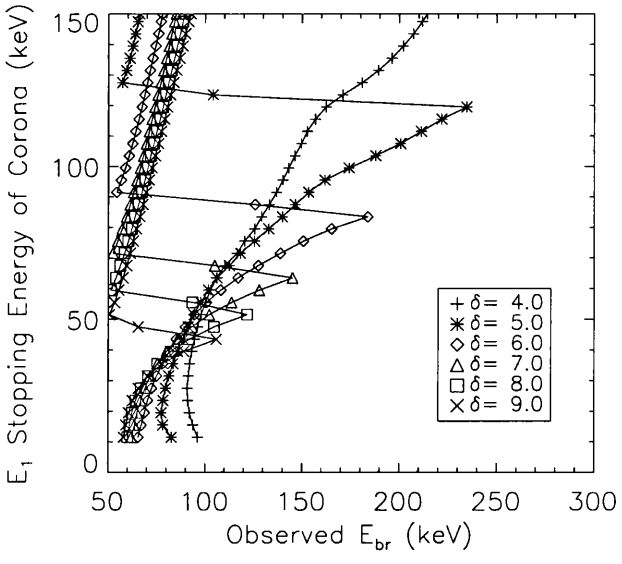

Figure 4.3: The variation of 'observed' spectral break point E_{br} with the coronal stopping energy E_1 for varying initial electron spectral indices δ between 4-9. The coronal stopping energy E_1 being the initial energy of an electron which has just enough energy to reach the transition region. The HXR spectra is generated assuming thick target bremsstrahlung from a non-uniformly ionised atmosphere, with a step-function ionisation profile and assuming the HXS response function.

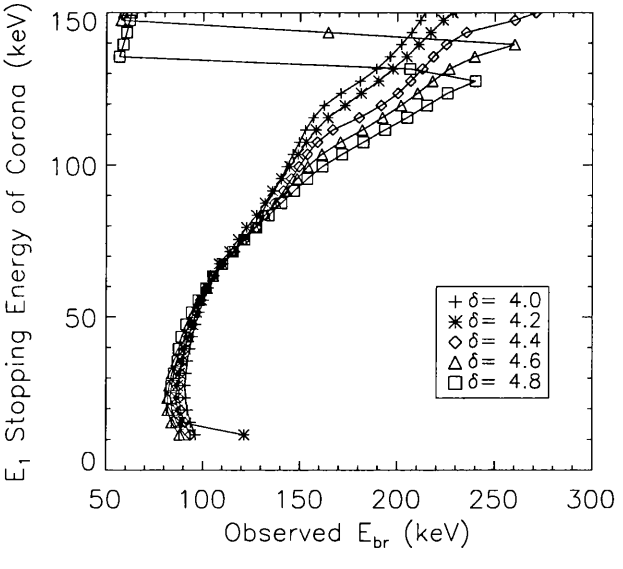

Figure 4.4: Same as for Figure 4.3. Here δ is varying only between 4-5.

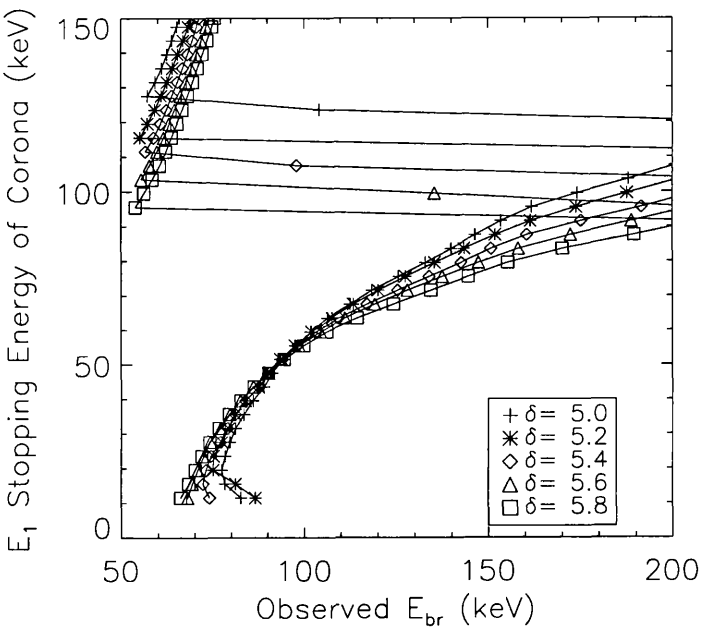

Figure 4.5: Same as for Figure 4.3. Here δ is varying only between 5-6.

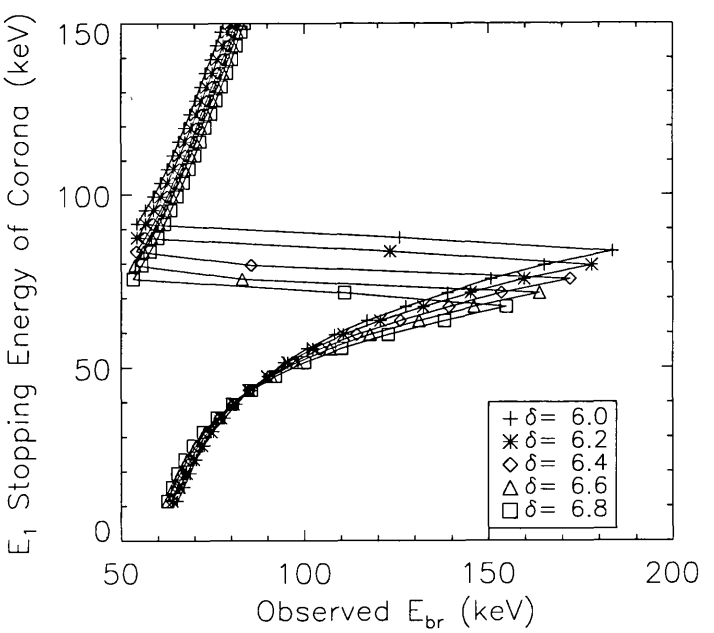

Figure 4.6: Same as for Figure 4.3. Here δ is varying only between 6-7.

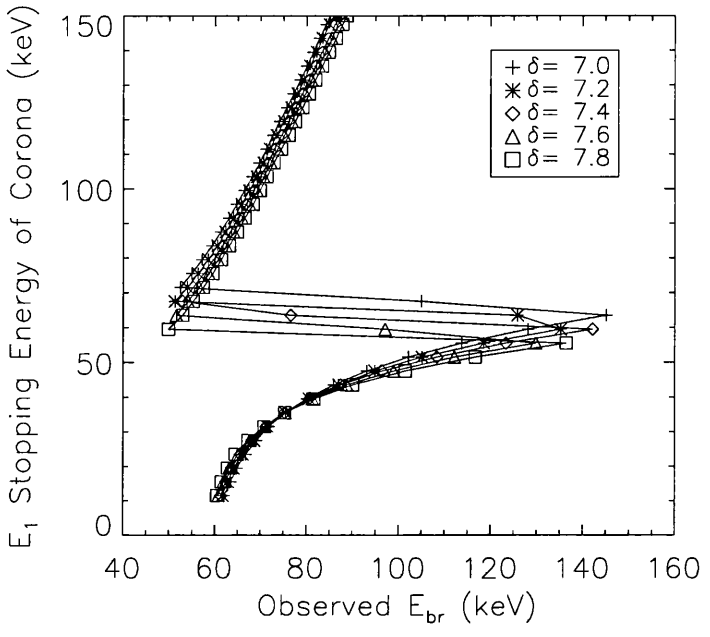

Figure 4.7: Same as for Figure 4.3. Here δ is varying only between 7-8.

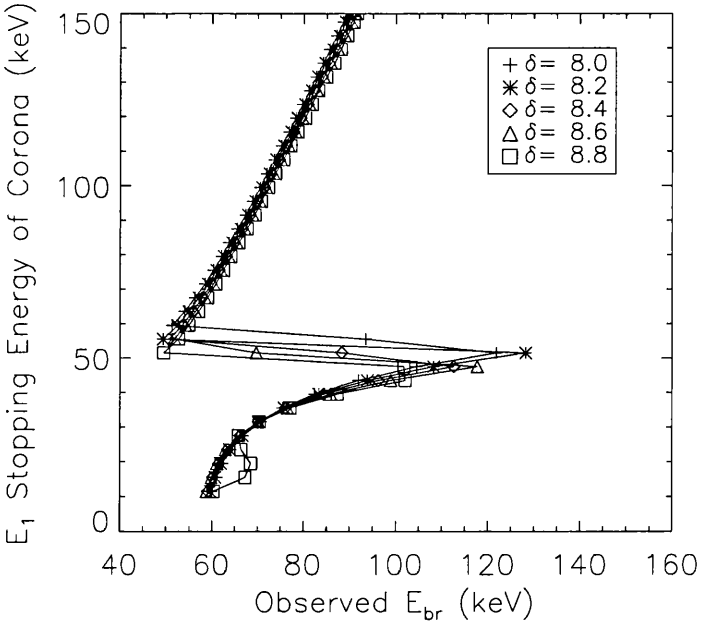

Figure 4.8: Same as for Figure 4.3. Here δ is varying only between 8-9.

by the low energy electrons. In the photon spectra below $\epsilon = E_1$, the contribution of these photons which are produce in the chromosphere is greater for harder electron spectra and therefore the break up point lower.

The variations of observed downwards break points with E_1 show more features. Firstly the range of observed break point is greater (from $\sim 50 - 250$ keV). More importantly though is the relatively small increases in E_{br} for large increases in E_1, at low E_1 values (20 keV). This is clearly seen in Figure 4.4, where between E_{br}=80 - 100 keV the graph is extremely steep. Indeed at these low E_1 values, for $\delta = 4$ the observed break point can increase with decreasing column density, cf. the small peak in Figure 4.2. At such low E_1 values the ability to model the spectra over this HXR range with a double power law is questionable. For larger δ the break point increases more smoothly and is also determined to be at lower photon energies. The behaviour of E_{br} against E_1 suggest that estimates of E_1 would be more stable for high E_1 and δ values, and at low δ values $\sim 5 - 6$ (frequently observed spectral indices) the estimates would be far more unreliable.

Analytic Expressions for Surface Profile

In order to obtain an approximate analytic relationship between the observed photon break point and the column density, we separated the surface profile into the two populations, break up and break down. When the fitted spectra was break up, for each curve of constant δ we fitted the variation of E_1 against E_{br} with a simple straight line, i.e. if $(\gamma_2 < \gamma_1)$ then

$$E_1 = \sum_{i=0}^{i=1} \mathrm{a}_i E_{br}^i. \tag{4.1}$$

The values of a_0 and a_1 being dependent on δ. Alternatively if the spectral break was down $(\gamma_2 > \gamma_1)$, then the variation of E_1 against E_{br} was fitted with the sum of of $\log_{10}(E_{br})^{1/2}$ i.e.

$$E_1 = \sum_{i=0}^{i=3} \mathrm{a}_i \left(\log_{10} E_{br}\right)^{i/2} \tag{4.2}$$

It should be noted that this fit did not include the region for $\delta < 5$ and $E_1 \lesssim 35$ keV. Both sets of parameters a_i where in turn fitted as a polynomial in δ, the spectral index of the electrons which produced the initial HXR spectra

$$\mathrm{a}_i = \sum_{i=0}^{i=n} \mathrm{b}_i \delta^i \qquad . \tag{4.3}$$

The number of terms, n, required for suitable fits were 2 and 5 for break up break down populations respectively. These co-efficients for b_i are given in Tables 4.1-4.2. The estimates of E_1 using these co-efficients were then calculated for each model, using the given spectral index and the determined E_{br}. The difference between these estimated E_1 values and those actually used is shown in Figure 4.9-4.11. Not surprising in the area below $\delta = 5$ and $E_1 = 35$ keV, the fits are wildly wrong. However above this region, the estimated E_1 is well determined with an error ~ 4 keV.

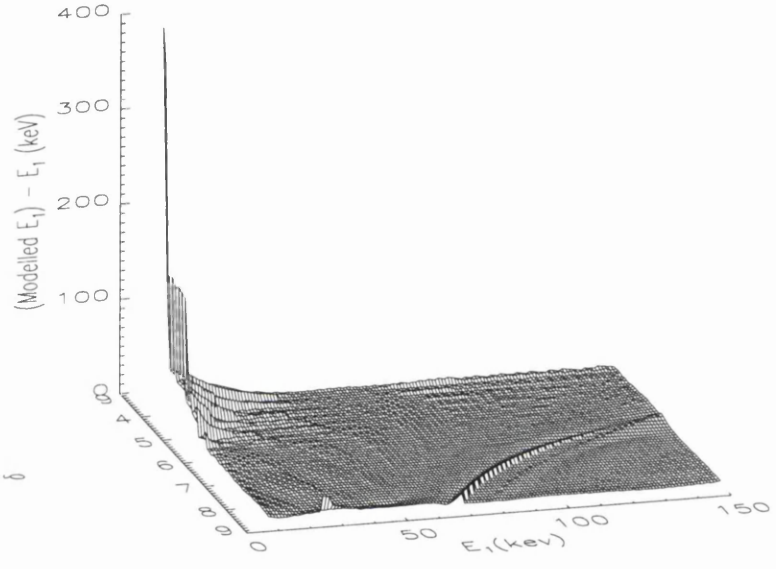

Figure 4.9: Difference in estimated E_1 and true E_1 given the fitting co-efficients in Table 4.1 and 4.2.

The estimation of E_1 from E_{br} in this analysis assumes a knowledge of δ. The value of δ though can be approximated from the observed photon spectral indices γ_1 and γ_2. For a break up, then

$$\delta \approx \gamma_1 + 1,$$

while for a break down spectra

$$\delta \approx \gamma_2 + 1.$$

Because of the high sensitivity in δ of the fitting, the a_i co-efficients were expressed as a polynomial in δ, the resultant estimates of E_1 using only approximate values of δ, which will inevitably incorporate an error value, are no longer credible. As a result, unless a

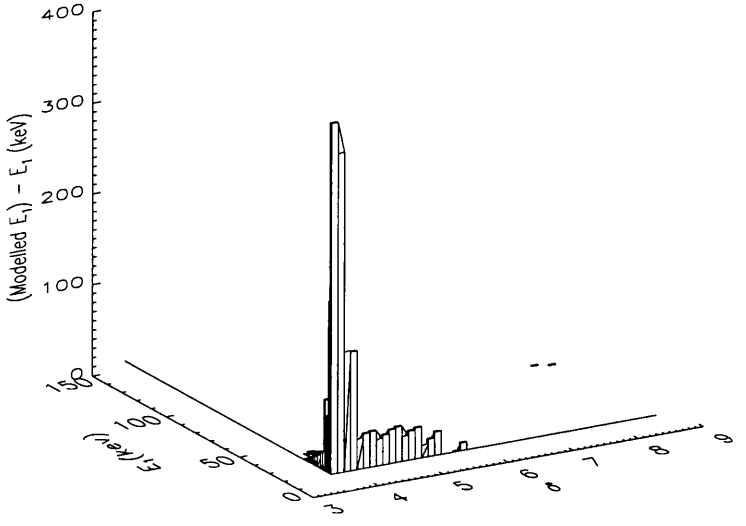

Figure 4.10: Difference in estimated E_1 and true E_1 given the fitting co-efficients in Table 4.1 and 4.2.

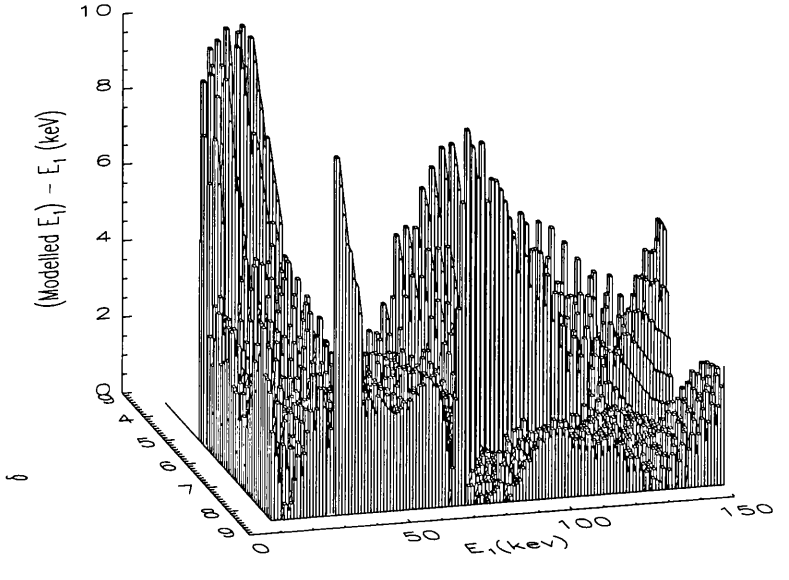

Figure 4.11: Difference in estimated E_1 and true E_1 given the fitting co-efficients in Table 4.1 and 4.2. Here only the range in δ and E_1 that was used in the fitting procedure is plotted.

procedure for determining δ extremely accurately is devised, the possibility of using this method to relate the double power law fit parameters of the HXR spectra to estimates of the coronal column density is fundamentally flawed.

Break Up Coefficients			
	b_0	b_1	b_2
a_0	245.622	-62.373	3.316
a_1	4.662	-0.474	0.0242

Table 4.1: Polynomial co-efficients for the variation of E_1 against E_{br} where the was an upwards break.

Break Down Coefficients						
	b_0	b_1	b_2	b_3	b_4	b_5
a_0	-9.963e5	5.597e5	-1.258e5	1.467e4	-944.2	27.56
a_1	3.153e6	-1.837e6	4.335e5	-5.359e4	3624	-108.0
a_2	-3.295e6	1.973e6	-4.823e5	6.193e4	-4312	129.9
a_3	1.138e6	-6.962e5	1.746e5	-2.301e4	1633	-49.50

Table 4.2: Polynomial co-efficients for the variation of E_1 against E_{br} where the was a downwards break.

4.4 HXR Spectra from Power law Injection Spectrum

To determine the possible information on E_1 in the HXR spectra, the spectra needs to be fitted by the three physical parameters A, δ and E_1 of the model. This requires determining the expression for thick target emission from a non-uniform atmosphere with power law injection spectra. The generalised thick target equation for a completely ionised atmosphere is given by

$$J(\epsilon) = \frac{c}{\epsilon}\int_{\epsilon}^{\infty} F_o^*(E_o)\int_{\epsilon}^{E_o}\frac{q(\epsilon,E)}{\lambda+1}dE_o dE. \tag{4.4}$$

Assuming Kramers' cross-section i.e. $q(\epsilon,E) = 1$, and changing the order of integration then

$$J(\epsilon) = \frac{c}{\epsilon}\int_{\epsilon}^{\infty}\frac{dE}{(\lambda+1)}\int_{E}^{\infty} F_o^*(E_o)dE_o \tag{4.5}$$

We showed previously in Equation 2.24 that

$$F_o^*(E_o) = F_o(E_o) + \frac{\nu F_o\left(\left(E_o^2 + E_1^2\right)^{\frac{1}{2}}\right)}{\left(E_o^2 + E_1^2\right)^{\frac{1}{2}}} \tag{4.6}$$

If we therefore assume a power law injection spectra, $F_o(E_o) = AE_o^{-\delta}$ then equation 4.5 reduces to

$$J(\epsilon) = \frac{Ac}{(\lambda+1)\epsilon}\int_\epsilon^\infty P(E_1, E)dE \tag{4.7}$$

where

$$P(E_1, E) = \int_E^\infty \left[E_o^{-\delta} + \nu E_o\left(E_o^2 + E_1^2\right)^{\frac{-(\delta+1)}{2}}\right] dE_o \tag{4.8}$$

$$= \frac{E^{1-\delta} + \nu\left(E^2 + E_1^2\right)^{\frac{1-\delta}{2}}}{\delta - 1}$$

i.e.

$$J(\epsilon) = \frac{Ac}{(\delta-1)(\lambda+1)\epsilon}\left[\frac{\epsilon^{2-\delta}}{\delta-2} + \nu Q(\epsilon, E_1)\right] \tag{4.9}$$

where we have defined

$$Q(\epsilon, E_1) = \int_\epsilon^\infty \left(E^2 + E_1^2\right)^{\frac{1-\delta}{2}} dE \tag{4.10}$$

If we let

$$Y = \frac{E^2}{E_1^2+E^2}$$

$$\text{then} \quad (E_1^2 + E^2) = \frac{E_1^2}{1-Y}$$

$$\text{and} \quad dE = \frac{E_1 dY}{2Y^{\frac{1}{2}}(1-Y)^{\frac{3}{2}}}$$

$$\text{with} \quad Y = 1 \text{ at E} = \infty \text{ and } \quad Y = \frac{\epsilon^2}{E_1^2+\epsilon^2} \text{ at E} = \epsilon$$

so

$$Q(\epsilon, E_1) = \int_{\frac{\epsilon^2}{\epsilon^2+E_1^2}}^1 \left(\frac{E_1^2}{1-Y}\right)^{\frac{1-\delta}{2}} \frac{E_1 dY}{2Y^{\frac{1}{2}}(1-Y)^{\frac{3}{2}}}$$

$$= E_1^{2-\delta}\int_{\frac{\epsilon^2}{\epsilon^2+E_1^2}}^1 Y^{-\frac{1}{2}}(1-Y)^{\frac{\delta-4}{2}} dY$$

$$= E_1^{2-\delta} I_b\left(\frac{\epsilon^2}{\epsilon^2+E_1^2}, \frac{1}{2}, \frac{\delta-2}{2}\right)$$

$I_b(a,p,q)$ is the difference between the Beta function $B(p,q)$ and the incomplete Beta function $\mathrm{I}_B(a,p,q)$. Therefore the photon spectra $J(\epsilon)$ for power law electron injection spectra into an atmosphere with the transition region at an electron stopping energy of E_1 can be expressed analytically as

$$J(\epsilon) = \frac{Ac}{(\lambda+1)(\delta-1)\epsilon}\left[\frac{\epsilon^{2-\delta}}{\delta-2} + \nu E_1^{2-\delta} I_b\left(\frac{\epsilon^2}{\epsilon^2+E_1^2}, \frac{1}{2}, \frac{\delta-2}{2}\right)\right]. \tag{4.11}$$

4.5 Nonuniform Model Parameters for HIREX data

Using the expression for thick target emission derived in Section 4.4, we attempted to model the hard X-ray spectra of the flare observed by *HIREX* on June 27th 1980, (cf. Chapter 3). The photon spectra were fitted using a standard non-linear least squares technique, the Levenberg-Marquardt Method (Press et al., 1995). The results of these fits for HXR spectra observed over the same time and energy resolution as used in Chapter 3 are shown in Figures 4.12-4.13 and Table 4.3. The data had no superhot component removed but were fitted above 20 keV only. For the last two time intervals this minimum energy was increased to 30 keV.

The values of A give the electron flux at 1keV ($10^{35}\mathrm{s}^{-1}$), while E_1 is in keV. The χ^2 values of the fits are comparable with those for a double power law, but not statistically better or worse. The evolution of E_1 shows a peak at 1616:50 with an E_1 value equivalent to $\sim 1.4 \times 10^{21}\mathrm{cm}^{-2}$ in coronal column density. An apparent close correlation between the beam energy content above 20 keV, (determined from the derived A and δ) and the derived E_1 is also found.

4.6 Conclusions

This analysis has shown that assuming the features observed in the HXR spectra are not signatures of the parent electron spectra, then they are consistent with a thick target model of non-uniform ionisation. In effect, spatial information of the flare loop, i.e. the coronal column density, can be modelled from spatially unresolved HXR spectra. In addition the evolution of the coronal depth during the flare may be determined, which timing variation models cannot achieve. Simple comparisons of column depth with the large scale beam parameters and energy budgets may provide insight into either atmospheric response or spatial evolution of of loop.

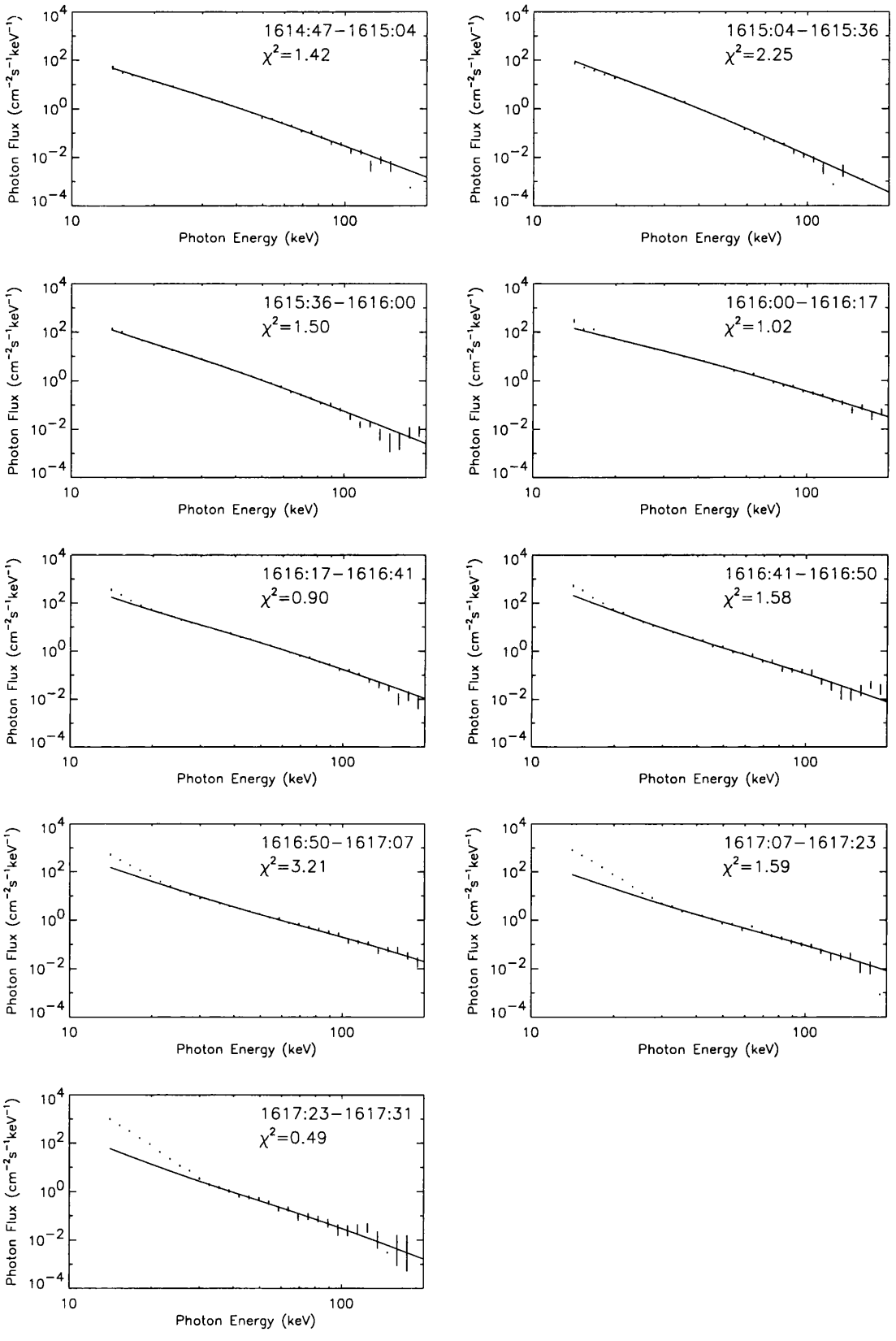

Figure 4.12: The best fits to the HIREX photon spectra (27 June 1980) for a non-uniform ionisation atmosphere with power law injection electron spectra model.

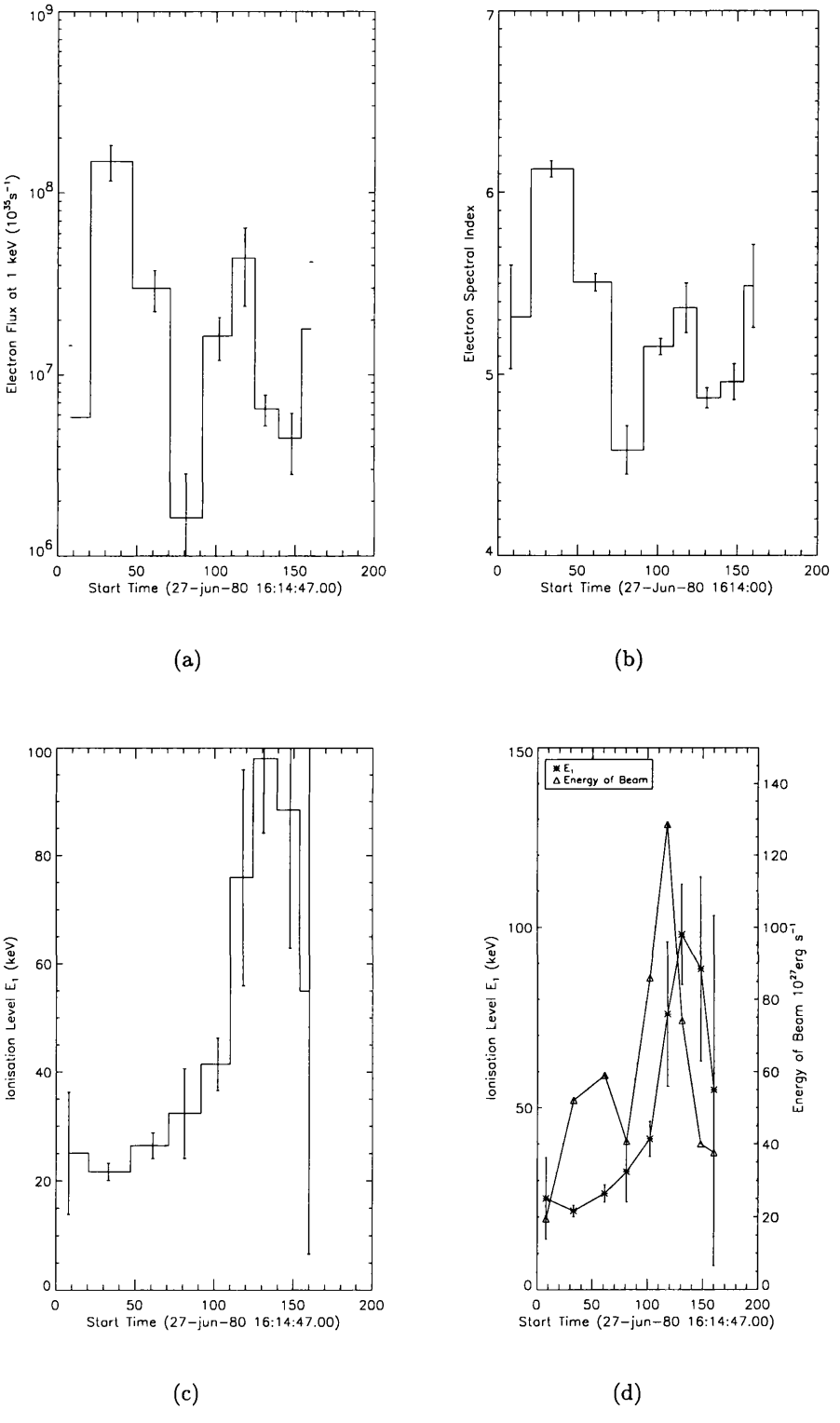

Figure 4.13: Evolution of A, the electron spectral flux constant (a), the spectral index δ (b), the stopping depth E_1 (c) and the energy contained in the electron beam above 20 keV (d).

Time	A	δ	E_1	χ^2
1614:47-1615:04	5.81 e 6	5.31	25.05	1.41
	±8.66 e 6	±0.29	±11.19	
1615:04-1615:36	1.49 e 8	6.13	21.62	2.24
	±3.27 e 7	±0.04	±1.58	
1615:36-1616:00	2.98 e 78 e 5	5.52	26.42	1.49
	±7.61 e 6	±0.05	±2.37	
1616:00-1616:17	1.61 e6	4.598	32.33	1.01
	±1.20 e 6	±0.13	±8.24	
1616:17-1616:41	1.63 e 7	5.15	41.42	0.89
	±4.33 e 6	±0.05	±4.82	
1616:41-1616:50	4.39 e 7	5.373	75.92	1.57
	±2.01 e 7	±0.13	±20.01	
1616:50-1617:07	6.46 e 6	4.87	98.03	3.21
	±1.24 e 6	±0.06	±13.89	
1617:07-1617:23	4.46 e 6	4.95	88.43	1.59
	±1.65 e 6	±0.10	±25.58	
1617:23-1617:31	1.79 e 7	5.48	54.95	0.49
	±2.38 e 7	±0.23	±48.37	

Table 4.3: Best fit parameters for an incomplete Beta function fit to the photon spectra of 27 June 1980 logarithmically binned into 37 data points over 9 time intervals from 1614:47-1617:31 UT.

Although we were unable to quantify a relationship between the spectral break point E_{br} and coronal column density, (without accurate knowledge of the injected electrons spectral index), the overall behaviour of γ_1, γ_2, and E_{br} with E_1 does allow interpretation of the general behaviour of HXR spectra as double power laws. Studies of HXR spectra as double power laws (Dulk et al., 1992, Winglee et al. 1991a,b) determined that the spectral breaks were almost always break down. This indicates that the high coronal column densities required for break up spectra to be observed (for frequently occurring δ of 5-6) are not present. Given also that the distribution of observed E_{br} peaks at $\sim$ 100 keV, then a typical coronal column density assuming this model would be equivalent to $E_1 \sim 50$ keV or $N_1 \sim 4 \times 10^{20}$ cm^{-2}.

The expected change in photon spectral index due to the non-uniform ionisation structure was estimated to be 1. Dulk et al. (1992) though observed this change to be $\sim 1-2$ i.e. the observed breaks are slightly steeper. This discrepancy may be accounted for by spectrometer differences or poor counting statistics in the high energy channels observed.

Alternatively, the modelled change in γ can be increased by increasing the relative efficiency of the chromosphere. The ratio of Coulomb logarithms although approximated to 2.8 may be slightly higher. It is also possible that energy losses rates due to non-Coulomb losses can markedly change across the transition region e.g. if a return current became unstable in the chromosphere. The possibility of this could be investigated by allowing λ to be a free parameter when fitting spectra with the beta function expression.

Chapter 5

YOHKOH HXS Estimates of Coronal Column Density

Dogged Persistence

A man looked out the window every night at 6 to watch the sun set. A large house blocked the way and the sun never set at 6 but that did not deter him. Proud and independent many people admired his dogged persistence for he was not frivolous. His neighbours were unable to renew their large house's insurance policy and became terrified.

Ivor Cutler - Private Habits

5.1 Introduction

In the previous chapters we have extensively discussed the effect non-uniform ionisation of the solar atmosphere has on the thick target bremsstrahlung spectra in flares. In this chapter we model hard X-ray emission observed by *YOHKOH* in terms of a power law electron spectra and step-function nonuniformly ionised atmosphere, derived in Chapter 4 and investigate if the derived column density estimates are viable. In addition we attempt to determine whether the correlation between the model parameters, specifically column density and electron beam energy flux, suggested in Chapter 4 is also present.

5.2 Data Analysis

5.2.1 HXS Spectrometer

The Wide Band Spectrometer (WBS) on board *YOHKOH* has spectroscopic capabilities in a wide energy band from soft X-rays to γ-rays. It consists of a soft X-ray spectrometer (SXS), hard X-ray spectrometer (HXS), γ-ray spectrometer (GRS) and radiation belt monitor (RBM). Of these, SXS, HXS, and GRS are used for solar flare observations, while RBM serves as an alarm for radiation belt passage.

The hard X-ray spectrometer consists of a NaI(Tl) scintillation detector optically coupled to a photomultiplier tube. The detector is 7.6 cm in diameter and 2.5 cm in thickness. This arrangement is covered with two kinds of stainless steel absorbers of 13.8 $cm^2 \times 0.08$ mm thickness and 31.8 $cm^2 \times 1$ mm thickness to suppress low energy X-ray counts.

The spectrometer covered the photon energy range from 20-657 keV from 1st. October 1991 to 9th June 1992. After this time the HXS amplification gain was changed and as a result the energy range now covers 24-830 keV. The energy resolution is $\sim$ 26% at 22 keV and $\sim$ 13% at 88 keV. Inflight energy calibration is achieved by detection of the 60 keV line emitted by an Am-241 radioactive source. In addition, the 191 keV line emitted by radioactive I-123 and the 511 keV line emitted by positron annihilation are used for inflight energy calibration.

The output of the detector is given as two pulse counts (PC1 and PC2) or a 32-channel pulse height spectrum. PC1 is over the range 20-65 keV or 20-75keV for the time intervals before and after the amplification gain change. Similarly the range for PC2 is 65-657keV or 75-830 keV respectively. These counts are produced every 0.125s (1s) in high (medium) bit rate mode. The 32-channel pulse height spectrum is produced every 1s (8s) in high (medium) bit rate mode. From the observed 32-channel energy loss spectrum, the incident X-ray spectrum can be deconvolved using the HXS response matrix. The response of the detector having been determined for 60 and 260 incident energy values over the detector energy range for both settings of the amplification gain.

5.2.2 Fitting Procedure For Non-uniformly Ionised Model

The procedure implemented to model the observed HXS hard X-ray count rates as due to thick target emission from a power law electron spectrum through a non-uniformly (step-function) ionised atmosphere follows the Levenberg-Marquardt method (Press et al., 1995). The model photon flux depends on three parameters : electron flux constant A, electron spectral index δ and column density from injection region to transition region. This column density being expressed as the injected energy of an electron which is stopped at the transition region E_1. The photon flux for this model is

$$J(\epsilon) = \frac{Ac}{(\lambda+1)(\delta-1)\epsilon}\left[\frac{\epsilon^{2-\delta}}{\delta-2} + \nu E_1^{2-\delta} I_b\left(\frac{\epsilon^2}{\epsilon^2+E_1^2}, \frac{1}{2}, \frac{\delta-2}{2}\right)\right] \tag{5.1}$$

where c is

$$c = \frac{Q_o}{4\pi R^2 K}$$

The model count rates are obtained by determining the photon flux at the 260 energy points the HXS response matrix is calibrated for, and then folding these fluxes through the response matrix. The χ^2 between the observed and model count rates is minimised to determine the best fit parameters for a nonuniformly ionised model.

As χ^2 i.e.

$$\chi^2(\mathbf{a}) = \sum_{i=1}^{N}\left[\frac{y_i - y(x_i;\mathbf{a})}{\sigma_i}\right]^2 \tag{5.2}$$

where N is the number of data points, y is the observed count rates and x the channel numbers varies nonlinearly with the M parameters, the minimization of χ^2 has to be achieved iteratively. The gradient of χ^2 with respect to the parameters $\mathbf{a}$ has components

$$\frac{\partial\chi^2}{\partial a_k} = -2\sum_{i=1}^{N}\frac{[y_i - y(x_i;\mathbf{a})]}{\sigma_i^2}\frac{\partial y(x_i;\mathbf{a})}{\partial a_k} \qquad k = 1, 2, \ldots M. \tag{5.3}$$

Taking an additional derivative gives the Hessian or curvature matrix

$$\frac{\partial^2\chi^2}{\partial a_k \partial a_l} = 2\sum_{i=1}^{N}\frac{1}{\sigma_1^2}\left[\frac{\partial y(x_i;\mathbf{a})}{\partial a_k}\frac{\partial y(x_i;\mathbf{a})}{\partial a_l} - [y_i - y(x_i;\mathbf{a})]\frac{\partial^2 y(x_i;\mathbf{a})}{\partial a_l \partial a_k}\right]. \tag{5.4}$$

If the parameters are sufficiently close to the minimum in χ^2 then the change from current parameters $\mathbf{a}$ to the minimizing one can be found by solving the set of linear equations

$$\sum_{l=1}^{M}\alpha_{kl}\partial a_l = \beta_k. \tag{5.5}$$

However if the parameters are far from the minimum then a more steep change in parameters is required i.e.

$$\partial a_l = \text{constant}_{\ l} \tag{5.6}$$

where

$$\beta_k \equiv -\frac{1}{2}\frac{\partial \chi^2}{\partial a_k} \quad \alpha_{kl} \equiv \frac{1}{2}\frac{\partial^2 \chi^2}{\partial a_k \partial a_l}.$$

The Hessian matrix includes the first and second derivatives of the model function with respect to their parameters. Inclusion of the second derivative term can destabilise the fit, therefore α is defined as

$$\sum_{i=1}^{N} \frac{1}{\sigma_i^2}\left[\frac{\partial y(x_i, \mathbf{a})}{\partial a_k}\frac{\partial y(x_i, \mathbf{a})}{\partial a_l}\right] \tag{5.7}$$

This change in the definition of α has no effect on the the final set of estimated parameters $\mathbf{a}$, as the condition for χ^2 to be minimised ($\beta_k = 0$ for all k) is independent of how α is defined. This change only alters the iterative route to the final estimate.

The Levenberg-Marquardt method is an iterative procedure which varies smoothly between applying the inverse-Hessian or steepest decent method in determining the suitable changes in $\mathbf{a}$, dependent on if a minimum is approached. By defining the matrix α' by

$$\alpha'_{jj} \equiv \alpha_{jj}(1 + \lambda) \alpha'_{jk} \equiv \alpha_{jk}$$

then both these methods are expressed by solving the set of linear equations

$$\sum_{l=1}^{M} \alpha'_{kl}\, \partial a_l = \beta_k. \tag{5.8}$$

When λ is very large, the matrix α' is forced top be diagonally dominant, so the steepest decent approach is adopted. On the other hand, as λ approaches zero, then the inverse Hessian method is in effect being implemented.

Thus given an initial guess for the set of fitted parameter $\mathbf{a}$, the Levenberg-Marquardt method is as follows :

- Determine $\chi^2(\mathbf{a})$.
- Pick a modest value of λ, e.g. $\lambda = 0.001$.
- † Solve the linear equations 5.8 for $\partial \mathbf{a}$ and evaluate $\chi^2(\mathbf{a} + \partial \mathbf{a})$.
- If $\chi^2(\mathbf{a} + \partial \mathbf{a}) \geq \chi^2(\mathbf{a})$,then increase λ by a factor (~ 10) then go back to step †
- If $\chi^2(\mathbf{a} + \partial \mathbf{a}) < \chi^2(\mathbf{a})$, then decrease λ by a factor (~ 10) then go back to step †.

These steps are repeated until χ^2 decreases by a negligible amount $\sim 10^{-3}$ of χ^2. For this minimum determined χ^2 and best fit parameters **a**, the covariance matrix

$$[C] \equiv [\alpha]^{-1} = \sum_{i=1}^{N} \frac{1}{\sigma_i^2} \left[\frac{\partial y(x_i, \mathbf{a})}{\partial a_k} \frac{\partial y(x_i, \mathbf{a})}{\partial a_l} \right] \tag{5.9}$$

is determined. The covariance matrix being the estimated standard errors in the fitted parameters **a**.

The final estimated parameters can depend strongly on the initial parameters used. Only local minima in χ^2 are determined not the global minimum. In an effort to be assured that each estimate of **a** is for a global minimum in χ^2 for each spectra the best fit parameters are determined for 5 different sets of initial conditions. The first two sets are derived from the double power law best fit parameters of the spectra. The third set uses previous best fit parameters, while the fourth and fifth are kept constant. The parameters with the minimum χ^2 from the sets is then taken as the global minimum.

The goodness-of-fit for the estimated model parameters is defined as

$$\Gamma\left(\frac{N-2}{2}, \frac{\chi^2}{2}\right)$$

Values of $\Gamma(\nu, \chi^2)$ greater than 0.001 are taken as indicating the the model as acceptable.

Correlation Analysis

Correlations of how the model parameters evolved during the course of the flare with respect to each other were determined. This included correlations for both the number flux of beam electrons and the energy flux contained in the beam. For these estimates a cut-off in the electron spectrum of 20 keV was assumed. To determine any correlations between the flare parameters Spearman's rank correlation of the two populations is determined i.e

$$r_s = \frac{\sum_{i=0}^{N-1}(Rx_i - \bar{Rx})(Ry_i - \bar{Ry})}{\sqrt{\sum_{i=0}^{N-1}(Rx_i - \bar{Rx})^2}\sqrt{\sum_{i=0}^{N-1}(Ry_i - \bar{Ry})^2}} \tag{5.10}$$

where Rx and Ry are the magnitude-based ranks among the populations X and Y respectively and where elements of identical magnitude are ranked using a rank equal to the mean of the ranks that would otherwise be assigned. The significance of a non-zero value of r_s is tested by

$$t = r_s \sqrt{\frac{N-2}{1-r_s^2}}.$$

In the following analysis only model parameters from fits with $\Gamma(\nu, \chi^2)$ greater than 0.001 are correlated.

5.3 15th November 1991 Flare

5.3.1 Description of Flare

The flare on the 15th of November was an intense X-ray event of GOES class X1.5 and H_α significance 2B. Located in active region 6919 (S14 W19) the flare commenced at 22:34 UT. With flare mode on *YOHKOH* being triggered at 22:34:38-22:44:37 UT, the entire event was observed by *YOHKOH* as well as in H_α, Ca_{II} K-line (Canfield et al., 1992, Wülser et al., 1994) and radio frequencies (80, 35, 17, 9.4 and 3.75 GHz) from Nobeyama and Toyokawa. The HXT observations have been extensively studied by Sakao (1994). The flare signatures also includes white light emission (Hudson et al., 1992) and significant line and continuum γ-ray emission (Yoshimori et al., 1992). In addition this event was also observed by the hard X-ray spectrometers aboard Ulysses, PVO and GRO allowing for stereoscopic analyses to be made (McTiernan et al., 1994).

As shown in Figure 5.1 and Figure 5.2, the hard X-ray event can be divided into three phases. (a) a precursor phase (22:34 -22:37 UT), (b) the main intense impulsive phase (22:37 - 22:38 UT) and (c) a post-impulsive decay phase (22:38 - 22:41 UT). The precursor phase has three small peaks rising to 2-3 time the background count rate (HXS). Spatially during this phase the HXR sources were found (Sakao et al., 1992) to extend to an area greater than 1', larger than during the impulsive phase, while BCS data indicated plasma upflows of $\sim 250\,\mathrm{km\,s^{-1}}$, (Culhane et al., 1993). In all the precursor phase signals that electron precipitation is occurring in large-scale magnetic loops other than the compact loops in which the impulsive bursts took place.

The impulsive burst comprised of three separate peaks. Detected by HXS these peaks rise to $\sim 1.2 \times 10^4$, 2.3×10^4 and 2.6×10^4 counts s^{-1}, with FWHM width of 16, 10 and 14 seconds. It should therefore be noted that peaks 2 and 3 are above the level (21000 counts s^{-1}) where dead time correction is considered reliable and some spectral distortion may occur over these time intervals. The spectral evolution of each peak demonstrates the common soft-hard-soft pattern (cf Figure 5.7). Spatially, in the the M2 band the source evolves from a single compact structure at the time of first peak, to two distinct sources which drift apart for the remainder of the flare (Figures 5.3, 5.4). While the H band displays the same spatial characteristics, the M1 band structure differs significantly between peaks. Here although M2 images display a double source, M1 images display only

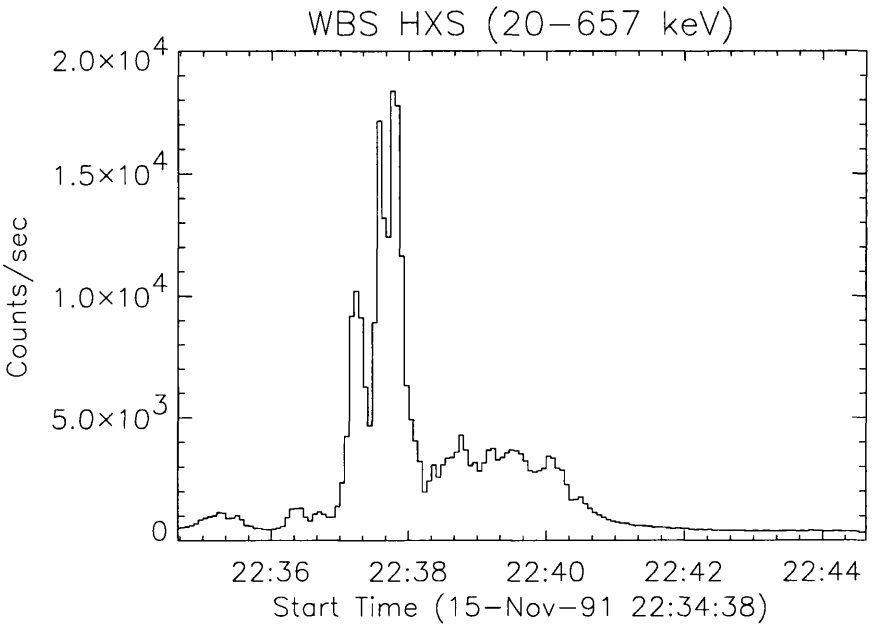

(a)

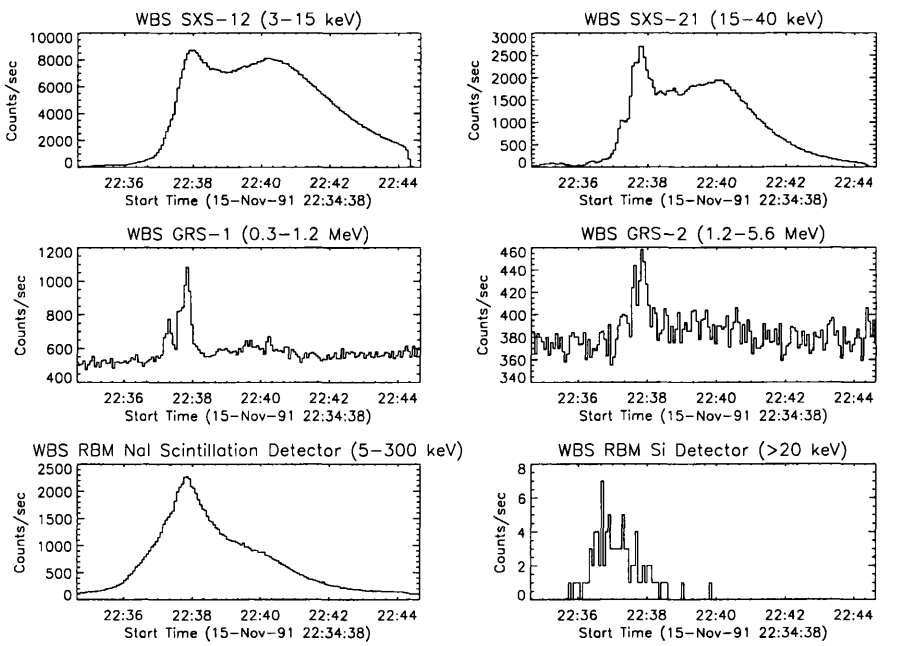

(b)

Figure 5.1: (a) Time profile of the total hard X-rays count rates measured by the hard X-ray spectrometer (HXS) onboard *YOHKOH* over the flare mode observing period of the class X1.5 flare on 15th November 1991 at 22:34 UT. (b) Similar light curves for the remaining WBS instruments.

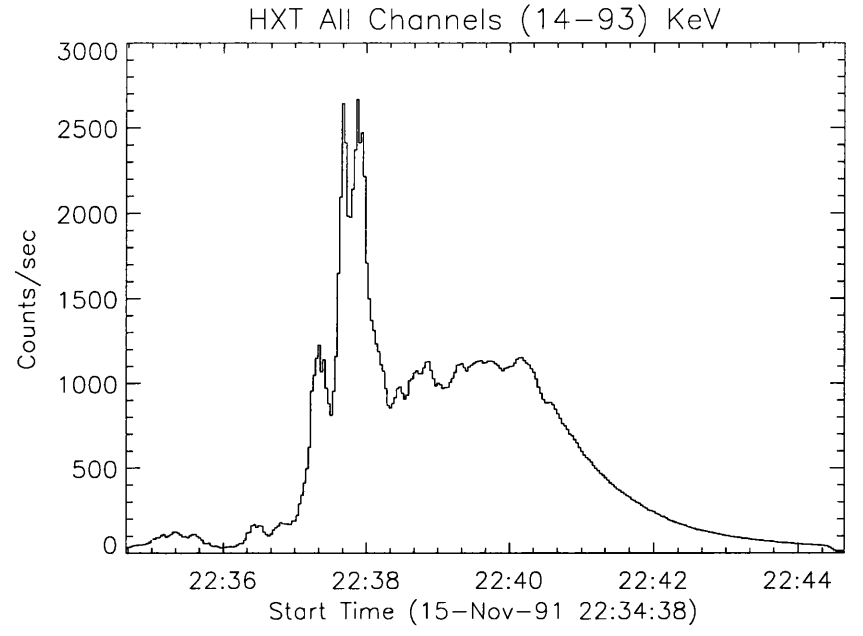

(a)

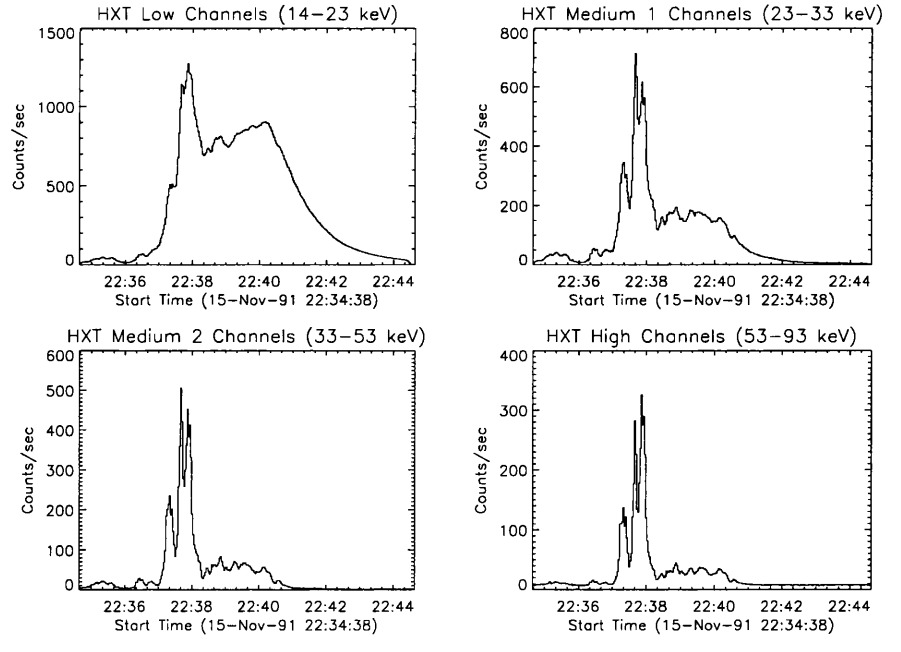

(b)

Figure 5.2: (a) Total light curve of all HXT channels and (b) individual light curves for the 4 HXT channels during the 15th of November 1991 event.

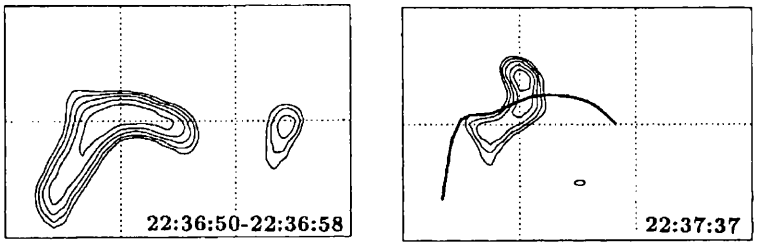

(a) (b)

Figure 5.3: Hard X-ray images for (a) during precursor phase (L channel) and (b) impulsive phase (M1 channel) clearly illustrating the greater spatial extent of the precursor hard X-ray sources compared to the impulsive phase sources. Line represents the magnetic neutral line derived from MSO magnetograms (Sakao *et al.*, 1992).

a single structure. This energy dependent structure behaviour may signify preferential trapping of lower energy electrons.

In the later stages of the flare (after 22:40:30), the hard X-ray time profile gradually decays indicating no additional particle acceleration. Proceeding this (22:38-22:40), while HXR counts have fallen significantly from impulsive phase levels, there is still evidence of continuing particle acceleration. In particular relatively intense microwave emission at 17 GHz is observed. However, as can be seen in Figure 5.2, compared to the peak count rate, the relative reduction to post-impulsive levels in band L is considerably smaller than in bands M1, M2 and H. Emphasising this point, the post-impulsive SXS (3-15 keV) count rates, shown in Figure 5.1, is of approximately the same magnitude as the impulsive phase. The spectral index derived from the ratio of adjacent HXT energy channels M2/M1 is $\sim$ 2.5 softer than that derived from H/M2. This would seem to indicate that the post-impulsive phase has a significant HXR contribution from hot thermal plasma estimated as exceeding 30MK (Sakao, 1994).

The results of the spectral fitting for the impulsive, precursor and post-impulsive phase of the 15th November flare are shown in Figures 5.7-5.9 (Impulsive), Figures 5.16-5.18 (Precursor) and Figures 5.25-5.27 (Post-Impulsive). They show a general soft-hard-soft spectral evolution over the impulsive and precursor phase. The coronal column density for the estimated E_1 values are shown in Figure ?? with the column density of the soft X-ray loop indicated as well. The soft X-ray loop column density is derived from emission

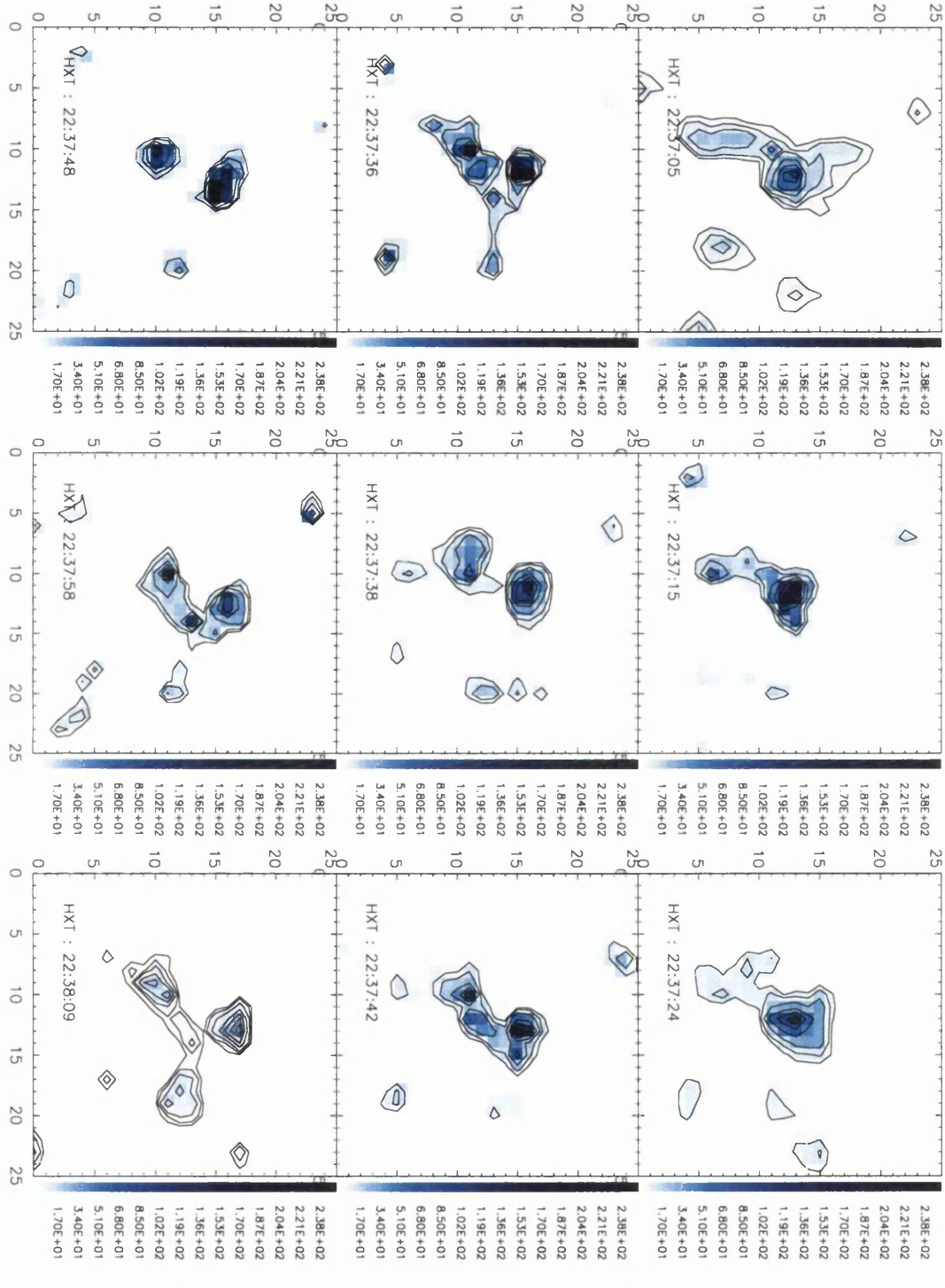

Figure 5.4: Selected M2 band reconstructed images of the 15th November event from 22:37:05 UT to 22:38:07UT. Each image, based on 200 cts/SC, shows a compact double footpoint source separating as the flare evolves. Overlaid are the contours at 0.25, 0.5 and 0.75 levels.

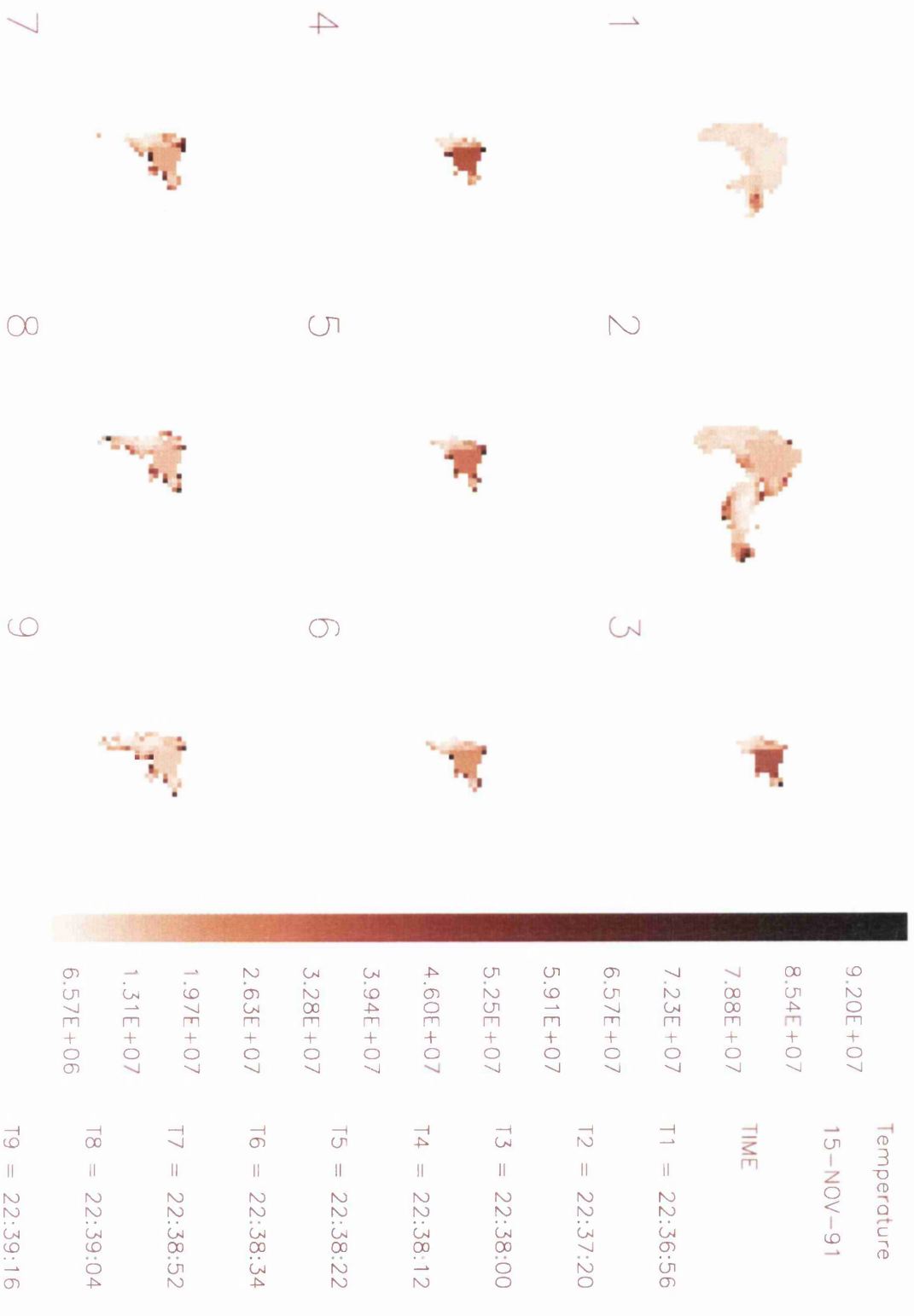

Figure 5.5: Maps of SXT derived temperature structure for 15 November 1991 flare, using filters Be119 and Al12.

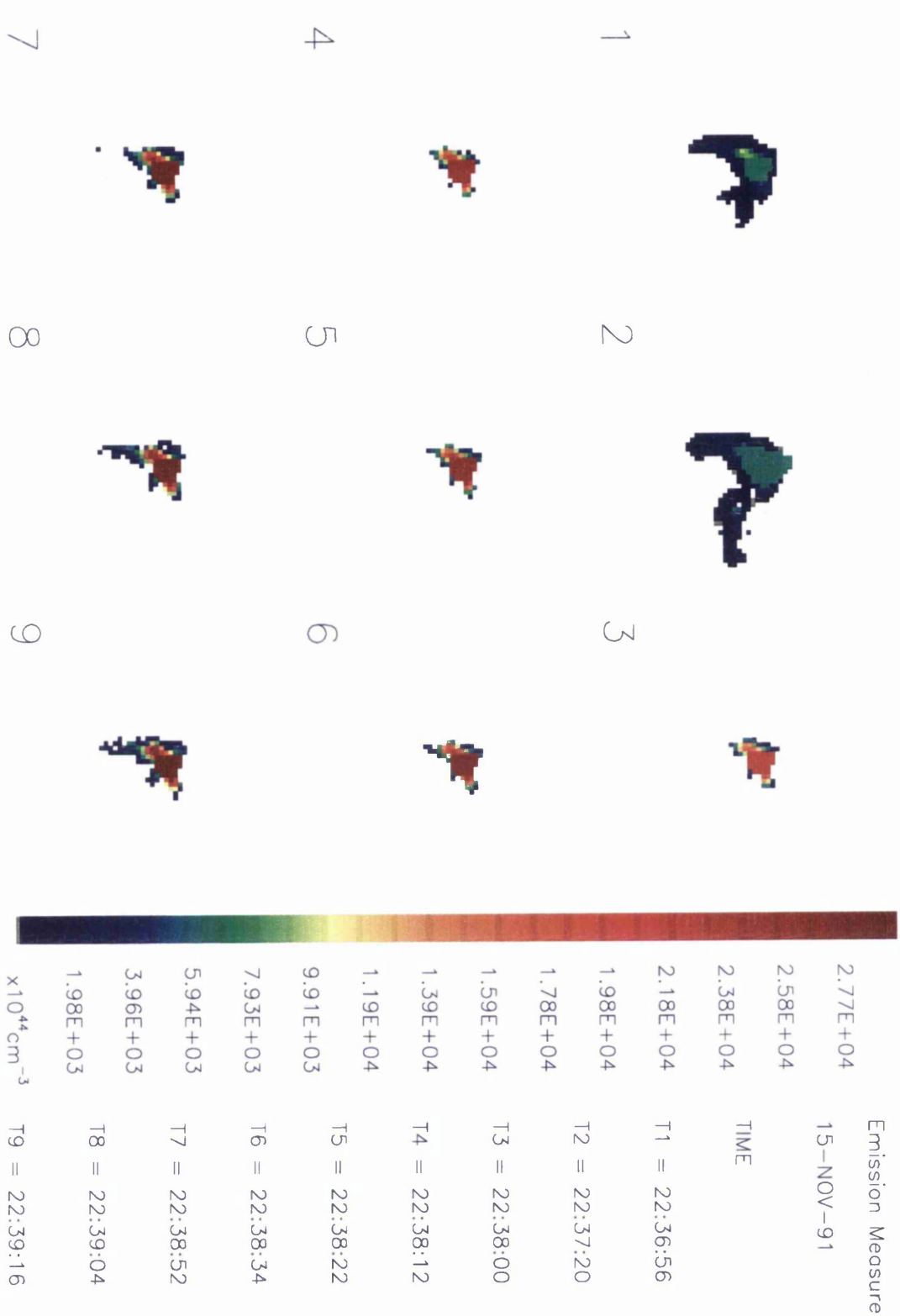

Figure 5.6: Equivalent maps of SXT emission measures estimated from temperature structure derived in Figure 5.5.

measure estimates using the Be and thin aluminium filter, with an assumed constant volume of 5.9×10^{26} cm^{-3} and loop length of 1×10^{9} cm. These two estimates correspond well given the uncertainty incorporated in each method. The hard X-ray density estimated from time-of-flight loop lengths and electron trapping timescale estimates of density, give coronal column density of $\approx 3.8 \pm 0.9 \times 10^{20}$ cm^{-2}. These equate to E_1 values of 51.7 ± 4.2 keV.

The correlations between model parameters are shown below.

Impulsive Phase

	Correlation Co-efficient	Significance
Electron Flux A and E_1	0.245	0.183
Spectral Index δ and E_1	-0.045	0.81
Electron Number Flux and E_1	0.830	4.5×10^{-4}
Electron Energy Flux and E_1	0.857	1.8×10^{-4}
Energy Flux and Count Rates	0.395	0.18

Precursor Phase

	Correlation Co-efficient	Significance
Electron Flux A and E_1	-0.30	0.623
Spectral Index δ and E_1	-0.30	0.623
Electron Number Flux and E_1	0.70	0.19
Electron Energy Flux and E_1	0.7	0.19
Energy Flux and Count Rates	-0.10	0.87

Post-Impulsive Phase

	Correlation Co-efficient	Significance
Electron Flux A and E_1	0.45	0.065
Spectral Index δ and E_1	0.34	0.18
Electron Number Flux and E_1	0.624	7.30×10^{-3}
Electron Energy Flux and E_1	0.629	6.72×10^{-3}
Energy Flux and Count Rates	0.585	0.013

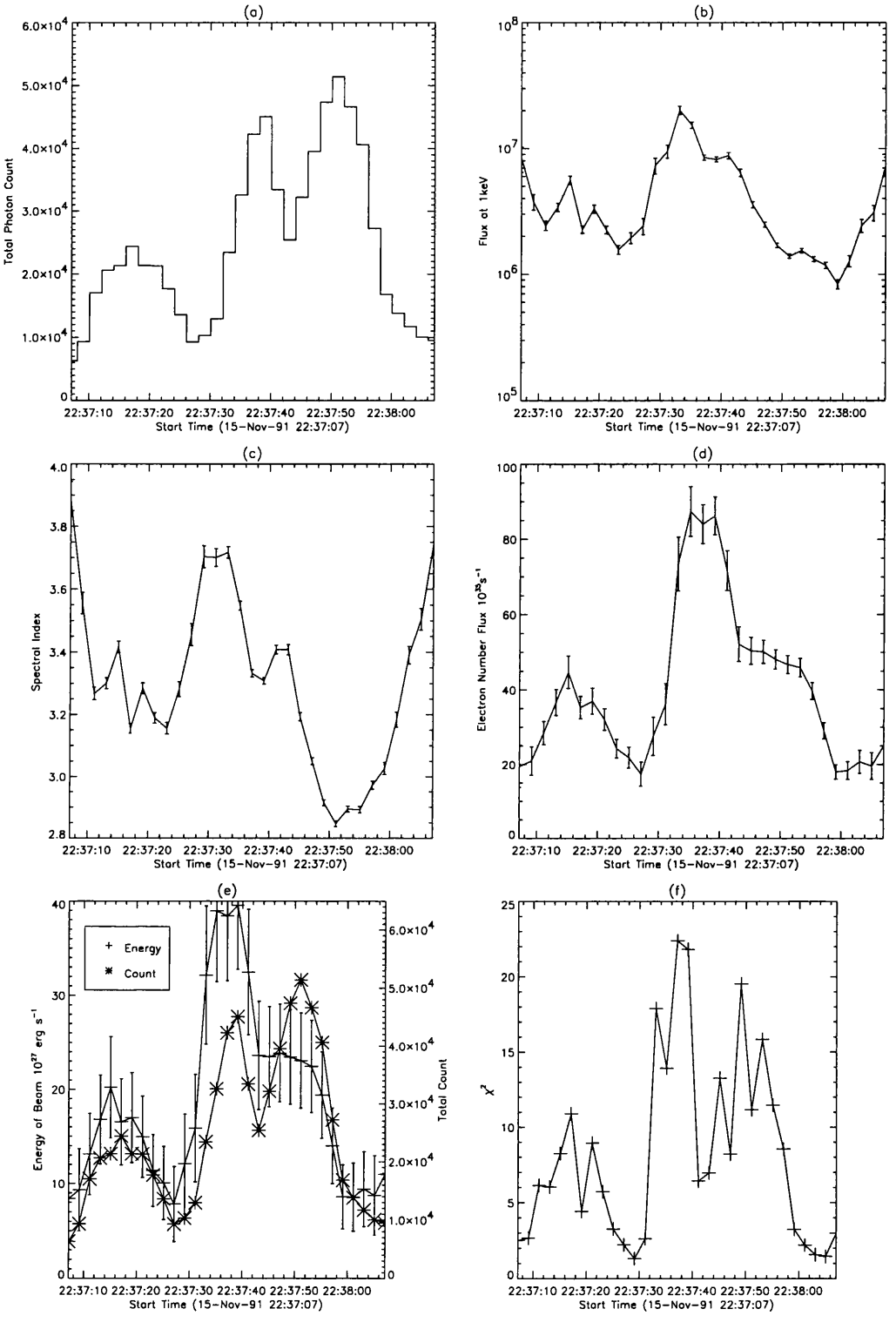

Figure 5.7: Evolution of single power law spectral fit parameters during the main impulsive phase of the 15-Nov-91 flare between 22:37:07-22:38:07. (a) is the total HXS-PH counts for each 2 s interval, (b) and (c) are the power law parameters i.e. the photon flux $\mathrm{keV}^{-1}\mathrm{s}^{-1}$ at 1 keV and photon spectral index. (d) and (e) indicates the inferred electron beam number flux and energy flux assuming an ionised atmosphere and an electron low energy cut-off at 20 keV. Finally (f) shows the reduced χ^2 for each spectral fit.

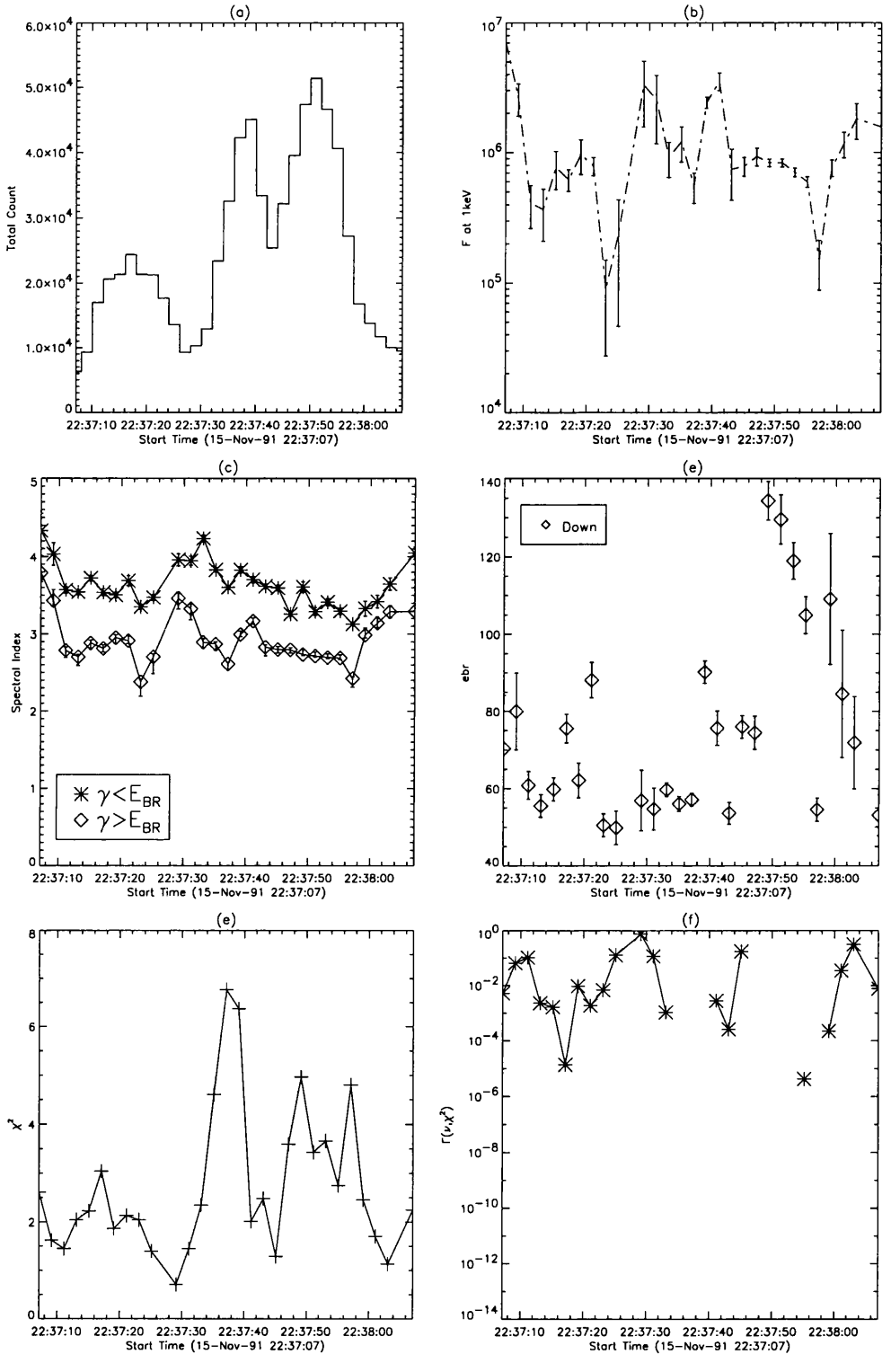

Figure 5.8: Evolution of double power law spectral fit parameters during the main impulsive phase of the 15-Nov-91 flare between 22:37:07-22:38:07. (a) is the total HXS-PH counts for each 2 s interval, (b) and (c) (d) and (e) are the power law parameters i.e. the photon flux $keV^{-1}s^{-1}$ at 1keV and photon spectral indices below and above the break point and the break point. Finally (f) shows the reduced χ^2 for each spectral fit and (g) the indicator of goodness-of fit for that χ^2.

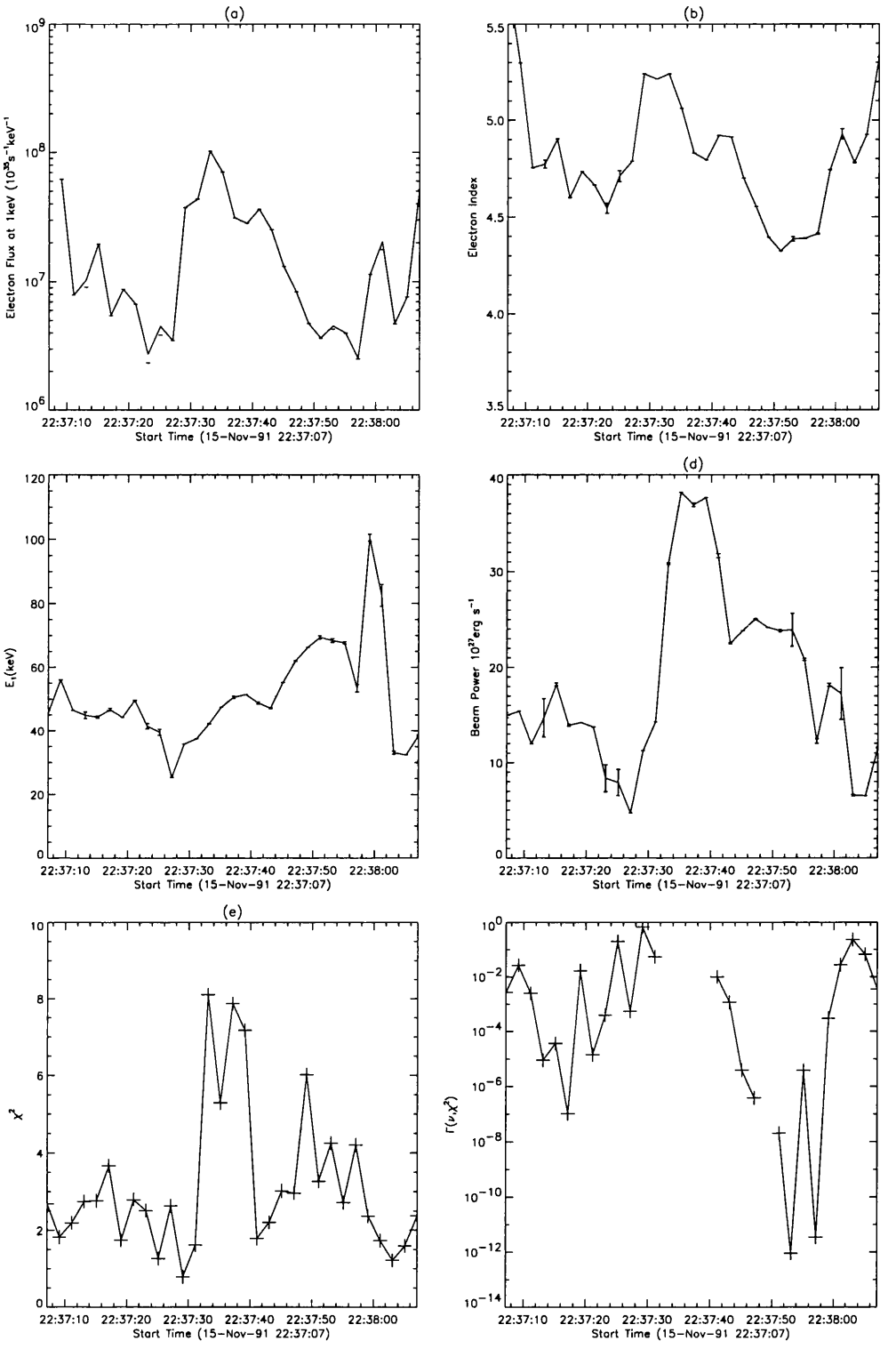

Figure 5.9: Evolution of spectral fit parameters for nonuniformly ionised atmosphere model during the main impulsive phase of the 15-Nov-91 flare between 22:37:07-22:38:07. (a) the electron flux keV^{-1}s^{-1} at 1 keV, (b) the electron spectral index and (c) the electron stopping energy of the transition region. (d) shows the estimate of electron beam energy flux for such parameters with cut-off energy at 20 keV. Finally (f) shows the reduced χ^2 for each spectral fit and (g) the indicator of goodness-of fit for that χ^2.

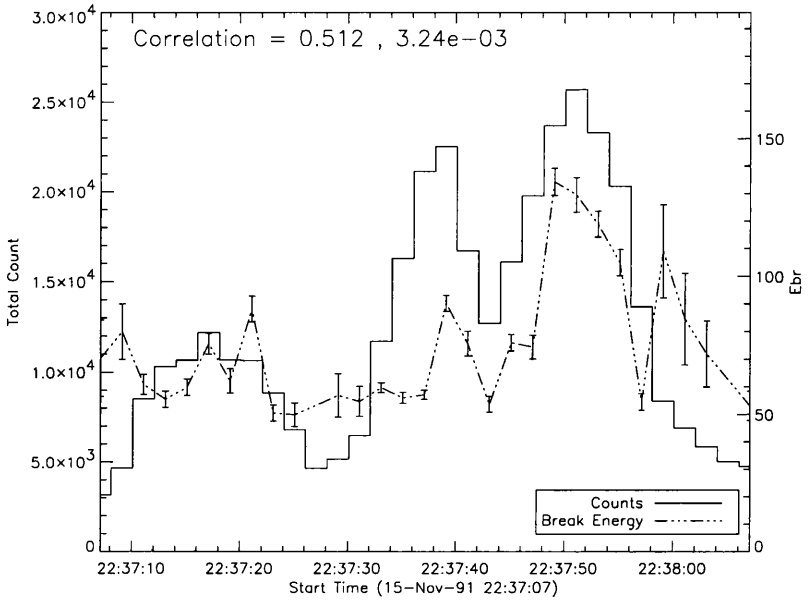

Figure 5.10: Comparison of evolution of observed count rates with the break energy of a double power law for the main impulsive phase of the 15-Nov-91 flare. The rank correlation for these parameters is also indicated.

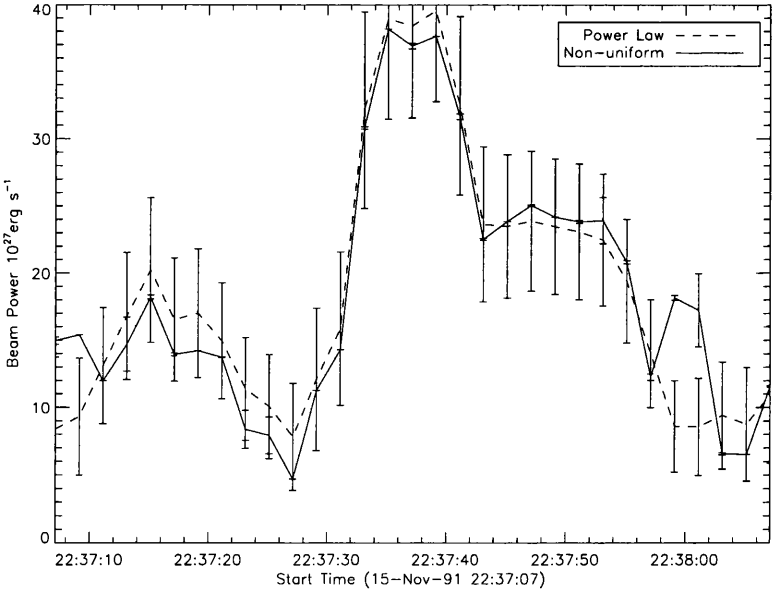

Figure 5.11: Comparison of beam flux for a nonuniform model and from the power law fit assuming an ionised atmosphere, for the main impulsive phase of the 15-Nov-91 flare.

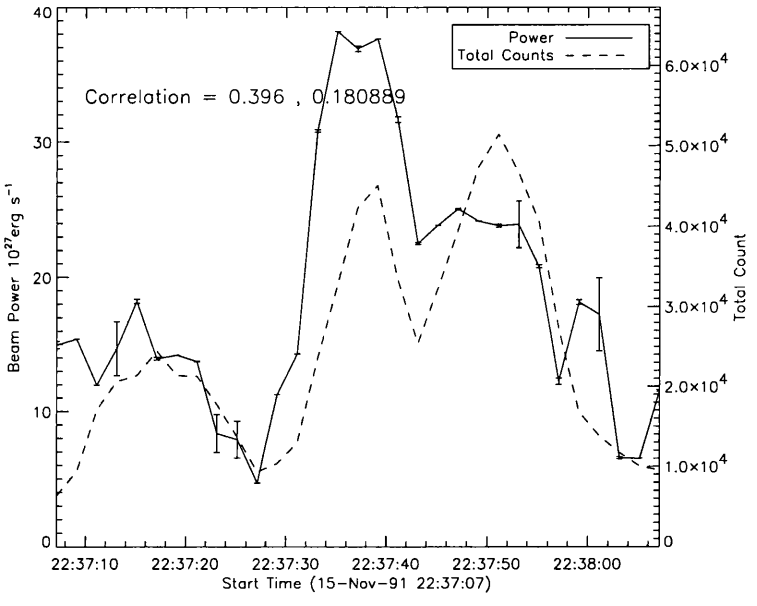

Figure 5.12: Comparison of evolution of nonuniform model electron beam energy flux with the total counts for each time interval, for the main impulsive phase of the 15-Nov-91 flare. The rank correlation for these parameters is also indicated.

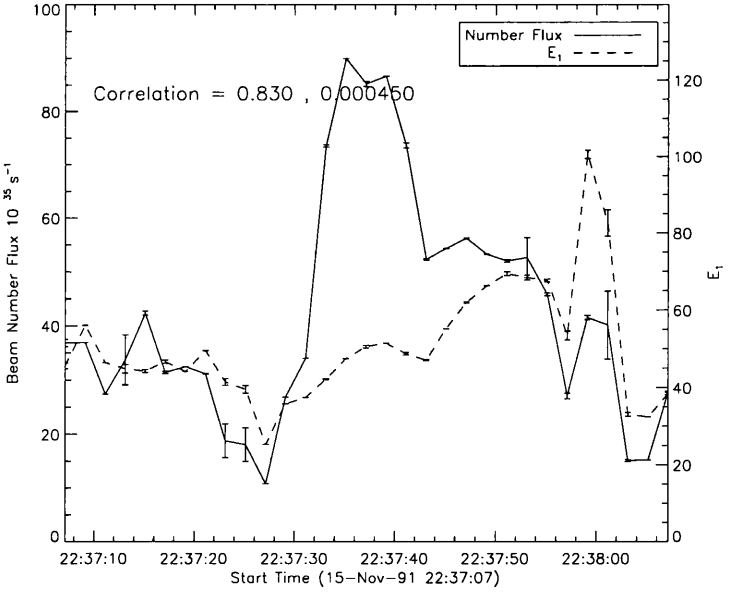

Figure 5.13: Comparison of evolution of nonuniform model electron beam number flux with the stopping energy of an electron which just reaches the chromosphere (E_1), for the main impulsive phase of the 15-Nov-91 flare. The rank correlation for these parameters is also indicated.

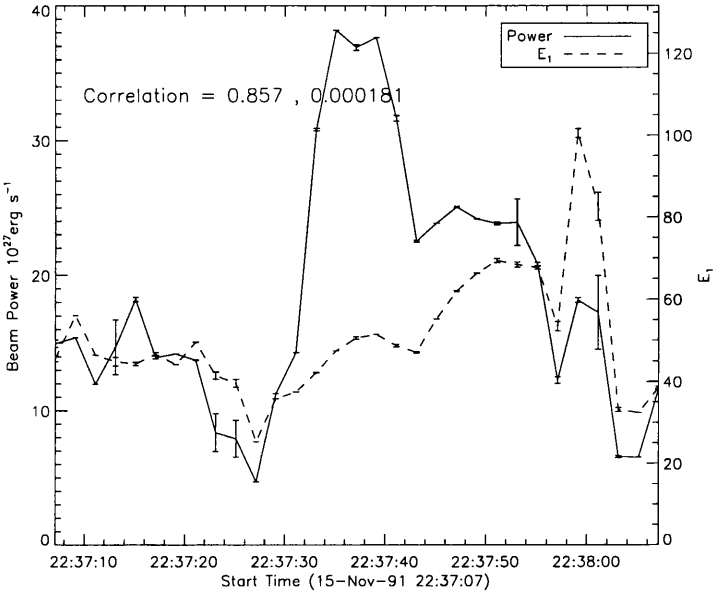

Figure 5.14: Comparison of evolution of nonuniform model electron beam energy flux with the stopping energy of an electron which just reaches the chromosphere (E_1), for the main impulsive phase of the 15-Nov-91 flare. The rank correlation for these parameters is also indicated.

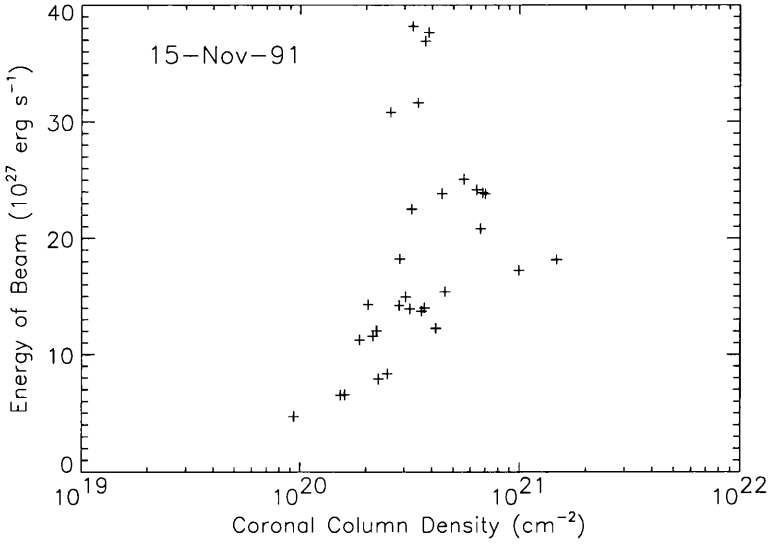

Figure 5.15: Correlation of electron beam flux and coronal column density determined from E_1, for the main impulsive phase of the 15-Nov-91 flare.

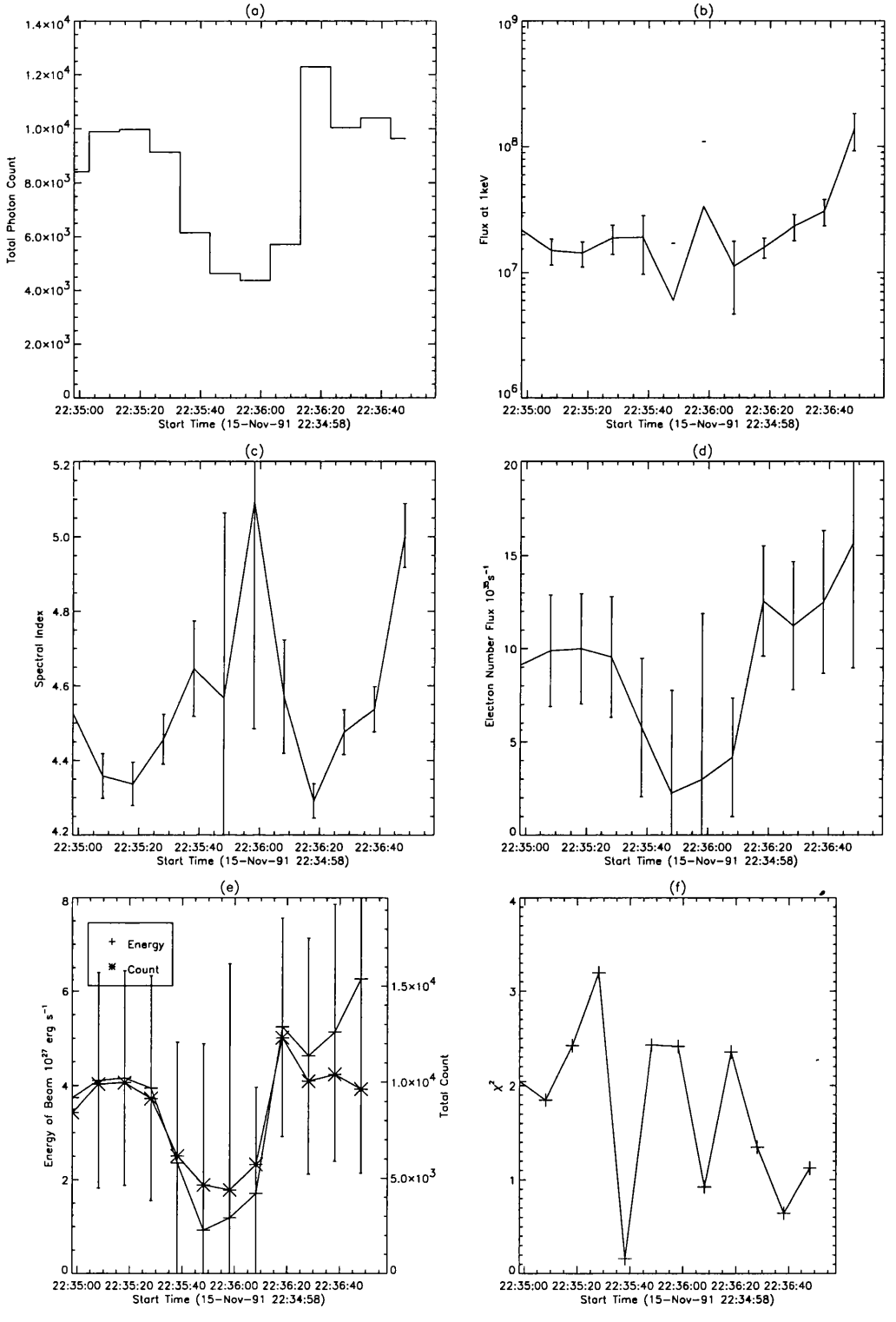

Figure 5.16: Same as in Figure 5.7 for the precursor phase of the 15-Nov-91 flare between 22:34:48-22:36:48.

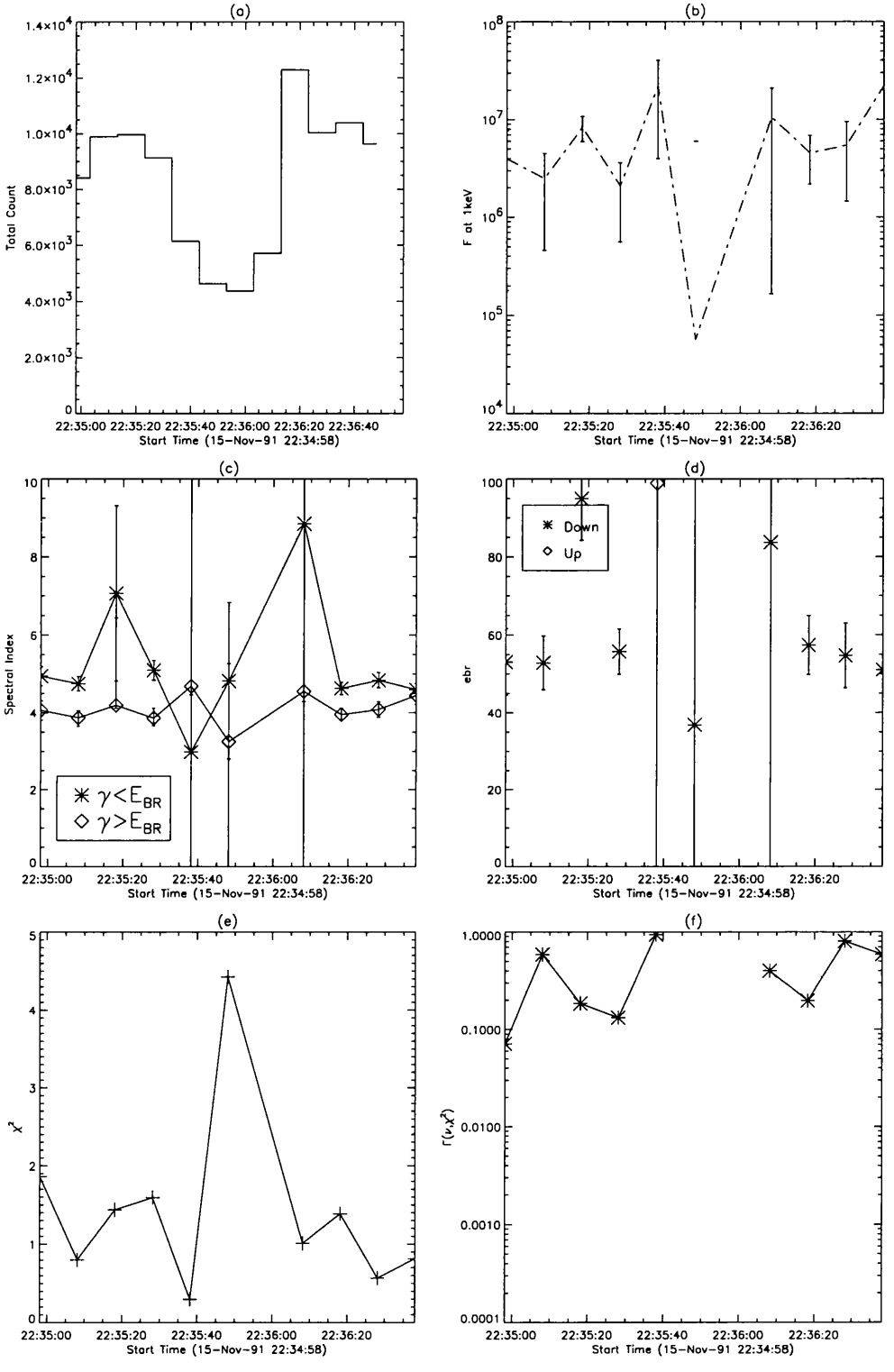

Figure 5.17: Same as in Figure 5.8 for the precursor phase of the 15-Nov-91 flare between 22:34:48-22:36:48.

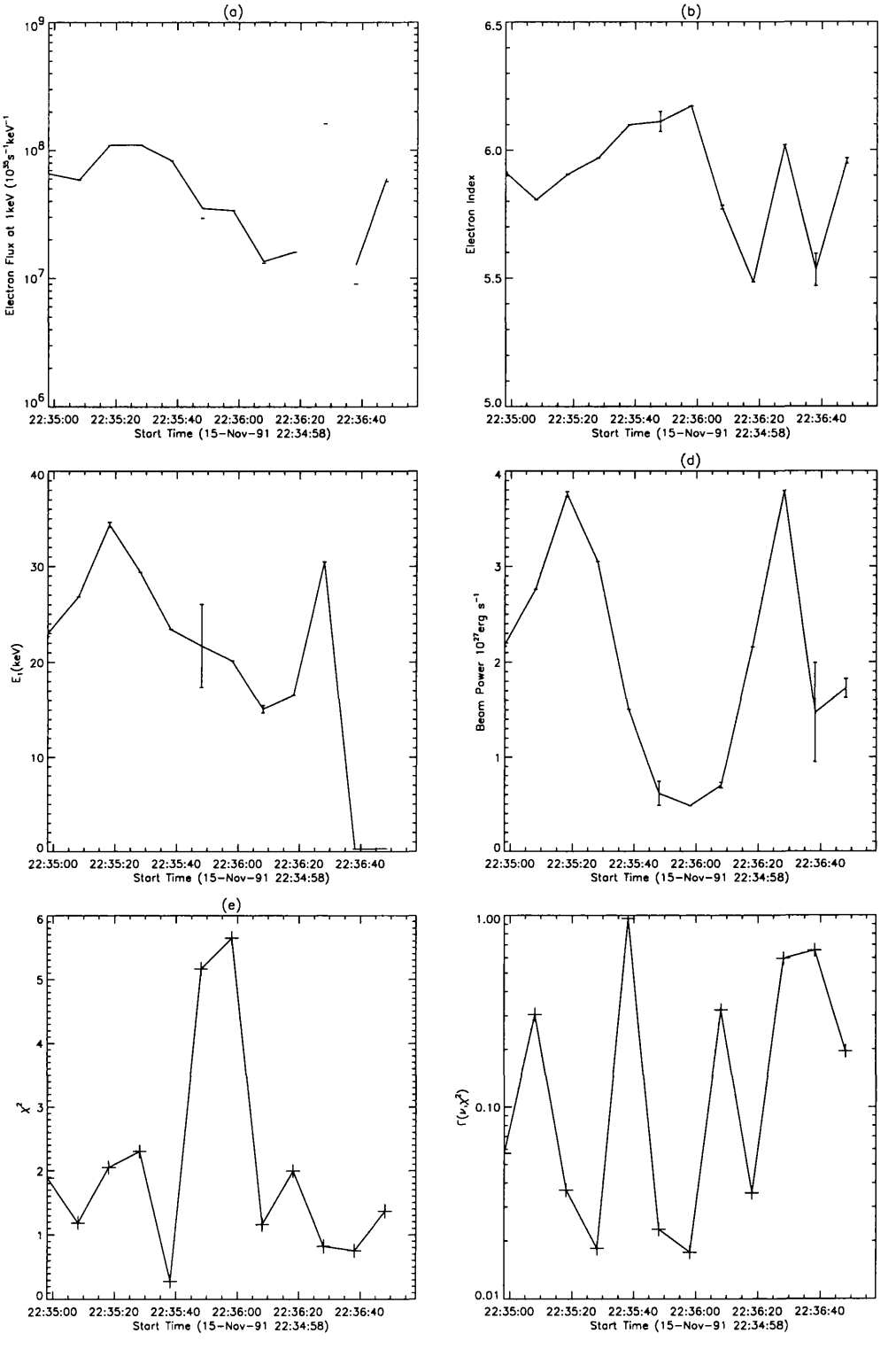

Figure 5.18: Same as in Figure 5.9 for the precursor phase of the 15-Nov-91 flare between 22:34:48-22:36:48.

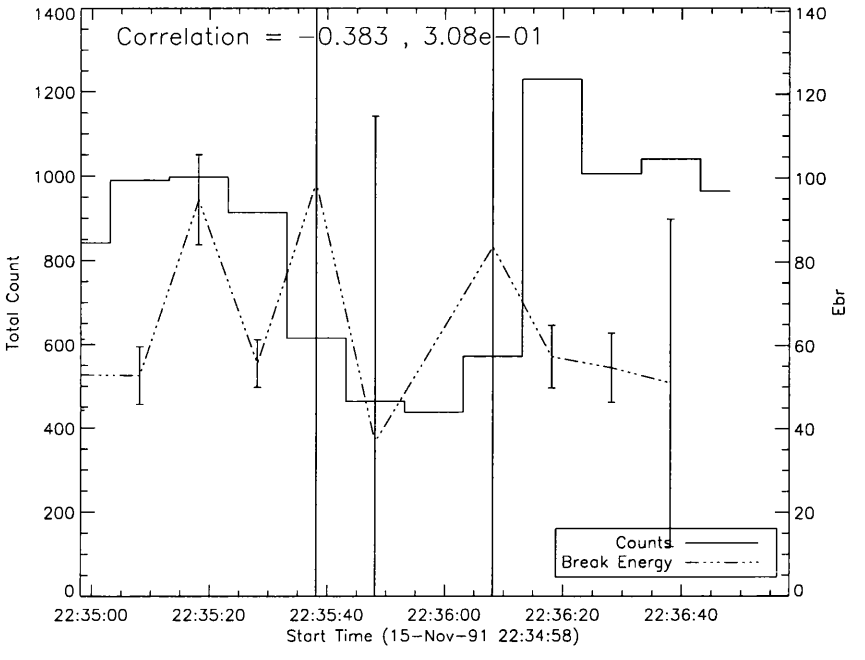

Figure 5.19: Same as in Figure 5.10 for the precursor phase of the 15-Nov-91 flare between 22:34:48-22:36:48.

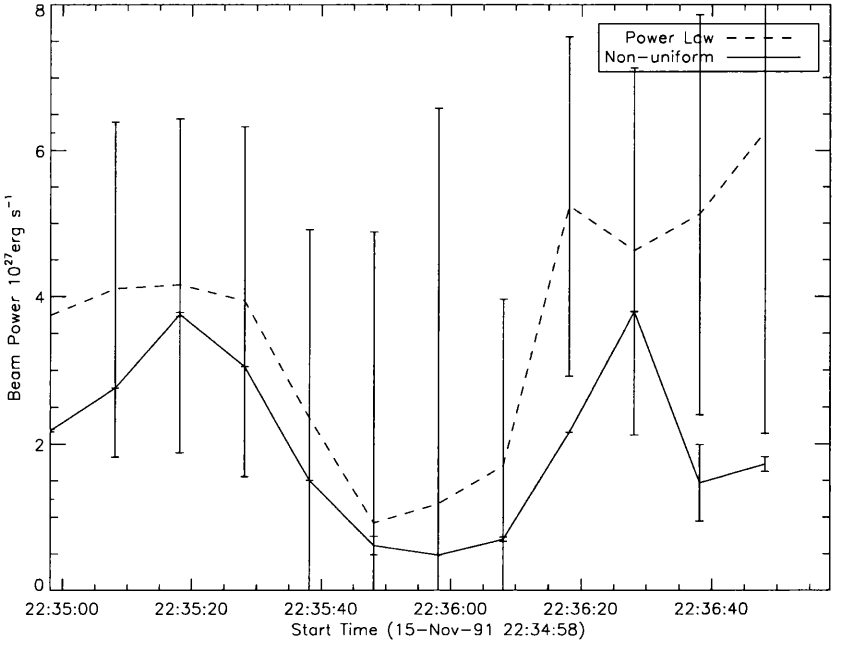

Figure 5.20: Same as in Figure 5.11 for the precursor phase of the 15-Nov-91 flare between 22:34:48-22:36:48.

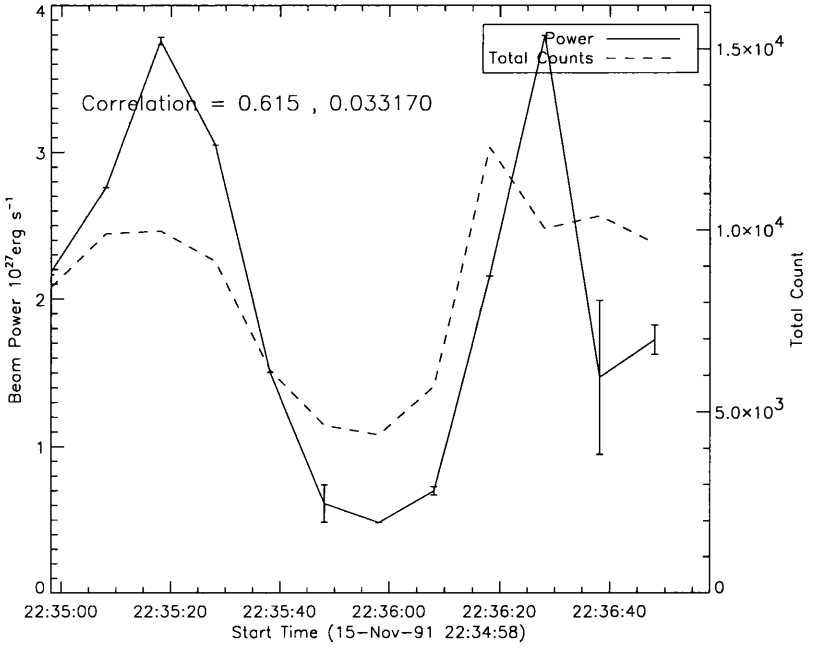

Figure 5.21: Same as in Figure 5.12 for the precursor phase of the 15-Nov-91 flare between 22:34:48-22:36:48.

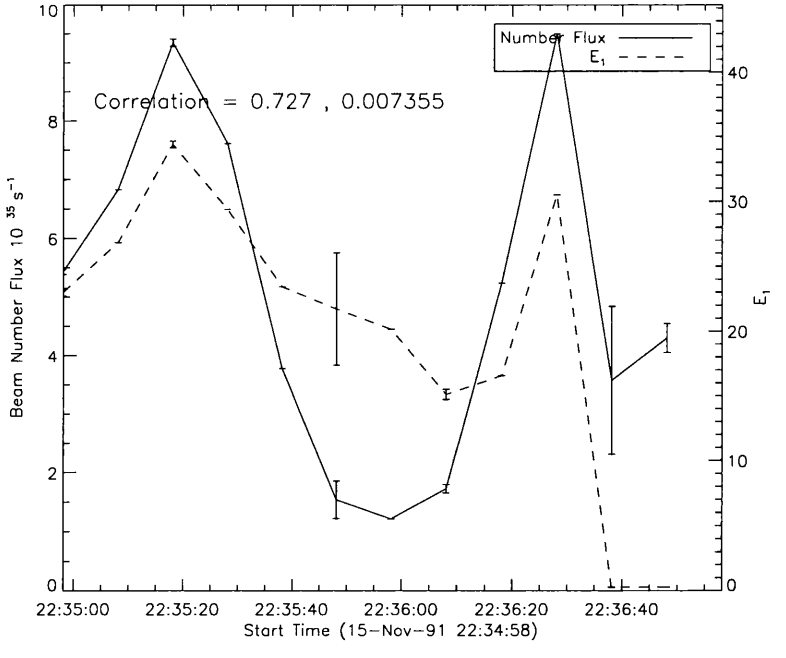

Figure 5.22: Same as in Figure 5.13 for the precursor phase of the 15-Nov-91 flare between 22:34:48-22:36:48.

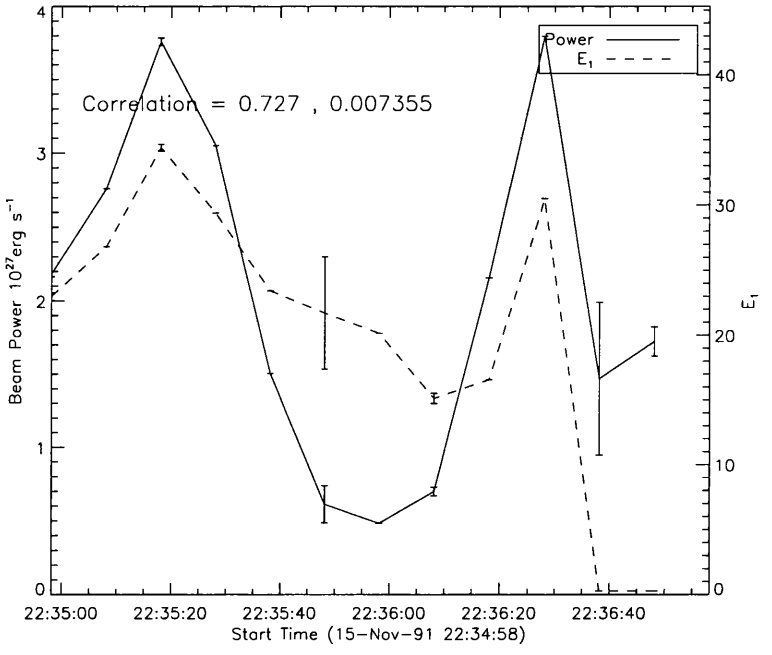

Figure 5.23: Same as in Figure 5.14 for the precursor phase of the 15-Nov-91 flare between 22:34:48-22:36:48.

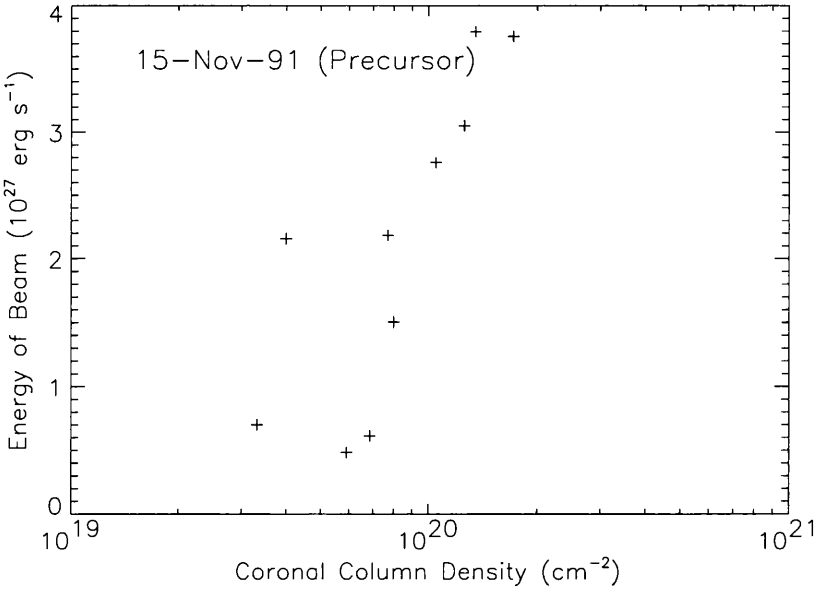

Figure 5.24: Same as in Figure 5.15 for the precursor phase of the 15-Nov-91 flare between 22:34:48-22:36:48.

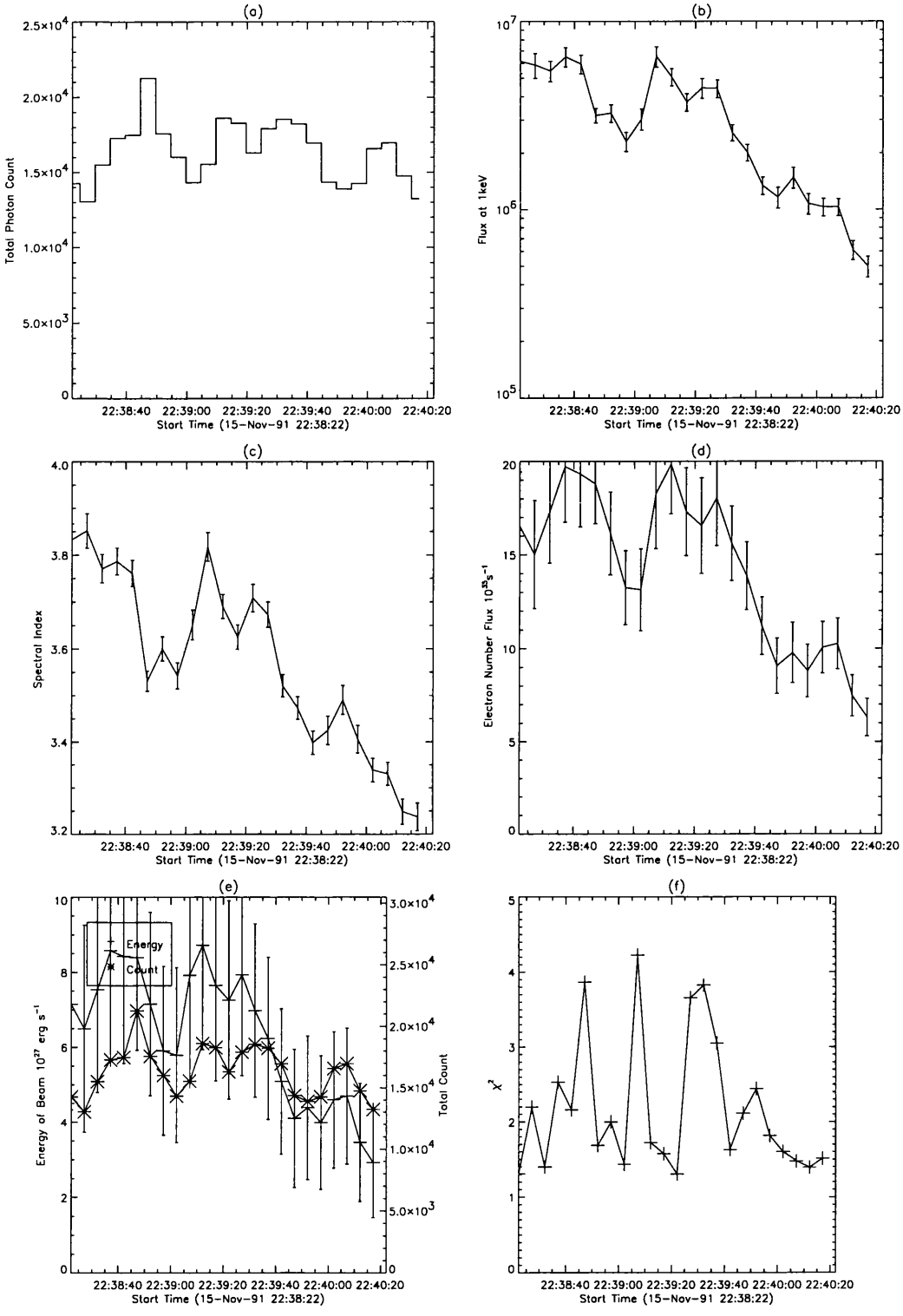

Figure 5.25: Same as in Figure 5.7 for the post-impulsive phase of the 15-Nov-91 flare between 22:38:22-22:40:17.

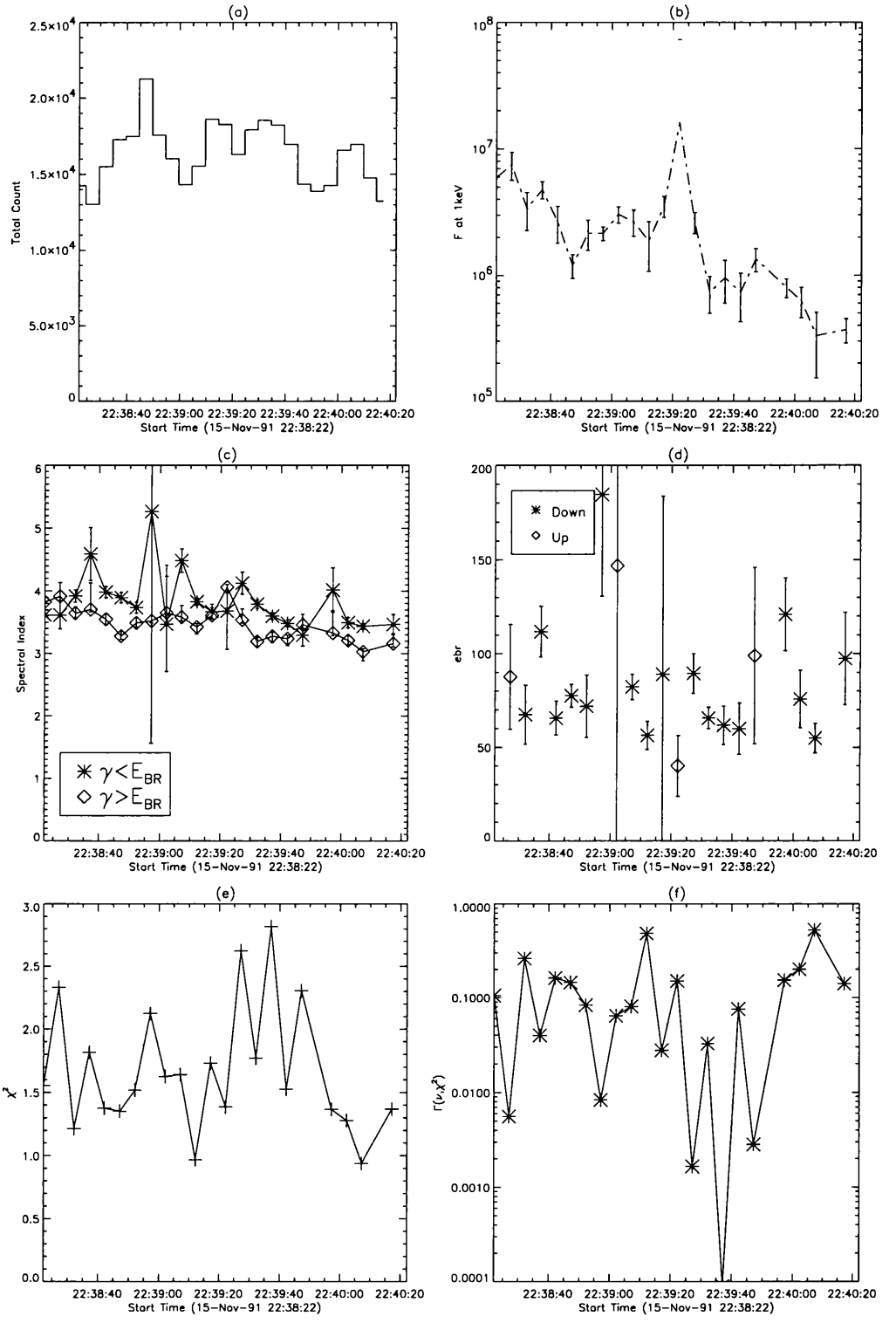

Figure 5.26: Same as in Figure 5.8 for the post-impulsive phase of the 15-Nov-91 flare between 22:38:22-22:40:17.

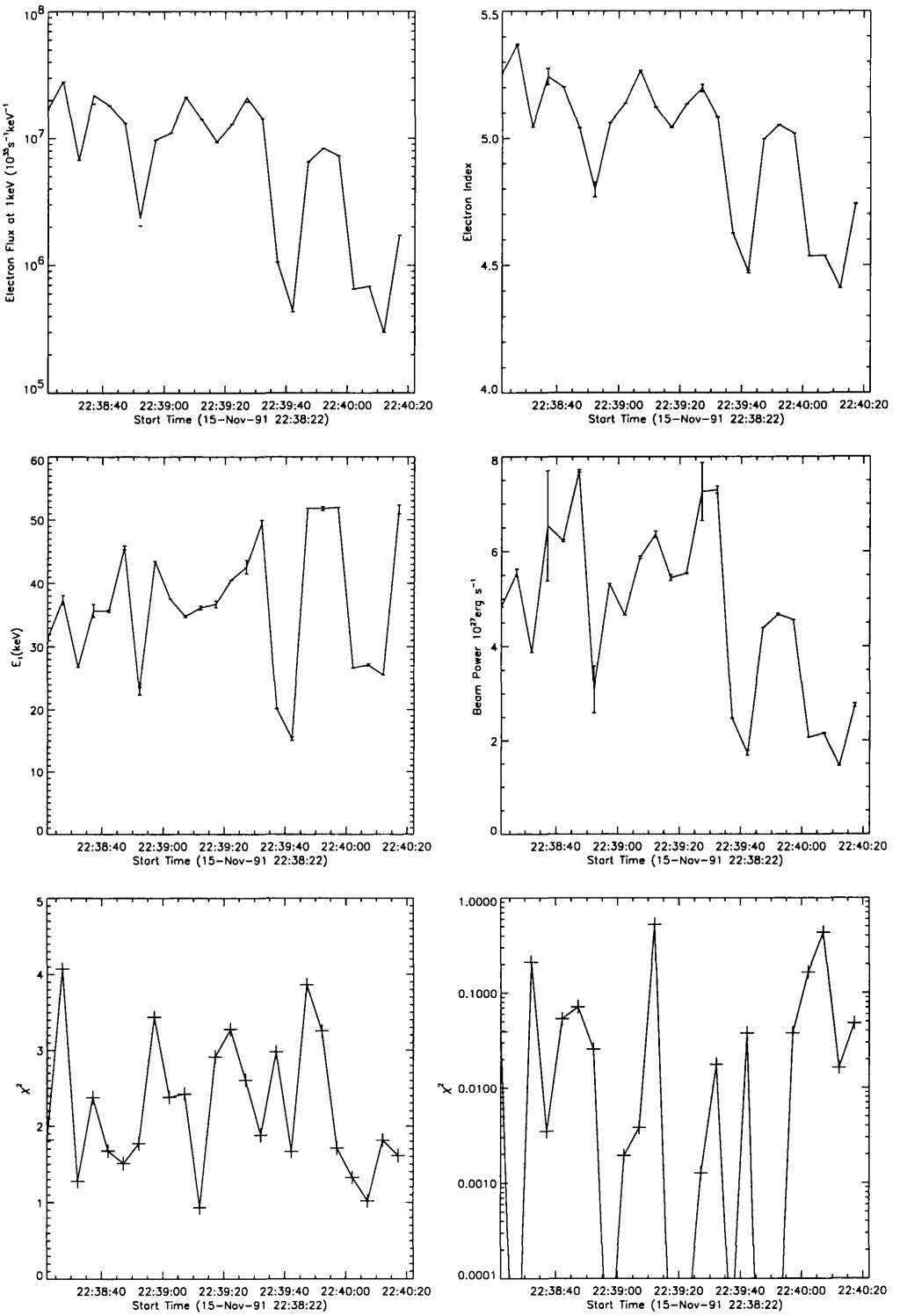

Figure 5.27: Same as in Figure 5.9 for the post-impulsive phase of the 15-Nov-91 flare between 22:38:22-22:40:17.

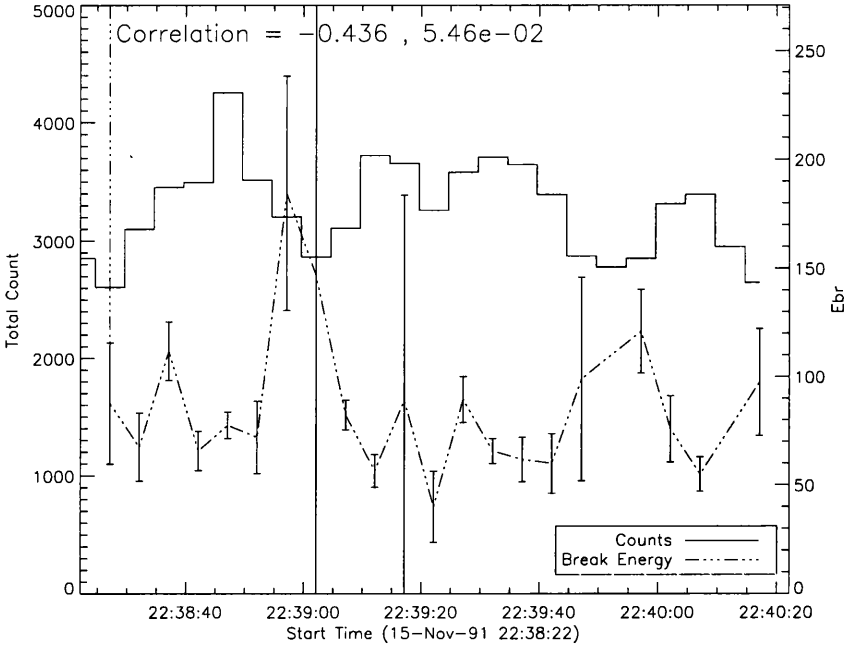

Figure 5.28: Same as in Figure 5.10 for the post-impulsive phase of the 15-Nov-91 flare between 22:38:22-22:40:17.

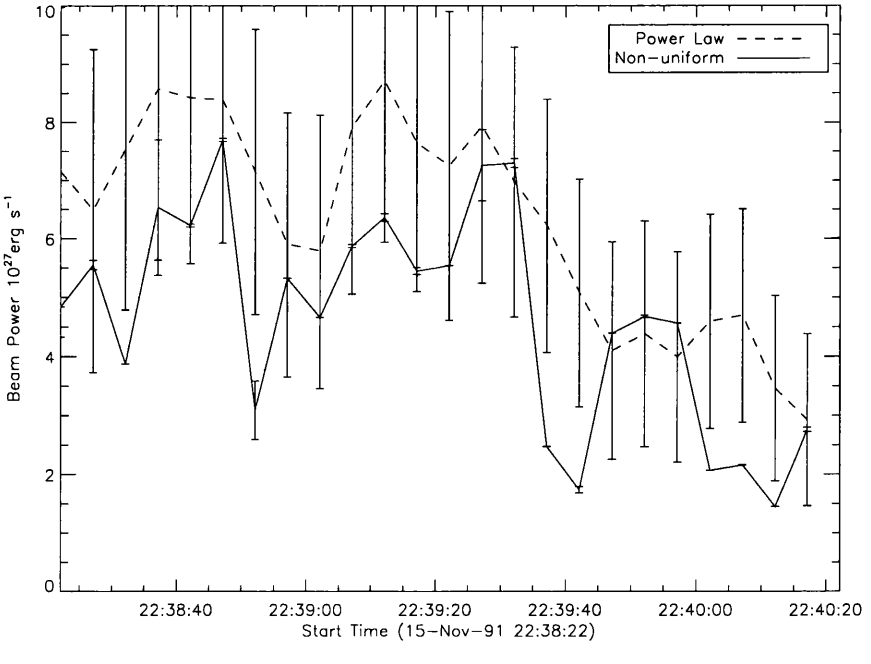

Figure 5.29: Same as in Figure 5.11 for the post-impulsive phase of the 15-Nov-91 flare between 22:38:22-22:40:17.

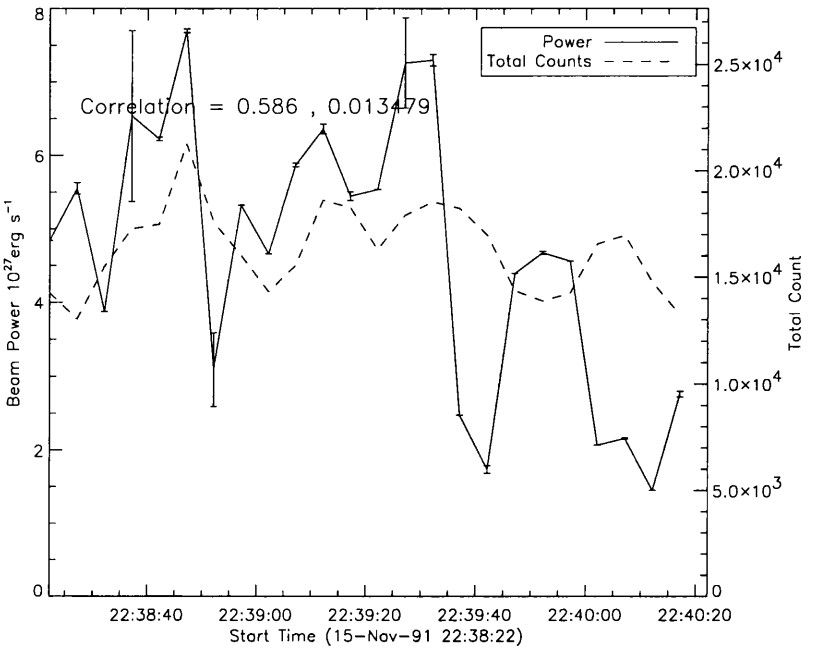

Figure 5.30: Same as in Figure 5.12 for the post-impulsive phase of the 15-Nov-91 flare between 22:38:22-22:40:17.

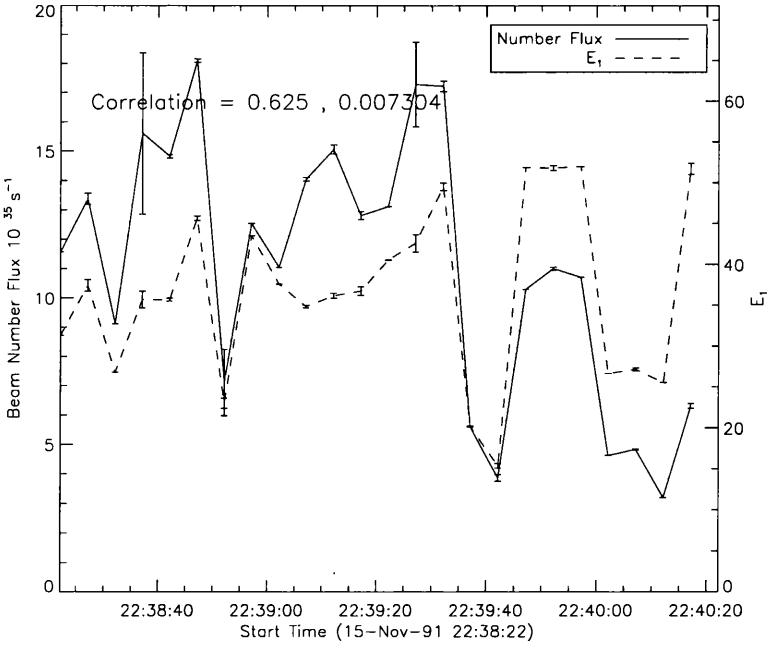

Figure 5.31: Same as in Figure 5.13 for the post-impulsive phase of the 15-Nov-91 flare between 22:38:22-22:40:17.

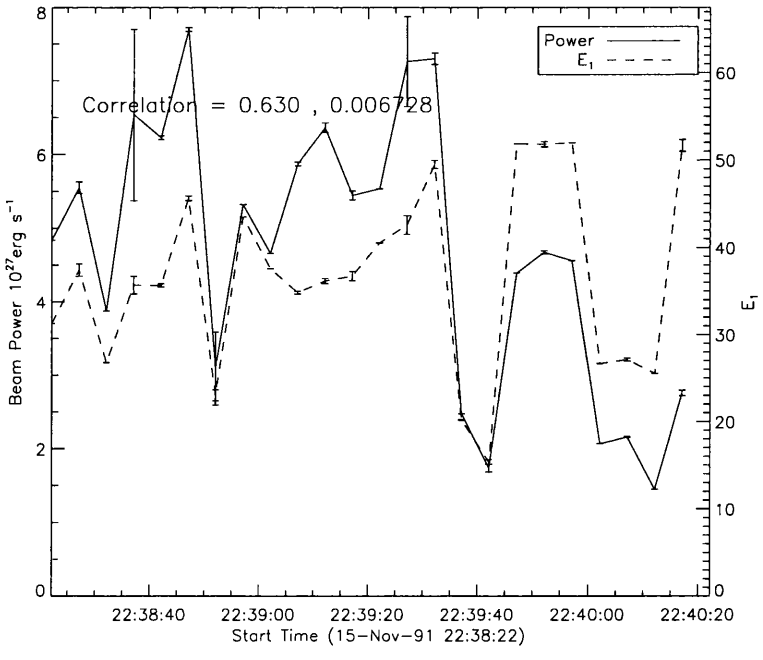

Figure 5.32: Same as in Figure 5.14 for the post-impulsive phase of the 15-Nov-91 flare between 22:38:22-22:40:17.

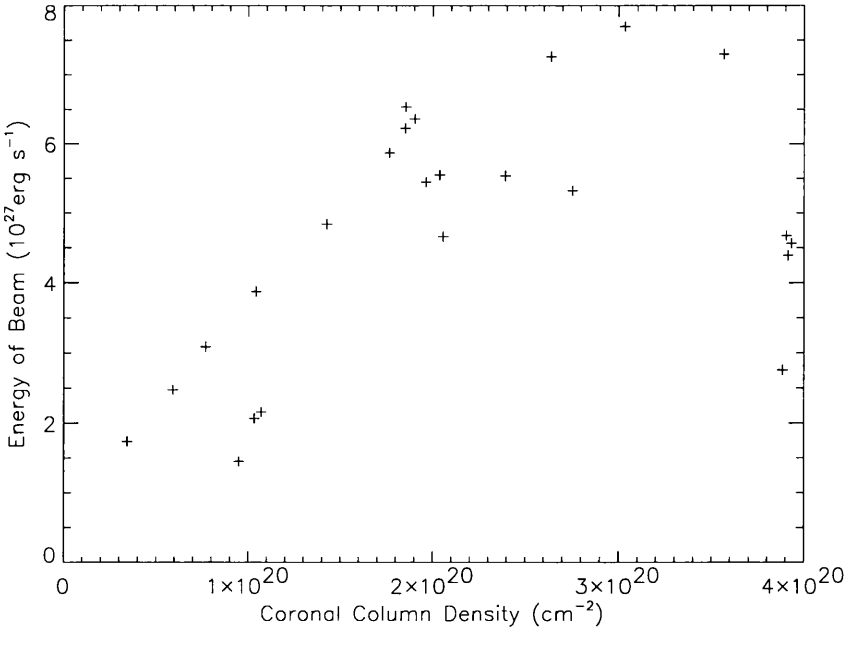

Figure 5.33: Same as in Figure 5.15 for the post-impulsive phase of the 15-Nov-91 flare between 22:38:22-22:40:17

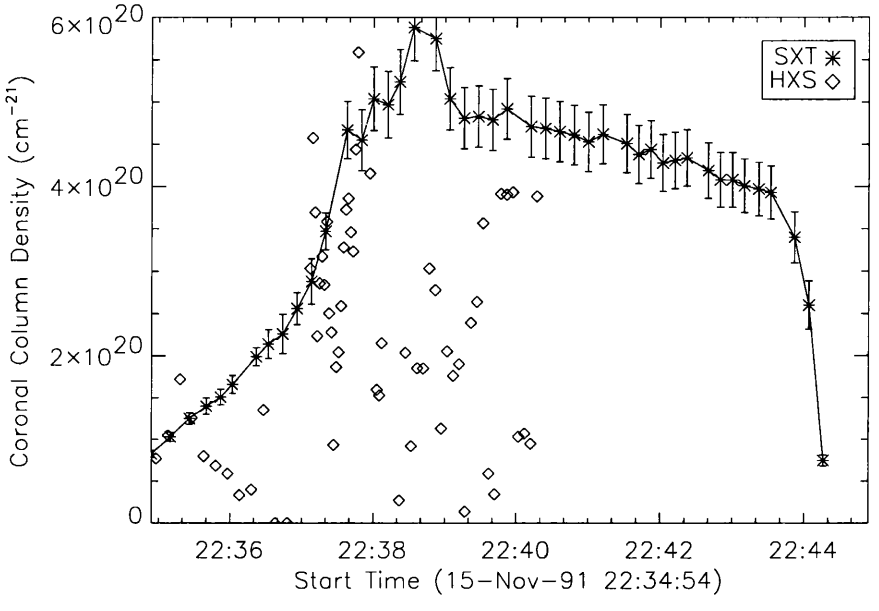

Figure 5.34: Comparison of coronal column density derived from estimates of E_1 from the HXS hard X-ray spectra and the column density determined for a $\sim 10^9 \mathrm{cm}^2$ loop with density determined from SXT Be/All ratio.

5.4 27th October 1991 Flare

The large X-ray flare on the 27th of October 1991 was detected by the GOES satellite, starting at 05:37 UT until 07:12 UT. It was determined as having a X6.1 classification and 3B H_α importance. This event occurred on the disk at S13E15 and is associated with NOAA active region 6891.

Yohkoh hard X-ray data is available from 05:39:29 UT to 05:41:35 for HXT, and 05:41:33 for WBS, unfortunately missing the initial and final development of the flare. The event shows $4-5$ distinct hard X-ray sources, which overall leads to a relatively large area of emission (cf. Figure 5.37. The HXS count rates peak at $\approx$ 05:40:28, (Figure 5.73), exceeding 4×10^4 counts per second. At such high count rates the deadtime correction is very uncertain and cannot be trusted.

For a single power law fit to the photon spectrum, (Figure 5.40), the spectral index γ indicates a hard electron spectrum. γ decreases from 3.8 at the beginning of the flare to a lowest estimate of 2.8, when count rates are maximum. The soft-hard-soft behaviour is displayed for each small peak in count rate. At each of these peaks the flux constant A also declines.

The double power law model parameters to the photon spectrum are shown in (Figure 5.40). The spectral indices over the event remain relatively constant $\gamma_1 \approx 3.0$ and $\gamma_2 \approx 4.0$. The spectral break always being determined to be break down. The break energies estimated for this event range between $\approx\ 40 - 200$ keV, with the evolution of break energy being closely related to the observed total count rate. This can be seen in Figure 5.43.

Finally the best fit parameters of the NUIPLE model to the photon count rates of this event gives electron fluxes of $\approx 1 \times 10^{43}$ at 1 keV, with the electron spectral index decreasing from $\sim 5.3\ -\ 4.5$. The decreases in spectral index coincides with the largest increases in observed flux, in a similar manner as the photon spectral index. Determined E_1 values peak at $\sim 120keV$. This corresponds to a high column density of $\sim 2\times10^{21}\mathrm{cm}^{-2}$.

For all of the spectra observed in the 27 October event, the reduced χ^2 for the three types of models are extremely poor and $\Gamma(\nu,\chi^2)$, the goodness-of -fit parameter, is evaluated in many cases to be zero. The validity of all three models for this event is therefore questionable. However, the residuals between observed channel count and modelled channel counts does not show any systematic behaviour, suggesting that a particular region of

the spectra is not being well fitted. This suggests that the high values of reduced χ^2 are a result of underestimated observed error. For the residuals to be of the same magnitude as the error estimates, the error estimates must be $\approx$ 4-5 times greater. This underestimation of the error on the observed count rate may be due to the unreliability of deadtime correction for this intense flare.

As a result of these extremely low values of $\Gamma(\nu, \chi^2)$ all spectra are below the criteria for further correlation analysis. For this event therefore, although the χ^2 calls into question the believability of the model and model parameters, the correlations between the estimated E_1, beam energy flux and beam number flux are derived using the determined best fit model parameters for all time intervals. The results are shown in Figures 5.43-5.48 with the rank-order correlation co-efficients summarised below.

	Correlation Co-efficient	Significance
Electron Flux A and E_1	0.051	0.710
Spectral Index δ and E_1	-0.460	3.54×10^{-4}
Electron Number Flux and E_1	0.889	5.64×10^{-20}
Electron Energy Flux and E_1	0.891	3.50×10^{-20}
Energy Flux and Count Rates	0.834	1.42×10^{-15}

For this event the correlations found are particularly high, including good correlations between observed photon count and energy content of the beam. Again the highest correlation is found between the evolution of E_1 and the beam energy flux, with a correlation r_s of 0.891.

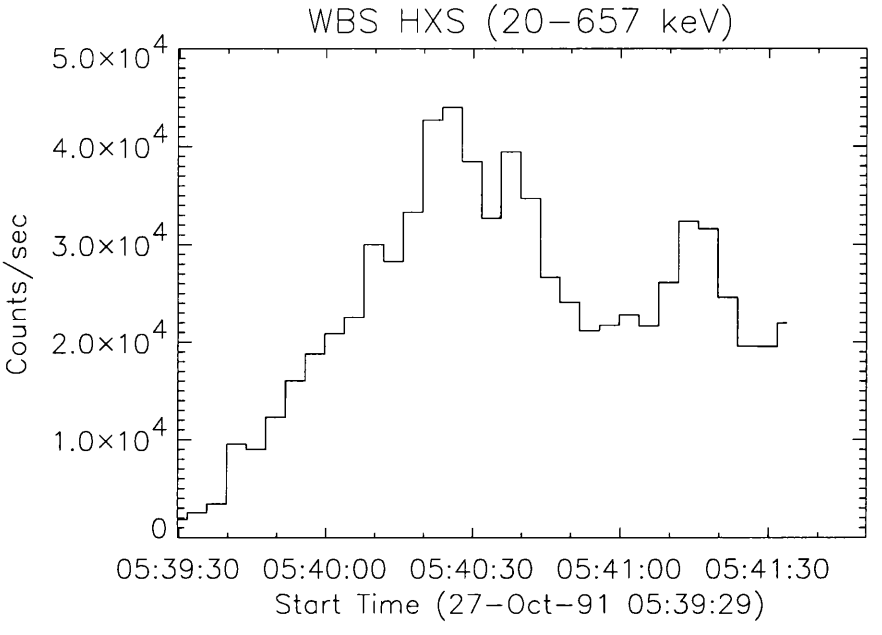

(a)

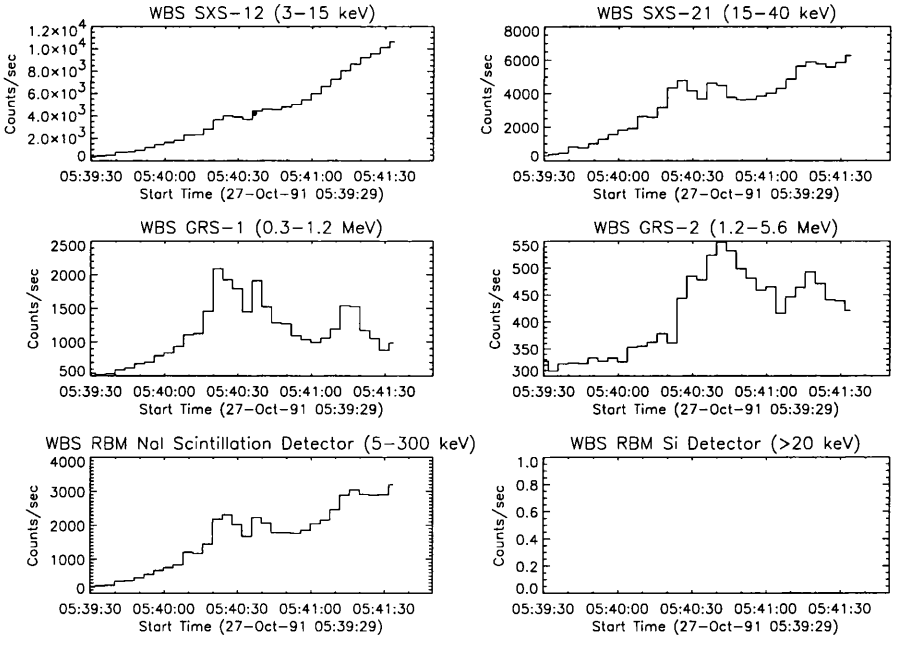

(b)

Figure 5.35: (a) Time profile of the total hard X-rays count rates measured by the hard X-ray spectrometer onboard *YOHKOH* over the observing period which included the class X6.1 flare on 27th October 1991 at 05:37 UT. (b) Similar of time profiles for remaining WBS instruments.

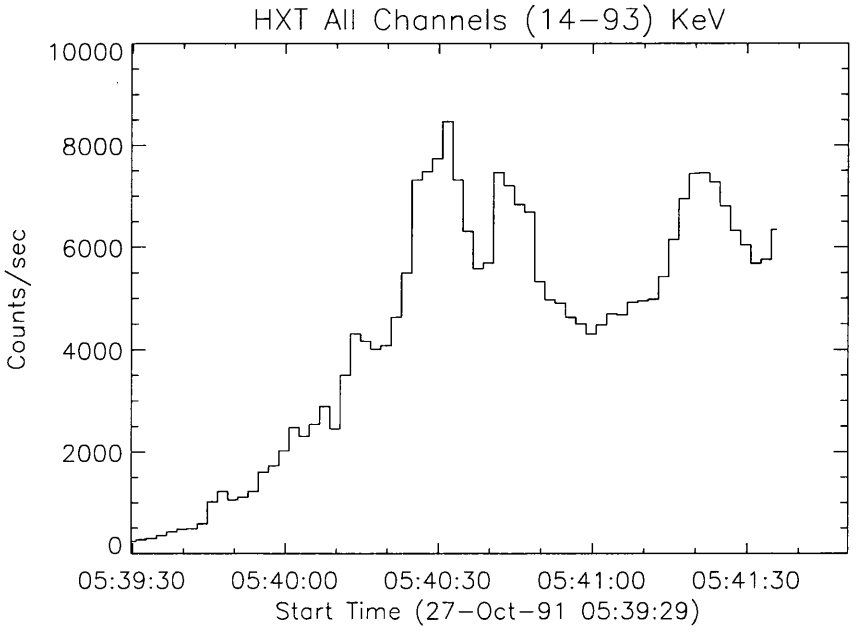

(a)

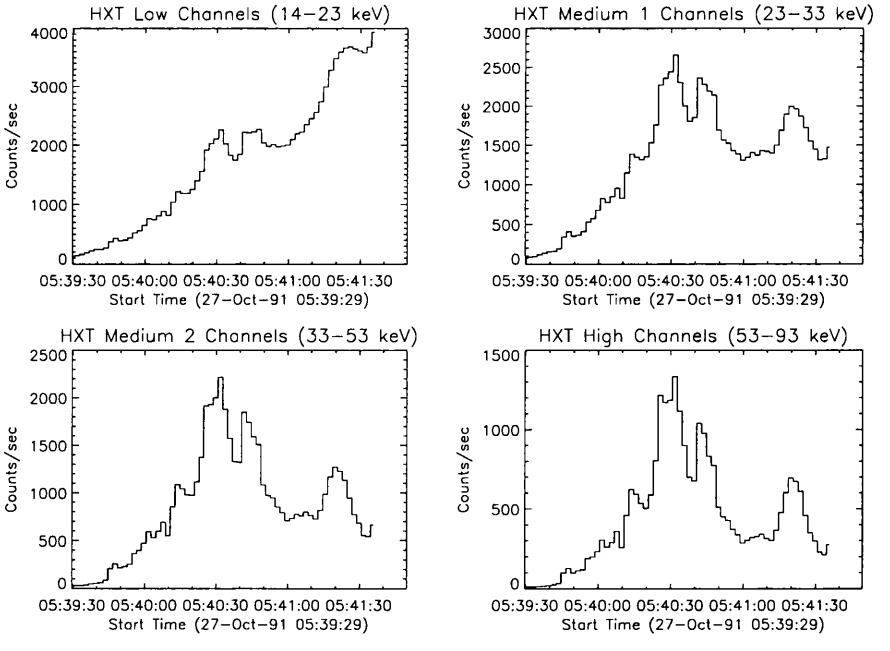

(b)

Figure 5.36: (a) Total light curve of all HXT channels and (b) individual light curves for the 4 HXT channels during the 27th October event.

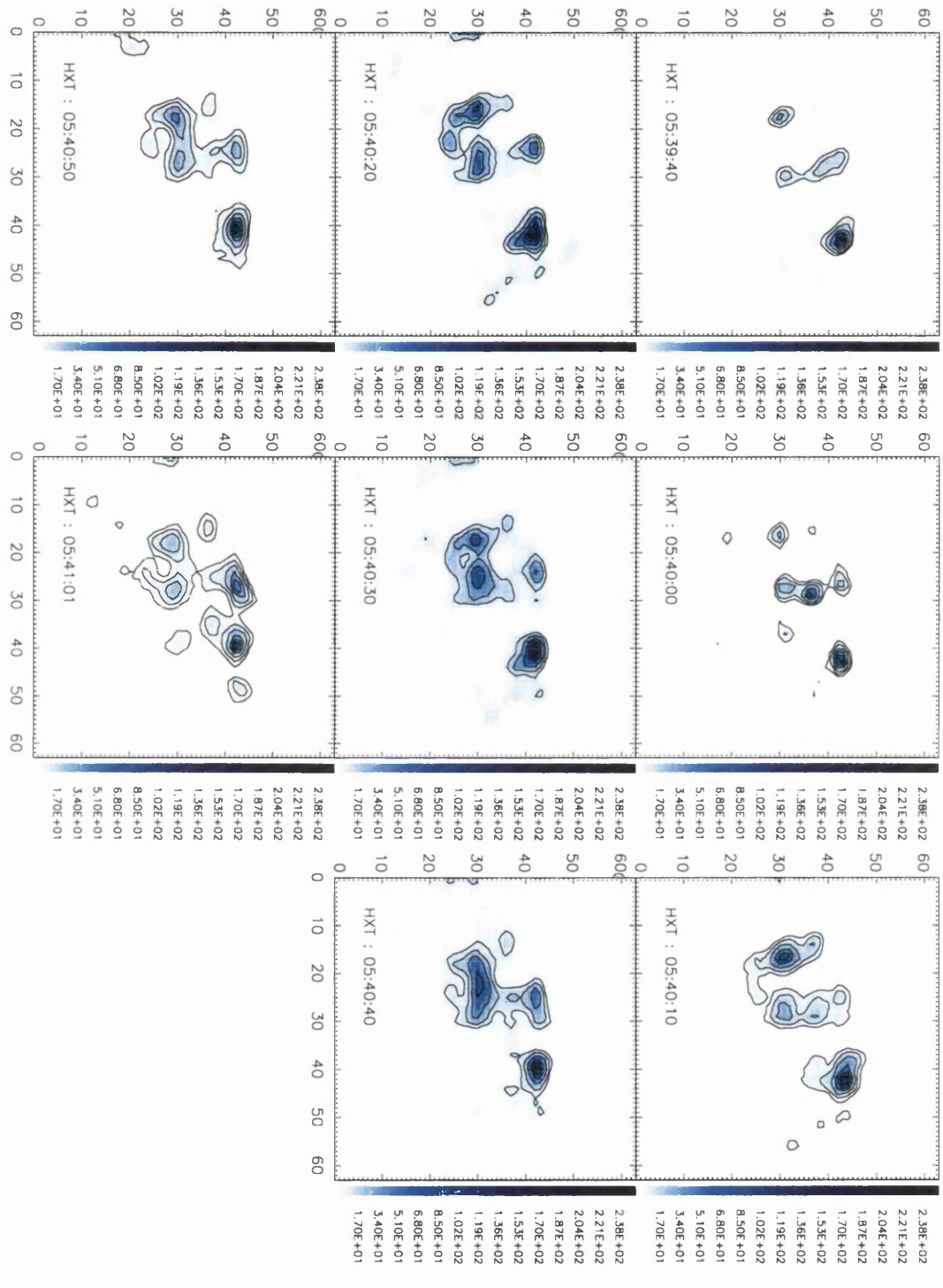

Figure 5.37: Selected M2 band reconstructed images of the 27th November event from 05:39:40 UT to 05:41:01 UT. Each image, based on 200cts/SC, shows the multiple source structure and large spatial extent of the total source.

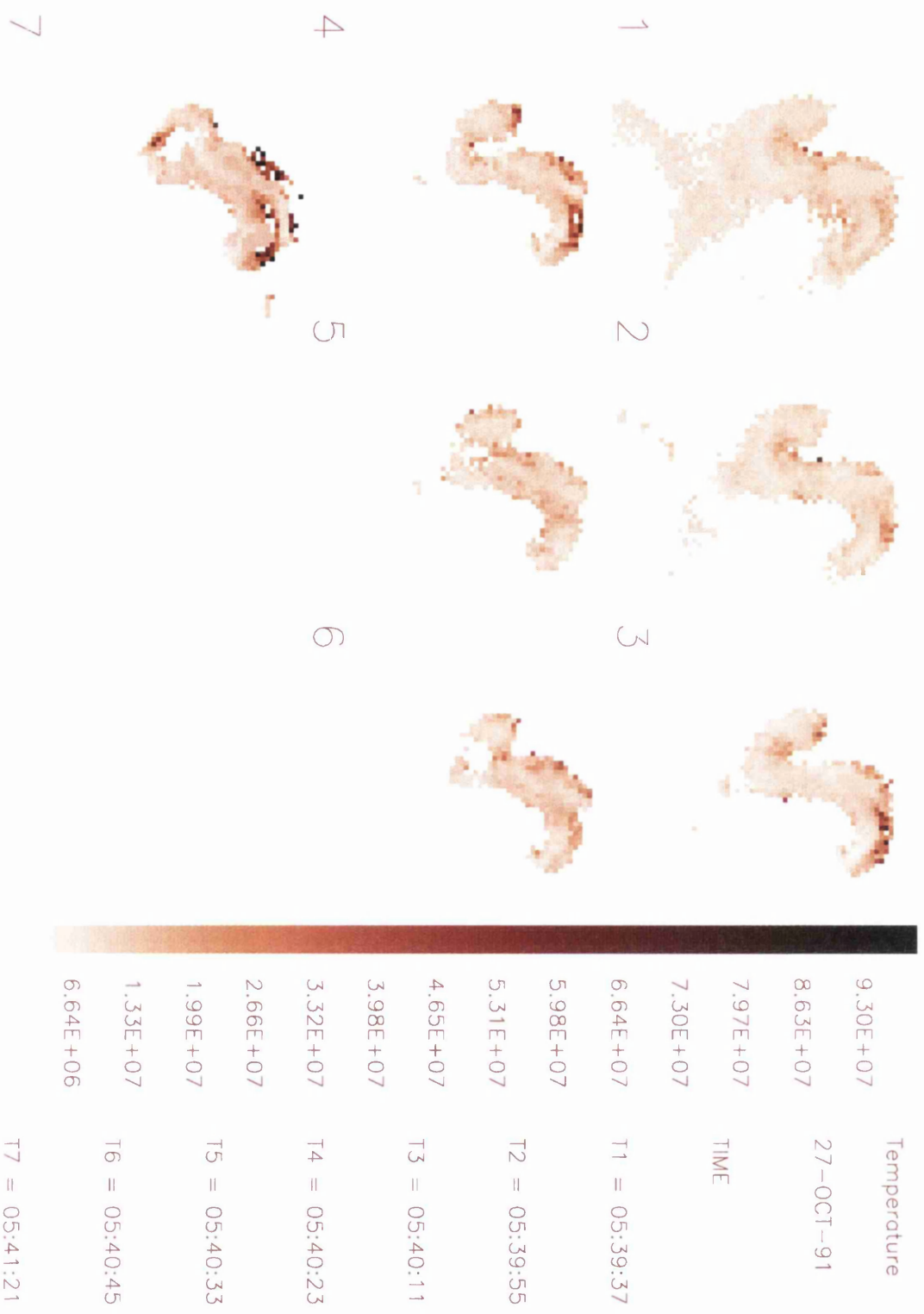

Figure 5.38: Maps of SXT derived temperature structure for the 27 October 1991 flare, using filters Be119 and Al112.

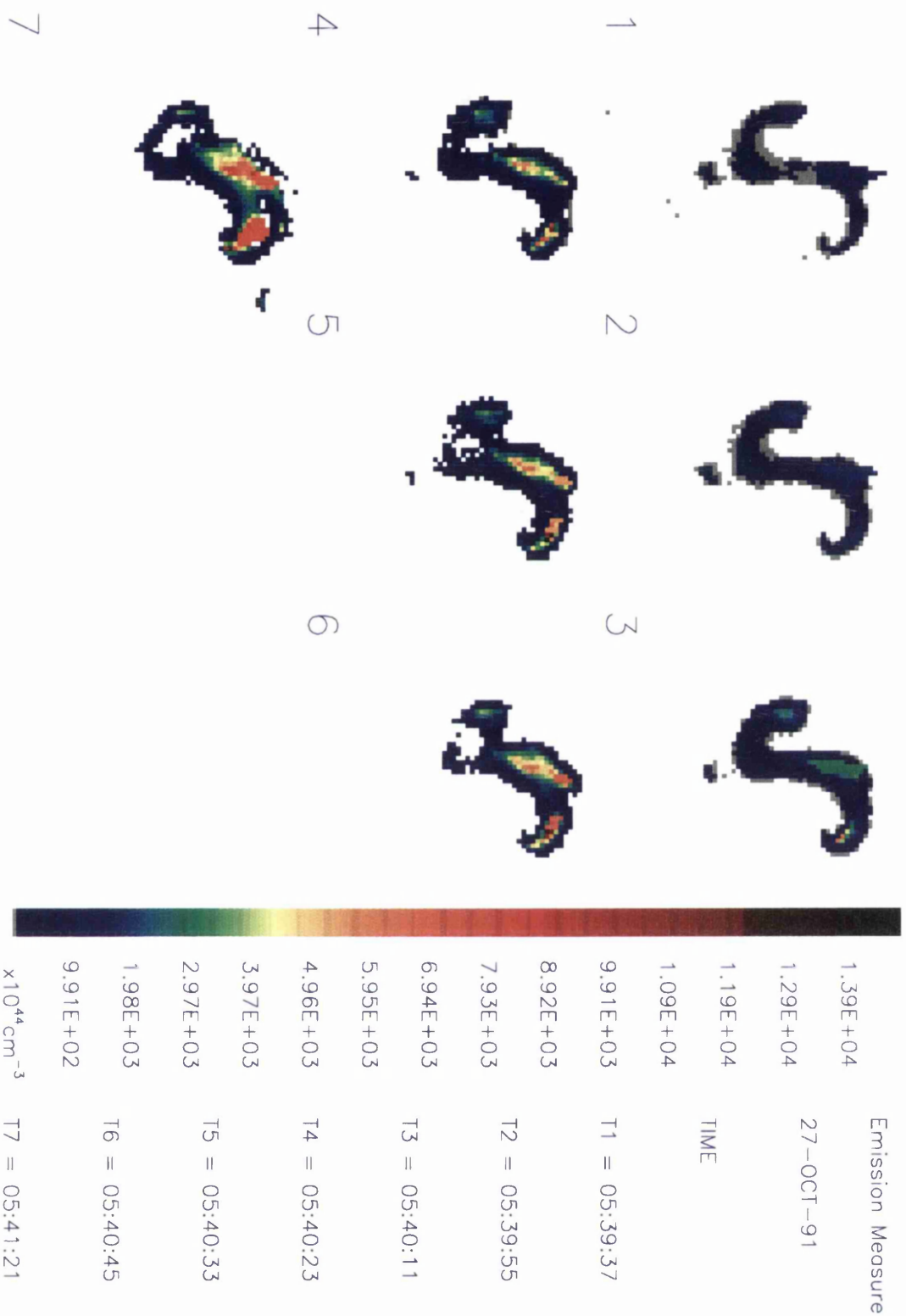

Figure 5.39: Equivalent maps of SXT emission measure estimated from temperature structure derived in Figure 5.38.

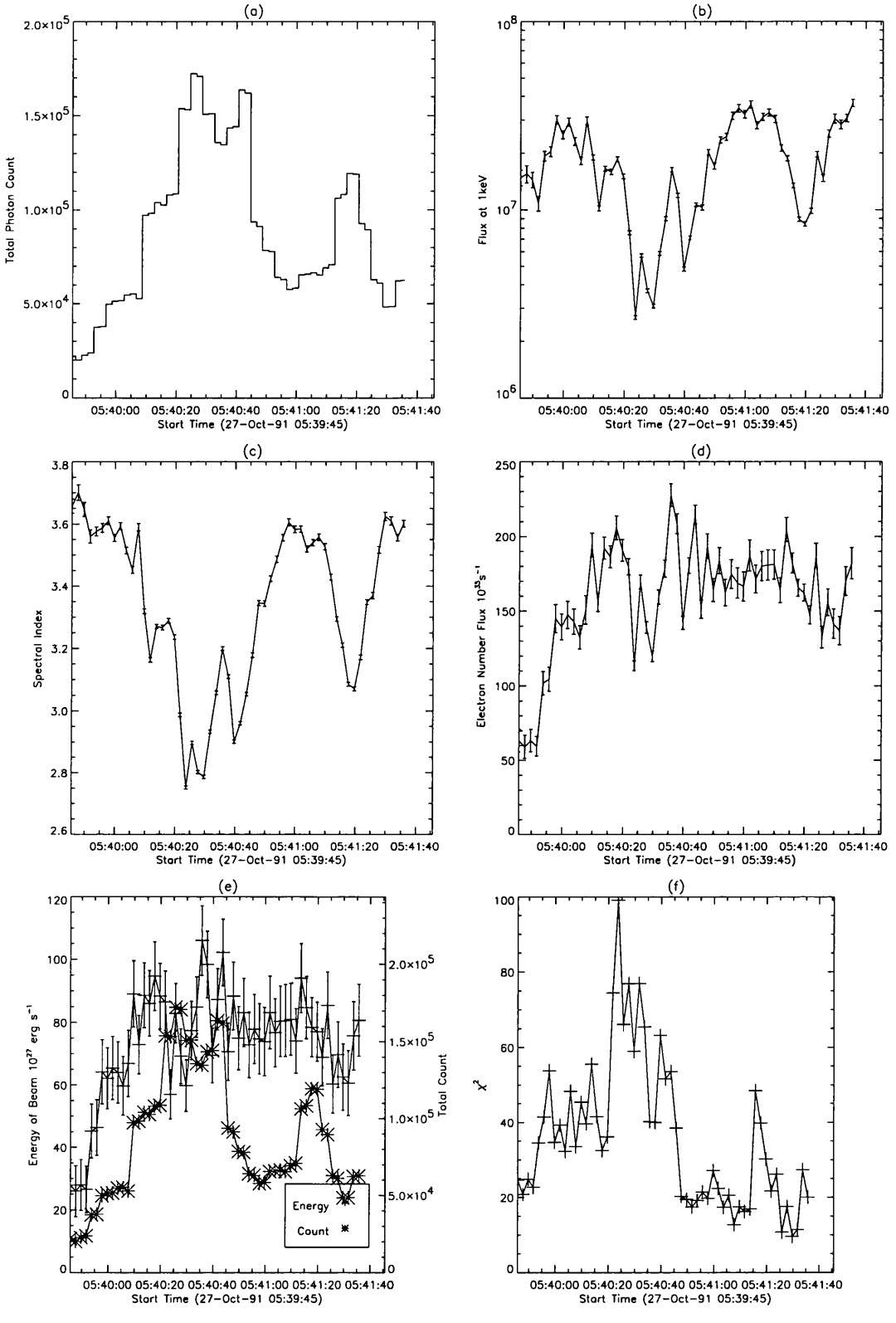

Figure 5.40: Evolution of single power law spectral fit parameters during the 27-Oct-91 flare between 05:39:45-05:41:45. (a) is the total HXS-PH counts for each 2 s interval, (b) and (c) are the power law parameters i.e. the photon flux $\mathrm{keV}^{-1}\mathrm{s}^{-1}$ at 1 keV and photon spectral index. (d) and (e) indicates the inferred electron beam number flux and energy flux assuming an ionised atmosphere and an electron low energy cut-off at 20 keV. Finally (f) shows the reduced χ^2 for each spectral fit.

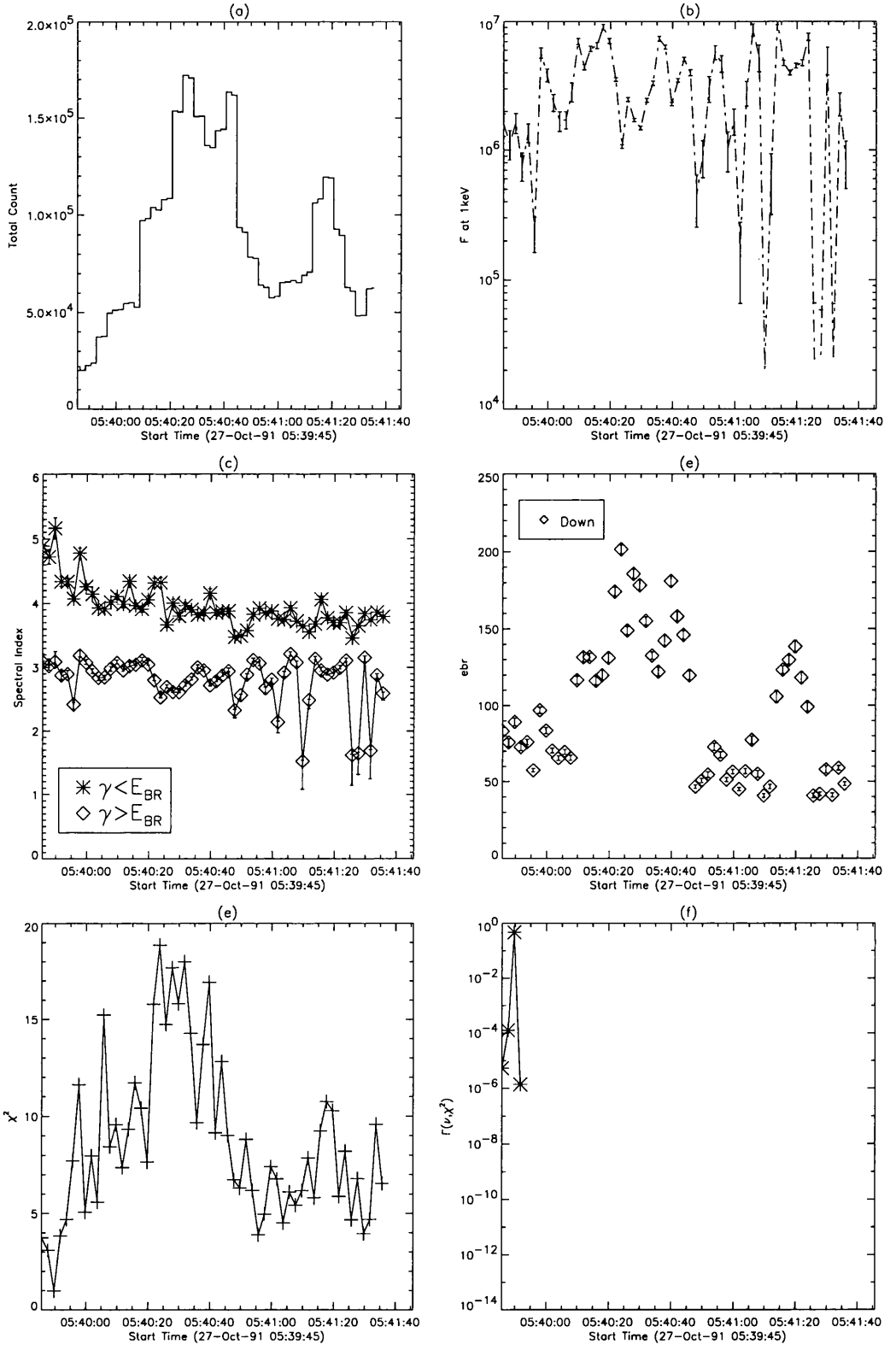

Figure 5.41: Evolution of double power law spectral fit parameters during the 27-Oct-91 flare between 05:39:45-05:41:45. (a) is the total HXS-PH counts for each 2 s interval, (b) and (c) (d) and (e) are the power law parameters i.e. the photon flux $keV^{-1}s^{-1}$ at 1 keV and photon spectral indices below and above the break point and the break point. Finally (f) shows the reduced χ^2 for each spectral fit and (g) the indicator of goodness-of fit for that χ^2.

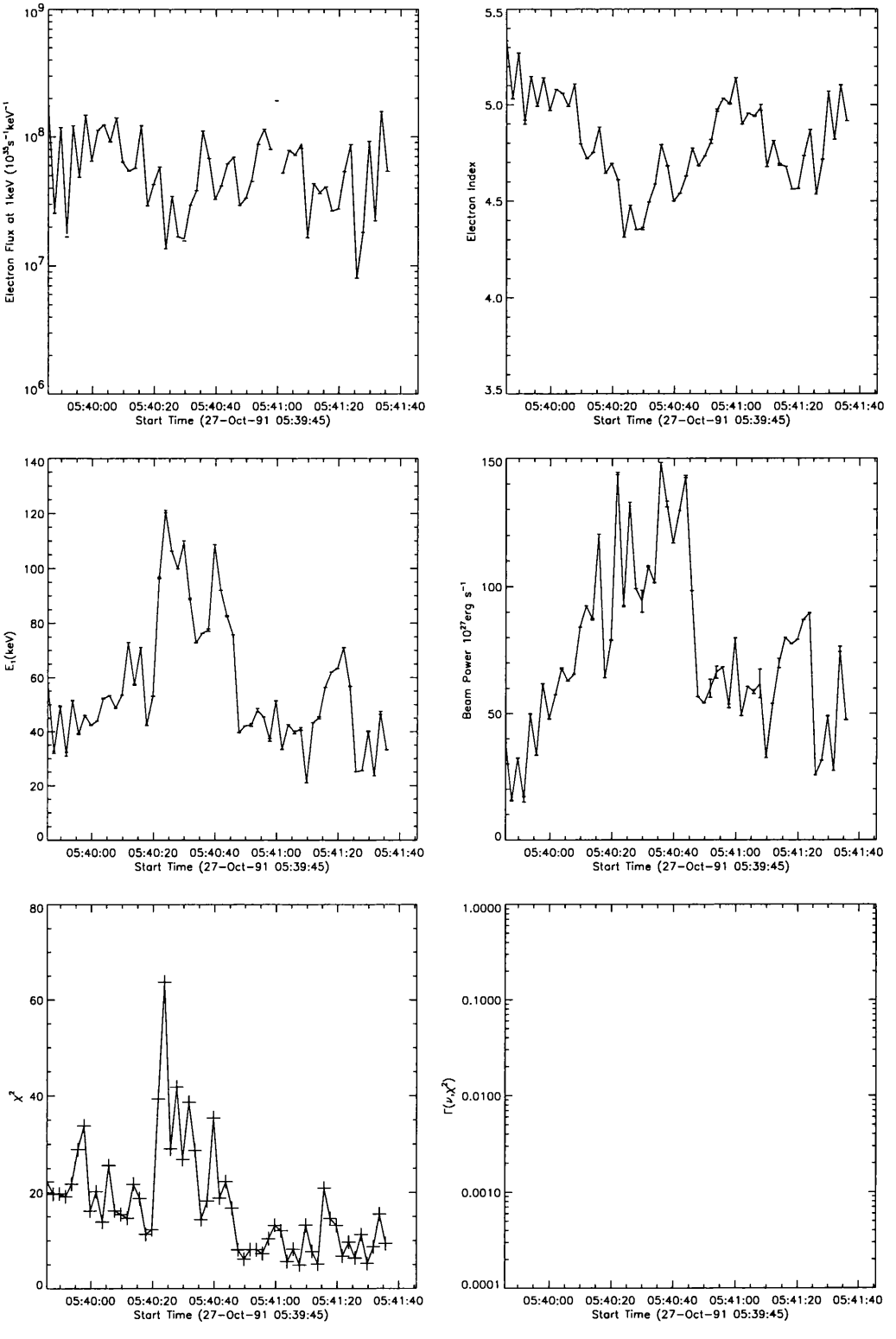

Figure 5.42: Evolution of spectral fit parameters for nonuniformly ionised atmosphere model during the 27-Oct-91 flare between 05:39:45-05:41:45. (a) the electron flux $keV^{-1}s^{-1}$ at 1 keV, (b) the electron spectral index and (c) the electron stopping energy of the transition region. (d) shows the estimate of electron beam energy flux for such parameters with cut-off energy at 20 keV. Finally (f) shows the reduced χ^2 for each spectral fit and (g) the indicator of goodness-of fit for that χ^2.

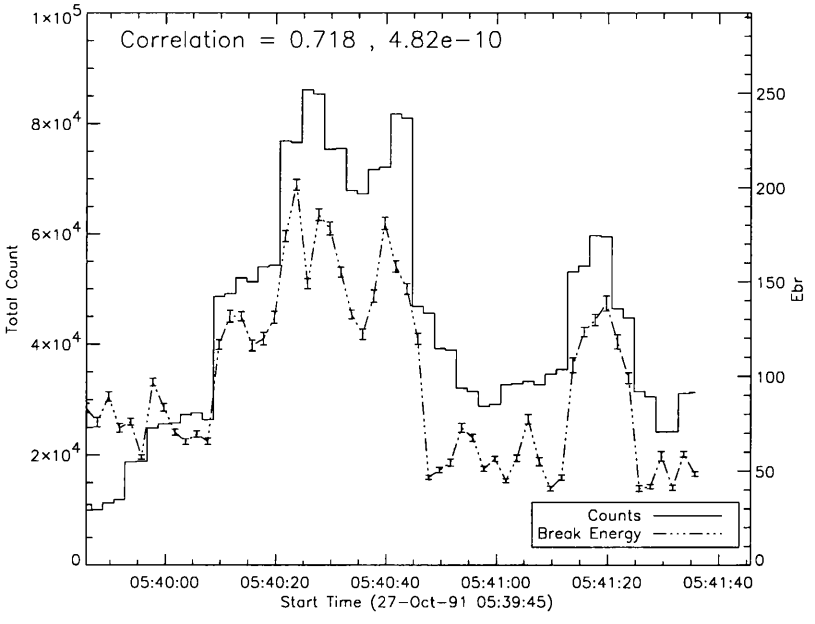

Figure 5.43: Comparison of evolution of observed count rates with the break energy of a double power law for the 27-Oct-91 flare. The rank correlation for these parameters is also indicated.

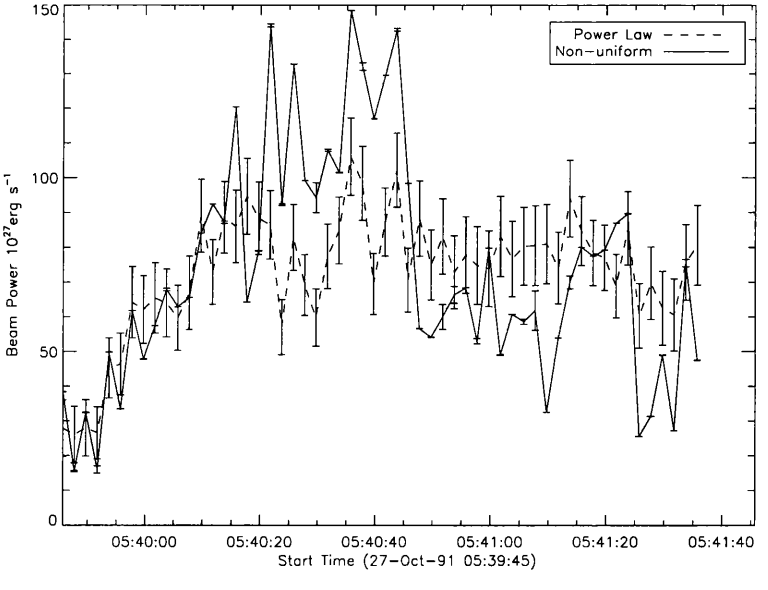

Figure 5.44: Comparison of beam flux for a nonuniform model and from the power law fit assuming an ionised atmosphere, for the 27-Oct-91 flare.

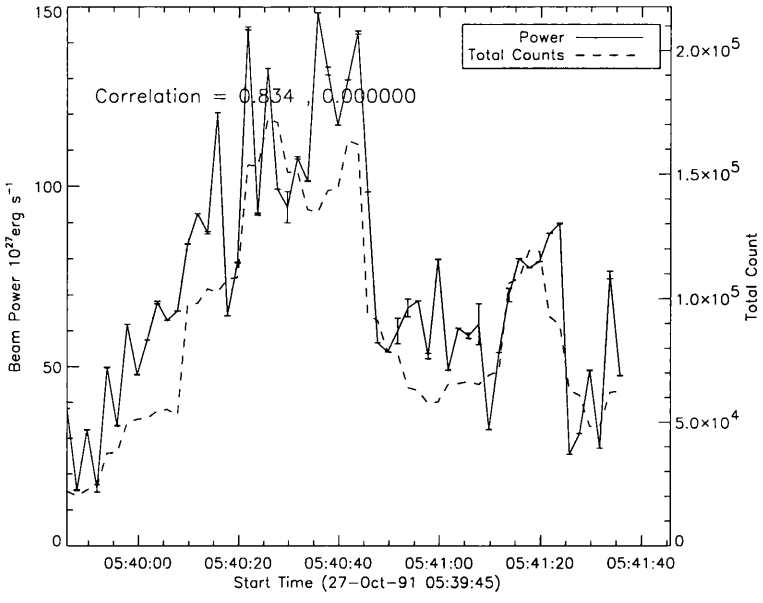

Figure 5.45: Comparison of evolution of nonuniform model electron beam energy flux with the total counts for each time interval, for the 27-Oct-91 flare. The rank correlation for these parameters is also indicated.

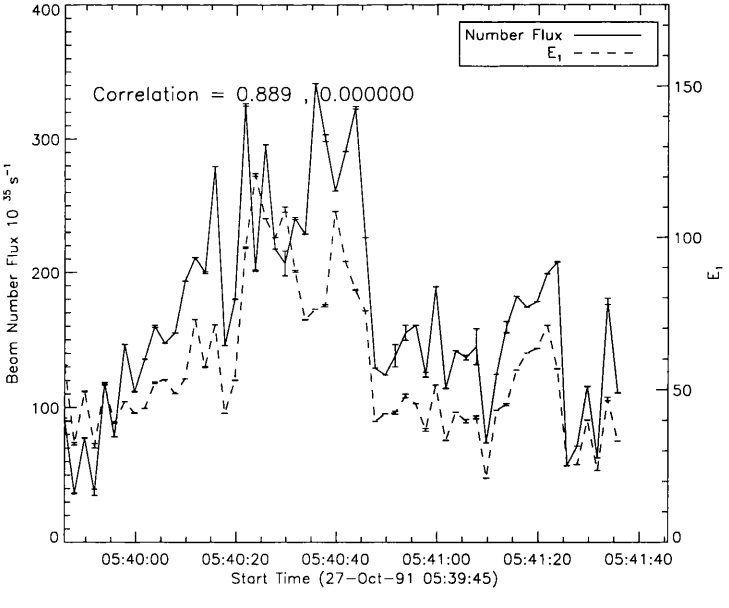

Figure 5.46: Comparison of evolution of nonuniform model electron beam number flux with the stopping energy of an electron which just reaches the chromosphere (E_1), for the 27-Oct-91 flare. The rank correlation for these parameters is also indicated.

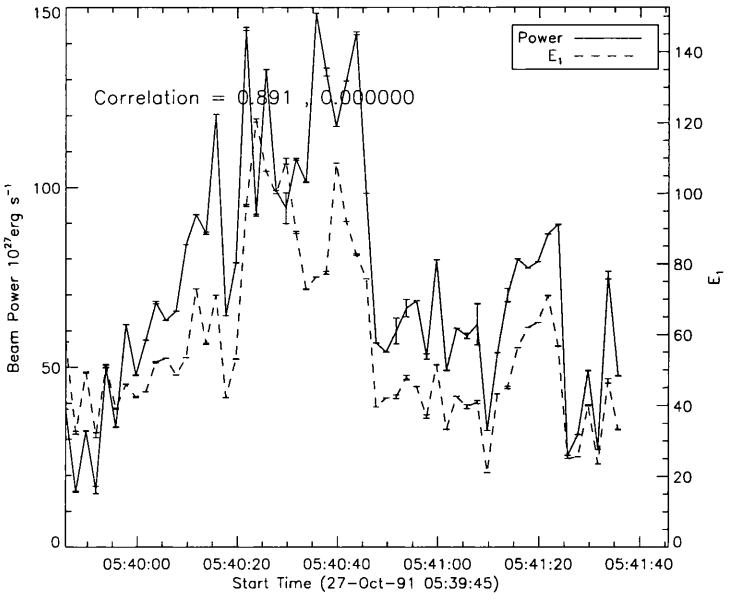

Figure 5.47: Comparison of evolution of nonuniform model electron beam energy flux with the stopping energy of an electron which just reaches the chromosphere (E_1), for the 27-Oct-91 flare. The rank correlation for these parameters is also indicated.

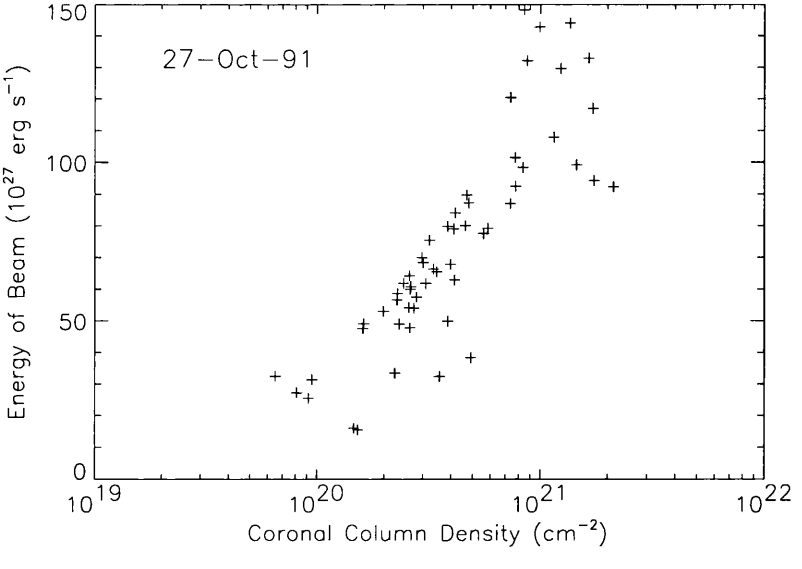

Figure 5.48: Correlation of electron beam flux and coronal column density determined from E_1, for the 27-Oct-91 flare.

5.5 9th November 1991 Flare

The flare on the 9th of November 1992 beginning at 20:51:45 was classified as an M1.4 class flare. It had an H_α importance of 1B and occurred on the disk at S14 W69. It is associated with active region 6906. The M2 band HXT images (cf. Figure 5.51) show a compact source evolving into a double source i.e. implying a simpler single loop geometry than in the 27 October event.

The profile of HXS count rates can be described as one simple peak, occurring at 20:52:13 and lasting $\sim$ 60 s (Figure 5.49). The count rates for this flare reached a maximum of 4000 counts per second. This is an order of magnitude less than the X flare on the 27th October. The time profile of the SXS(15-40 keV) shows great similarity to that of the HXS count rates. Also the profiles of each separate HXT channel have no significant difference (Figure 5.50). It is unlikely therefore that there is a strong thermal component to the detected hard X-rays for this event.

The best fit parameters to the single and double power law models and the NUIPLE model are shown in Figures 5.54-5.56. The single power law models again show the soft-hard-soft spectral evolution of the peak. The double law model are all break down, the break being at $\approx$ 80 keV. There are higher break points observed but these are later in the flare, thus there is no observed correlation between break energy and total counts. The reduced χ^2 for these models is $\sim 2-3$, with the $\Gamma(\nu, \chi^2)$ showing that such models are acceptable in most cases.

For the NUIPLE model both the electron flux and spectral index are at their smallest for the peak in counts. The E_1 estimates are mostly between $40-60$ keV. This value compares well with the estimates from time-of-flight loop lengths and trapping density estimates by Aschwanden and Benz (1997) and Aschwanden et al., 1996a. The density estimates given are $1.57 \pm 0.33 \times 10^{11}$ cm^{-3} and loop lengths of $16.0 \pm 4.2 \times 10^8$ cm leading to a coronal column density estimate of $2.51 \pm 0.84 \times 10^{20}$ cm^{-2} and therefore E_1 values of 41.53 ± 6.98 keV. However the estimate for the time interval at $\approx$ 20:52:21 (time interval 13) is in excess of 150 keV which is clearly inconsistent with the value.

The correlations between these model parameters, shown in Figures 5.57-5.62 are summarised below. The time interval with high E_1 estimate is included in these correlations as the models goodness-of-fit at this interval was above the specified criteria.

	Correlation Co-efficient	Significance
Electron Flux A and E_1	0.421	0.117
Spectral Index δ and E_1	0.242	0.383
Electron Number Flux and E_1	0.757	1.08×10^{-3}
Electron Energy Flux and E_1	0.728	2.06×10^{-3}
Energy Flux and Count Rates	0.125	0.657

While there is poor correlation between the electron beam flux and total counts for this event, the correlation between the estimated E_1 and electron number flux or energy flux is again high (Figure 5.62).

5.6 26th January 1992 Flare

The flare on the 26 January 1992 commenced at 15:21 UT and has GOES class X1.0 with H_α importance 3B. Occurring at S16W66 it is associated with NOAA active region 7012. The time profile of hard X-ray count rates has one large peak at approximately 15:28, with a count rate of $\sim 1.2 \times 10^4$, below the level where dead time correction may cause spectral distortion.

The model parameters fits are shown in Figures 5.64-5.66. The estimated E_1 values for this event ranges between $\sim 20 - 40$ keV. These equate to coronal column density values of $\sim 0.6 - 2.5 \times 10^{20}$ cm^{-2}. The correlation between NUIPS model parameters were:

	Correlation Co-efficient	Significance
Electron Flux A and E_1	0.302	0.315
Spectral Index δ and E_1	0.192	0.529
Electron Number Flux and E_1	0.758	2.66×10^{-3}
Electron Energy Flux and E_1	0.785	21.45×10^{-3}
Energy Flux and Count Rates	0.219	0.470

cf. Figures 5.67-5.72. Again for this event a high correlation between beam energy flux and E_1 is found, though not between photon count rates and beam flux or the double power law break energies.

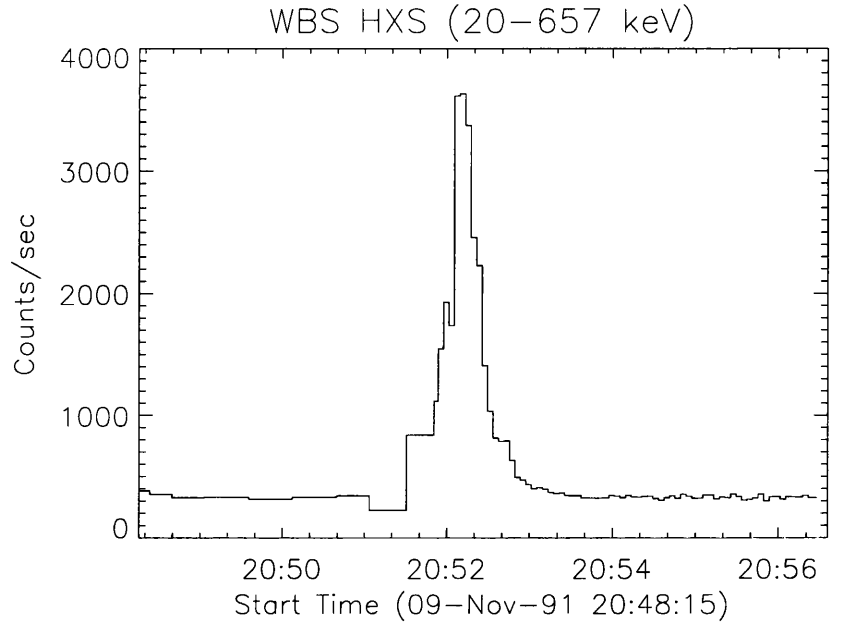

(a)

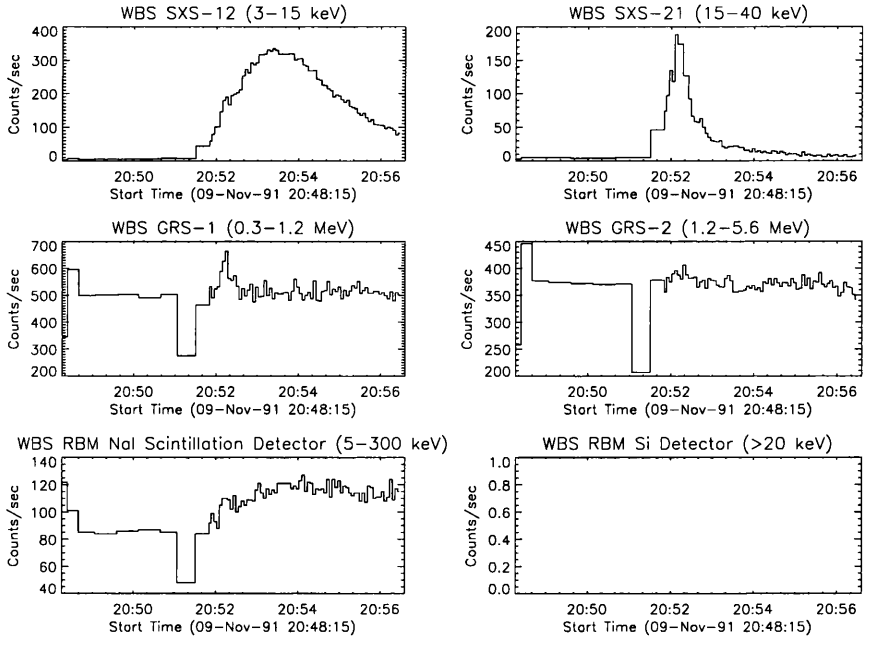

(b)

Figure 5.49: (a) Time profile of the total hard X-rays count rates measured by the hard X-ray spectrometer (HXS) onboard *YOHKOH* over the flare mode observing period of the flare on 9th November 1991. (b) Similar light curves for the remaining WBS instruments.

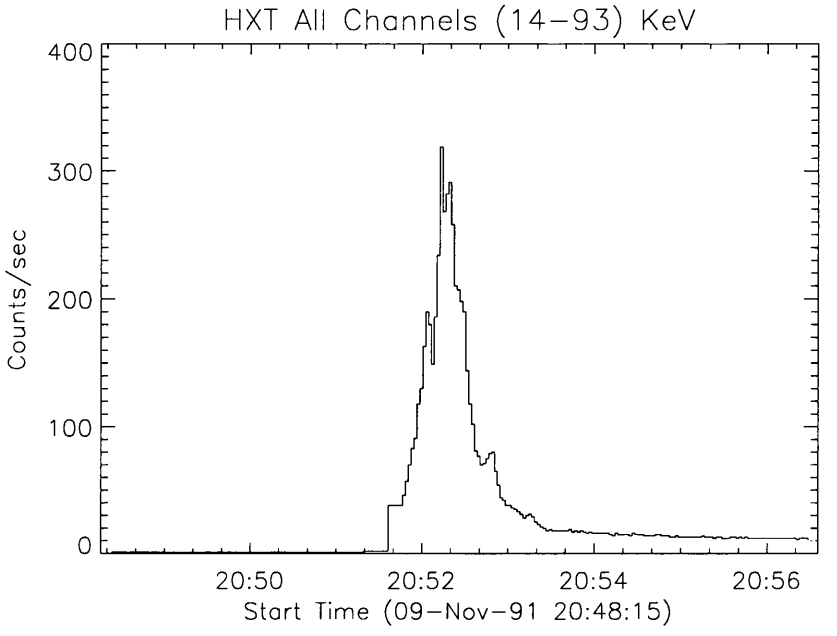

(a)

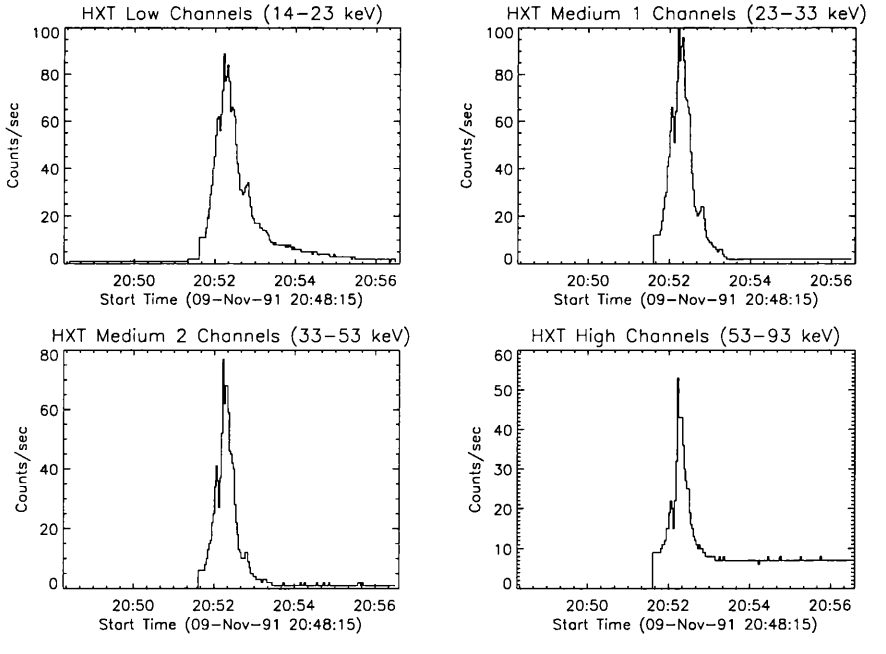

(b)

Figure 5.50: (a) Total light curve of all HXT channels and (b) individual light curves for the 4 HXT channels during the 9th of November 1991 event.

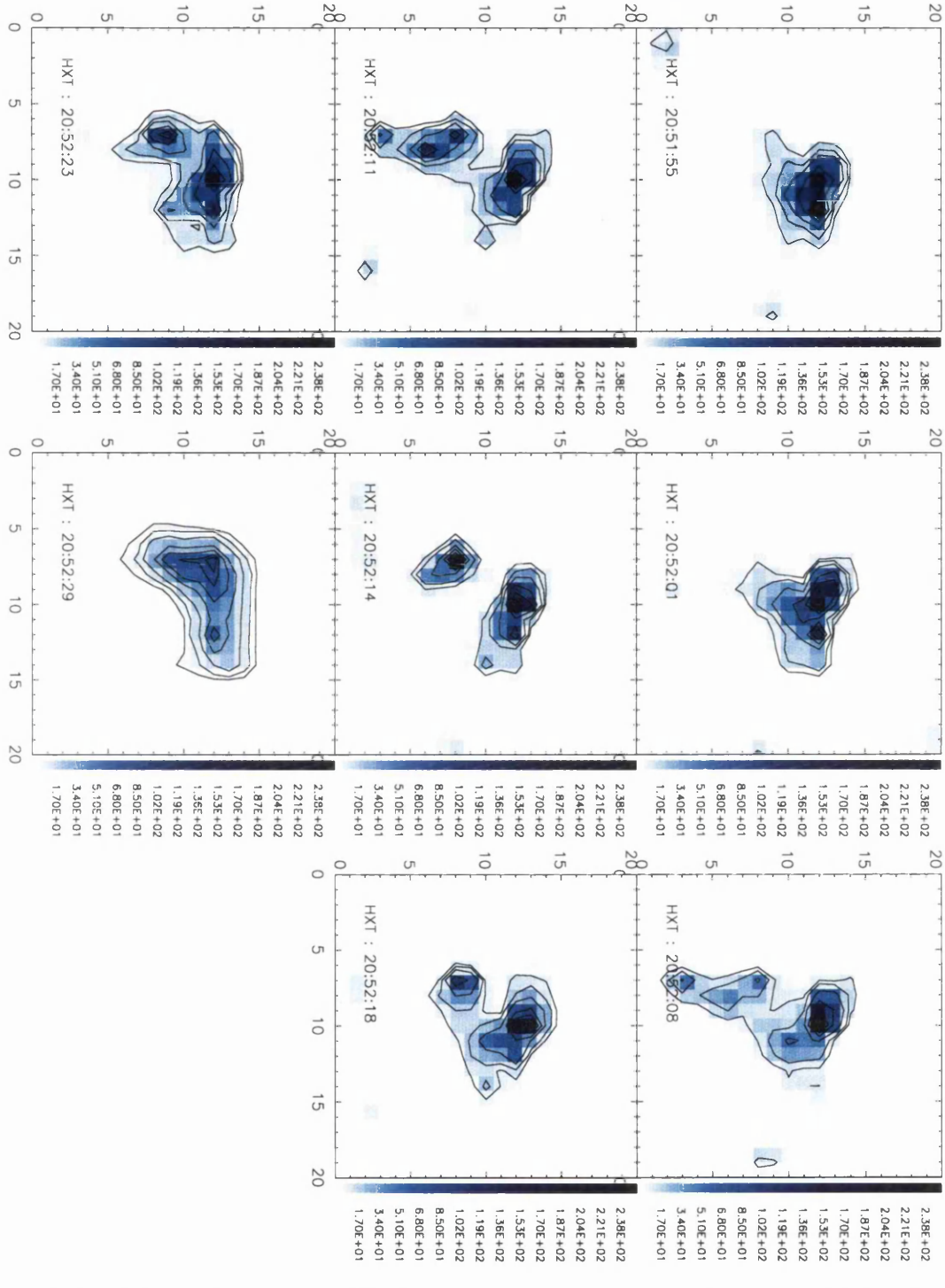

Figure 5.51: Selected M2 band reconstructed images of the 9th November flare 1992 event from 20:51:55 UT to 20:52:29 UT. Each image, based on 200 cts/SC, shows the compact single source evolving into a double footpoint structure

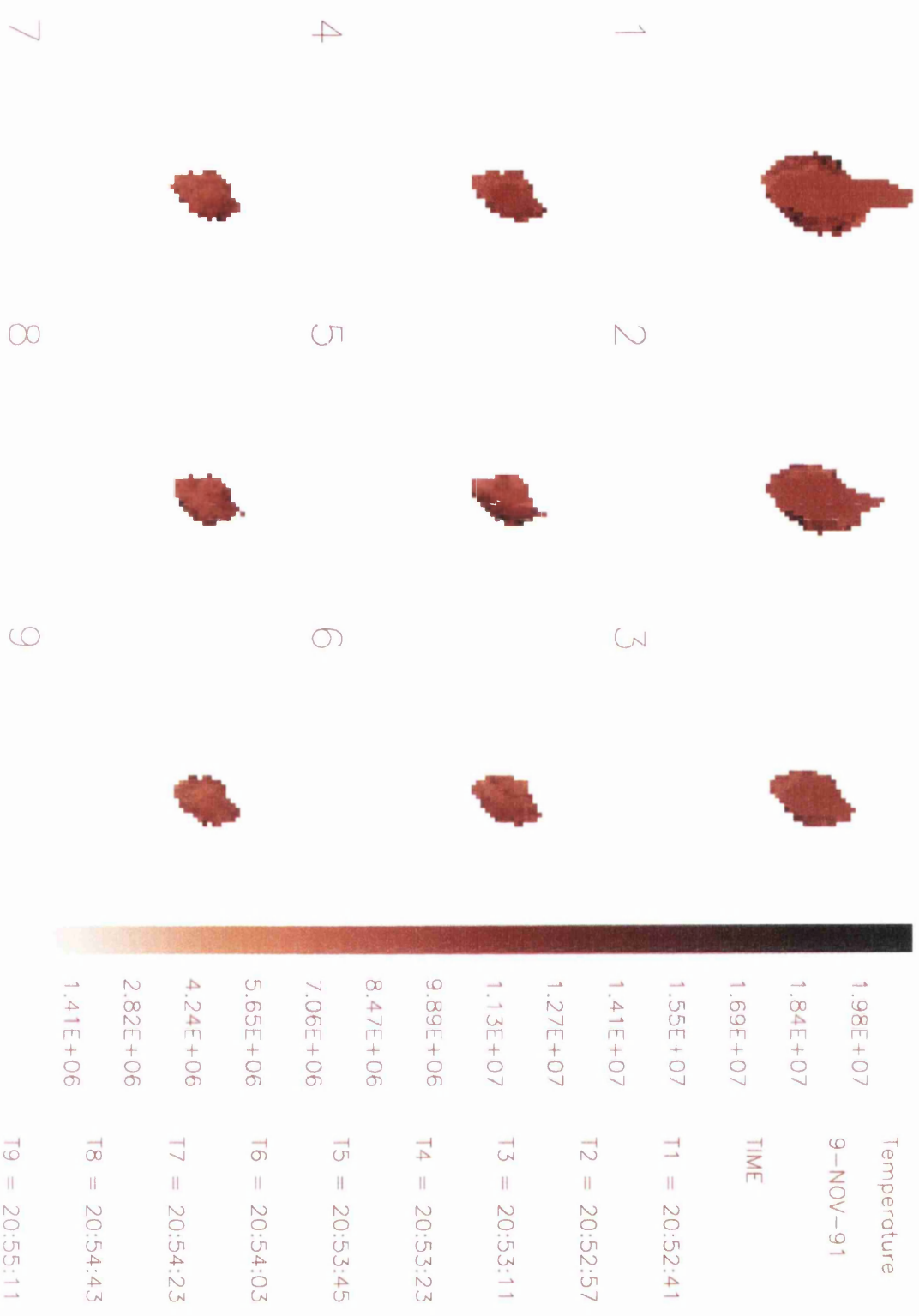

Figure 5.52: Maps of SXT derived temperature structure for the 9 November 1991 event, using filters BE119 and Al12.

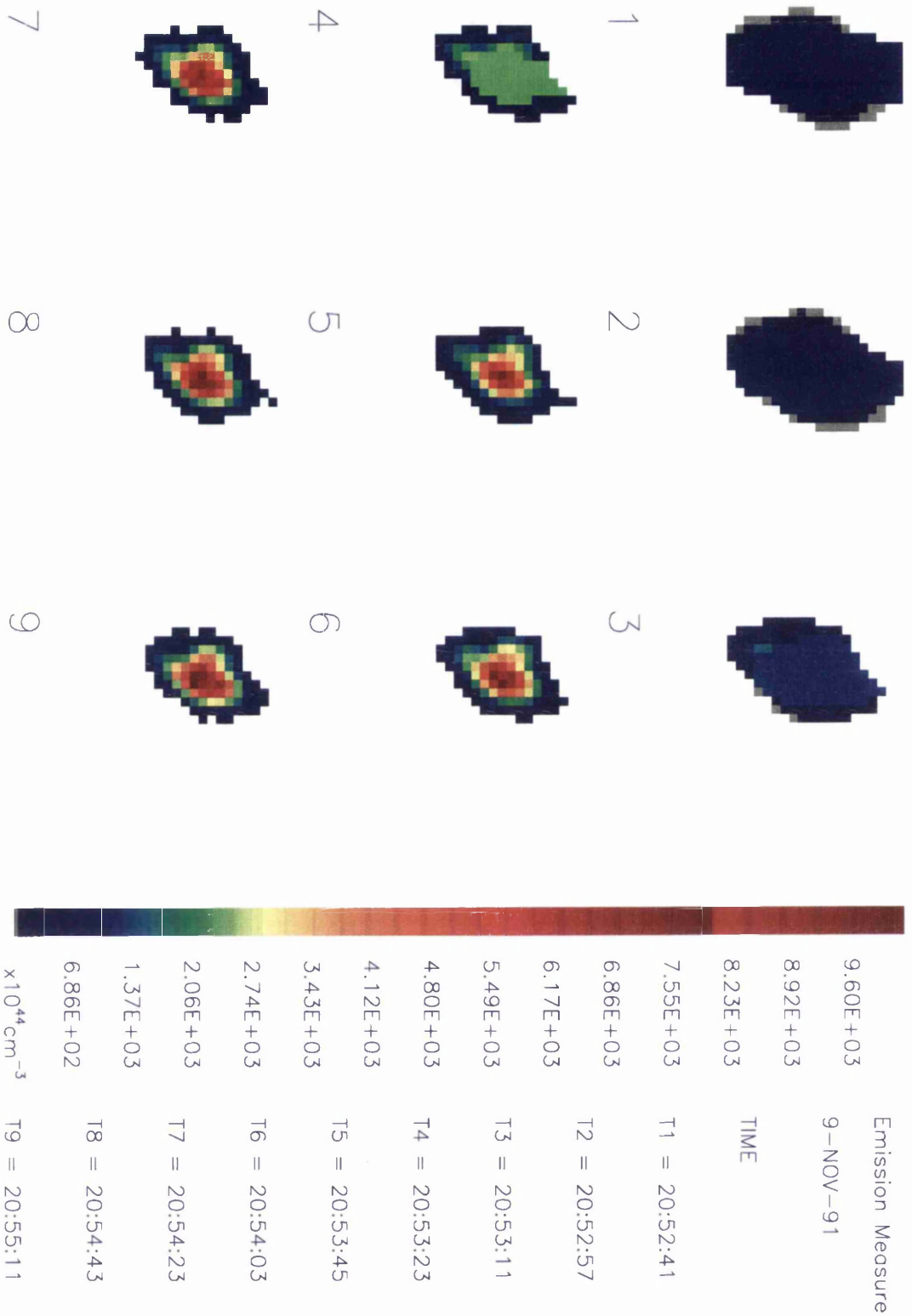

Figure 5.53: Equivalent maps of SXT emission measures estimated from temperature structure derived in Figure 5.52.

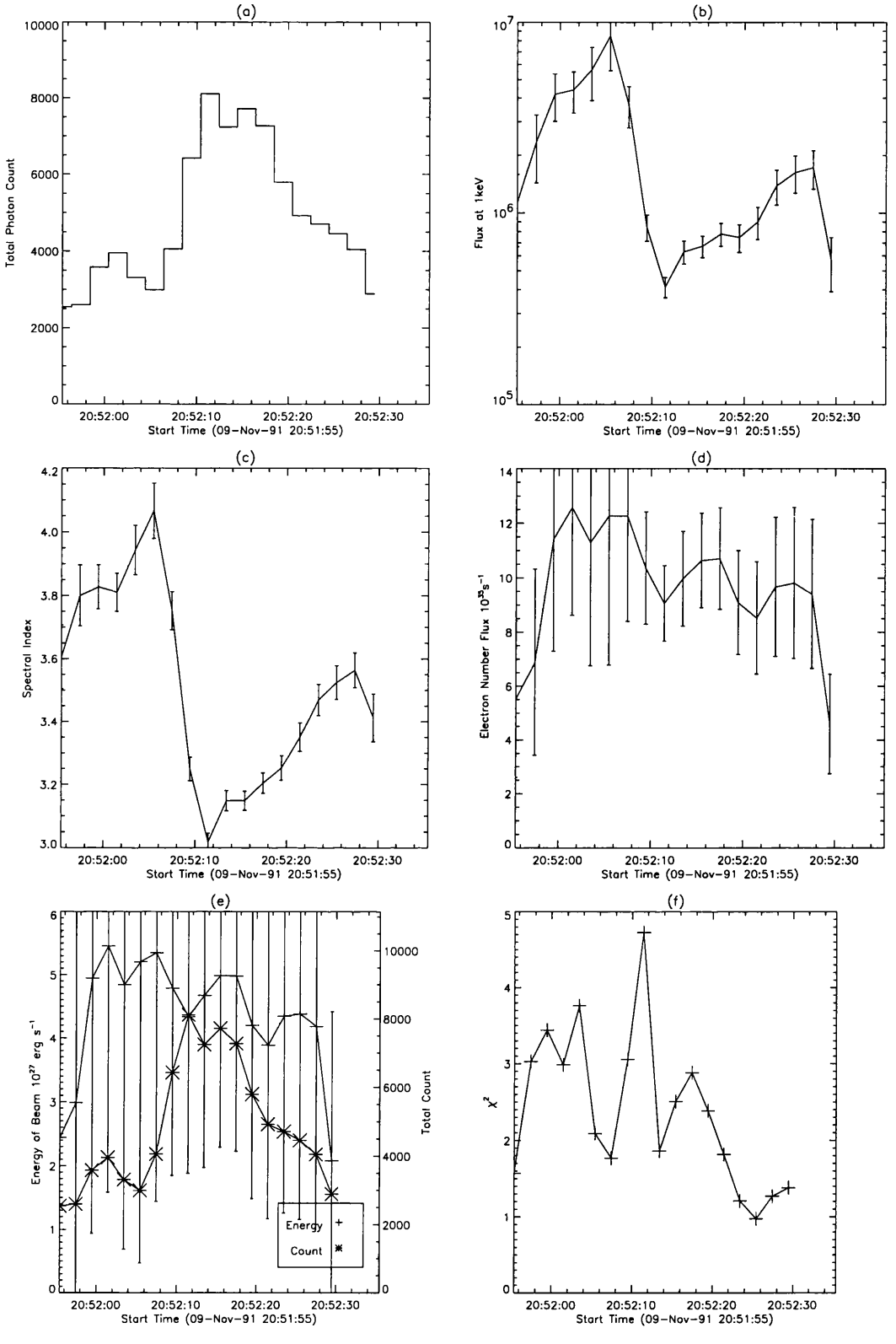

Figure 5.54: Evolution of single power law spectral fit parameters during the 9-Nov-91 flare between 20:51:55-20:52:29. (a) is the total HXS-PH counts for each 2 s interval, (b) and (c) are the power law parameters i.e. the photon flux $\mathrm{keV}^{-1}\mathrm{s}^{-1}$ at 1 keV and photon spectral index. (d) and (e) indicates the inferred electron beam number flux and energy flux assuming an ionised atmosphere and an electron low energy cut-off at 20 keV. Finally (f) shows the reduced χ^2 for each spectral fit.

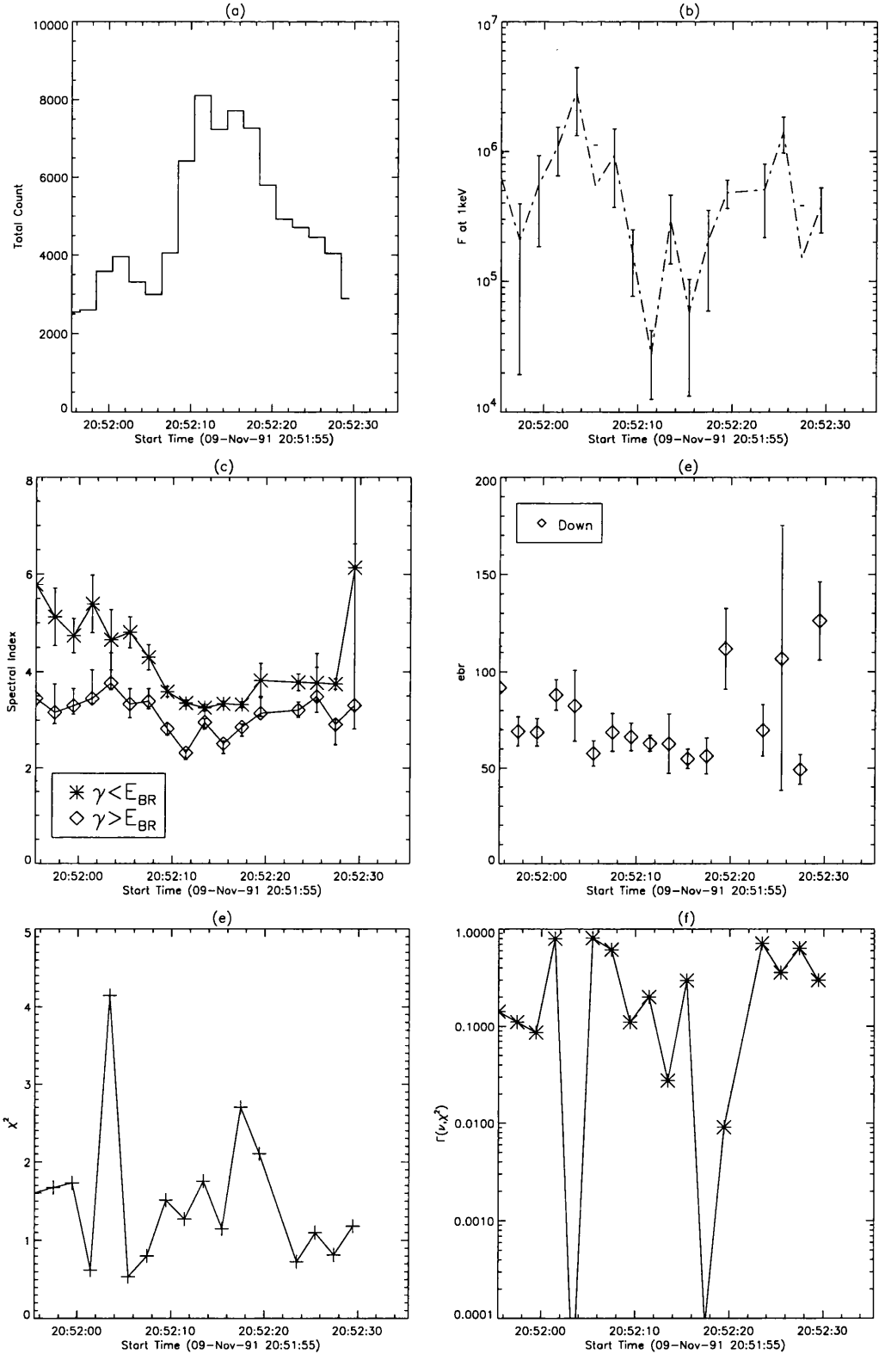

Figure 5.55: Evolution of double power law spectral fit parameters during the 9-Nov-91 flare between 20:51:55-20:52:29. (a) is the total HXS-PH counts for each 2 s interval, (b) and (c) (d) and (e) are the power law parameters i.e. the photon flux $keV^{-1}s^{-1}$ at 1 keV and photon spectral indices below and above the break point and the break point. Finally (f) shows the reduced χ^2 for each spectral fit and (g) the indicator of goodness-of fit for that χ^2.

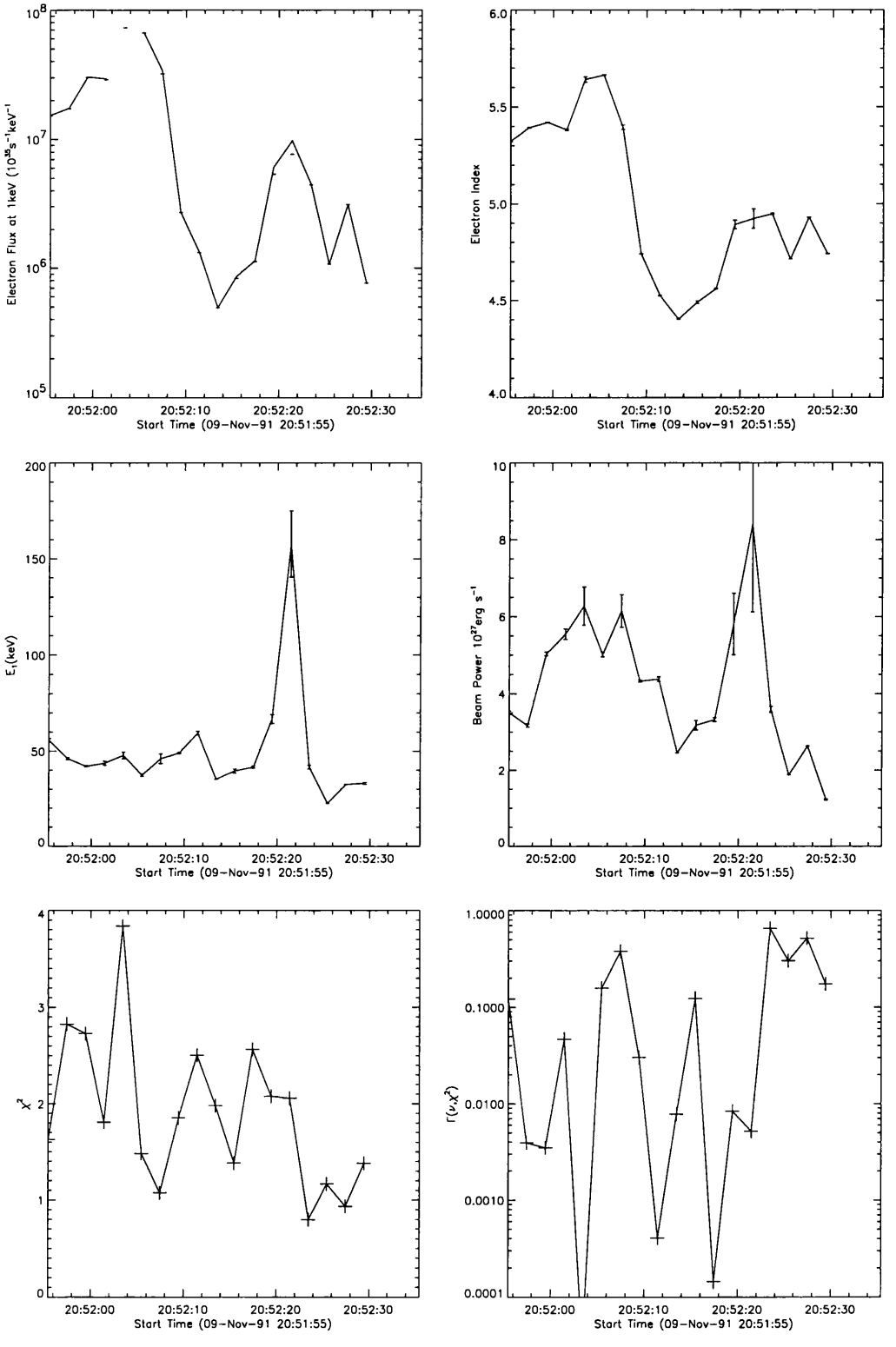

Figure 5.56: Evolution of spectral fit parameters for nonuniformly ionised atmosphere model during the 9-Nov-91 flare between 20:51:55-20:52:29. (a) the electron flux keV^{-1}s^{-1} at 1 keV, (b) the electron spectral index and (c) the electron stopping energy of the transition region. (d) shows the estimate of electron beam energy flux for such parameters with cut-off energy at 20 keV. Finally (f) shows the reduced χ^2 for each spectral fit and (g) the indicator of goodness-of fit for that χ^2.

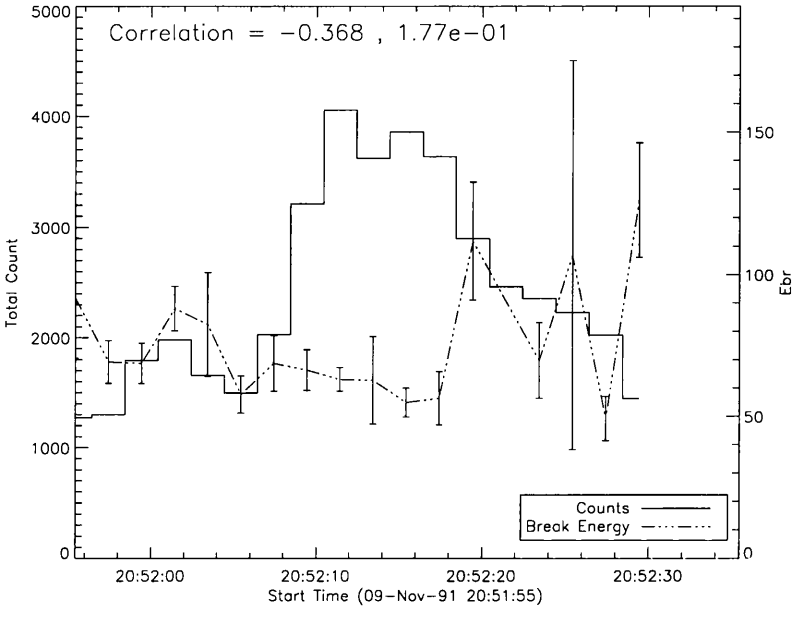

Figure 5.57: Comparison of evolution of observed count rates with the break energy of a double power law for the 9-Nov-91 flare. The rank correlation for these parameters is also indicated.

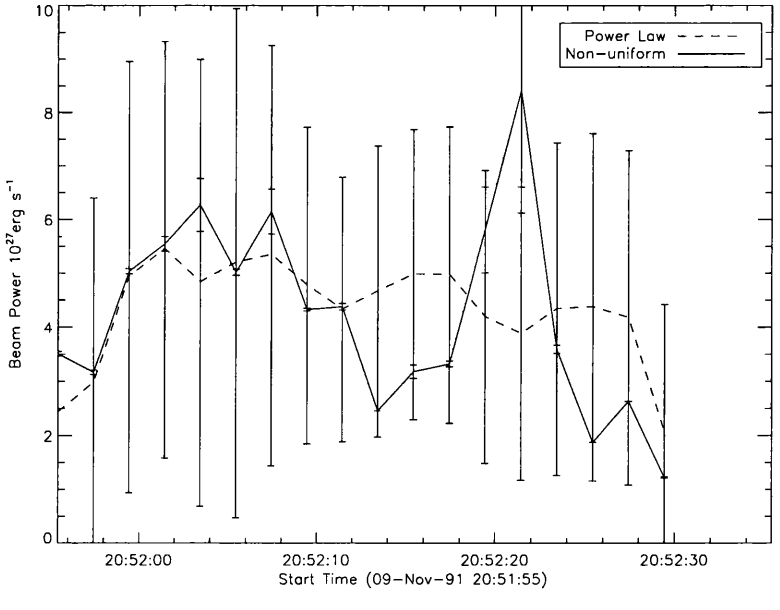

Figure 5.58: Comparison of beam flux for a nonuniform model and from the power law fit assuming an ionised atmosphere, for the 9-Nov-91 flare.

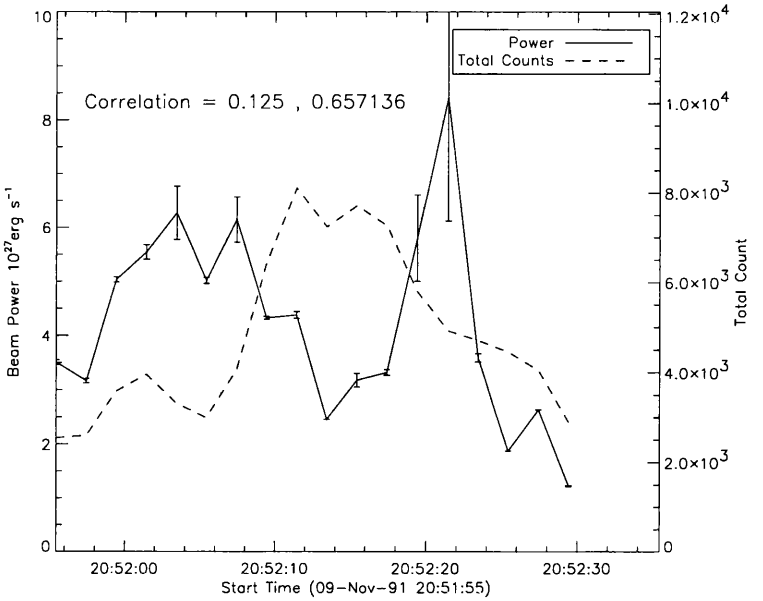

Figure 5.59: Comparison of evolution of nonuniform model electron beam energy flux with the total counts for each time interval, for the 9-Nov-91 flare. The rank correlation for these parameters is also indicated.

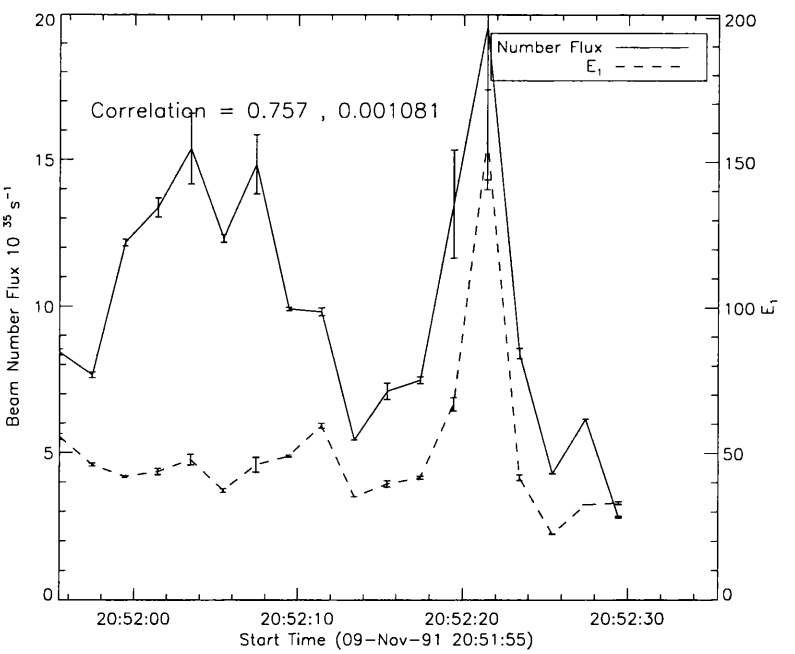

Figure 5.60: Comparison of evolution of nonuniform model electron beam number flux with the stopping energy of an electron which just reaches the chromosphere (E_1), for the 9-Nov-91 flare. The rank correlation for these parameters is also indicated.

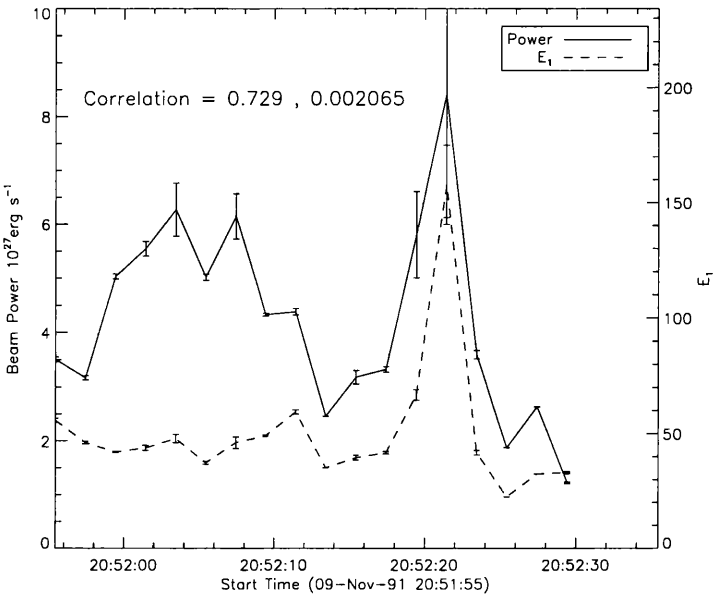

Figure 5.61: Comparison of evolution of nonuniform model electron beam energy flux with the stopping energy of an electron which just reaches the chromosphere (E_1), for the 9-Nov-91 flare. The rank correlation for these parameters is also indicated.

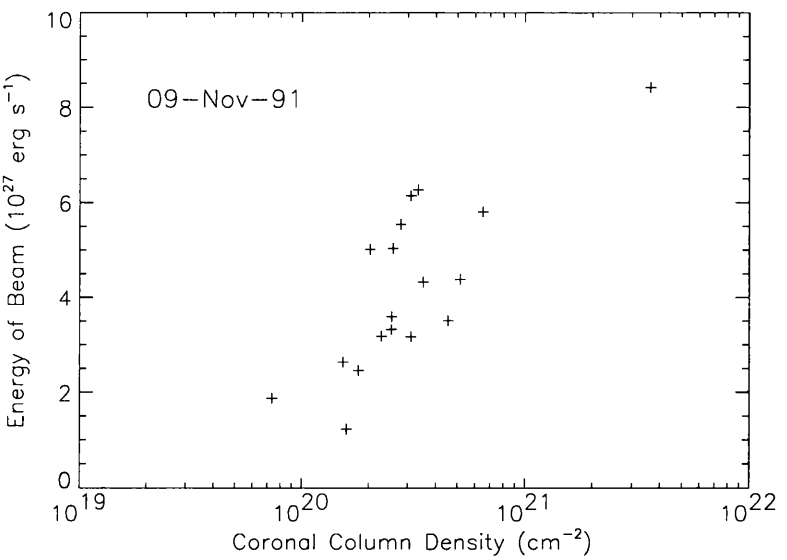

Figure 5.62: Correlation of electron beam flux and coronal column density determined from E_1, for the 9-Nov-91 flare.

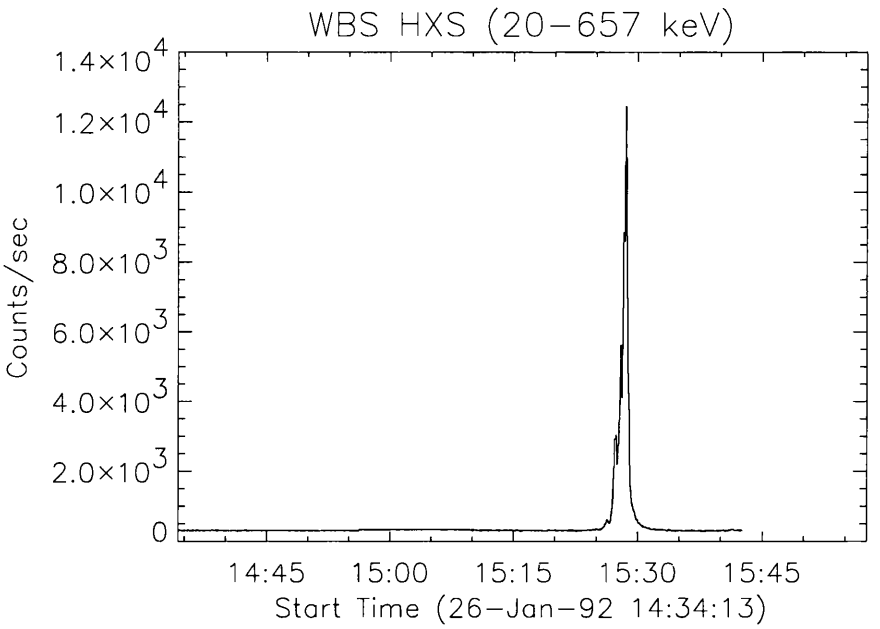

(a)

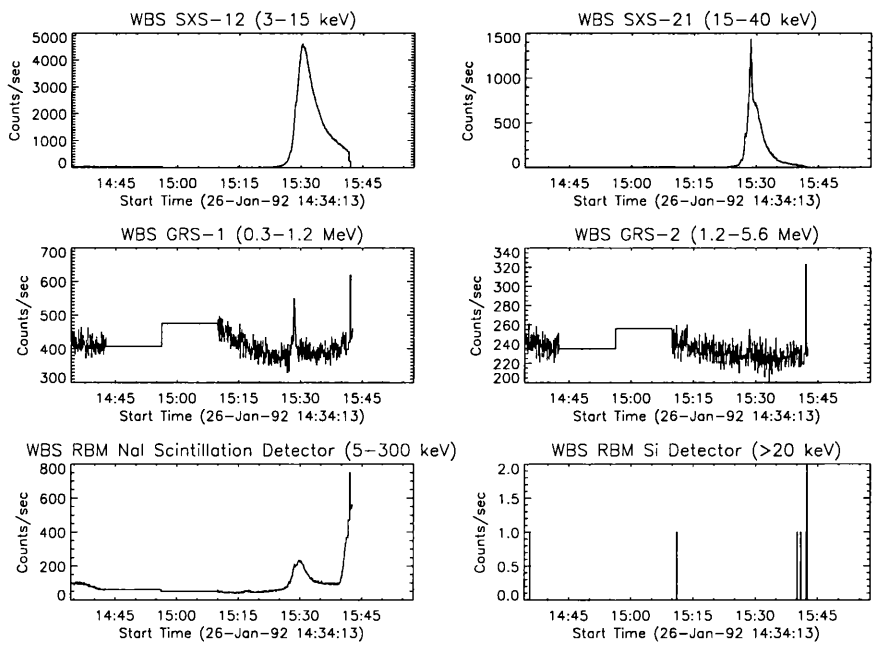

(b)

Figure 5.63: (a) Time profile of the total hard X-rays count rates measured by the hard X-ray spectrometer onboard *YOHKOH* over the observing period which included the class X1.0 flare on 26th January 1992 at 15:28:39 UT. (b) Similar of time profiles for remaining WBS instruments.

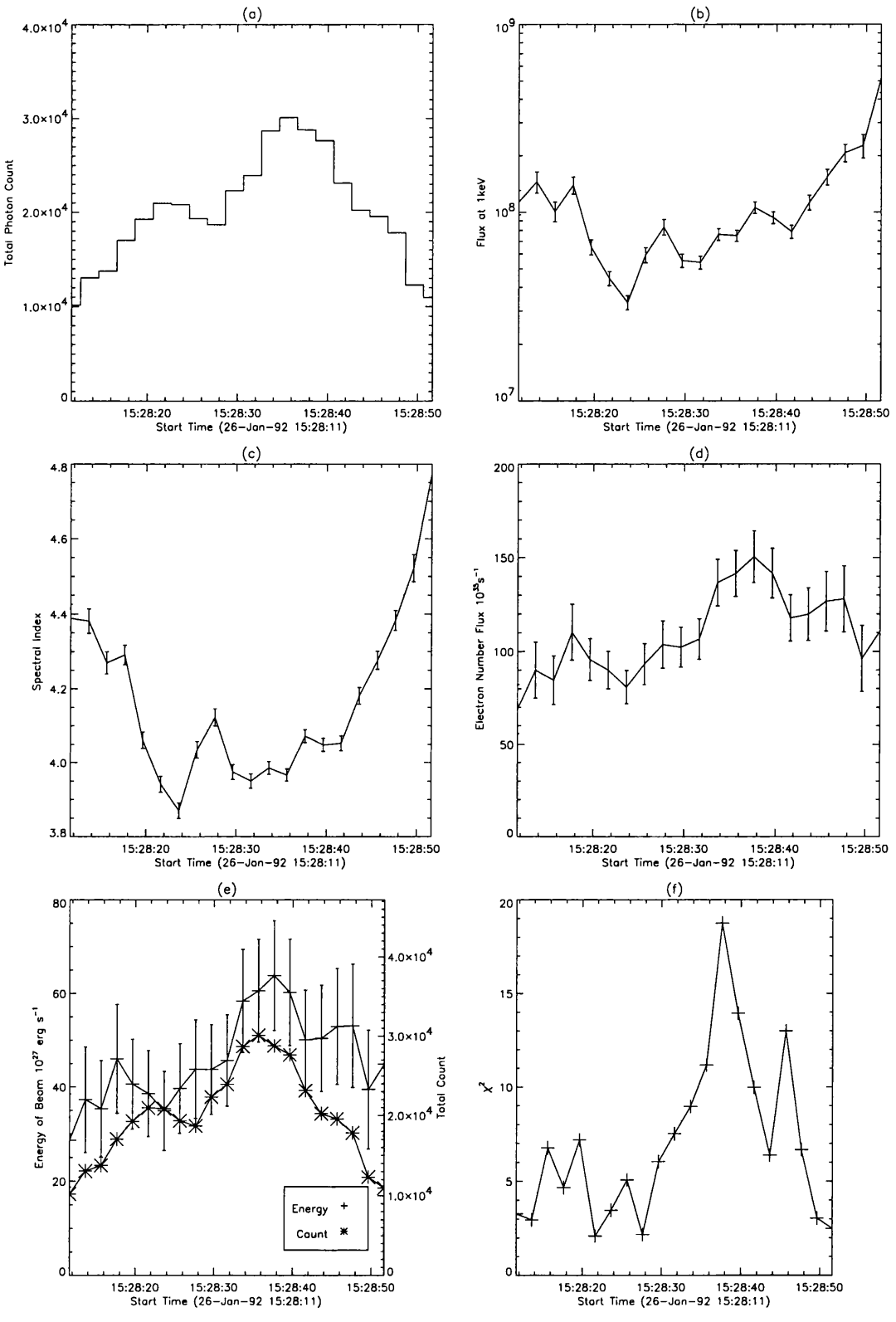

Figure 5.64: Evolution of single power law spectral fit parameters during the 26-Jan-92 flare between 15:28:11-15:28:51. (a) is the total HXS-PH counts for each 2s interval, (b) and (c) are the power law parameters i.e. the photon flux $\mathrm{keV}^{-1}\mathrm{s}^{-1}$ at 1keV and photon spectral index. (d) and (e) indicates the inferred electron beam number flux and energy flux assuming an ionised atmosphere and an electron low energy cut-off at 20 keV. Finally (f) shows the reduced χ^2 for each spectral fit.

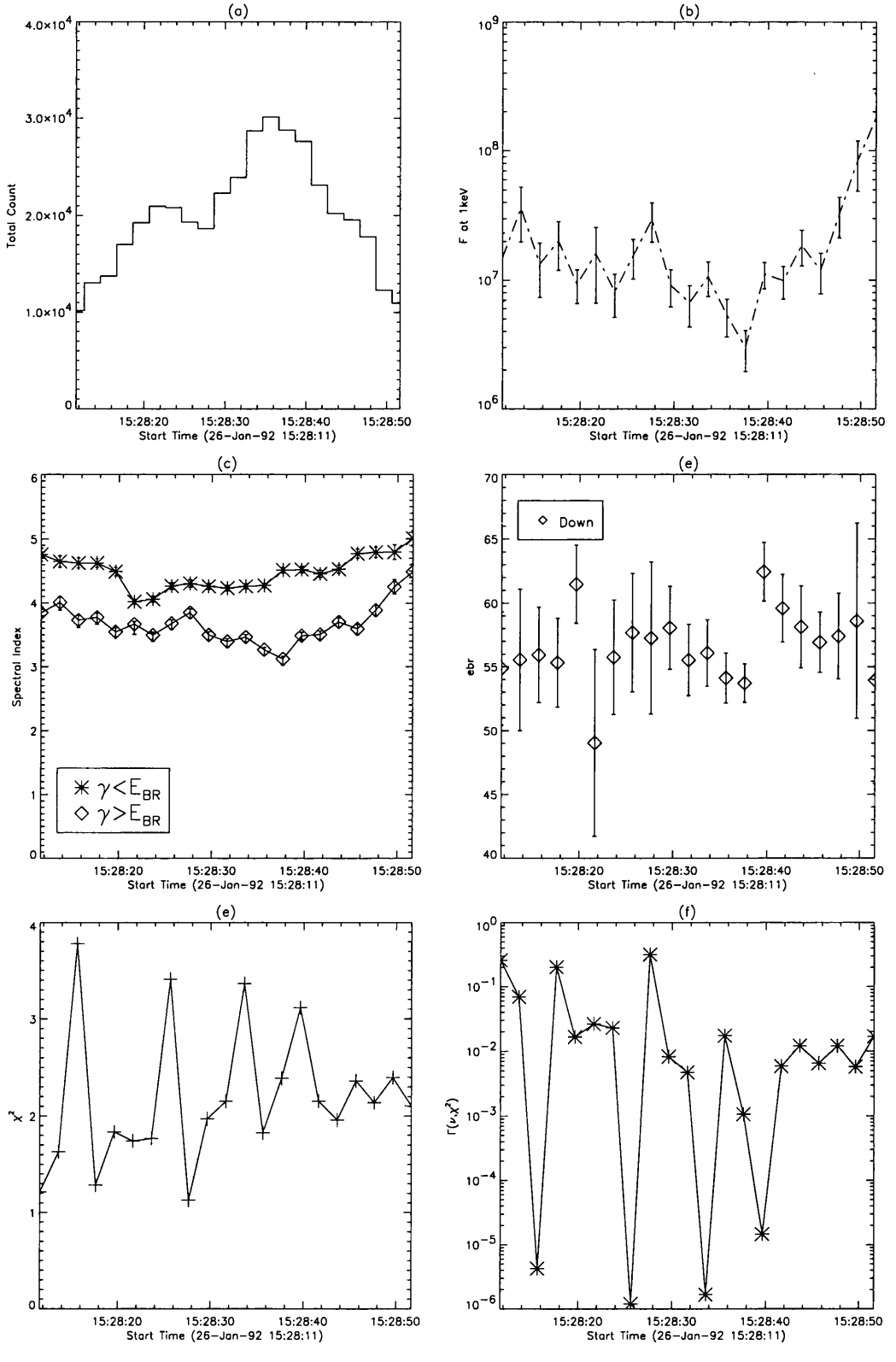

Figure 5.65: Evolution of double power law spectral fit parameters during the 26-Jan-92 flare between 15:28:11-15:28:51. (a) is the total HXS-PH counts for each 2 s interval, (b) and (c) (d) and (e) are the power law parameters i.e. the photon flux $keV^{-1}s^{-1}$ at 1 keV and photon spectral indices below and above the break point and the break point. Finally (f) shows the reduced χ^2 for each spectral fit and (g) the indicator of goodness-of fit for that χ^2.

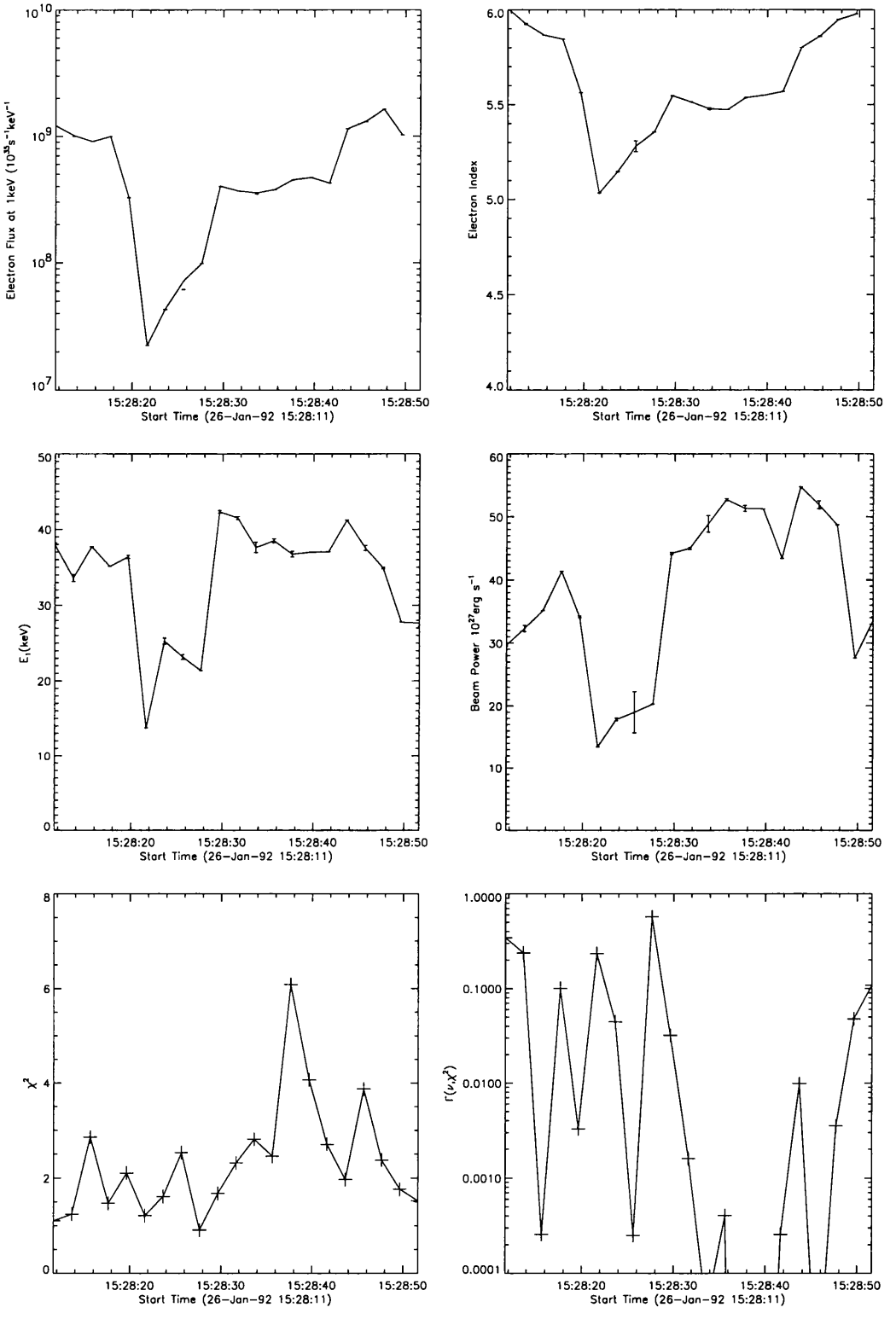

Figure 5.66: Evolution of spectral fit parameters for nonuniformly ionised atmosphere model during the the 26-Jan-92 flare between 15:28:11-15:28:51. (a) the electron flux $\mathrm{keV}^{-1}\mathrm{s}^{-1}$ at 1 keV, (b) the electron spectral index and (c) the electron stopping energy of the transition region. (d) shows the estimate of electron beam energy flux for such parameters with cut-off energy at 20 keV. Finally (f) shows the reduced χ^2 for each spectral fit and (g) the indicator of goodness-of fit for that χ^2.

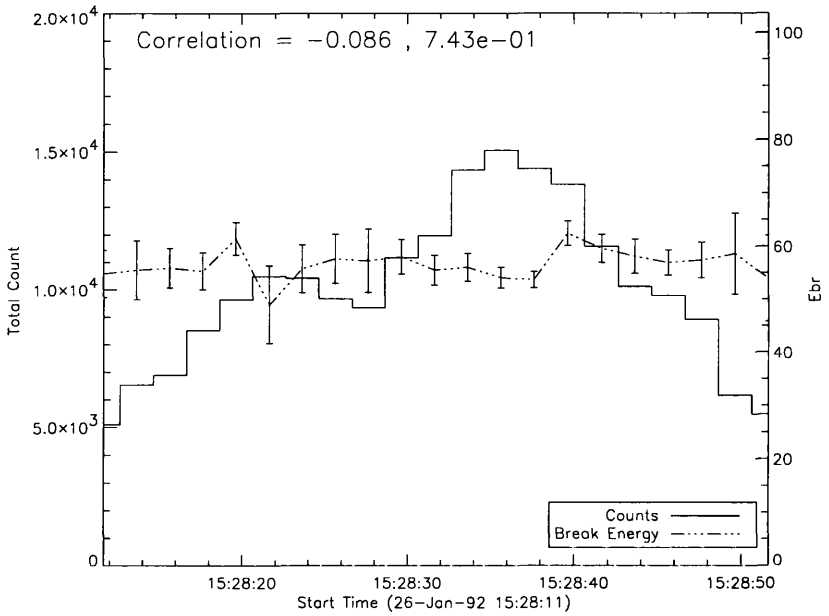

Figure 5.67: Comparison of evolution of observed count rates with the break energy of a double power law for the 26-Jan-92 flare. The rank correlation for these parameters is also indicated.

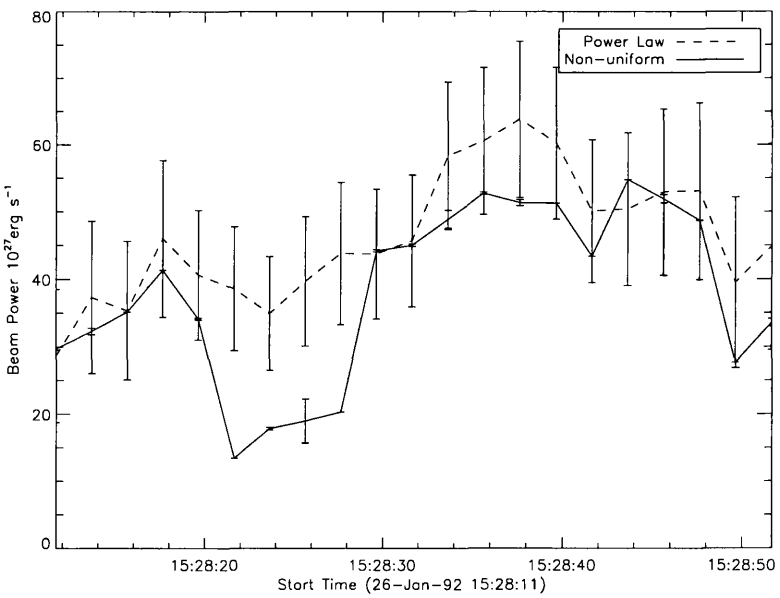

Figure 5.68: Comparison of beam flux for a nonuniform model and from the power law fit assuming an ionised atmosphere, for the 26-Jan-92 flare.

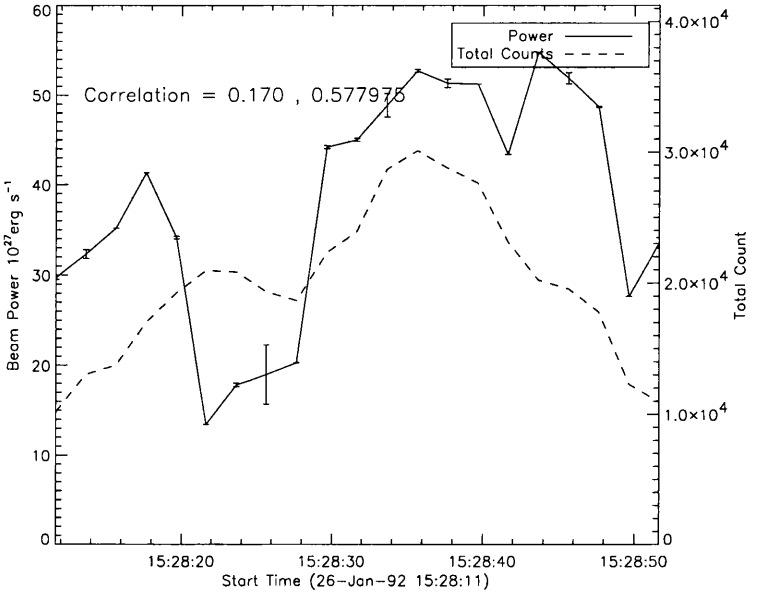

Figure 5.69: Comparison of evolution of nonuniform model electron beam energy flux with the total counts for each time interval, for the 26-Jan-92 flare. The rank correlation for these parameters is also indicated.

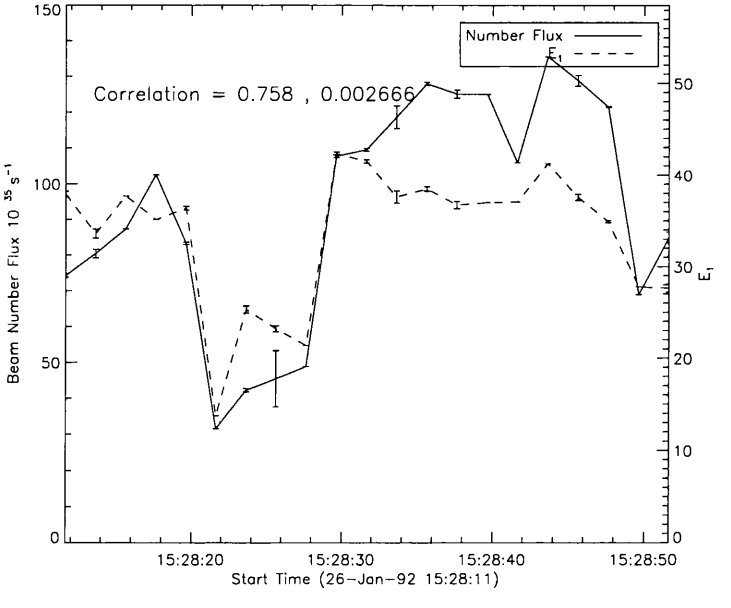

Figure 5.70: Comparison of evolution of nonuniform model electron beam number flux with the stopping energy of an electron which just reaches the chromosphere (E_1), for the 26-Jan-92 flare. The rank correlation for these parameters is also indicated.

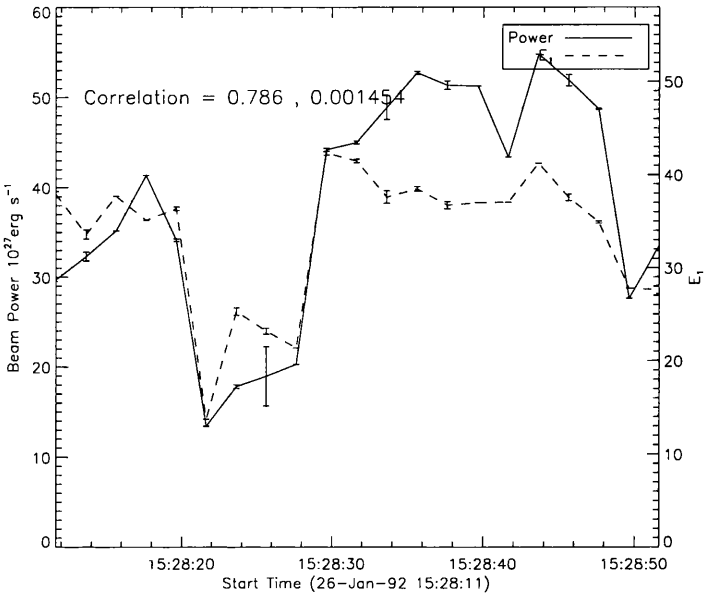

Figure 5.71: Comparison of evolution of nonuniform model electron beam energy flux with the stopping energy of an electron which just reaches the chromosphere (E_1), for the 26-Jan-92 flare. The rank correlation for these parameters is also indicated.

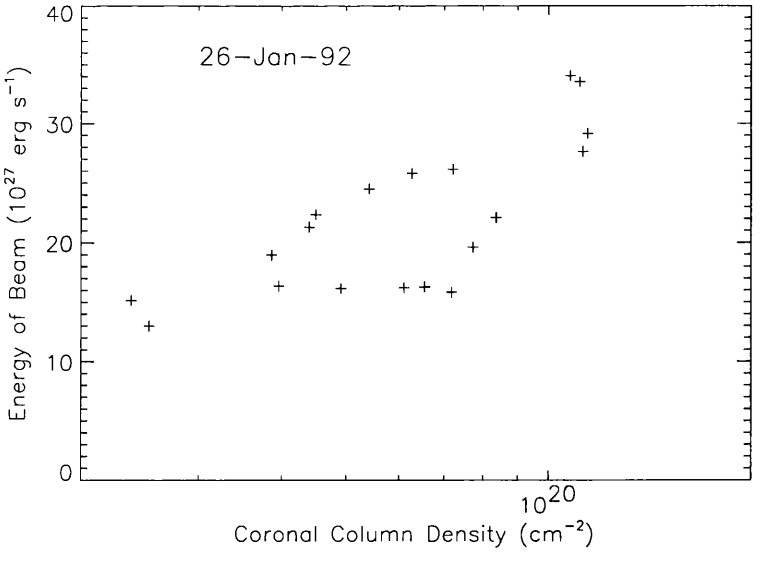

Figure 5.72: Correlation of electron beam flux and coronal column density determined from E_1, for the 26-Jan-92 flare.

5.7 4th December 1991 Flare

The flare on 4th December commenced at 17:42 UT has a GOES class of M4.1 and H_α importance SF. Occurring at N18E56 it is associated with NOAA active region 6952. The estimated trapping density and time-of-flight loop length for this flare is given by Aschwanden as $1.23 \pm 0.29 \times 10^{11}$ cm^{-3} and $19.6 \pm 2.8 \times 10^8$ cm respectively. This therefore leads to column density of $2.41 \pm 0.66 \times 10^{20}$ cm^{-2} or E_1 value of 40.6 ± 5.6keV.

The best fit model parameters for this event are shown in Figures 5.74-5.76. The estimated E_1 ranged between 20-100 keV, although these large values of E_1 were determined at the start and end of the flare when counts were relatively low. The correlations between the NUIPLE model parameters were (cf. Figures (5.77-5.82)

	Correlation Co-efficient	Significance
Electron Flux A and E_1	0.672	0.023
Spectral Index δ and E_1	0.436	0.180
Electron Number Flux and E_1	0.827	1.67×10^{-3}
Electron Energy Flux and E_1	0.827	1.67×10^{-3}
Energy Flux and Count Rates	-0.06	0.85

Once again a high correlation is found between E_1 and energy flux of the electron beam.

5.8 Conclusions

From the modelling of HXR spectra as due to thick target bremsstrahlung from a power law electron distribution through a nonuniformly ionised atmosphere a strong correlation between the energy flux of the electron beam and the column density from acceleration region to transition region is found. This correlation can be seen clearly in Figure 5.83. As well as showing the correlation for each flare, we can also see a strong dependence on the size of the flare. Both M class flares (9 November and the 4 Dec) have similar correlations along with the precursor and post-impulsive phase of the 15 Nov flare. The larger X class flares of 27 Oct and 26 Jan appears to have a similar correlations. The majority of

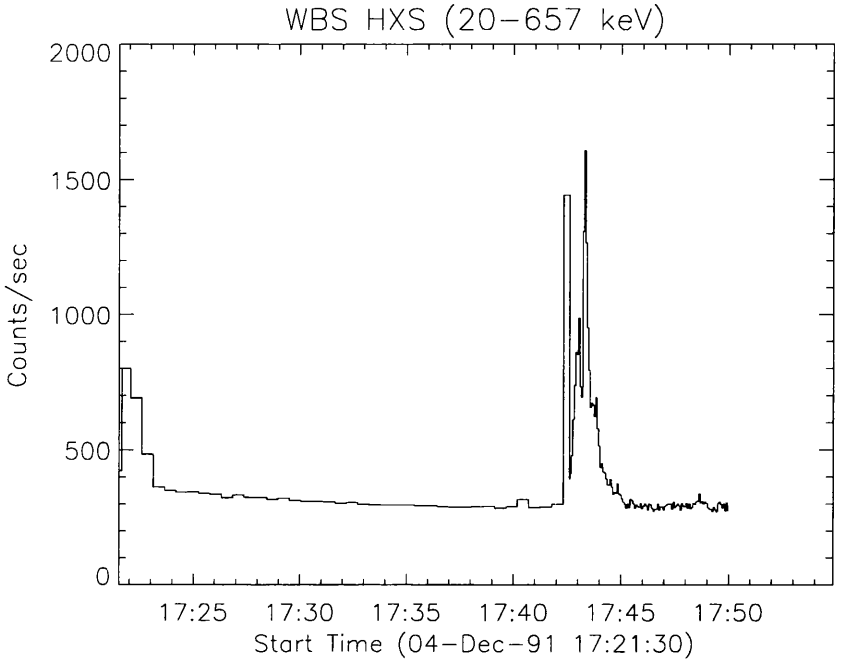

(a)

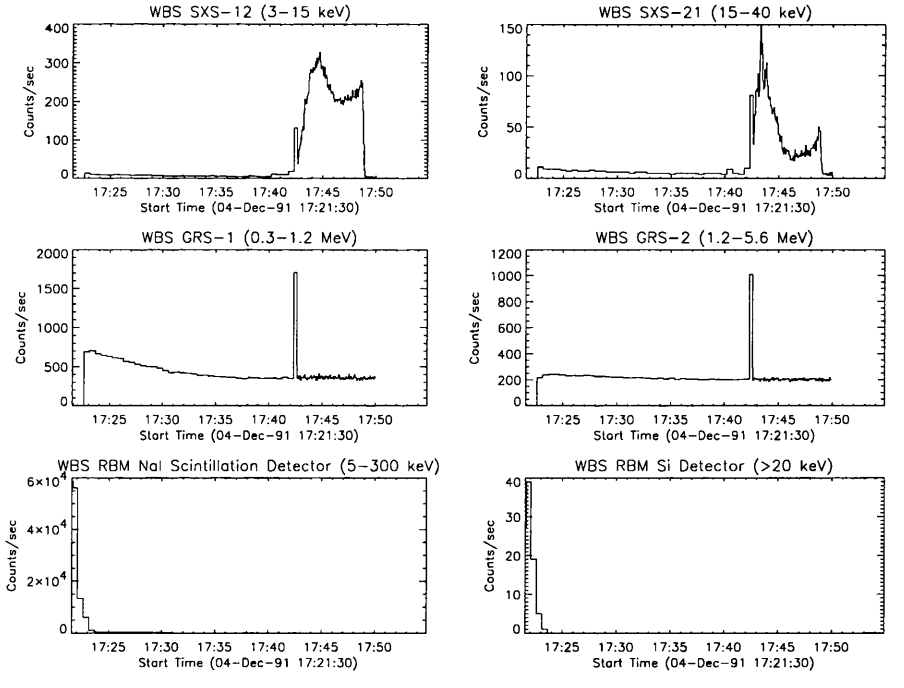

(b)

Figure 5.73: (a) Time profile of the total hard X-rays count rates measured by the hard X-ray spectrometer onboard *YOHKOH* over the observing period which included the class M4.1 flare on 4th December 1991 at17:42:34 UT. (b) Similar of time profiles for remaining WBS instruments.

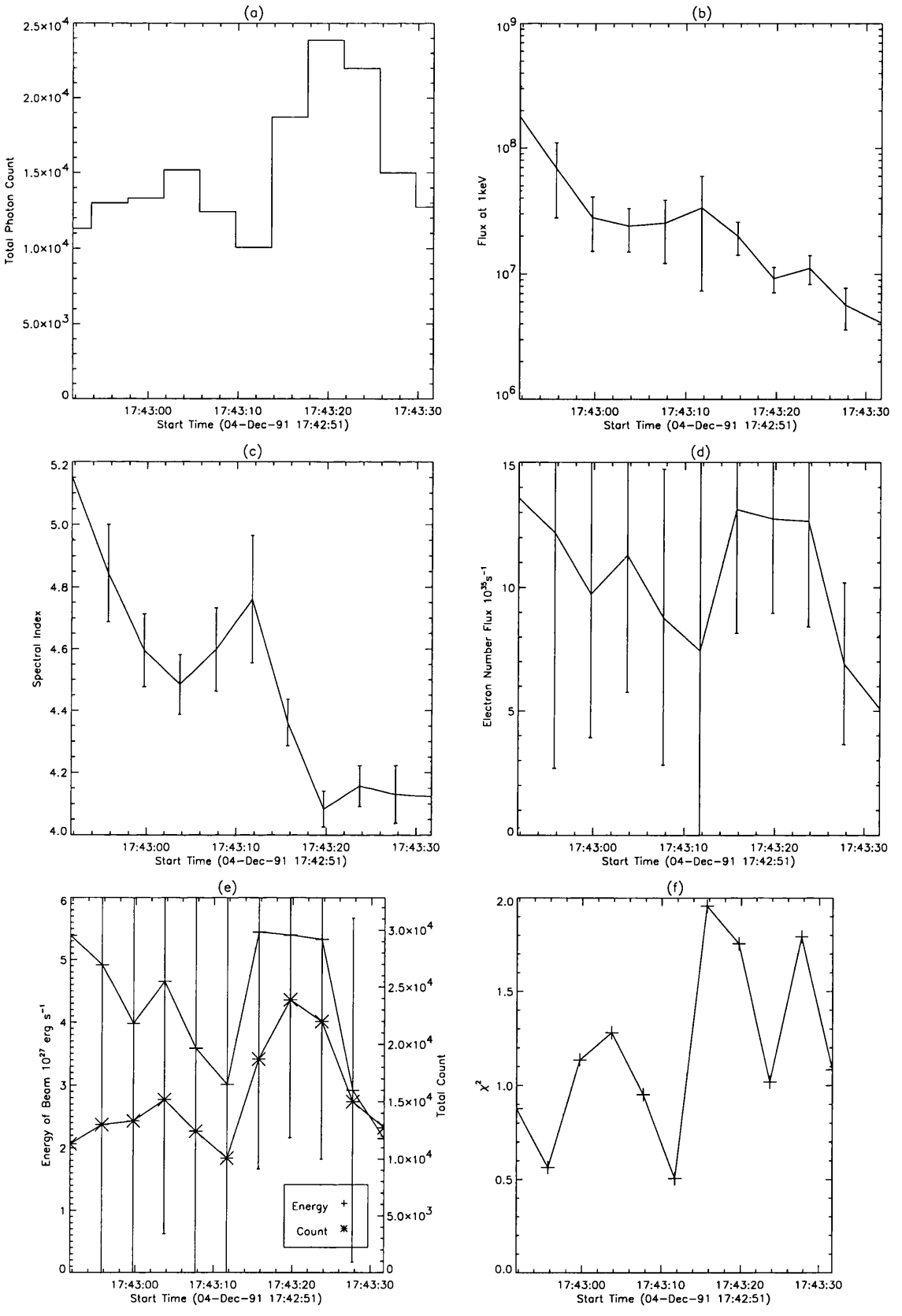

Figure 5.74: Evolution of single power law spectral fit parameters during the 4-Dec-91 flare between 17:42:51-17:43:31. (a) is the total HXS-PH counts for each 4s interval, (b) and (c) are the power law parameters i.e. the photon flux $\mathrm{keV}^{-1}\mathrm{s}^{-1}$ at 1keV and photon spectral index. (d) and (e) indicates the inferred electron beam number flux and energy flux assuming an ionised atmosphere and an electron low energy cut-off at 20 keV. Finally (f) shows the reduced χ^2 for each spectral fit.

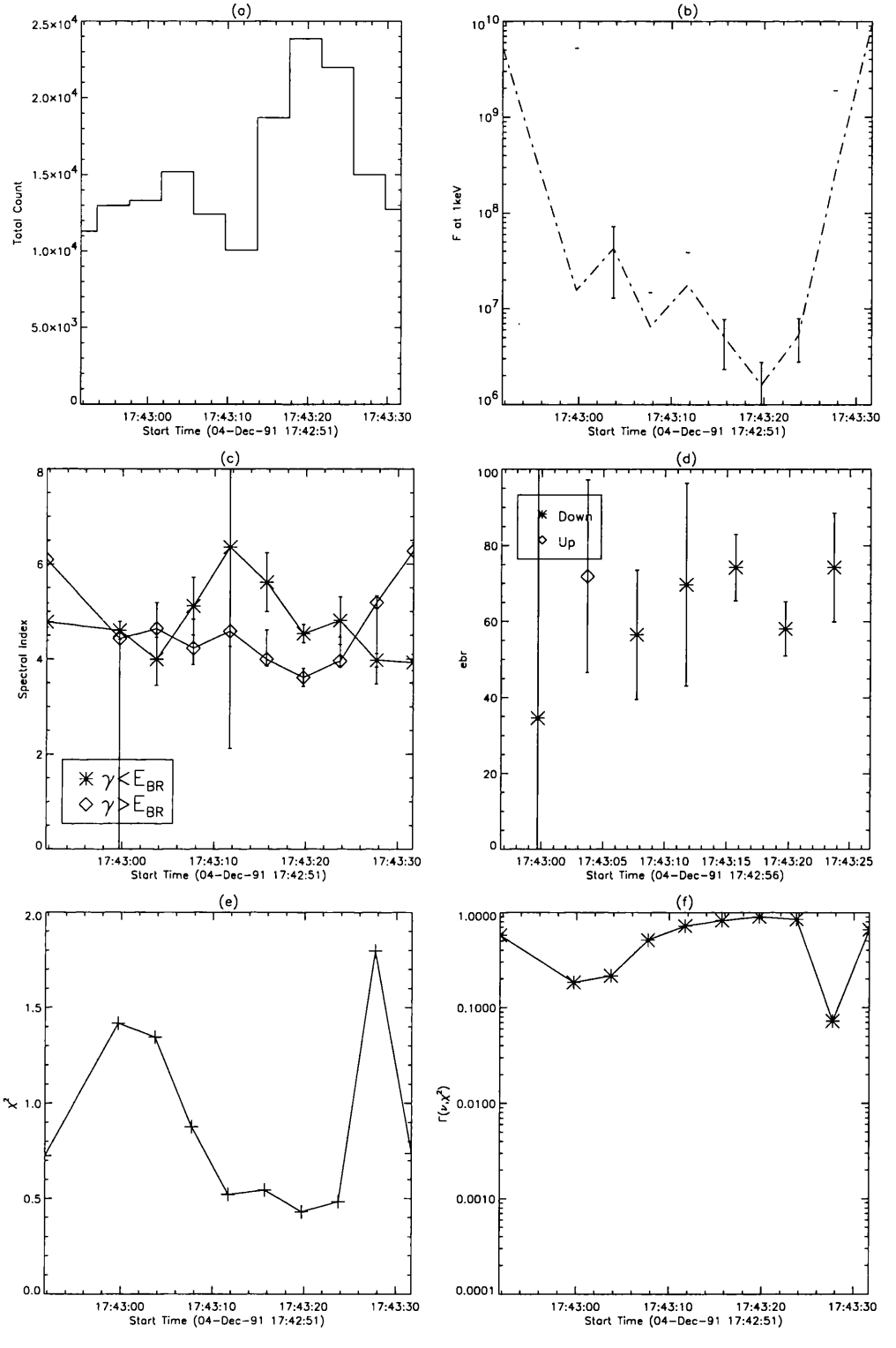

Figure 5.75: Evolution of double power law spectral fit parameters during the 4-Dec-91 flare between 17:42:51-17:43:31. (a) is the total HXS-PH counts for each 4 s interval, (b) and (c) (d) and (e) are the power law parameters i.e. the photon flux $\mathrm{keV}^{-1}\mathrm{s}^{-1}$ at 1 keV and photon spectral indices below and above the break point and the break point. Finally (f) shows the reduced χ^2 for each spectral fit and (g) the indicator of goodness-of fit for that χ^2.

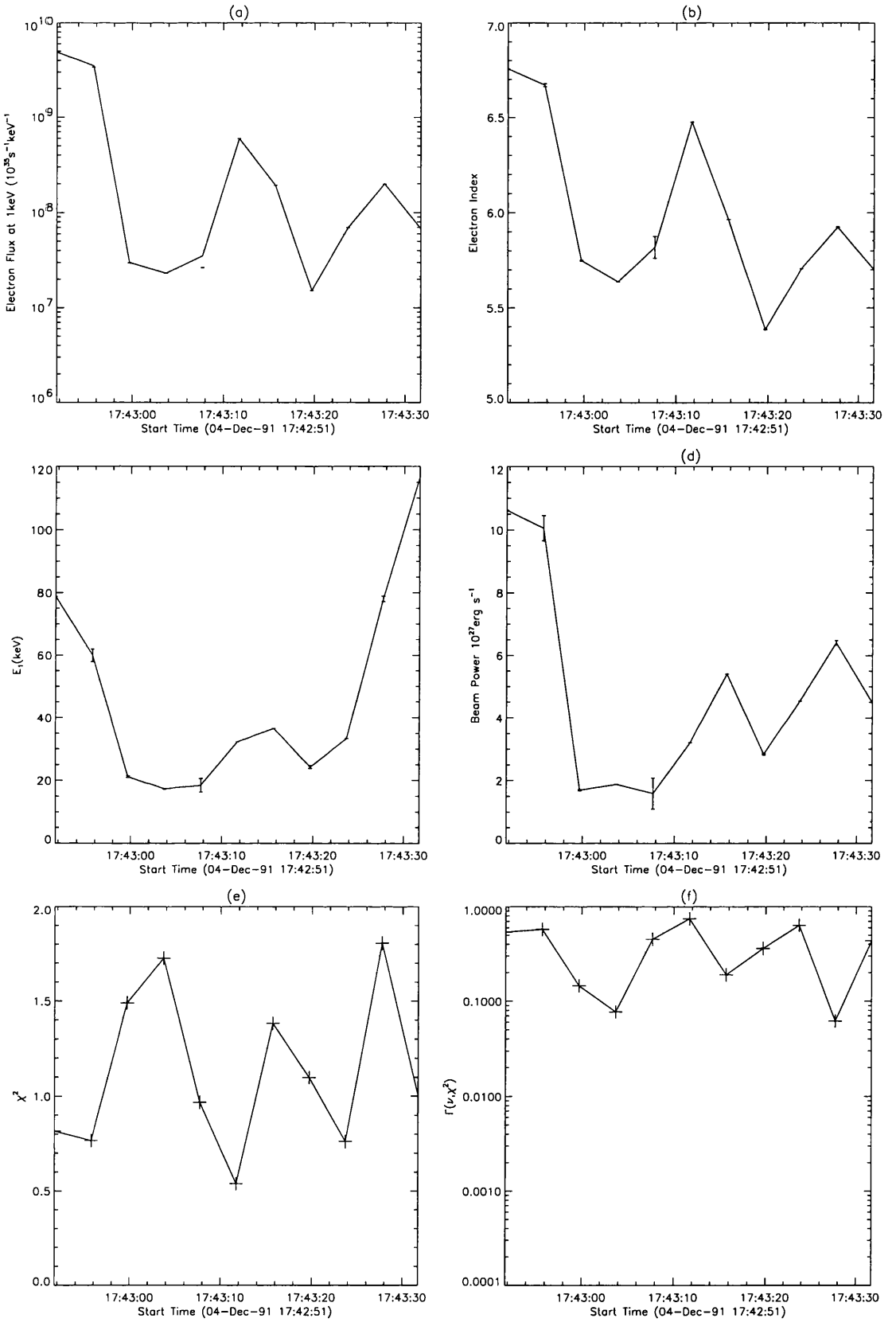

Figure 5.76: Evolution of spectral fit parameters for nonuniformly ionised atmosphere model during the 4-Dec-91 flare between 17:42:51-17:43:31. (a) the electron flux keV^{-1}s^{-1} at 1 keV, (b) the electron spectral index and (c) the electron stopping energy of the transition region. (d) shows the estimate of electron beam energy flux for such parameters with cut-off energy at 20 keV. Finally (f) shows the reduced χ^2 for each spectral fit and (g) the indicator of goodness-of fit for that χ^2.

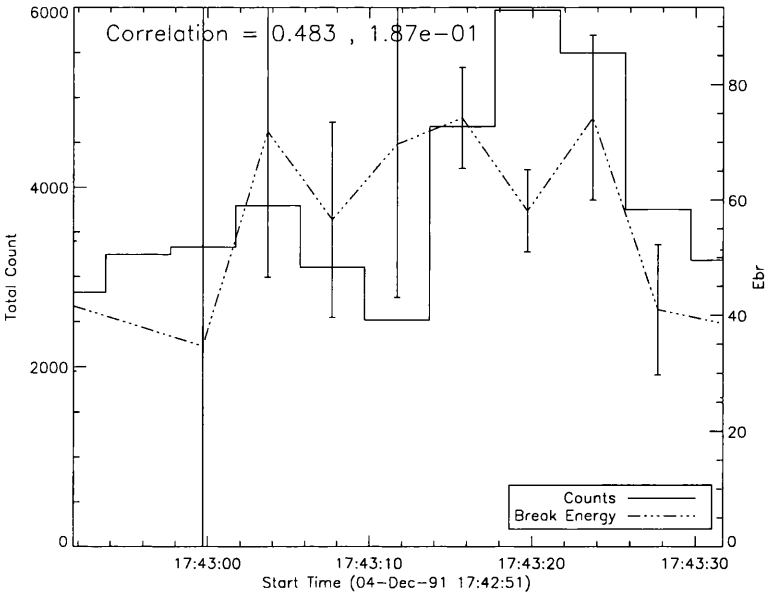

Figure 5.77: Comparison of evolution of observed count rates with the break energy of a double power law for the 4-Dec-91 flare. The rank correlation for these parameters is also indicated.

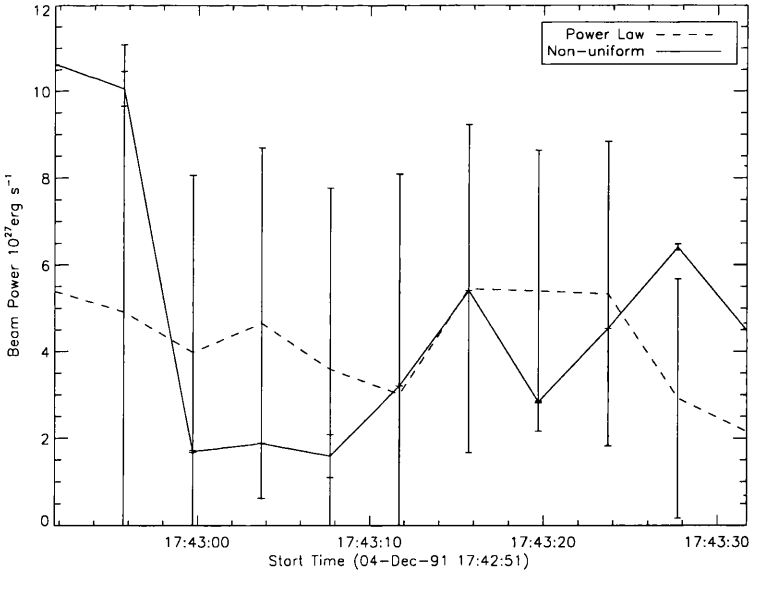

Figure 5.78: Comparison of beam flux for a nonuniform model and from the power law fit assuming an ionised atmosphere, for the 4-Dec-91 flare.

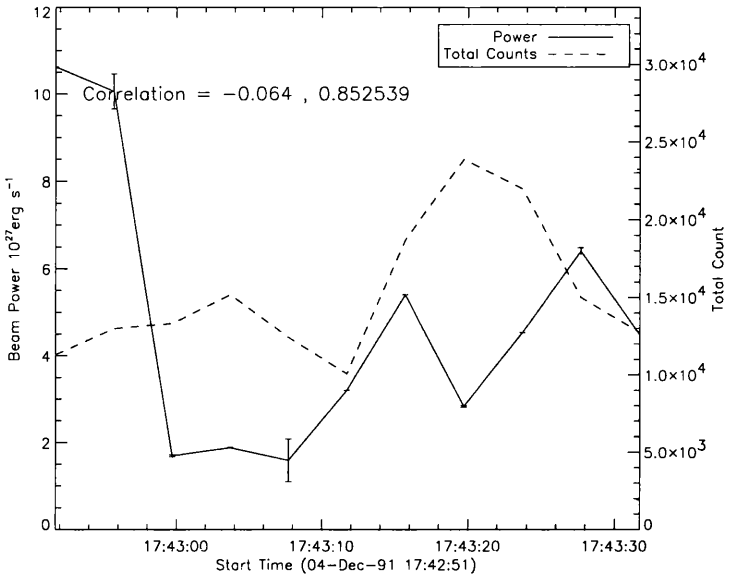

Figure 5.79: Comparison of evolution of nonuniform model electron beam energy flux with the total counts for each time interval, for the 4-Dec-91 flare. The rank correlation for these parameters is also indicated.

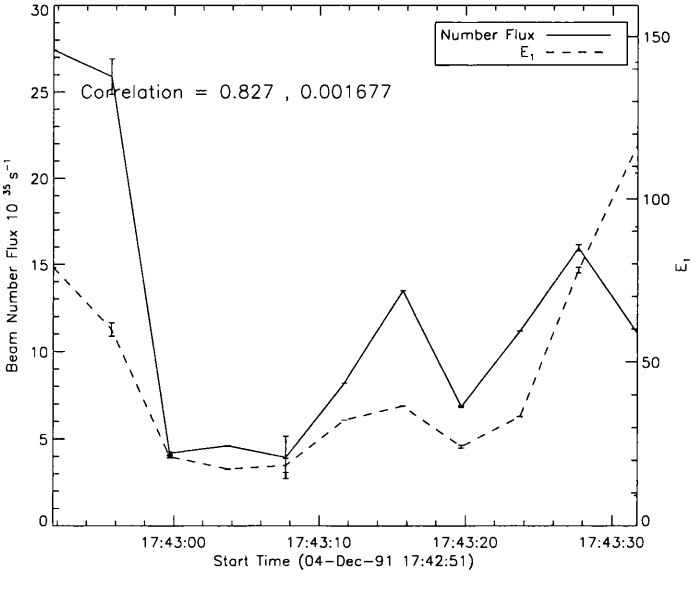

Figure 5.80: Comparison of evolution of nonuniform model electron beam number flux with the stopping energy of an electron which just reaches the chromosphere (E_1), for the 4-Dec-91 flare. The rank correlation for these parameters is also indicated.

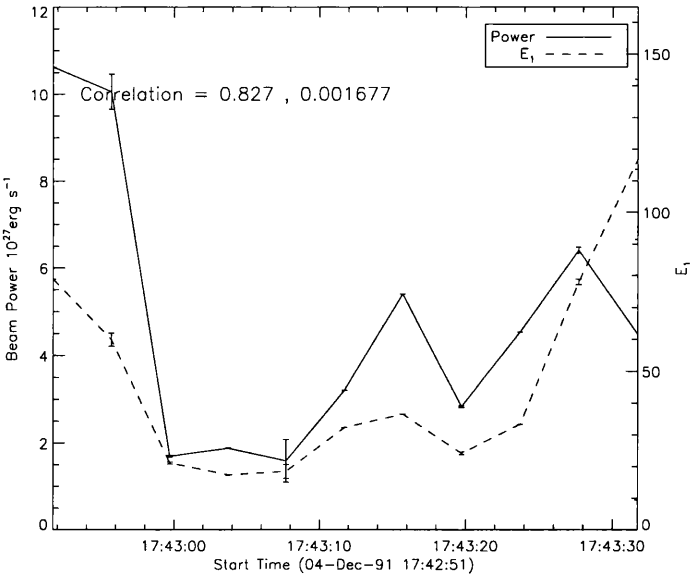

Figure 5.81: Comparison of evolution of nonuniform model electron beam energy flux with the stopping energy of an electron which just reaches the chromosphere (E_1), for the 4-Dec-91 flare. The rank correlation for these parameters is also indicated.

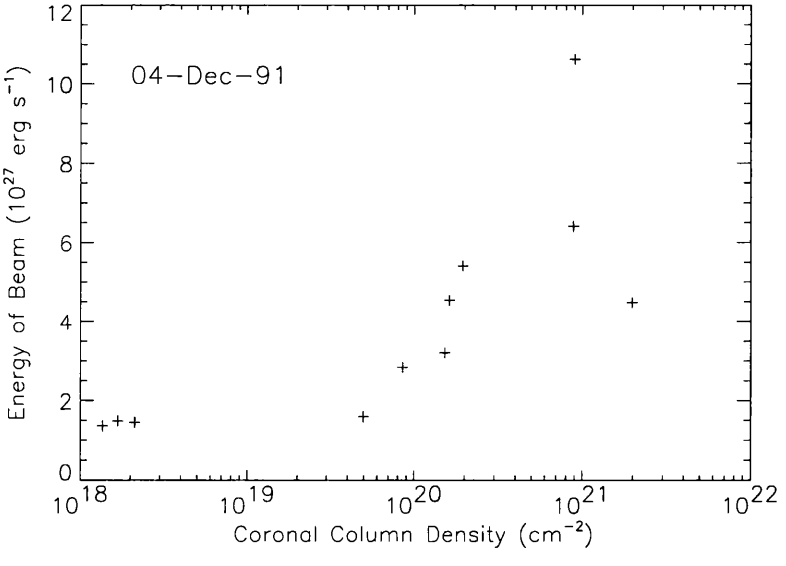

Figure 5.82: Correlation of electron beam flux and coronal column density determined from E_1, for the 4-Dec-91 flare.

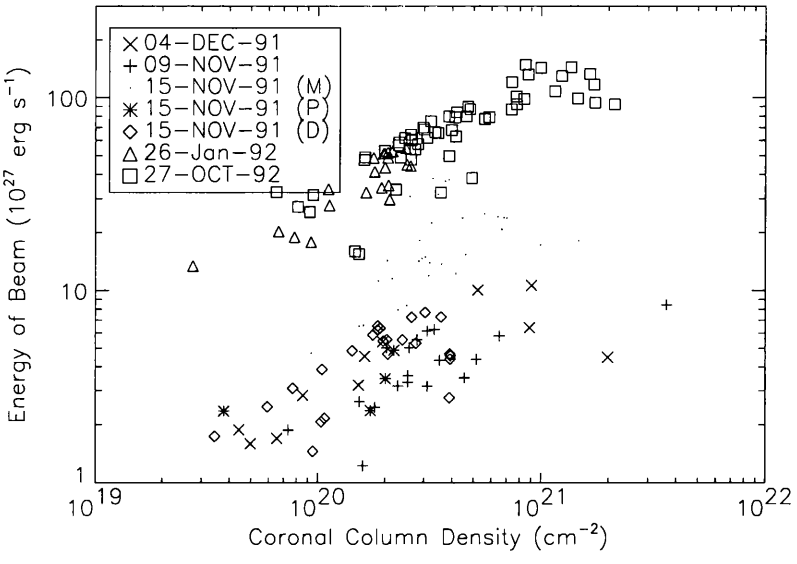

Figure 5.83: Correlation of electron beam flux and coronal column density determined from E_1, for all flares analysed.

values of coronal column density obtained are physically realistic. In comparison with the coronal column density derived from hard X-ray timing hard X-ray timing models they are not inconsistent. In addition the estimates of column density of the SXT loop are also roughly consistent although these estimates depend greatly on the geometry and size of loop assumed. The key difference between HXR column density estimates and SXT estimates is their time evolution. While the SXT column density increases steadily over the flare, the HXR column density estimates have a highly structured time evolution.

The structured evolution of coronal column density and correlation between beam energy flux must imply that the hard X-ray electrons are travelling through loops where no accumulation of evaporated material is occurring, as in the soft X-ray loop. Therefore either the hard X-ray loop is open and evaporated material is escaping or the acceleration region is moving and the hard X-ray producing electrons are injected into larger and larger loops. An open loop model though would require that the evaporated material had a velocity sufficient to travel the length of the loop within the observed time resolution of the spectra i.e. in this case $\sim$ 2 s. Such velocities ($\sim$ 5000kms^{-1} for loop length 1×10^9cm are highly unlikely. It is much more likely that this observed correlation indicates the upward motion of the acceleration region through the atmosphere.

Chapter 6

Conclusions and Future Work

" A conclusion is the place where you get tired of thinking"

Arthur Block

6.1 Introduction

The purpose of this chapter is to provide a general overview of the work described in the previous chapters and overall conclusions to the results of this thesis. In addition suggestions for improvements to the analysis and possibilities for further developing this work are made.

6.2 Overview

The aim of this project was to extensively investigate the effects inclusion of the nonuniform ionisation profile of the solar atmosphere has on the HXR thick target bremsstrahlung spectra first discussed in Brown (1973a). This previous analysis considered only the properties of the resultant photon spectrum. Here we have expanded this work to determine the effects on the inversion of the HXR spectra for the parent electron spectra. In addition, as the change in ionisation imparts some information on the spatial characteristic of the flare into the spatially unresolved HXR spectra we have developed a method to determine the amount of material between acceleration/injection region and the transition region.

6.3 Conclusions

6.3.1 Non-Uniqueness of Inverted Parent Electron Spectra

By approximating the ionisation profile of the solar atmosphere by a step function, the electron spectra for a nonuniform atmosphere can be related to that of a uniformly ionised atmosphere by a functional equation. This equation clearly shows that in certain conditions two or more different but physically acceptable electron spectra can produce identical photon spectra. This mathematical non-uniqueness of the inversion will cause great uncertainty in interpreting the characteristics of the electron spectra from the view point of understanding the particle acceleration process.

6.3.2 Supplementary Beam

The functional equation relating electron spectra for a nonuniformly and uniformly ionised atmosphere also shows clearly that for equivalent photon spectra, the spectra from the uniformly ionised source must be supplemented above a critical energy. This critical energy is the stopping energy of the corona, the initial energy of an electron which has thermalised (zero energy) at the transition region. Thus for all electrons which enter the chromosphere the flux at the electron energy at the chromosphere has to be increased by a factor ~ 1.818.

This supplementary beam is qualitatively similar to that of a secondary component identified in the thick target electron spectra of the 27th June 1980 flare. With regularised numerical inversion of this high resolution HXR spectra we showed that smooth power law electron spectra was possible with a suitably chosen depth of chromosphere. The significant difference in electron spectra, for an ionised atmosphere, from the two different inversion techniques and bremsstrahlung cross-sections used by Lin et al 1993 and in this thesis prevents this secondary component as simply being interpreted as due to not accounting for the change in ionisation.

6.3.3 Determining Column Density of the Corona

By assuming that the main spectral feature observed in the HXR spectra (i.e. the break in the power law) is caused by the increased bremsstrahlung efficiency of the chromosphere and not an original feature in the electron spectra (i.e. electron spectra is a power law)

then the HXR spectra can be expressed analytically as the combination of a power law and incomplete beta function. This analytic expression is only for a step-function ionisation profile and Kramer's bremsstrahlung cross-section.

The HXR spectra can be forward fitted with the Non-Uniformly Ionised Power Law Electron spectra model (NUIPLE) to determine the three variables of this model i.e. electron flux constant, electron spectra index and electron stopping energy of corona. As this stopping energy can be easily converted into a column density of the total material the electron passed through to reach the chromosphere this fitting procedure allows estimation of the coronal column density. The estimated values for a selection of flares observed by HXS onboard YOHKOH are consistent with alternative estimates from either soft X-ray density estimates or hard X-ray trapping estimates and time-of-flight loop lengths. However all three methods for determining the coronal column density require vast simplifications of the models and in the case of the SXT loop, there is no certainty that the estimate should be consistent as it is likely the path of the hard X-ray producing electrons and SXT loop are not spatially coincident.

6.3.4 Correlation between Beam Flux and Coronal Column Density

The estimated NUIPLE model parameters of electron beam flux constant and electron spectral index allows the energy flux of the electron beam to be calculated. This is provided a low energy cut-off in the electron spectra is assumed, in this analysis a constant value of $E_{min} = 20$ keV was chosen. The evolution of total beam flux and coronal column density showed a significant correlation. This correlation not only indicates the close relationship between injected beam energy flux and chromospheric evaporation, but as the total column density varies with the beam flux and not a cumulative function of the beam flux i.e. not the total amount of evaporated material, then this would suggest that the beam is continually entering unheated and unevaporated loops. For this to occur we would expect that the acceleration region is moving upward through the atmosphere. This model is also consistent with observations of the hard X-ray footpoints sources separating during the course of the flare and electron time-of flight loop length measurements which put the acceleration region well above the soft X-ray loop. In addition the correlation between coronal column density and beam energy flux for each flare or period of flare analysed seems significant. Together though they show a clear separation in the relationship between

column density and beam flux for large X class flares or the smaller M class flares.

6.4 Improvements to Analyses

As always improvements to the analysis techniques used in this thesis can be made. One of the major improvements to be made is the estimation of the errors on the parameters of the NUIPLE model spectral fits. At present these error estimates, calculated from the diagonal elements of the Hessian are extremely underestimated. While this underestimation may be generated by the partial derivatives of the beta function being numerically approximated rather than analytically expressed it is more likely that the error is caused by computation accuracy limitation invoked because of poor scaling of the problem. With appropriate scaling the estimated error should become physically reasonable. The magnitude of the spectral parameters and correlations between them should be unaffected by this scaling. As when the curvature matrix was changed, the final estimates are unaltered, only the route to find the best fit is changed.

There is evidence that the χ^2 space has many local minima, thus, as in all least-square fitting, we must always be aware that the estimated parameters are only at a local minimum in χ^2 and that the global best fit may not have been achieved. One way to prevent this would be to apply a genetic algorithm in fitting. Not only would this method try to ensure a global minimum but the high dependency on determining accurately the initial estimates would be removed although improving the approximated relationship between the double power law parameters and the column density and spectral index would also help.

The oscillatory and divergent nature of some of the reconstructed electron spectra in Chapter 3 would indicate that a positivity constraint needs to be explicitly demanded of the smoothing function. When the ratio of counts and background is small at high energy the positivity constraint would stop the rapid decline seen. Alternatively tighter restrictions on the energy range of inversion, to include only channels with flux well above noise levels may improve the situation.

6.5 Further Work

Possibilities for future hard X-ray analysis abound with the imminent launch of HESSI. In the context of this thesis two main areas of further work are clearly evident. Firstly the dependence of the reconstructed electron spectra on either bremsstrahlung cross-section or amount of smoothing, seen clearly in the difference between Lin and Johns recovered electron spectra and our own, needs further investigation. With inversion of high resolution HXR spectra becoming possible for many flares, the differences in recovered electron for different inversion techniques must be understood or at least appreciated.

Secondly the apparent correlation between beam flux and coronal column density needs to be investigated further. One priority is to ensure that the correlation is not somehow an artifact of the fitting procedure. If for generated spectra, for which we know there to be no correlation between beam parameters and atmosphere parameters, the correlation is still found, then we will be forced to assume the correlation is merely a quirk of the fitting routines. If this proves not to be the case then further investigation on how the relationship between column density and beam flux differs depending on size/class of flare. Also the amount of evaporation is not simply dependent on the beam flux, but on the initial column density, the cut-off in the spectrum and spectral index and many others. The question to be answered is does the inferred amount of evaporation estimated from the increases in column density agree with the existing models on chromospheric evaporation. It would also be interesting to determine how well the modelled height distribution of the hard X-rays along the loop match the observations for such estimated column densities.

Bibliography

Alexander, D. and Metcalf, T. R.: 1997, *Astrophys. J.*, **489**, 442.

Alfvén, H. A.: 1939, *Phys. Rev.*, **55**, 245.

Aschwanden, M. J. and Benz, A. O.: 1997, *Astrophys. J.*, **480**, 825.

Aschwanden, M. J., Hudson, H., Kosugi, T., and A., S. R.: 1996a, *Astrophys. J.*, **464**, 985.

Aschwanden, M. J., Hudson, H., Kosugi, T., and Schwartz, R. A.: 1996c, *Astrophys. J.*, **470**, 1198.

Aschwanden, M. J., Wills, M. J., Hdson, H. S., Kosugi, T., and Schwartz, R. A.: 1996b, *Astrophys. J.*, **468**, 398.

Bai, T.: 1982, *Astrophys. J.*, **259**, 341.

Bai, T. and Dennis, B. R.: 1985, *Astrophys. J.*, **292**, 699.

Bai, T., Hudson, H. S., Pelling, R. M., Lin, R. P., and Schwartz, R. A.: 1983, *Astrophys. J.*, **267**, 433.

Bai, T. and Ramaty, R.: 1979, *Astrophys. J.*, **227**, 1072.

Baker, C. T. H.: 1977, *The Numerical Treatment of Integral Equations,*, Oxford University Press, Oxford.

Benka, S. G. and Holman, G. D.: 1992, *Astrophys. J.* **391**, 854.

Benka, S. G. and Holman, G. D.: 1994, *Astrophys. J.*, **435**, 469.

Bhatia, A. K., Fawcett, B. C., Lemen, J. R., Mason, H. E., and Phillips, K. J. H.: 1989, *Monthly Notices Roy. Astron. Soc.*, **240**, 421.

Brown, J. and Melrose, D. B.: 1977, *Solar Physics* **52**, 117.

Brown, J. C.: 1971, *Solar Physics,* **18**, 489.

Brown, J. C.: 1972, *Solar Physics,* **26**, 441.

Brown, J. C.: 1973a, *Solar Physics,* **28**, 151.

Brown, J. C.: 1973b, *Solar Physics,* **31**, 143.

Brown, J. C.: 1975, in S. R. Kane (ed.), *Solar γ-, X-, and EUV Radiation,*, p. 245., IAU in cooperation with COSPAR, D. Reidel.

Brown, J. C. and Bingham, R.: 1984, *Astron. Astrophys.,* **131**, L11.

Brown, J. C., Conway, A. J., and Aschwanden, M. J.: 1998a, *Astrophys. J.,* **509**, 911

Brown, J. C., Craig, I. J. D., and Karpen, J. T.: 1980, *Solar Physics,* **67**, 143.

Brown, J. C. and Emslie, A. G.: 1988, *Astrophys. J.,* **331**, 554.

Brown, J. C. and MacKinnon, A. L.: 1985, *Astrophys. J. Lett.,* **292**, L31.

Brown, J. C., McArthur, G. K., Barrett, R. K., McIntosh, S. W., and Emslie, A. G.: 1998b, *Solar Physics* **179**, 379.

Brown, J. C. and McClymont, A. N.: 1975, *Solar Physics,* **41**, 135.

Brown, J. C., Melrose, D. B., and Spicer, D. S.: 1979, *Astrophys. J.,* **228**, 592.

Canfield, R. C., Hudson, H. S., Leka, K. D., Mickey, D. L., Metcalf, T. R., Wülser, J.-P., Acton, L. W., Strong, K., Kosugi, T., Sakoa, T., Tsuneta, S., Culhane, J. L., Phillips, A., and Fludra, A.: 1992, *Publ. Astron. Soc. Japan,* **44**, L111.

Chubb, T. A., Kreplin, R. W., and Freidman, H.: 1966, *J. Geophys. Res.,* **71**, 3611.

Cliver, E. W., Dennis, B. R., Kiplinger, A. L., Kane, S. R., Neidig, D. F., Shelsey, N. R., and Koomen, M. J.: 1986, *Astrophys. J.,* **305**, 920.

Conway, A. J., MacKinnon, A. L., Brown, J. C., and McArthur, G.: 1998, *Astron. Astrophys.,* **331**, 1103.

Craig, I. J. D. and Brown, J. C.: 1986, *Inverse Problems in Astronomy*, Hilger,Bristol.

Crannell, C. J., Frost, K. J., Matzler, C., Ohki, K., and Saba, J. L.: 1978, *Astrophys. J.,* **223**, 620.

Cromwell, D., McQuillan, P., and Brown, J. C.: 1988, *Solar Physics* **115**, 289.

Culhane, J. L., Phillips, A. T., Pike, C. D., Fludra, A., Betley, R. D., Bromage, B. J., Doschek, G. A., Hiei, E., Inda, M., Mariska, J. T., Phillips, K. J. H., Sterling, A. C., and Watanabe, T.: 1993, *Adv. Space Res.,* **13(9)**, 303.

Datlowe, D. W., O'Dell, S. L., Peterson, L. E., and Elcan, M. J.: 1977, *Astrophys. J.,* **212**, 561.

Dennis, B. R., Frost, K. J., and Orwig, L. E.: 1981, *Astrophys. J. Lett.,* **244**, L167.

Dennis, B. R., Holman, G. D., Hudson, H. S., Kosugi, T., Strong, K. T., and Zarro, D.: 1994, in S. Enome and T. Hirayama (eds.), *Proceedings of the Kofu Symposium*, pp

217–219.

Duijveman, A., Hoyng, P., and Machado, M. E.: 1982, *Solar Physics,* **81**, 137.

Dulk, G. A., Kiplinger, A. L., and Winglee, R. M.: 1992, *Astrophys. J.,* **389**, 756.

Elcan, M. J.: 1978, *Astrophys. J. Lett.,* **236**, L99.

Ellison, D. C. and Ramaty, R.: 1985, *AStrophys. J.,* **298**, 400.

Emslie, A. G.: 1978, *Astrophys. J.,* **224**, 941.

Emslie, A. G.: 1980, *Astrophys. J.,* **235**, 1055.

Emslie, A. G.: 1981a, *Astrophys. J.,* **244**, 653.

Emslie, A. G.: 1981b, *Astrophys. J.,* **249**, 817.

Emslie, A. G. and Brown, J. C.: 1980, *Astrophys. J.,* **237**, 1015.

Emslie, A. G., Coffey, N., and Schwartz, R. A.: 1989, *Solar Physics,* **127**, 313.

Emslie, A. G., Henoux, J. C., Mariska, J. T., and Newton, E. K.: 1996, *Astrophys. J.,* **399**, 714.

Emslie, A. G. and Smith, D. F.: 1984, *Astrophys. J.,* **279**, 882.

Feldman, U., Hiei, E., Phillips, K. J. H., Brown, C. M., and Lang, J.: 1994, *Astrophys. J.,* **421**, 843.

Fenimore, E. E., Laros, J. G., Klebesadel, R. W., Stockdale, R. E., and Kane, S. R.: 1982, in R. E. Lingefelter, H. S. Hudson, and D. M. Worrall (eds.), *Gamma-Ray Transients and Related Astrophysical Phenomena,*, AIP, New York,, p. 201.

Fletcher, L.: 1995, *Astron. Astrophys.* **303**, L9.

Fletcher, L.: 1996, *Astron. Astrophys.* **310**, 661.

Fletcher, L.: 1997, *Astron. Astrophys.* **326**, 1259.

Forbes, T. G., Malherbe, J.-M., and Priest, E. R.: 1989, *Solar Physics* **120**, 285.

Frost, K. J.: 1969, *Astrophys. J. Lett.,* **158**, L159.

Frost, K. J. and Dennis, B. R.: 1971, *Astrophys. J.,* **165**, 655.

Gerassimenko, M. and Nolte, J. T.: 1978, *Solar Physics,* **57**, 103.

Golub, G. H., Heath, M., and Wahba, G.: 1979, *Technometrics* **21**, 215.

Goodrich, C. C. and Scudder, J. D.: 1984, *Journ. Geophys. Res.,* **89**, 6654

Gradshtein, I. S. and Ryzhik, I. M.: 1994, *Tables of Integrals, Series and Products,*, Academic Press, New York.

Hamilton, R. J., Lu, E. T., and Petrosian, V.: 1990, *Astrophys. J.,* **354**, 726.

Hamilton, R. J. and Petrosian, V.: 1992, *Astrophys.. J.,* **398**, 350.

Henoux, J. C., Chambe, G., Smith, D., Tamres, D., Feautrier, N., Rovira, M., and Sahal-Brechot, S.: 1990, *Astrophys. J. Suppl.,* **73**, 303

Henoux, J. C., Fang, C., and Gan, W. Q.: 1993, *Astron. Astrophys.,* **274**, 923.

Holman, G. D.: 1985, *Astrophys. J.,* **293**, 584.

Holman, G. D. and Benka, S. G.: 1992, *Astrophys. J. Lett.,* **400**, L79.

Holman, G. D., Kundu, M., and Kane, S.: 1989, *Astrophys. J.* **345**, 1050.

Hoyng, P., Brown, J. C., and van Beek, H.: 1976, *Solar Physics,* **48**, 197.

Hoyng, P., Melrose, D. B., and Adams, J. C.: 1979, *Astrophys. J.,* **230**, 950.

Hudson, H. S., Acton, L. W., Hirayama, T., and Uchida, Y.: 1992, *Publ. Astron. Soc. Japan,* **44**, L77.

Hudson, H. S., Canfield, R. C., and Kane, S. R.: 1978, *Solar Physics,* **60**, 137.

Isenberg, P. A.: 1986, *Journ. Geophys. Res.,* **91**, 1699.

Johns, C. and Lin, R. P.: 1992, *Solar Physics,* **137**, 121.

Kahler, S. W.: 1971a, *Astrophys. J.,* **163**, 365.

Kahler, S. W.: 1971b, *Astrophys. J.,* **168**, 319.

Kane, S. R.and Anderson, K. A., Evans, W. D., Klebesdel, R. W., and Laros, J.: 1979, *Astrophys. J.,* **233**, L151

Kane, S. R.: 1974, in G. Newkirk (ed.), *Coronal Disturbances*, IAU Symp. No 57.

Kane, S. R. and Anderson, K. A.: 1970, *Astrophys. J.,* **162**, 1003.

Kane, S. R., Fenimore, E. E., KLebesadel, R. W., and Laros, J. G.: 1988, *Astrophys. J.,* **326**, 1017.

Kiplinger, A. L.: 1995, *Astrophys. J.,* **453**, 973.

Kiplinger, A. L., Dennis, B. R., Emslie, A. G., Frost, K. J., and Orwig, L. E.: 1983, *Solar Physics* **86**, 239

Kiplinger, A. L., Dennis, B. R., Frost, K. J., and Orwig, L. E.: 1984, *Astrophys. J. Lett.,* **287**, L105.

Kock, H. W. and Motz, J. W.: 1959, *Rev. of Modern Physics,* **31(4)**, 920.

Korchak, A. A.: 1967a, *Astron. Zh.,* **44**, 328.

Korchak, A. A.: 1971, *Solar Physics,* **18**, 284.

Kosugi, T., Dennis, B. R., and Kai, K.: 1988, *Astrophys. J.,* **324**, 1118.

Krall, K. R., Reichmann, E. J., Wilson, R. M., Henze, W., and Smith, J. B.: 1980, *Solar Physics,* **66**, 371.

Kuczma, M.: 1968, *Functional Equations in a Single Variable*, Vol. 46 of *Polska Akademia Nauk, Monografie Matematyczna.*, PWN-Polish Scientific Publisher

Landau, L. D. and Lifshitz, E. M.: 1960., *Electrdynamics of Continuos Media*, Oxford : Pergamon.

LaRosa, T. N. and Shore, S. N.: 1998, *Astrophys. J.*, **503**, 429.

Lawson, J. D.: 1957, *Jour. Electron. Contr.*, **3**, 587.

Leach, J.: 1984, *Ph.D. thesis*, Stanford University.

Leach, J. and Petrosian, V.: 1983, *Astrophys. J.*, **269**, 715.

Lee, M. A.: 1982, *Journ. Geophys. Res.*, **87**, 5063.

Lin, R. and Schwartz, R.: 1987, *Astrophys. J.*, **312**, 462.

Lin, R., Schwartz, R. A., Pelling, R. M., and Hurley, K. C.: 1981, *Astrophys. J. Lett.*, **251**, L109.

Lin, R. P.: 1974, *Space Sci. Rev.*, **16**, 189.

Lin, R. P. and Johns, C. M.: 1993, *Astrophys. J. Lett.*, **417**, L53.

Linford, G. A. and Wolfson, C. J.: 1988, *Astrophys. J.*, **331**, 1036.

Litvinenko, Y. E.: 1996, *Astrophys. J.*, **462**, 997.

Machado, M. E., Avrett, E. H., Vernazza, J. E., and Noyes, R. W.: 1980, *Astrophys. J.* **242**, 336.

Machado, M. E., K., O., Emslie, A. G.and Fishman, G. J., Meegan, C., Wilson, R., and Paciesas, W. S.: 1993, *Adv. Space Res.*, **13(9)**, 175

Machado, M. E. and Linsky, J. L.: 1975, *Solar Physics*, **42**, 395.

MacKinnon, A. L. and Brown, J. C.: 1989, *Astron. Astrophys.*, **215**, 371.

MacKinnon, A. L., C., B. J., and Hayward, J.: 1985, *Solar Physics* **99**, 231.

MacKinnon, A. L. and Craig, I. J.: 1991, *Astron. Astrophys.*, **251**, 693.

Martens, P. C. H.: 1988, *Astrophys. J. Lett.*, **330**, L131.

Masuda, S.: 1993, *Ph.D. thesis*, University of Tokyo.

Masuda, S., Kosugi, T.and Hara, H., Sakoa, T., Shibata, K., and Tsuneta, S.: 1995, *Publ. Astron. Soc. Japan*, **47**, 677

Matthews, S. A., Brown, J. C., and Van Driel-Gesztelyl, L.: 1998, *Astron. Astrpohys.*, **340**, 277.

Matzler, C., Bai, T., Crannell, C. J., and Frost, K. J.: 1978, *Astrophys. J.*, **223**, 1058.

McClements, K. G.: 1987, *Astron. Astrophys.*, **175**, 255.

McClements, K. G. and Brown, J. C.: 1986, *Astron. Astrophys.*, **165**, 235

McKenzie, D. L., Broussard, R. M., Landecker, P. B., Rugge, H. . R., Young, R. M., Doschek, G. A., and Feldman, U.: 1980, *Astrophys. J. Lett.*, **238**, L43.

McTiernan, J. M., Kane, S. R., Hurley, K., Laros, J. G., Fenimore, E. E., Klebsadel, R. W., Sommer, M., and Yoshimori, M.: 1994, in S. Enome and T. Hirayama (eds.), *Proceedings of Kofu Syposium*, pp 389–392.

McTiernan, J. M. and Petrosian, V.: 1990b, *Astrohys. J.*, **359**, 540.

Melrose, D. B. and Brown, J. C.: 1976, *Monthly Notices Roy. Astron. Soc.*, **176**, 15.

Mewe, R., Gronenschild, E. N., and Van den Oord, G. H. J.: 1985, *Astron. Astrophys. Supp. Ser.*, **62**, 197.

Mewe, R., Lemen, J. R., and Van den Oord, G. H. J.: 1986, *Astron. Astrophys. Supp. Ser.*, **65**, 511.

Moghaddam-Taaheri, E. and Goertz, C. K.: 1990, *Astrophys. J.*, **352**, 361.

Moore, R. *et al.*: 1980, in P. A. Sturrock (ed.), *Solar Flares,*, p341., Colorado Associated University Press.

Morrison, M.: 1994, *Yohkoh Analysis Guide*, Lockheed Palo Alto Research.

Mott, N. F. and Massey, H. S. W.: 1965, *The Theory of Atomic Collisions*, Oxford University Press, 3rd. edition

Mozer, F. S., Cattell, C. A., Hudson, M. K., Lysak, R. L., Temerin, M., and Torbert, R. B.: 1980, *Space Sci. Rev.*, **27**, 155.

Newton, E. K. and Giblin, T. W.: 2000, *Astrophys. J.*, submitted.

Nitta, N. and Kentaro, Y.: 1997, *Astrophys. J.*, **484**, 927.

Pallavicini, R., Serio, S., and Vaina, G. S.: 1977, *Astrophys. J..*, **216**, 108

Papadopoulos, K.: 1977, *Rev. Geophys. Sp. Sci.*, **15**, 113.

Peterson, L. E. and Winckler, J. R.: 1959, *J. Geophys. Res.*, **64**, 697.

Petschek, H. E.: 1964, in W. N. Hess (ed.), *Physics of Solar Flares*, AAS-NASA

Phillips, K. J. H.: 1991, *Phil. Trans. R. Soc. A.*, **336**, 461.

Phillips, K. J. H., Bhatia, A. K., Mason, H. E., and Zarro, D. M.: 1996, *Astrophys. J.*, **466**, 549.

Piana, M., Brown, J. C., and Thompson, A. M.: 1995, *Solar Physics,* **156**, 315.

Press, W. H., Teukolsky, S. A., Vettering, W. T., and Flannery, B. P.: 1995, *Numerical Recipes*, Cambridge University Press, 2nd edition, Chapter 15.

Ramaty, R.: 1986, *Physics of the Sun. Vol II: The Solar Atmosphere.*, p. 291.

Ramaty, R., Mandzhavidze, N., Kozlovsky, B., and Murphy, R. J.: 1995, *Astrophys J.*, **455**, L193.

Rowland, H. L. and Vlahos, L.: 1985, *Astron. Astrophys.* **142**, 219.

Sakao, T.: 1994, *Ph.D. thesis*, University of Tokyo.

Sakao, T., Kosugi, T., Masuda, S., Inda, M., Makishima, K., Canfield, R. C., Hudson, H. S., Metscalf, T. R., Wülser, J.-P., Acton, L. W., and Ogawara, Y.: 1992, *Publ. Astron. Soc. Japan,* **44**, L83.

Share, G. H. and Murphy, R. J.: 1995, *Astrophys. J.*, **452**, 933.

Shibata, K.: 1995, *Astrophys. J.*, **451**, L83.

Simnett, G. M.: 1996, *Space Sci. Rev.*, **73**, 387.

Simnett, G. M. and Haines, M. G.: 1991, *Solar Physics.*, **130**, 253.

Smith, D. F.: 1980, *Solar Physics,* **66**, 135.

Spicer, D. S. and Sudan, R. N.: 1984, *Astrophys. J.*, **280**, 448.

Spitzer, L.: 1962, *Physics of Fully Ionised Gases*, interscience, New York, 2nd. edition

Sweet, P. A.: 1959, *Phil. Mag., Ser. 8,* **4**, 1155.

Sweet, P. A.: 1969, *Ann. Rev. Astr. Ap.*, **7**, 149.

Tanaka, K.: 1987, *Publ. Astron. Soc. Japan* **38**, 225.

Tanaka, K. and Zirin, H.: 1985, *Astrophys. J.*, **299**, 1036

Thompson, A. M.: 1990, *Astron. Astrophys.*, **240**, 209.

Thompson, A. M., Brown, J. C., Craig, I. J. D., and Fulber, C.: 1992, *Astron. Astrophys.*, **265**, 278.

Tsuneta, S.: 1985, *Astrophys. J.*, **290**, 353.

Tsuneta, S., Masuda, S., Kosugi, T., and Sato, J.: 1997, *Astrophys. J.*, **478**, 787.

Underwood, J. H. and McKenzie, D. L.: 1977, *Solar Physics,* **53**, 47.

van den Oord, G. H. J.: 1990, *Astron. Astrophys.*, **234**, 496.

van den Oord, G. H. J.: 1994, in *Fragmented Energy Release in Sun and Stars : the interface between MHD and Plasma Physics*, Kluwer.

Wheatland, M. S. and Melrose, D. B.: 1995, *Solar Physics,* **158**, 283.

Winglee, R. M., Dulk, G. A., Bornmann, P. L., and Brown, J. C.: 1991b, *Astrophys. J.* **375**, 366.

Winglee, R. M., Kiplinger, A. L., Zarro, D. M., Dulk, G. A., and Lemen, J. R.: 1991a,

Astrophys. J., **375**, 382.

Winglee, R. M., Pritchett, P. L., and Dulk, G. A.: 1988a, *Astrophys. J.*, **327**, 968.

Winglee, R. M., Pritchett, P. L., and Dulk, G. A.: 1988b, *Astrophys. J.*, **329**, 440.

Wülser, J.-P., Canfield, R. C., Acton, L. W., Culhane, J. L., Phillips, A., Fludra, A., Sakao, T., Masuda, S., Kosugi, T., and Tsuneta, S.: 1994, *Astrophys. J.*, **424**, 459.

Yoshimori, M., Takai, Y., Morimoto, K., Suga, K., Ohki, K., Watanabe, T., Yamagami, T., Kondo, I., and J., N.: 1992, *Publ. Astron. Soc. Japan*, **44**, L51.

Zarro, D. M., Mariska, J. T., and Dennis, B. R.: 1994, in S. Enome and t. Hirayama (eds.), *Proceedings of the Kofu Symposium*, pp 221–224.

Zharkova, V. V. and Syniavskii, D. V.: 1997, *Astron. Astrophys.*, **320**, L13.

Zirin, H.: 1988, *Astrophysics of the Sun*, C.U.P.

Zirin, H. and Tanaka, K.: 1973, *Solar Physics*, **32**, 173.